FZD-512

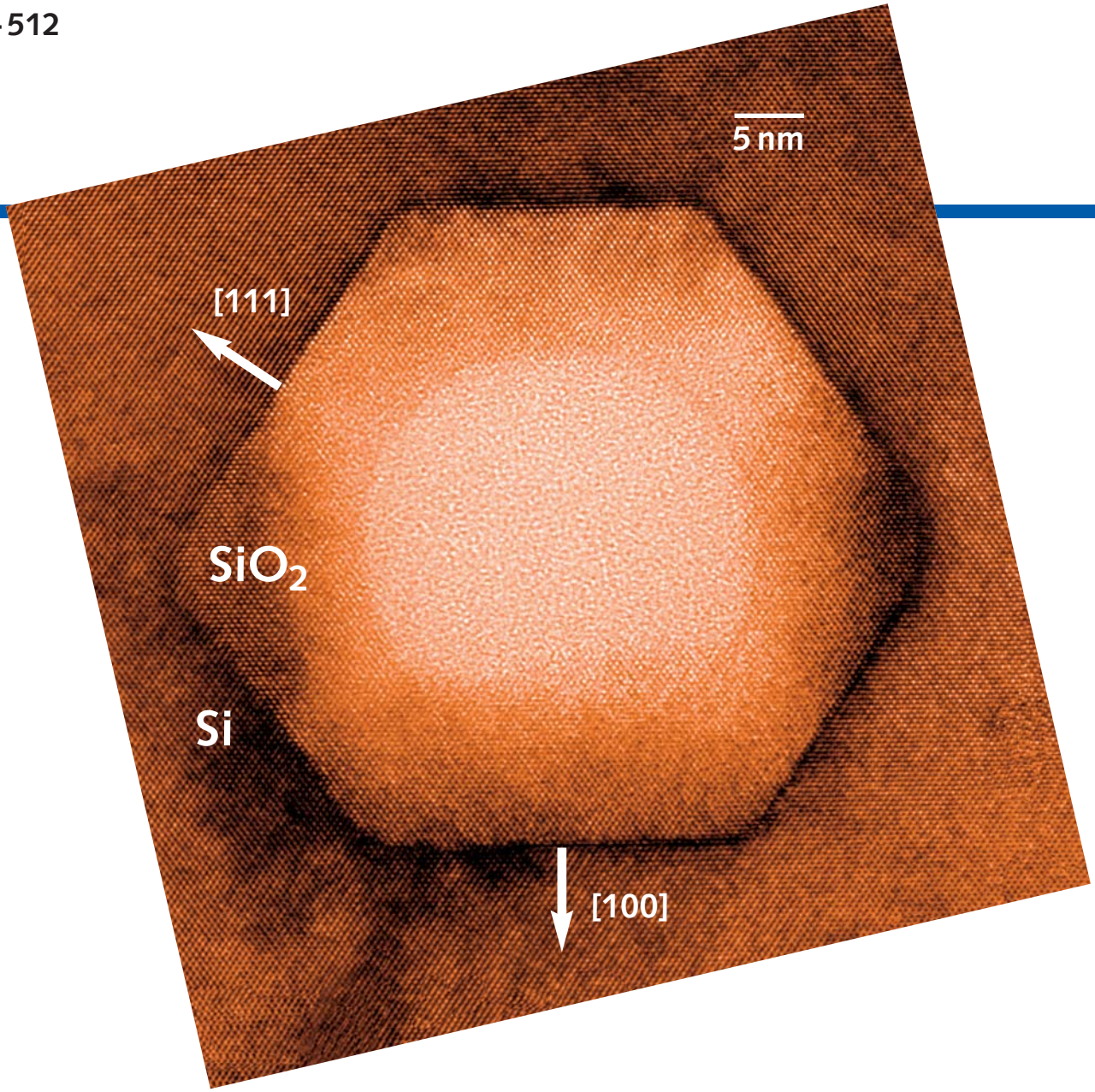

Wissenschaftlich-Technische Berichte
FZD-512 2009 · ISSN 1437-322X

ANNUAL REPORT 2008

INSTITUTE OF ION-BEAM PHYSICS AND MATERIALS RESEARCH

Forschungszentrum
Dresden Rossendorf

Wissenschaftlich-Technische Berichte
FZD – 512
2009

Annual Report 2008

Institute of Ion Beam Physics and Materials Research

Editors:

J. von Borany, V. Heera,
M. Helm, W. Möller

Cover Picture:

Graphically adapted nanosized cavity in Si with oxide grown at the inner surface, obtained after implantation of 45 keV He^+ at a fluence of $4x10^{16}$ cm^{-2} and 160 keV O^+ at 10^{17} cm^{-2}, and subsequent annealing. The oxidation proceeds with different speed along the different crystalline directions, so that the originally spherical cavity is turned into a facetted precipitate. Depending on the available oxygen content and the annealing conditions, the cavity can be partly or completely filled with amorphous SiO_2.

For further information see:
X. Ou et al., Appl. Phys. Lett. **93**, 161907 (2008),
reprinted at pp. 31-33 of this Annual Report.

Forschungszentrum Dresden - Rossendorf e.V.
Institut für Ionenstrahlphysik und Materialforschung
Postfach 51 01 19
D-01314 Dresden
Bundesrepublik Deutschland

Direktoren	Prof. Dr. Wolfhard Möller	Prof. Dr. Manfred Helm
Telefon	+ 49 (351) 260 2245	+ 49 (351) 260 2260
Telefax	+ 49 (351) 260 3285	+ 49 (351) 260 3285
E-mail	w.moeller@fzd.de	m.helm@fzd.de
Homepage	http://www.fzd.de/FWI	

Preface by the Directors

The "Advanced Materials" program activities of Forschungszentrum Dresden-Rossendorf (FZD) are to a large fraction delivered by the Institute of Ion Beam Physics and Materials Research (IIM) in the fields of semiconductor physics and materials research using ion beams. The institute operates a national and international Ion Beam Center (IBC), which, in addition to its own scientific activities, makes available fast ion technologies to universities, other research institutes, and industry. Parts of its activities are also dedicated to exploit the infrared/THz free-electron laser at the 40 MeV superconducting electron accelerator ELBE for condensed matter research. For both facilities the institute holds EU grants for funding access of external users. Cooperation with the High Magnetic Field Laboratory Dresden (HLD), another institute of FZD, has produced first novel results.

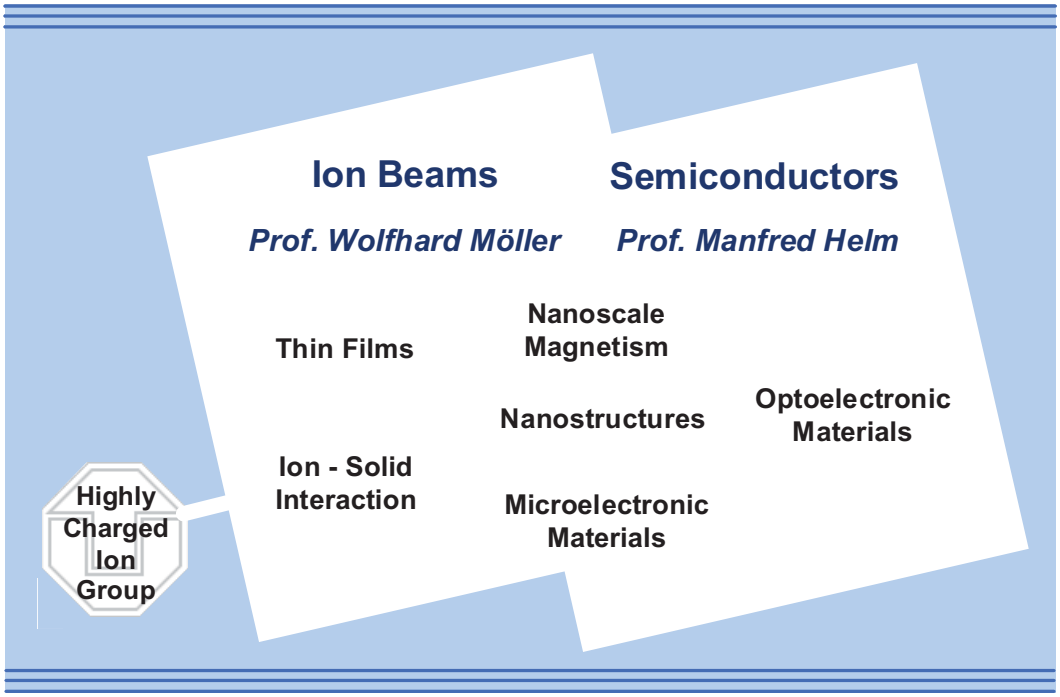

The diagram displays the presently six R&D topics of the institute, together with the associated Highly Charged Ion (HCI) Group of the TU Dresden. Our research activities span a wide range of topics relevant for future information processing and energy technology, be it in the realm of nanoelectronics, optoelectronics, magnetoelectronics, spintronics and solar technology. Highlights of last year's research are presented in this Annual Report through reprints of short papers that were published in leading international journals. IIM staff published more than 140 papers in peer-reviewed journals in 2008. Thereof, more than 50 contributions to high-impact journals (impact factor larger than 3) confirm a continuous enhancement of the average quality of the scientific output during recent years.

2008 has also been an excellent year with respect to third party funding, which, at a total amount of about 7.5 million euro, exceeded the average of the past years by about 300%. Main contributions are from a project "Concepts of multifunctional memories" funded by the German Federal Government, and by the Free State of Saxony for the installation of a 6 MV electrostatic tandem accelerator, which will replace the outdated 5 MV device which had been running for more than 30 years. This investment points into the future of the Ion Beam Centre, as does the successful application for an EC Integrated Infrastructure Initiative SPIRIT, which, under the coordination of FZD, combines 11 leading European institutions for transnational use of ion technologies and their development. Another essential part of funding arises from direct contracts with industry, including

also local microelectronics and other high-tech industry. Thus also our funding spectrum reflects our span from successful basic science to relevant applied research.

We further recall the very positive statements by the German Wissenschaftsrat (Science Council) after the evaluation of FZD in November 2007, which opened the way for a future membership in the German Helmholtz Science Organisation (from 2011). In September 2008, the institute together with the Institute of Surface Modification, Leipzig, organized the 16th International Conference on Ion Beam Modification of Materials at Dresden, with 330 participants from all over the world.

Special thanks are due to Dr. Rainer Grötzschel, who officially retired in December after heading our division of Ion Beam Analysis since the foundation of the Forschungszentrum Rossendorf in 1992. With his deep expertise and intense dedication, he has been one of the key persons in developing the ion beam centre, expanding its international reputation, and making it attractive for numerous external users from science and industry worldwide. We are very happy that Rainer will still be at the laboratory part-time, at least for another year.

We cordially thank all partners, friends, and organizations who supported our progress in 2008. Special thanks are due to the Executive Board of the Forschungszentrum Dresden-Rossendorf, the Minister of Science and Arts of the Free State of Saxony, and the Minister of Education and Research of the Federal Government of Germany. Numerous partners from universities, industry and research institutes all around the world contributed essentially, and play a crucial role for the further development of the institute. Last but not least, the directors would like to thank all IIM staff for their efforts and excellent contributions in 2008.

Prof. Wolfhard Möller

Prof. Manfred Helm

Contents

Selected Publications

Statistics

Selected Publications

Copyright Remarks

The following journal articles are reprinted with kind permission from

R. Heller, S. Facsko, R. A. Wilhelm, and W. Möller
Defect mediated desorption of the KBr(001) surface induced by single highly charged ion impact
Physical Review Letters, Vol. **101**, Issue 9, Art.No. 096102, 2008.

Q. Xu, L. Hartmann, S. Zhou, A. Mücklich, M. Helm, G. Biehne, H. Hochmuth, M. Lorenz, M. Grundmann, and H. Schmidt
Spin manipulation in Co-doped ZnO
Physical Review Letters, Vol. **101**, Issue 7, Art.No. 076601, 2008.

Q. Xu, H. Schmidt, S. Zhou, K. Potzger, M. Helm, H. Hochmuth, M. Lorenz, A. Setzer, P. Esquinazi, C. Meinecke, and M. Grundmann
Room temperature ferromagnetism in ZnO films due to defects
Applied Physics Letters, Vol. **92**, Issue 8, Art.No. 082508, 2008.

K. Potzger, S. Zhou, Q. Xu, A. Shalimov, R. Grötzschel, H. Schmidt, A. Mücklich, M. Helm, and J. Fassbender
Ferromagnetic structurally disordered ZnO implanted with Co ions
Applied Physics Letters, Vol. **93**, Issue 23, Art.No. 232504, 2008.

S. Zhou, Q. Xu, K. Potzger, G. Talut, R. Grötzschel, J. Fassbender, M. Vinnichenko, J. Grenzer, M. Helm, H. Hochmuth, M. Lorenz, M. Grundmann, and H. Schmidt
Room temperature ferromagnetism in carbon-implanted ZnO
Applied Physics Letters, Vol. **93**, Issue 23, Art.No. 232507, 2008.

M. Voelskow, R. Yankov, W. Skorupa, J. Pezoldt, and T. Kups
Buried melting in germanium implanted silicon by millisecond flash lamp annealing
Applied Physics Letters, Vol. **93**, Issue 15, Art.No. 151903, 2008.

X. Ou, R. Kögler, A. Mücklich, W. Skorupa, W. Möller, X. Wang, J.W. Gerlach, and B. Rauschenbach
Efficient oxygen gettering in Si by coimplantation of hydrogen and helium
Applied Physics Letters, Vol. **93**, Issue 16, Art.No. 161907, 2008.

R. Kögler, X. Ou, W. Skorupa, and W. Möller
The origin of the energy-dose window in separation-by-implanted-oxygen materials processing
Applied Physics Letters, Vol. **92**, Issue 18, Art.No. 181906, 2008.

L. Rebohle, J. Lehmann, S. Prucnal, A. Kanjilal, A. Nazarov, I. Tyagulskii, W. Skorupa, and M. Helm
Blue and red electroluminescence of Europium-implanted metal-oxide-semiconductor structures as a probe for the dynamics of microstructure
Applied Physics Letters, Vol. **93**, Issue 7, Art.No. 071908, 2008.

J. M. Sun, L. Rebohle, S. Prucnal, M. Helm, and W. Skorupa
Giant stability enhancement of rare-earth implanted SiO_2 light emitting devices by an additional SiON protection layer
Applied Physics Letters, Vol. **92**, Issue 7, Art.No. 071103, 2008.

D. Stehr, M. Wagner, H. Schneider, M. Helm, A. M. Andrews, T. Roch, and G. Strasser
Two-color pump-probe studies of intraminiband relaxation in doped GaAs/AlGaAs superlattices
Applied Physics Letters, Vol. **92**, Issue 5, Art.No. 051104, 2008.

F. Peter, S. Winnerl, H. Schneider, M. Helm, and K. Köhler
Terahertz emission from a large-area GaInAsN emitter
Applied Physics Letters, Vol. **93**, Issue 10, Art.No. 101102, 2008.

H. Schneider, H. C. Liu, S. Winnerl, O. Drachenko, M. Helm, and J. Faist
Room-temperature midinfrared two-photon photodetector
Applied Physics Letters, Vol. **93**, Issue 10, Art.No. 101114, 2008.

PRL **101,** 096102 (2008) PHYSICAL REVIEW LETTERS week ending 29 AUGUST 2008

Defect Mediated Desorption of the KBr(001) Surface Induced by Single Highly Charged Ion Impact

R. Heller,* S. Facsko, R. A. Wilhelm, and W. Möller

Institute of Ion Beam Physics and Materials Research, Forschungszentrum Dresden-Rossendorf, Bautzner Landstr. 128, 01328 Dresden, Germany

(Received 16 May 2008; published 26 August 2008)

The individual impacts of slow (300 eV/amu) highly charged Xe ions induce nanometer sized pitlike structures on the KBr (001) surface. The volume of these structures shows a strong dependence on the ions potential energy. Total potential sputter yields from atomically flat (001) terraces are determined by imaging single ion impact sites. The dependence of the sputter yield on the ions initial charge state combined with structure formation at low and high-fluence irradiations indicates that agglomeration of defects into complex centers plays a major role in the desorption process induced by the potential energy.

DOI: 10.1103/PhysRevLett.101.096102 PACS numbers: 68.43.−h, 61.72.J−, 61.80.Jh, 79.20.Rf

Slow highly charged ions (HCIs) open specific posibilities of surface structuring due to the dissipation of their potential energy [1]. The high local electronic excitation within the impact site of an HCI is comparable to that induced by swift heavy ion bombardment [2,3] and surface treatment by ultra short laser pulses [4]. However, slow HCI impact is characterized by a much sharper localization of electronic excitation in normal and lateral direction, respectively. Correspondingly, HCIs have been proposed as a tool for surface modifications and analysis on the nanometer scale [5,6]. The potential energy as a unique parameter of HCIs has brought out many new interesting phenomena in ion surface interaction within the last decades as, e.g., hollow atom formation [7], increased secondary electron yields [8], and potential sputtering [9,10]. Furthermore, the potential energy conversion may result in permanent local changes of the electronic structure or changes in the topography of insulating materials [11]. Recently, HCI induced hillock structures have been observed on CaF_2 which have been explained by a solid-liquid phase transition at the surface induced solely by the excitation from the potential energy [12]. For metallic systems the potential energy dissipation was found to contribute less effectively to surface nanostructuring [13].

While energy deposition and sputtering with singly charged ions is mostly well understood, potential sputtering (PS) of insulators by highly charged ions has been much less investigated. Aumayr *et al.* determined total sputter yields of multiply charged Ar and Xe ions on insulating (LiF, NaCl, SiO_2, and MgO), semiconducting (Si and GaAs) and metallic (Au) surfaces by means of a micro balance technique [14]. For insulators, a strongly enhanced sputtering with increasing potential energy was obtained whereas the kinetic energy influences the sputter yield only to a minor extent. The potential sputtering of alkali halides and SiO_2 was explained by desorption mediated by defects created by the electronic excitation [15]. This mechanism had already been identified in the 1970's to be responsible for the electron and ion induced desorption of alkali halides [16,17]. As a special behavior, the sputtering of MgO shows a pronounced synergism of the potential and the kinetic energy. This so-called kinetically assisted potential sputtering was ascribed to the interaction of kinetically induced lattice distortion with the electronic defects induced by the potential energy dissipation [18]. For semiconductors and metals, no influence of the potential energy on the sputter yields could be identified. The results described above were obtained with polycrystalline samples, and comparatively high ion fluences (10^{13}–10^{15} cm^{-2}) were applied. Thus collective or roughness effects could not be ruled out and local changes of the surface topography associated with potential sputtering could not be observed.

In the present Letter we describe atomic force microscopy studies of KBr(001) single crystals after low-fluence bombardment with multiply charged ($Q = 3, \ldots, 34$) slow Xe ions. We show that individual HCI impact leads to the formation of nanometer sized pitlike structures with the depth of one atomic layer. From the atomic force microscopy (AFM) images total sputter yields from atomically flat terraces are determined quantitatively and the morphological changes induced by the potential energy deposition are observed microscopically. Evidence is found that the desorption process is initiated by complex defect centers induced by the high excitation from the potential energy.

KBr single crystals were cleaved in (001) direction in air. Via a transfer system, they were brought into an irradiation chamber with a base pressure of 1×10^{-9} mbar. Subsequently, the samples were heated to a temperature of about 450 K for at least 1 h in order to remove possible contaminants from the surface. During irradiation the samples were kept at room temperature. Highly charged Xe ions ($Q = 3, \ldots, 34$) were delivered from an electron beam ion trap (EBIT) [19]. After charge separation via a dipole bending magnet, the ions were decelerated to a fixed kinetic energy of 300 eV/amu by means of a two stage deceleration lens system. A circular ion beam spot of about 2 mm diameter was scanned at

normal incidence over an area of 1 cm × 1 cm on the target. After irradiation with fluences from 5×10^9 cm^{-2} to 2×10^{13} cm^{-2} and fluxes between 1×10^5 and 5×10^8 ions/s which are fairly low enough to prevent any collective effects, the samples were taken out of the vacuum chamber and immediately transferred into the UHV-AFM device (base pressure 1×10^{-10} mbar). The surface topography of the irradiated samples was observed applying contact atomic force microscopy in constant force mode with commercially available silicon cantilevers (tip radius nominally 7 nm) and typically applied forces of 2–3 nN.

Figure 1 shows topographic contact mode AFM images of the virgin surface (a), and after irradiation with Xe^{34+} ions with a potential energy of 23 keV, a kinetic energy of 300 eV/amu, and a fluence of 7×10^9 cm^{-2} (b). Freshly cleaved KBr surfaces typically exhibit large atomically flat terraces of up to 1 μm × 1 μm separated by single-step edges, as seen at the upper right edge of frame (a). The irradiated surface features small rectangular pit-like structures with a lateral size of 15–25 nm and a depth of ≈0.35 nm, corresponding to one atomic layer. The pit density is in fair agreement with the applied fluence, so we conclude that each HCI creates one pit. The irradiation procedure was repeated on numerous samples for different ion charge states from 3 to 34 to identify the influence of the potential energy on the pit formation.

For each irradiated sample several AFM images were recorded within the beam spot and statistically analyzed with respect to the pit density and volume. Figure 2 shows the measured dependence of the pit volume on the potential energy. The error bars represent the statistical error resulting from the different measurements. The pit volume shows a well-defined linear dependence on the potential energy. Because the pits are only one monolayer deep the volume increase originates from an increased average lateral size (see insets of Fig. 2). The lateral dimensions of the structures are subject to an error by the convolution with the tip shape. With a nominal tip curvature radius of around 7 nm, the error of the volume results as ≈10 nm^3, which is well within the shown error bars. The minimum resolvable pit volume is around 10 nm^3. The right axis in Fig. 2 represents the total sputter yield, which is determined from the pit volume. In the potential energy range of 2–23 keV sputter yields of 800 to 2800 atoms (K + Br) per incident HCI are obtained.

For samples irradiated with lower charge states Q of 3, 5, and 10 no pits could be identified, although the extrapolation of the dashed line in Fig. 2 would predict a size which should be observable within the experimental resolution. Furthermore, one would expect that the extrapolation of the data from Fig. 2 to zero potential energy results in the collisional sputter yield. However, TRIM simulations for Xe ions with a kinetic energy of 300 eV/amu give a sputter yield of only 5 atoms per incident ion, corresponding to a pit volume of <1 nm^3. This is 2 orders of magnitude below the value expected from the extrapolation, which might indicate that kinetically assisted potential sputtering is also effective in KBr.

It is well known that during electron bombardment of alkali halides monoatomic deep pits are created at the surface by electron stimulated desorption (ESD), which grow and interlink at increasing irradiation time, resulting in a layer by layer erosion [20–22]. A keV electron creates a large number of electron-hole pairs along its trajectory through an ionic crystal. Because of the strong electron-phonon coupling of the ionic lattice these defects become rapidly self-trapped (self-trapped exciton—STE) [21] and subsequently decay into color centers, i.e., an H center (an interstitial molecular halide ion) and an *F* center (an electron at an anion site). The independent diffusion of both centers and their subsequent recombination with the surface lead to the desorption of halide atoms and alkali atoms, respectively. When the H center recombines with the surface a loosely bound halogen ad-atom is created

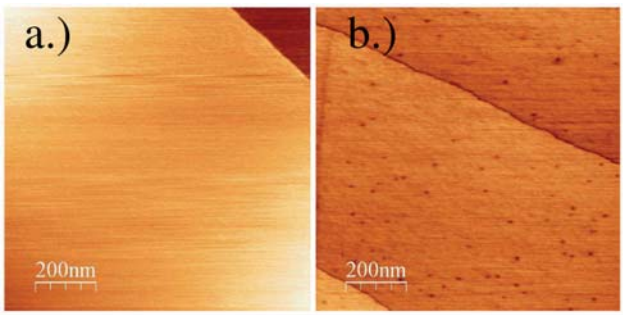

FIG. 1 (color online). Contact mode AFM topographic images of a KBr(001) surface (a) unirradiated, and (b) irradiated with Xe^{34+} at a kinetic energy of 300 eV/amu and a fluence of 7×10^9 cm^{-2}. Created nanopits are seen as dark spots in (b).

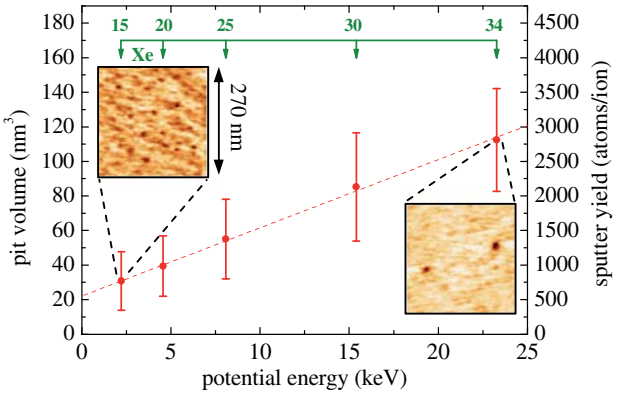

FIG. 2 (color online). Pit volume (left axis) and corresponding total sputter yield (right axis) as a function of the potential energy of the ions. The corresponding charge states are given on the upper scale. The insets show topographic AFM images (270 nm × 270 nm) for irradiation with the lowest and highest charge state, at fluences of 3.5×10^{10} cm^{-2} and 3×10^9 cm^{-2}, respectively.

which evaporates thermally. Further, the F center could recombine with the surface by neutralizing an alkali ion leading to its desorption, but as pointed out by Puchin *et al.* [23], an energy deficit exists for this process as long as the F center resides in its ground state. The $2p$-excited F^* center was found to have enough energy to initiate the alkali atom desorption, and low coordinated surface sites (i.e., terrace edges, kinks, and corners) were found to be preferential points for the desorption process.

Whereas the growth of pits during electron bombardment represents a collective effect requiring several F^* centers to diffuse from the bulk to the surface, the formation of pits by single impact of an HCI, as presented in this work, has to be related to the simultaneous creation of numerous defects within a small area. The interaction between the HCI and the crystal starts from a critical distance r_c ($\approx$1 nm) above the surface (see Ref. [24] and references therein). From this point electrons are resonantly captured from the valence band of the surface into highly excited Rydberg states of the approaching ion. A hollow atom (HA) is formed [25]. Subsequent deexcitation of the HA proceeds via nonradiative Auger decay leading to the emission of low energy electrons ($\approx$1 eV–100 eV). The electron capture by the incoming ions leaves unbalanced holes within the valence band of the crystal surface. During the impact of the HCI a significant fraction of its potential energy is emitted by energetic (up to keV) inner-shell Auger electrons within the first atomic layers of the crystal on a fs time scale [26]. Further holes are created by resonant neutralization, continuing until the HCI is fully relaxed by Auger decays. These holes can convert into STE by trapping available electrons from the HA decay. Thus a significant number of electronic defects is created within the impact site. In addition high energy Auger electrons from the inner-shell deexcitation can initiate defect creation processes like in the case of ESD. However, the process differs from ESD in two essential points: (i) defect creation takes places in a predamaged surface and (ii) the density of the electrons is much higher than during ordinary electron bombardment.

While the pit growth during ESD can be explained by preferential annihilation of F^* centers at existing step edges, the mechanisms for the creation of the first pits at the very beginning of the desorption process remained so far unclear. Therefore, it was suggested that several F/F^* centers could agglomerate into X centers which should be able to initiate desorption even at the perfect 001 surface [21,27]. However, for ESD it was estimated that the density of F/F^* centers created along the electron trajectory is too low to render this process dominant. In contrast, the HCI impact creates numerous F/F^* centers within a small volume of only a few nm^3. In this way, the interaction between defects becomes increasingly important. Since the number of created defects within the volume of interaction depends on the initial charge state (potential energy) of the projectile only, the observed increased volume of the pits for higher charged states becomes plausible. From the absence of pits for the lowest Xe charge states ($Q = 3$, 5, and 10) we conclude that a certain number of defects per unit area is necessary to induce this defect agglomeration and thus the desorption.

The defects described above may also be generated by collisional damage along the ion track, which is associated with the kinetic energy of the ion. From TRIM using standard parameters, a total number of roughly 500 collisionally generated Frenkel pairs is obtained which are generated per incident ion within a depth of about 50 nm. Assuming that a significant fraction of these would contribute to desorption via diffusion to the surface, the observed offset in Fig. 2 could be interpreted as an enhancement by kinetic energy deposition, provided the potential energy is sufficient for pit formation.

In order to further elucidate the role of defect agglomeration we performed additional irradiation at higher fluences for two selected charge states $Q = 3$ and $Q = 25$. As shown above, single Xe ion impact for $Q = 3$ does not create any *individual* pits. In contrast, high-fluence irradiation results in the formation of well-defined pits as seen in Fig. 3(a). However, the density of pits is about 3 orders of magnitude less than the applied ion fluence. In accordance with the above considerations, these structures are ascribed to originate from diffusing F^* centers created in the bulk along the ion trajectories (independent on their charge state). This picture is confirmed by the following observations: (i) the pits show a significantly larger spread of their width [see Fig. 3(c)] compared to the pits formed by individual ions of sufficiently high charge state [see Fig. 3(d)], and (ii) within a certain distance to existing terrace edges no pits are found. An F^* center that reaches the surface in the proximity of such a step edge will rather recombine at the low coordinated surface site than create a new pit. Because of the additional desorption from terrace edges for the high-fluence–low-charge state irradiation it is not possible anymore to evaluate sputter yields from the pit volume as described above. Figure 3(b) shows the surface topography after bombardment with Xe^{25+} ions with a fluence of 1×10^{11} cm^{-2}, which is 100 times higher than in Fig. 1. The corresponding size and depth distribution of pits are shown in Figs. 3(d) and 3(f), respectively. Compared to the low-fluence case, the width distribution broadens by a factor of about two and is only slightly shifted to larger width. However, the depth distribution is now composed of two peaks corresponding to one monolayer and two monolayers, respectively. This is attributed to two subsequent hits of the same surface area. From Fig. 2, the mean pit area at $Q = 25$ is $A = V/0.35$ nm $\approx$ 150 nm^2 for single ion impact. For the present fluence $\Phi = 1 \times 10^{11}$ cm^{-2} a significant overlap probability $\omega = A \times \Phi = 0.15$ results in rough agreement with the experimental finding [see Fig. 3(f)]. From these measurements we can conclude that the formation of an individual pit by HCI impact is associated with the simultaneous creation and

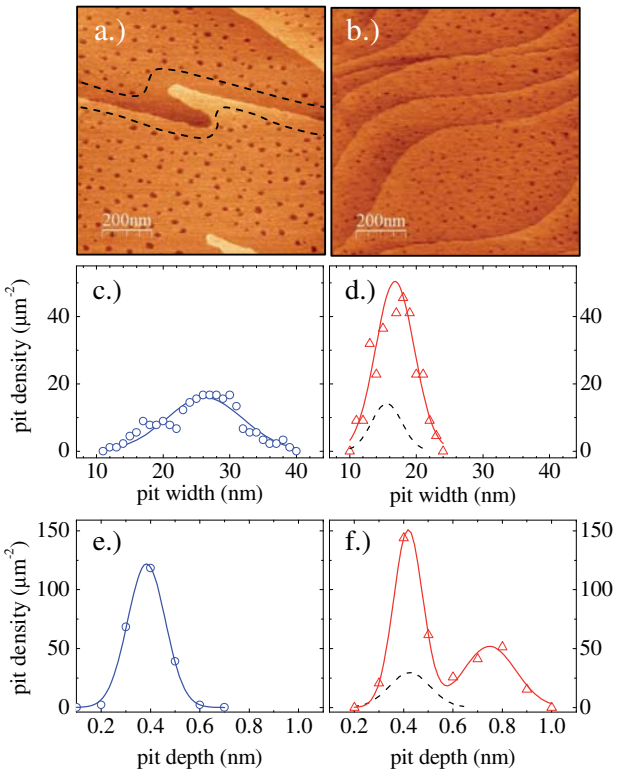

FIG. 3 (color online). Topographic contact AFM images (a), (b) and corresponding distributions of pit width (c), (d) and pit depth (e),(f) for: (a),(c),(e) pits created by collective effects during high-fluence irradiation with Xe^{3+}, $\Phi = 2 \times 10^{13}$ cm^{-2}, and (b),(d),(f) pits created by single and double impact of Xe^{25+}, $\Phi = 1 \times 10^{11}$ cm^{-2}. The fluence in (b),(d),(f) is 200 times smaller than in (a),(c),(e) but also 10 times higher than for the single impact irradiation like shown in Fig. 1. The dashed lines in (c),(f) show the corresponding size distribution from a low-fluence ($\Phi < 1 \times 10^{10}$ cm^{-2}) irradiation.

agglomeration of numerous Frenkel defects within a certain area, in clear contrast to diffusion driven pit creation induced by high-fluence irradiation at low charge state.

In summary, single impact of highly charged Xe ions was found to initiate the formation of pit structures on KBr (001) with lateral sizes of 10–25 nm and monoatomic depth. The mean pit volume and thereby the total sputter yield depend linearly on the potential energy of the ions. The pit formation is ascribed to a desorption mediated by defects, which are generated by the release of the potential energy of the ions close to the surface and by collisional damage along the ion track. The creation of individual pits by each projectile and complementary high-fluence irradiations with low charge state offer evidence for the formation of F center agglomerates (X centers) on the KBr surface within the impact sites.

This work was financially supported by the European project ITS LEIF (No. RII3/026015) JRA6. We thank N. Stolterfoht and Z. Pesic for helpful discussion and valuable comments on the manuscript.

*r.heller@fzd.de
www.fzd.de

[1] D. Kost, S. Facsko, W. Möller, R. Hellhammer, and N. Stolterfoht, Phys. Rev. Lett. **98**, 225503 (2007).
[2] F. Thibaudau, J. Cousty, E. Balanzat, and S. Bouffard, Phys. Rev. Lett. **67**, 1582 (1991).
[3] E. Akcoltekin, T. Peters, R. Meyer, A. Duvenbeck, M. Klusmann, I. Monnet, H. Lebius, and M. Schleberger, Nature Nanotech. **2**, 290 (2007).
[4] A. C. Tien, S. Backus, H. Kapteyn, M. Murnane, and G. Mourou, Phys. Rev. Lett. **82**, 3883 (1999).
[5] F. Aumayr and H. P. Winter, e-J. Surf. Sci. Nanotech. **1**, 171 (2003).
[6] F. Schenkel *et al.*, Phys. Scr. **T80A**, 73 (1999).
[7] A. Arnau *et al.*, Surf. Sci. Rep. **27**, 113 (1997).
[8] H. Kurz, K. Toglhofer, H. P. Winter, F. Aumayr, and R. Mann, Phys. Rev. Lett. **69**, 1140 (1992).
[9] T. Schenkel *et al.*, Nucl. Instrum. Methods Phys. Res., Sect. B **161**, 65 (2000).
[10] F. Aumayr, P. Varga, and H. P. Winter, Int. J. Mass Spectrom. **192**, 415 (1999).
[11] I. C. Gebeshuber, S. Cernusca, F. Aumayr, and H. P. Winter, Int. J. Mass Spectrom. **229**, 27 (2003).
[12] A. S. El-Said *et al.*, Nucl. Instrum. Methods Phys. Res., Sect. B **258**, 167 (2007).
[13] J. M. Pomeroy, A. C. Perrella, H. Grube, and J. D. Gillaspy, Phys. Rev. B **75**, 241409(R) (2007).
[14] F. Aumayr and H. Winter, Phil. Trans. R. Soc. London **362**, 77 (2004).
[15] M. Sporn, G. Libiseller, T. Neidhart, M. Schmid, F. Aumayr, H. P. Winter, P. Varga, M. Grether, D. Niemann, and N. Stolterfoht, Phys. Rev. Lett. **79**, 945 (1997).
[16] D. J. Elliott and P. D. Townsend, Philos. Mag. **23**, 249 (1971).
[17] J. P. Biersack and E. Santner, Nucl. Instrum. Methods **132**, 229 (1976).
[18] G. Hayderer *et al.*, Phys. Rev. Lett. **86**, 3530 (2001).
[19] G. Zschornack, F. Grossmann, R. Heller, M. Kreller, U. Kentsch, S. Landgraf, and Ovsyannikov, Nucl. Instrum. Methods Phys. Res., Sect. B **256**, 565 (2007).
[20] B. Such, P. Czuba, P. Piatkowski, and M. Szymonski, Surf. Sci. **451**, 203 (2000).
[21] B. Such, J. Kolodziej, P. Czuba, P. Piatkowski, P. Struski, F. Krok, and M. Szymonski, Phys. Rev. Lett. **85**, 2621 (2000).
[22] H. Hoche, J. P. Toennies, and R. Vollmer, Phys. Rev. Lett. **71**, 1208 (1993).
[23] V. Puchin, A. Shluger, Y. Nakai, and N. Itoh, Phys. Rev. B **49**, 11364 (1994).
[24] L. Hagg, C. O. Reinhold, and J. Burgdörfer, Phys. Rev. A **55**, 2097 (1997).
[25] J. Burgdörfer, P. Lerner, and F. W. Meyer, Phys. Rev. A **44**, 5674 (1991).
[26] H. Winter and F. Aumayr, J. Phys. B **32**, R39 (1999).
[27] J. J. Kolodziej *et al.*, Surf. Sci. **482**, 903 (2001).

PRL **101,** 076601 (2008) PHYSICAL REVIEW LETTERS week ending 15 AUGUST 2008

Spin Manipulation in Co-Doped ZnO

Qingyu Xu,[1,*] Lars Hartmann,[2] Shengqiang Zhou,[1] Arndt Mcklich,[1] Manfred Helm,[1] Gisela Biehne,[3] Holger Hochmuth,[3] Michael Lorenz,[3] Marius Grundmann,[3] and Heidemarie Schmidt[1]

[1]*Institut für Ionenstrahlphysik und Materialforschung, Forschungszentrum Dresden-Rossendorf e.V., Bautzner Landstraße 128, 01328 Dresden, Germany*

[2]*Solarion AG/Photovoltaics, Ostende 5, 04288 Leipzig, Germany*

[3]*Universität Leipzig, Fakultät für Physik und Geowissenschaften, Institut für Experimentelle Physik II, Linnéstrasse 5, 04103 Leipzig, Germany*

(Received 28 April 2008; published 11 August 2008)

We report the clearly observed tunneling magnetoresistance at 5 K in magnetic tunnel junctions with Co-doped ZnO as a bottom ferromagnetic electrode and Co as a top ferromagnetic electrode prepared by pulsed laser deposition. Spin-polarized electrons were injected from Co-doped ZnO to the crystallized Al_2O_3 and tunnelled through the amorphous Al_2O_3 barrier. Our studies demonstrate the spin polarization in Co-doped ZnO and its possible application in future ZnO-based spintronics devices.

DOI: 10.1103/PhysRevLett.101.076601 PACS numbers: 72.25.Dc, 73.40.Lq, 75.47.De, 75.50.Pp

Both charge and spin degrees of freedom play an important and indispensable role in realizing functionalities in future semiconductor spintronics [1]. The manipulation of spins in spintronics consists of three processes: spin generation, transport, and detection [2]. Nowadays, ferromagnetic metals are successfully used to generate polarized spins for the injection into semiconductors, but the efficiency of the spin injection from ferromagnetic metals to semiconductors is very low, due to the large mismatch of the resistance between metals and semiconductors [2,3]. Diluted magnetic semiconductors (DMSs) are considered to be very important materials in future semiconductor spintronics applications due to the simultaneous control of electrons' charge and spin. DMS materials combining semiconducting *and* magnetic properties are expected to improve the efficiency of spin injection. Mn-doped GaAs is a successful DMS which has been studied in the context of spintronics applications [4,5]. However, the Curie temperature below 173 K limits applications at room temperature [6]. For practical applications, a DMS exhibiting ferromagnetism at room temperature (or above) is required. ZnO has been studied extensively for different magnetic dopants after the theoretical prediction of room temperature ferromagnetism in magnetic doped ZnO [7–9]. The published experimental results on magnetic properties are contradictory [10], and, until now, the research work on ZnO is still concentrating on the realization of intrinsic ferromagnetism [11,12]. However, the demonstration of the spin polarization in Co-doped ZnO is still lacking.

Recently, Song *et al.* published a study on spin polarization in Co-doped ZnO-based magnetic tunnel junction (MTJ) structures [13,14]. However, the reported tunneling magnetoresistance (TMR) [13,14] is similar to the magnetoresistance (MR) probed on single layer Co-doped ZnO films [15]. On the other hand, Co-doped ZnO has been classified as being a ferromagnetic semiconductor by the theoretical work and magnetization measurements [7–9,12], which needs further demonstration by spin-polarized transport properties. Here we report on spin manipulation in Co-doped ZnO and the observation of TMR in a MTJ using Co-doped ZnO as one ferromagnetic electrode. The clear demonstration of the spin manipulation in Co-doped ZnO greatly facilitates the final application of magnetic doped ZnO in future semiconductor spintronics devices.

The Al-doped ZnO buffer layer, the Co-doped ZnO bottom electrode, and the Al_2O_3 barrier layer were subsequently deposited on *a*-plane sapphire substrates by pulsed laser deposition (PLD) from the ceramic targets $Zn_{0.99}Al_{0.01}O$, $Zn_{0.945}Co_{0.05}Al_{0.005}O$, and Al_2O_3, respectively. Circular Co dots with an area of 2.3×10^{-3} cm^2 (diameter 540 μm) were deposited by thermal evaporation in a BAL-TEC MED020. The thickness of each layer was controlled by the number of laser pulses with an energy density of 2 J cm^{-2}. The cross-sectional transmission electron microscopy (TEM) images were taken by an FEI Titan 80–300 S/TEM. The exact composition of Co-doped ZnO was determined to be $Zn_{0.91}Co_{0.09}O$ by combined Rutherford backscattering spectrometry (RBS) and particle-induced x-ray emission (PIXE) measurements. The thickness of Co-doped ZnO and Al-doped ZnO determined by TEM was 180 and 220 nm, respectively. The thickness of Al_2O_3 was selected when the resistance of the junction sample drastically increased with increasing Al_2O_3 layer thickness [16]. Magnetotransport measurements with the field applied in the film plane were performed in two-point geometry as shown in Figs. 1(a) and 1(b) at 5 K. A constant current was applied by a Keithley 2400 source meter for the MR measurements. The *M-H* loop was measured by a superconducting quantum interference device magnetometer with the magnetic field applied in the film plane at 5 K. The applied maximum magnetic field was 6 T.

Though doping with Al can greatly improve the conductivity of ZnO, the resistance is still too large after

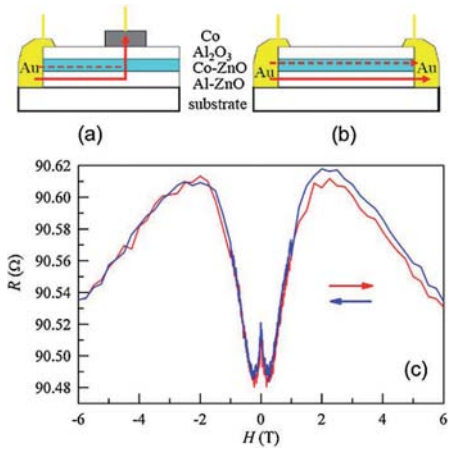

FIG. 1 (color online). Two-point measurements for (a) TMR structure and (b) bottom electrode on the MTJ sample. The red arrows indicate the moving direction of the electrons. (c) The MR effect at 5 K of the bottom electrode measured in (b); the arrows show the field sweep direction.

patterning Al-doped ZnO into several micrometer-wide stripes as the bottom electrode of the MTJ structure. Thus, an alternative geometry was applied for measuring the TMR effect, as shown in Fig. 1(a). The large area makes the resistance of the bottom electrode small, on the order of 100 Ω, which is much smaller than the junction resistance. Because of the double layer structure of the Al_2O_3 barrier layer (which will be explained later), the flowing direction of electrons is important for the final explanation of the observed spin-polarized transport phenomenon. During the measurements, the higher voltage was applied on the Co top electrode and lower voltage on the ZnO bottom electrode through the Au contact; thus, the current will pass from the Co top electrode to the ZnO bottom electrode. Since the charge carriers are electrons with negative charges, the electrons will pass from the ZnO bottom electrode to the Co top electrode, as the red arrows show in Fig. 1(a). The Ohmic contacts on doped ZnO were confirmed by the linear I-V curves measured by the two-point geometry shown in Fig. 1(b). The MR effects of the bottom electrode [Fig. 1(c)], namely, the Al-doped and Co-doped ZnO layers together, have been measured in the geometry shown in Fig. 1(b). The observed small negative MR at low field has been observed on single Al-doped ZnO layers [17]. The positive MR at intermediate field and negative MR at high field originate from Co-doped ZnO [15]. Because of the thickness-dependent defect formation of Co-doped ZnO, small inhomogeneities of Co-doped ZnO will strongly influence the current flow, with very thin Co-doped ZnO films being highly resistive [18]. However, the resistance is very small measured in the geometry of Fig. 1(b) with the current in plane for the parallel alignment of the highly conductive Al-doped ZnO and highly resistive Co-doped ZnO. As the positive MR is very strong in highly resistive Co-doped ZnO [15], the positive MR can still be observed in the geometry of Fig. 1(b). Thus, we conclude that the current passes through the Al-doped ZnO layer and the Co-doped ZnO layer, as shown by the red lines in Figs. 1(a) and 1(b). In the MTJ structure shown in Fig. 1(a), the current tunnels with the highest probability perpendicular from the bottom electrode through the Al_2O_3 barrier layer to the Co top electrode.

Figure 2 shows the field dependence of resistance at 5 K with different applied constant currents. The MR curves contain two main parts: the butterfly MR curves below 1 T, which do not coincide, and the MR curves at fields above 1 T, which coincide for the field swept from 6 to −6 T and from −6 to 6 T. It must be noted that the MR curves at high field ($H > 1$ T) are very similar to the MR curves probed on single layer Co-doped ZnO [15], though the magnitude of resistance changes with different applied current. As explained already, the resistivity in Co-doped ZnO is not uniform, and a highly resistive Co-doped ZnO layer exists [18]. The resistance is very large measured in the geometry of Fig. 1(a) with the current perpendicular to the layer for the serial alignment of the highly conductive Al-doped ZnO and highly resistive Co-doped ZnO layers. We tend to relate the high field MR ($H > 1$ T) behavior of the investigated MTJ sample to the MR of the Co-doped ZnO [15].

The main, most interesting phenomenon is the low field butterfly positive MR behavior, as shown in Fig. 2. In contrast to the normally observed TMR effect, double peaks have been observed in each swept curve which locate at both sides of 0 T. We label the lower peak at the starting field minor peak and the higher peak at the end field major peak for each sweep direction. As one can see, with increasing applied current, the MR effect becomes weaker, which is a typical phenomenon of TMR [19]. When applying a current of 1 μA, the butterfly positive MR disap-

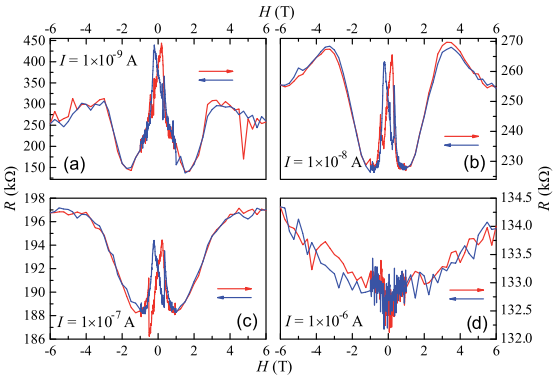

FIG. 2 (color online). Field-dependent resistance of the TMR sample measured at 5 K with field applied in the film plane in the geometry shown in Fig. 1(a). The applied constant current is (a) 1×10^{-9} A, (b) 1×10^{-8} A, (c) 1×10^{-7} A, and (d) 1×10^{-6} A. The arrows show the field sweep direction.

pears. The junction was destroyed, and no butterfly positive MR at low field could be observed afterwards even with a smaller applied current. Figure 3(a) shows the MR curve with 0.01 μA applied current before and after applying 1 μA. A clear butterfly positive MR can be seen in the curve before applying 1 μA [Fig. 2(d)]. After applying 1 μA [Fig. 2(d)], no such MR behavior can be observed anymore even with 0.01 μA. The disappearance of the butterfly positive MR behavior at low field is due to the broken junction after applying a large current; thus, the difference of the resistance before and after applying 1 μA can be roughly attributed to the tunnel resistance of the MTJ sample. Figure 3(b) shows the difference of resistance calculated from MR curves shown in Fig. 3(a). At 0 T, the junction resistance is on the order of 10 kΩ, which is 1 order smaller than the total resistance of the sample (on the order of 100 kΩ) but much larger than the resistance of the bottom electrode (on the order of 100 Ω). Figure 3(c) shows the MR curve in the range from -1 to 1 T, and Fig. 3(d) shows the field-dependent magnetization curve with the field applied in the film plane. Besides the narrow major loop with larger magnetization and smaller coercivity from the Co top electrodes, another loop as indicated by black arrows in Fig. 3(d) with small magnetization and larger coercivity due to the Co-doped ZnO bottom electrode can also be seen. However, normally the coercivity in ferromagnetic ZnO is small ($<$0.1 T) [20]. The larger coercivity ($\sim$0.25 T) in this Co-doped ZnO with an underlying Al-doped ZnO buffer layer might be related to the different strain and defect formation compared to Co-doped ZnO directly deposited on sapphire. The two-step reversal in the magnetization curve [Fig. 3(d)] indicates a good decoupling of the two magnetic layers, so that an antiparallel alignment of the magnetization is obtained between the two coercive fields. With increasing the field above the position of the major peak at $\sim$0.25 T, the resistance starts to decrease. This can be explained by the change from antiparallel to parallel aligned magnetization in the Co top electrode and in the Co-doped ZnO bottom electrode. The magnetic fields corresponding to the different transitions in the MR curves are larger than those observed for the magnetization curve. This is due to the fact that the tunneling is sensitive to the magnetization of the interface, which can switch at higher field than the bulk [21]. However, no indication is observed in *M-H* loop, which could be related to the observed minor peaks in MR curves. A similar MR curve was observed in the $SrTiO_3/LaAlO_3$ interface; the additional suppression around zero field might be due to additional spin or domain reorientation effects [22].

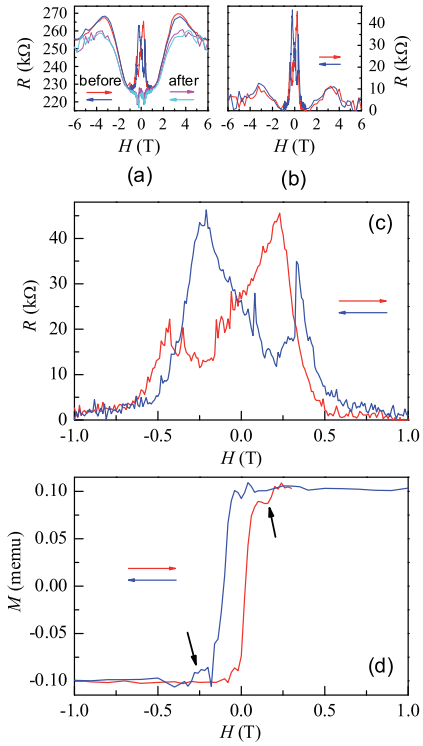

FIG. 3 (color online). (a) The field dependence of resistance of the TMR sample measured at 5 K in the geometry shown in Fig. 1(a) applying a constant current of 1×10^{-8} A before and after the application of 1 μA [Fig. 2(d)] with field applied in the film plane. (b) The field-dependent resistance difference by subtracting the resistance before and after applying 1 μA is shown in (a). (c) The zoom view of the MR curve shown in (b) with field from -1 to 1 T. (d) The magnetization curve of the TMR sample at 5 K. The arrows indicate the field sweep direction. Besides the major loop with larger magnetization and smaller coercivity ($\sim$0.05 T), another loop with smaller magnetization and larger coercivity ($\sim$0.25 T) can also be seen, as shown by the short black arrows.

The cross-sectional TEM image of the MTJ sample is shown in Fig. 4(a). The thickness of the Al_2O_3 layer amounts to about 100 nm. After the growth of about 80 nm crystallized Al_2O_3, the structure changes to about 20 nm nearly amorphous Al_2O_3. A sharp interface can be clearly seen in the Al_2O_3 layer. The contrast in the 80 nm

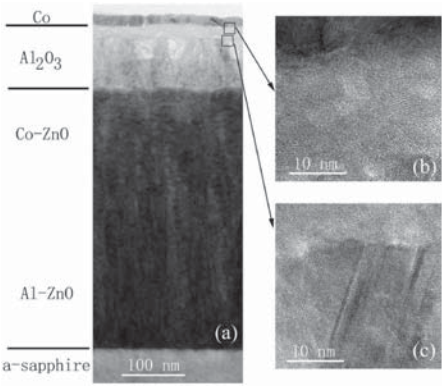

FIG. 4. (a) The cross-sectional TEM image of the TMR sample. (b) and (c) are the HREM images taken from the marked region in (a).

crystallized Al_2O_3 layer is due to the different orientation of the grains. The change of the orientation of the grains during growth might relate to the final nearly amorphous Al_2O_3 layer. The elemental distribution profile measured by energy dispersive x ray (EDX) (with resolution of at least 0.5 at. %) in scanning transmission electron microscopy (STEM) mode confirms that these two layers are both Al_2O_3. The high resolution electron microscopy (HREM) images show that the bottom thicker Al_2O_3 layer is crystallized with columnar grain structure and the top thinner Al_2O_3 layer is almost amorphous. However, detailed investigation of the structure of the thinner amorphous Al_2O_3 layer indicates that this layer has small crystallized Al_2O_3 grains with random orientations. The approximately 80 nm thick crystallized Al_2O_3 layer is expected to be more conductive due to high defect density, while the approximately 20 nm thick amorphous Al_2O_3 layer will act as a tunneling barrier due to its nearly amorphous structure [16]. Though 20 nm is too thick for tunneling, the thickness of amorphous Al_2O_3 layer might not be uniform. Also, residual small grains may reduce the effective tunneling barrier thickness. The resistance of the junction is not very high, even 1 order smaller than the whole sample. With this Al_2O_3 layer structure in mind, we can understand the spin manipulation process in the MTJ structure. The spin-polarized current is generated in the Co-doped ZnO bottom electrode, and polarized spins will be injected into the thicker crystallized Al_2O_3 layer. Normally, the spin coherence length in semiconductors is extremely long [23]; the spin polarization will be conserved in the 80 nm thick crystallized Al_2O_3 layer. Then tunneling occurs at the 20 nm thick amorphous Al_2O_3 layer, and the polarized spins are detected by the Co top electrode. Thus, in the presented MTJ structure, spin generation in DMS (Co-doped ZnO), spin injection from DMS to crystalline Al_2O_3, and spin-polarized tunneling through amorphous Al_2O_3 have been realized.

In summary, MTJ samples with Co-doped ZnO as the bottom ferromagnetic electrode and Co as the top ferromagnetic electrode have been prepared by PLD. An Al_2O_3 barrier layer has been successfully prepared on Co-doped ZnO with a crystallized structure in the bottom and a nearly amorphous structure in the top. A clear TMR effect observed at 5 K demonstrates the spin-polarized transport including the spin injection from Co-doped ZnO to the crystallized Al_2O_3 and tunneling through the amorphous Al_2O_3. Our results demonstrate the spin polarization in Co-doped ZnO and its possible application in future spintronics devices with ZnO-based DMS.

This work is partially (Q. X., L. H, S. Z., H. H., and H. S.) supported by BMBF (Grants No. FKZ03N8708 and No. CHN 05/010). The authors thank G. Ramm for the target preparation, R. Schmidt-Grund and C. Sturm for ellipsometry measurements, D. Spemann for the RBS/PIXE measurement, Dr. Jürgen Fassbender for fruitful discussions, and Dr. Kay Potzger for fruitful discussions.

*Corresponding author.
xuqingyu_1974@yahoo.com

[1] H. Akinaga and H. Ohno, IEEE Trans. Nanotechnol. **1**, 19 (2002).
[2] I. Žutić, J. Fabian, and S. Das Sarma, Rev. Mod. Phys. **76**, 323 (2004).
[3] G. Schmidt *et al.*, Phys. Rev. B **62**, R4790 (2000).
[4] Y. Ohno *et al.*, Nature (London) **402**, 790 (1999).
[5] M. Tanaka and Y. Higo, Phys. Rev. Lett. **87**, 026602 (2001).
[6] T. Jungwirth *et al.*, Phys. Rev. B **72**, 165204 (2005), and references therein.
[7] T. Dietl *et al.*, Science **287**, 1019 (2000).
[8] K. Sato and H. Katayama-Yoshida, Jpn. J. Appl. Phys. **39**, L555 (2000).
[9] K. Sato and H. Katayama-Yoshida, Jpn. J. Appl. Phys. **40**, L334 (2001).
[10] C. Liu, F. Yun, and H. Morkoç, J. Mater. Sci.: Mater. Electron. **16**, 555 (2005).
[11] M. Gacic *et al.*, Phys. Rev. B **75**, 205206 (2007).
[12] A. J. Behan *et al.*, Phys. Rev. Lett. **100**, 047206 (2008).
[13] C. Song *et al.*, Appl. Phys. Lett. **91**, 042106 (2007).
[14] C. Song *et al.*, Appl. Phys. Lett. **91**, 172109 (2007).
[15] Q. Xu *et al.*, Phys. Rev. B **73**, 205342 (2006).
[16] We controlled the Al_2O_3 layer thickness by the laser pulse number. The resistance of the MTJ will increase abruptly with increasing the laser pulse number (thickness of the Al_2O_3 layer) above a critical value. The thickness of the Al_2O_3 layer of the sample studied in this Letter is just above this critical value. The TEM investigation shows that the bottom Al_2O_3 layer was polycrystalline, and the top part was nearly amorphous, indicating the structure change during the growth of the Al_2O_3 layer. The interdiffusion between neighboring layers has been excluded by EDX. Thus we can conclude that the crystallized Al_2O_3 layer is conductive. The drastic increase of resistance of the MTJ sample is due to the formation of the top amorphous Al_2O_3 layer. Spin-polarized electrons tunneled through this amorphous Al_2O_3 layer.
[17] T. Fukumura *et al.*, Appl. Phys. Lett. **75**, 3366 (1999).
[18] Q. Xu *et al.*, J. Appl. Phys. **100**, 013904 (2006).
[19] J. S. Moodera *et al.*, Phys. Rev. Lett. **74**, 3273 (1995).
[20] S. A. Chambers *et al.*, Mater. Today **9**, 28 (2006).
[21] J. M. De Teresa *et al.*, Phys. Rev. Lett. **82**, 4288 (1999).
[22] A. Brinkman *et al.*, Nature Mater. **6**, 493 (2007).
[23] J. H. Lee, S. Y. Park, Kyung-In Jun, K.-H. Shin, Jinki Hong, K. Rhie, and B. C. Lee, Phys. Status Solidi B **241**, 1506 (2004).

APPLIED PHYSICS LETTERS **92**, 082508 (2008)

Room temperature ferromagnetism in ZnO films due to defects

Qingyu Xu,[1,a)] Heidemarie Schmidt,[1] Shengqiang Zhou,[1] Kay Potzger,[1] Manfred Helm,[1] Holger Hochmuth,[2] Michael Lorenz,[2] Annette Setzer,[2] Pablo Esquinazi,[2] Christoph Meinecke,[2] and Marius Grundmann[2]

[1]*Institut für Ionenstrahlphysik und Materialforschung, Forschungszentrum Dresden-Rossendorf e.V., Bautzner Landstraße 128, 01328 Dresden, Germany*

[2]*Institut für Experimentelle Physik II, Universität Leipzig, Linnéstraße 5, 04103 Leipzig, Germany*

(Received 1 February 2008; accepted 4 February 2008; published online 29 February 2008)

ZnO films were prepared by pulsed laser deposition on *a*-plane sapphire substrates under N_2 atmosphere. Ferromagnetic loops were obtained with the superconducting quantum interference device at room temperature, which indicate a Curie temperature much above room temperature. No clear ferromagnetism was observed in intentionally Cu-doped ZnO films. This excludes that Cu doping into ZnO plays a key role in tuning the ferromagnetism in ZnO. 8.8% negative magnetoresistance probed at 5 K at 60 kOe on ferromagnetic ZnO proves the lack of *s-d* exchange interaction. Anomalous Hall effect (AHE) was observed in ferromagnetic ZnO as well as in nonferromagnetic Cu-doped ZnO films, indicating that AHE does not uniquely prove ferromagnetism. The observed ferromagnetism in ZnO is attributed to intrinsic defects. © *2008 American Institute of Physics*. [DOI: 10.1063/1.2885730]

The search of diluted magnetic semiconductor is a subject of current interest due to the possibility to control spin and charge simultaneously for future spintronics. Mn-doped GaAs is a successful diluted magnetic semiconductor (DMS), however, the highest Curie temperature T_C is only 173 K, far below room temperature.[1] Magnetic doped ZnO was intensively studied after the theoretical predication of room temperature ferromagnetism in Mn-doped, *p*-type conducting ZnO.[2] Because of good solubility into ZnO, most of the magnetic doping were 3*d* transition metals, such as Mn, Co, Fe, Ni, etc.[3] However, ZnO is intrinsically *n*-type conducting. Diverse magnetic properties were observed, for example, ferromagnetism, paramagnetism, antiferromagnetism, etc.[4] The observed ferromagnetism in magnetic doped ZnO is in general very weak[5] and, therefore, an extrinsic origin due to magnetic impurities could not be excluded.[6]

Gacic *et al.* reported that the magnetic properties in Co-doped ZnO consist of two parts, strong temperature dependent paramagnetism which follows the Brillouin function and temperature independent ferromagnetism, while x-ray magnetic circular dichroism measurements only revealed a paramagnetic behavior of the active Co-dopant atoms,[7] in contrast to similar measurements on similar samples reported earlier.[8] These results indicate that a specific parameter is not yet well controlled.

Recently, we have reported ferromagnetic properties in Mn-doped ZnO prepared under N_2 atmosphere.[9] These results indicate that the observed ferromagnetism might not originate from the active magnetic dopant atoms, but from vacancies in the ZnO lattice, as other results in undoped ZnO (Refs. 10 and 11) as well as in other oxides such as TiO_2 already indicate.[12,13] In this paper, we prepared undoped ZnO films under N_2 atmosphere that show clear room temperature ferromagnetic signals from defects. The importance of defects in triggering magnetic order in otherwise diamagnetic materials appears to be a key issue, as the main ferromagnetic paradigm, namely graphite, already demonstrated.[14]

ZnO films were grown from a ZnO ceramic target on 10×10 mm^2 *a*-plane sapphire substrates by pulsed laser deposition (PLD) using a KrF excimer laser in N_2 atmosphere (0.3 mbar) with substrate temperature T_s of 570 °C. The deposition conditions (N_2 pressure and substrate temperature) were selected to prepare conducting films. The film thickness was controlled by the number of laser pulses with an energy density of 2 J cm^{-2} and *ex situ* determined by modeling spectral ellipsometry data measured in the energy range from 1 to 4 eV. The composition of the films was determined by combined Rutherford backscattering spectrometry (RBS) and particle induced x-ray emission (PIXE) measurements. The crystal structure of the films was characterized by x-ray diffraction (XRD) measurements with θ-2θ scans using a Cu Kα source. The XRD pattern (Fig. 1) shows the *c*-axis orientation without impurity phases within the resolution. Magnetization *M* versus temperature *T* from 5 to 300 K and versus magnetic field *H* from 0 to 60 kOe was measured with a superconducting quantum interference device magnetometer with the magnetic field applied in the film plane. The *a*-plane sapphire substrates, which show sometimes weak ferromagnetic signals, were measured separately after etching off the film by an HCl dip.[15,16] Magnetotransport measurements with the field applied parallel to the *c* axis were performed in van der Pauw configuration between 5 to 290 K.

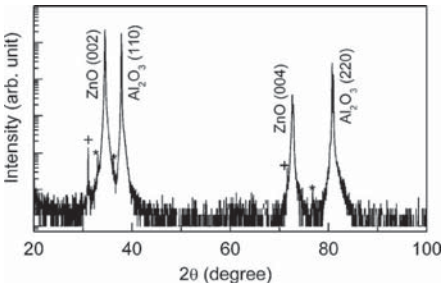

FIG. 1. XRD pattern of a ZnO film prepared under N_2 atmosphere on *a*-plane sapphire substrate. The weak diffraction peaks corresponding to Cu Kβ and W Lα are labeled by "+" and "*" respectively.

a)Author to whom correspondence should be addressed. Electronic mail: xuqingyu_1974@yahoo.com.

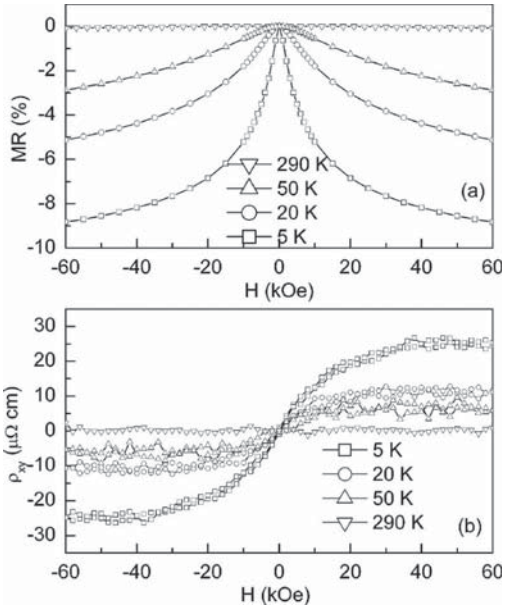

FIG. 2. The field dependent (a) MR and (b) anomalous Hall resistivity of the ZnO film from Fig. 1.

Figure 2 shows the magnetotransport properties of the ZnO film prepared under N_2 atmosphere. Due to the lack of *s-d* exchange interaction, in contrast to magnetic doped ZnO,[17] negative magnetoresistance (MR) {defined as $[R(H)\text{-}R(0)/R(0)]$} of 8.8% at 5 K under 60 kOe was observed and the MR effect decreases with temperature [Fig. 2(a)]. The negative slope of the Hall curves shows the *n*-type conductivity from 5 to 290 K. After subtraction of the ordinary Hall effect (OHE) (the slope of the Hall curve at high field), anomalous HE (AHE) was observed [Fig. 2(b)].

Figure 3 shows the magnetic properties of ZnO films after the subtraction of the magnetic signal from substrate. Figure 3(a) shows the *M-H* loops of a ZnO film at 5 and 290 K. Clear hysteresis loops were observed at 5 and 290 K. The coercivity fields at 290 and 5 K are 50 and 67 Oe, respectively. The difference between the saturation magnetization at 5 and 290 K is small, suggesting that the ferromagnetism in ZnO remains much above 290 K. The inset of Fig. 3(a) shows the high field part of the *M-H* curve up to 60 kOe at 5 K. Contrary to the strong paramagnetic signals (which follow the usual Brillouin function at high fields) obtained in the magnetic-doped ZnO prepared under similar condition,[7] no obvious paramagnetic contribution was observed in the undoped ZnO film, as the temperature dependent magnetization curves also indicate [see Fig. 3(b)]. The difference between field cooled (FC) and zero-field zero-field cooled (ZFC) curves decreases with temperature, resembling partially the temperature dependence of the small hysteresis.

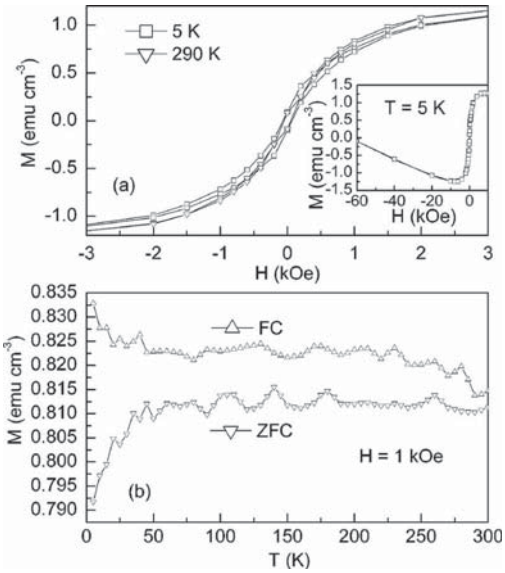

FIG. 3. (a) The *M-H* loops, (b) ZFC and FC *M-T* curves of the ZnO film from Figs. 1 and 2. The sample was cooled under 1 kOe for FC curve.

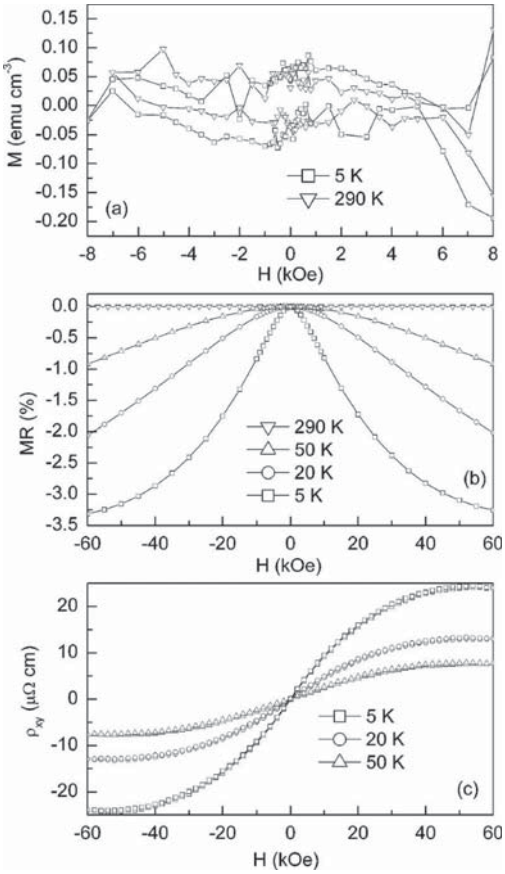

FIG. 4. The *M-H* loops (a), the field dependent MR (b) and anomalous Hall resistivity (c) of $Zn_{0.985}Cu_{0.015}O$ film.

RBS/PIXE were done to check the impurities. The measured impurities are S 0.03%, Cu 0.12%, Ca 0.06%, Fe 0.01%, and (Ti) 0.01%. The N concentration is less than the RBS (N is not detectable in PIXE for our setup) detection limit (less than 0.11 atoms in the ZnO molecule). The influence of the small amount of nonmagnetic impurities like S, Ti, and Ca can be excluded. The measured amount of Fe was always observed in our previous ZnO and doped ZnO and showed no influence on the ferromagnetic properties.[18]

Recently, room temperature ferromagnetism was reported in Cu-doped ZnO.[19] To check the influence of Cu impurities, Cu was intentionally doped into ZnO films under N_2 atmosphere by PLD. The composition of the prepared films was $Zn_{0.985}Cu_{0.015}O$ with 0.01% Fe impurity inside. The XRD spectrum of $Zn_{0.985}Cu_{0.015}O$ film shows similar structure as the ZnO film (Fig. 1) without impurity phases. Figure 4(a) shows the *M-H* loops of $Zn_{0.985}Cu_{0.015}O$ at 5 and 290 K. A linear background was subtracted from the *M-H* loops. Figure 4(a) shows that no clear ferromagnetism was

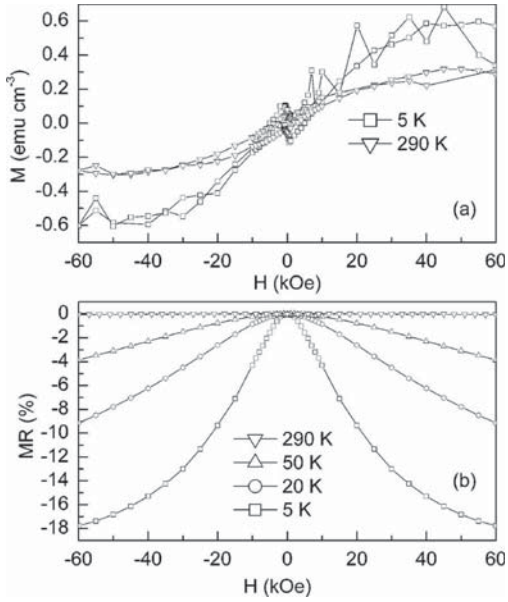

FIG. 5. (a) The *M-H* loops and (b) field dependent MR of ZnO film prepared under higher substrate temperature (655 °C).

observed for the Cu-doped film excluding Cu impurities as the reason for the ferromagnetism in ZnO. Similar negative MR was observed from 5 to 290 K, as shown in Fig. 4(b). Interestingly, clear AHE was also observed in $Zn_{0.985}Cu_{0.015}O$, as shown in Fig. 4(c), after the subtraction of the OHE part, indicating that AHE should not be used as an indication of intrinsic ferromagnetism in DMS.

The origin of the ferromagnetism in pure ZnO was attributed to oxygen vacancies[10] or to defects on Zn sites.[11] Recent theoretical calculations indicate that the ferromagnetism in ZnO might originate from Zn vacancies and not from oxygen vacancies.[20] Deep level transient spectroscopy (DLTS) on ferromagnetic Mn-doped ZnO prepared under N_2 atmosphere showed that Zn vacancies were present.[9] Thus, it is reasonable to attribute the observed ferromagnetism to Zn vacancies in ZnO films.

Another undoped ZnO film was prepared under 0.3 mbar N_2 but at a higher substrate temperature (655 °C). This ZnO film showed a better crystal structure with fewer defects, as the increase in the resistivity from 0.08 Ω cm (T_s=570 °C) to 2 Ω cm (T_s=655 °C) suggests. Figure 5(a) shows the *M-H* loops at 5 and 290 K. A linear background was subtracted from the *M-H* curves. No clear ferromagnetic hysteresis loop can be observed, indicating that the observed ferromagnetism in undoped ZnO originates from defects. Larger MR values are obtained for this film prepared at high-substrate temperature [see Fig. 5(b)]. Note the difference in the field dependence of the MR curves between the samples [see Figs. 2(a), 4(b), and 5(a)], especially in the low field region. This difference indicates the difference in the magnetic contributions between the samples.[21] Further extensive experimental and theoretical studies on the influence of defects in ZnO are needed to understand their magnetic contributions and how to control them in ZnO to obtain room or even higher temperature magnetic order.

In summary, ZnO films were prepared under N_2 atmosphere by PLD. Clear hysteresis loop was observed up to 290 K in ZnO prepared with lower substrate temperature. The extrinsic impurity origin was excluded. The absence of ferromagnetism in ZnO film produced at higher substrate temperature indicates that defects in ZnO should play an important role in triggering magnetic order. Our results further show that AHE cannot be used as an indication of intrinsic ferromagnetism. Our results suggest that a careful control of defects in ZnO and not the doping with magnetic ions might be a possible, better way to obtain reproducible intrinsic, homogeneous room temperature ferromagnetism in ZnO.

This work is partially (Q.X., H.S., and H.H.) supported by BMBF (Grant Nos. FKZ03N8708 and CHN 05/010). The authors would like to thank G. Ramm for the target preparation and R. Schmidt-Grund and C. Sturm for ellipsometry measurements.

[1]T. Jungwirth, K. Y. Wang, J. Mašek, K. W. Edmonds, J. König, J. Sinova, M. Polini, N. A. Goncharuk, A. H. MacDonald, M. Sawicki, A. W. Rushforth, R. P. Campion, L. X. Zhao, C. T. Foxon, and B. L. Gallagher, Phys. Rev. B **72**, 165204 (2004), and references therein.
[2]T. Dietl, H. Ohno, F. Matsukura, J. Cibert, and D. Ferrand, Science **287**, 1019 (2000).
[3]M. Venkatesan, C. B. Fitzgerald, J. G. Lunney, and J. M. D. Coey, Phys. Rev. Lett. **93**, 177206 (2004).
[4]C. Liu, F. Yun, and H. Morkoç, J. Mater. Sci.: Mater. Electron. **16**, 555 (2005).
[5]G. L. Liu, Q. Cao, J. X. Deng, P. F. Xing, Y. F. Tian, Y. X. Chen, S. S. Yan, and L. M. Mei, Appl. Phys. Lett. **90**, 052504 (2007).
[6]R. Seshadri, Curr. Opin. Solid State Mater. Sci. **9**, 1 (2005).
[7]M. Gacic, G. Jakob, C. Herbort, and H. Adrian, Phys. Rev. B **75**, 205206 (2007).
[8]J. R. Neal, A. J. Behan, R. M. Ibrahim, H. J. Blythe, M. Ziese, A. M. Fox, and G. A. Gehring, Phys. Rev. Lett. **96**, 197208 (2006).
[9]Q. Xu, H. Schmidt, L. Hartmann, H. Hochmuth, M. Lorenz, A. Setzer, P. Esquinazi, C. Meinecke, and M. Grundmann, Appl. Phys. Lett. **91**, 092503 (2007).
[10]S. Banerjee, M. Mandal, N. Gayathri, and M. Sardar, Appl. Phys. Lett. **91**, 182501 (2007).
[11]N. H. Hong, J. Sakai, and V. Brizé, J. Phys.: Condens. Matter **19**, 036219 (2007).
[12]T. Pabisiak and A. Kiejna, Solid State Commun. **144**, 324 (2007).
[13]S. Duhalde, M. F. Vignolo, and F. Golmar, Phys. Rev. B **72**, 161313 (2005).
[14]P. Esquinazi, *Handbook of Magnetism and Advanced Magnetic Materials*, edited by H. Kronmüller and S. Parkin (Wiley, Chichester, United Kingdom, 2007), Vol. 4, p. 2256.
[15]R. Salzer, D. Spemann, P. Esquinazi, R. Höhne, A. Setzer, A. K. Schindler, H. Schmidt, and T. Butz, J. Magn. Magn. Mater. **317**, 53 (2007).
[16]A. Che Mofor, A. El-Shaer, A. Bakin, A. Waag, H. Ahlers, U. Siegner, S. Sievers, M. Albrecht, W. Schoch, N. Izyumskaya, V. Avrutin, S. Sorokin, S. Ivanov, and J. Stoimenos, Appl. Phys. Lett. **87**, 062501 (2005).
[17]Q. Xu, L. Hartmann, H. Schmidt, H. Hochmuth, M. Lorenz, D. Spemann, and M. Grundmann, Phys. Rev. B **76**, 134417 (2007).
[18]Q. Xu, L. Hartmann, H. Schmidt, H. Hochmuth, M. Lorenz, A. Setzer, P. Esquinazi, C. Meinecke, and M. Grundmann, Thin Solid Films **516**, 1160 (2008).
[19]D. B. Buchholz, R. P. H. Chang, J. H. Song, and J. B. Ketterson, Appl. Phys. Lett. **87**, 082504 (2005).
[20]I. Opahle (personal communication) (Dec. 4, 2007).
[21]M. Csontos, T. Wojtowicz, X. Liu, M. Dobrowolska, B. Jankó, J. K. Furdyna, and G. Mihály, Phys. Rev. Lett. **95**, 227203 (2005).

APPLIED PHYSICS LETTERS **93**, 232504 (2008)

Ferromagnetic structurally disordered ZnO implanted with Co ions

K. Potzger,[1,a)] Shengqiang Zhou,[1] Qingyu Xu,[1,2] A. Shalimov,[1] R. Groetzschel,[1] H. Schmidt,[1] A. Mücklich,[1] M. Helm,[1] and J. Fassbender[1]
[1]*Institut für Ionenstrahlphysik und Materialforschung, Forschungszentrum Dresden-Rossendorf e.V., Bautzner Landstraße 128, 01328 Dresden, Germany*
[2]*Department of Physics, Southeastern University, Nanjing 211189, China*

(Received 11 September 2008; accepted 10 November 2008; published online 10 December 2008)

We present superparamagnetic clusters of structurally highly disordered Co–Zn–O created by high fluence Co ion implantation into ZnO (0001) single crystals at low temperatures. This secondary phase cannot be detected by common x-ray diffraction but is observed by high-resolution transmission electron microscopy. In contrast to many other secondary phases in a ZnO matrix, it induces low-field anomalous Hall effect and is thus a candidate for magnetoelectronics applications. © *2008 American Institute of Physics*. [DOI: 10.1063/1.3040696]

Recently, much effort has been undertaken for the creation of diluted magnetic semiconductors (DMSs) based on transition metal (TM) doped ZnO. Theoretically, both antiferromagnetic superexchange as well as ferromagnetic *d-d* double exchange are present in those materials.[1] Both become stronger with increasing TM to Zn ratio. It was recently proven that $Zn_{1-x}Co_xO$ with a perfect crystalline lattice is basically paramagnetic with evidence for antiferromagnetic coupling.[2] Concordantly, we suggest the enhancement of the Co to Zn ratio along with the creation of crystalline disorder and nanostructures for ferromagnetism in Co implanted ZnO. Bond angle disorder can, for example, weaken antiferromagnetic superexchange.[3] Experimentally, ferromagnetic hysteresis loops have been observed in several disordered/defective TM oxide nanostructures.[4–6] It was shown that CoO nanoparticles become ferromagnetic after annealing in nitrogen.[4] Dutta *et al.*[4] considered uncompensated spins at the surface to be only a negligible contribution to the room-temperature ferromagnetism of the greenish-turquoise CoO nanoparticles. The existence of ferromagnetic Co–Zn–O crystalline/amorphous core-shell nanostructures has been shown in Ref. 5. A detailed investigation on the ferromagnetic properties of disordered NiO was given by Yi *et al.*[6] Supposing that disordered Co–Zn–O also exhibits ferromagnetic properties, we created it by Co ion implantation into hydrothermal ZnO (0001) single crystals from Crystec. We used an implantation energy of 80 keV and an angle of 7° in order to avoid channeling effects. The target holder was cooled by liquid nitrogen during implantation. We have chosen two Co fluences, i.e., 8×10^{16} and 16×10^{16} Co^+/cm^2 [the corresponding samples are further called ZnO(8) and ZnO(16)]. Such large fluences are expected to heavily disorder the crystal structure.[7] Nevertheless, after implantation the crystals appear greenish and transparent.

The formation of a nanoscale secondary phase from this large Co concentration can lead to superparamagnetism. Exactly such behavior was observed by means of superconducting quantum interference device (SQUID) (QD MPMS XL) magnetometry. Figure 1(a) shows zero-field-cooled/field-cooled (ZFC/FC) magnetization versus temperature curves obtained at a magnetic field of 100 Oe applied parallel to the sample surface. As expected, the thermomagnetic irreversibility temperature increases with increasing fluence. Ferromagnetic hysteresis loops with a saturation magnetization of $0.05\mu_B$/Co ion for ZnO(8) (not shown) and $0.35\mu_B$/Co ion for ZnO(16) [Fig. 1(b)] were observed. For the calculation of the magnetization, we took into account the resputtered Co ions with a percentage of 19% and 43% for ZnO(8) and ZnO(16), respectively. Those values were calculated using TRIDYN (Ref. 8) (see also below). The experimental data on magnetization (Fig. 1) are modelled using a Preisach approach (red solid curves) described by Song *et al.*[9] The temperature dependence of the parameters p describing the magnetic properties of the (nano)phase is usually expressed by the critical temperature T_C and the critical exponent Γ: $p=p_0(1-T/T_C)^\Gamma$, with p substituted by the mean magnetic moment μ of an individual cluster, the mean coercivity H_c, or the dispersions σ_i and σ_c of the interparticle interaction and coercive fields. All parameters p_0 as well as T_C increase with increasing fluence: μ_0 ($10.000\mu_B\rightarrow150.000\mu_B$), H_{c0} (100 Oe→200 Oe), σ_{i0} (150 Oe→200 Oe), σ_{c0} (250 Oe →400 Oe), and T_C (250 K→600 K). Due to coalescence, the total number of clusters N with respect to a 1 cm^2 area implanted decreases from 52×10^{10} to 25×10^{10}. Although the cluster moments found by the Preisach model are somewhat idealized, an assumption of a Co spin moment of $3\mu_B$ for both samples roughly suggests a particle diameter increase by a factor of 2.5. The presence of large ferromagnetic domains for ZnO(16) is also evident from atomic/magnetic force microscopy (AFM/MFM). The micrographs [Figs. 1(c) and 1(d)] were recorded with a Veeco/DI Multimode. Magnetic contrast shows an array of domains with sizes of $0.5,\ldots,1$ μm, which partially follow topography. It was recorded at room temperature in remanent state. Note the peculiarity that the ZnO surface contains self-arranged hillocks created due to ion impact [Fig. 1(c)]. Their origin is not the ion beam erosion but rather corresponds to the decomposition of ZnO, as observed during vacuum annealing of ZnO substrates.[10]

Although superparamagnetic clusters are present, θ-2θ scans using a Siemens D5000 x-ray diffractometer in Bragg–Brentano as well as 2θ scans in glancing incidence geometry revealed no crystalline phases other than wurtzite ZnO to be present in ZnO(16) (not shown). Metallic crystalline Co

a)Electronic mail: k.potzger@fzd.de.

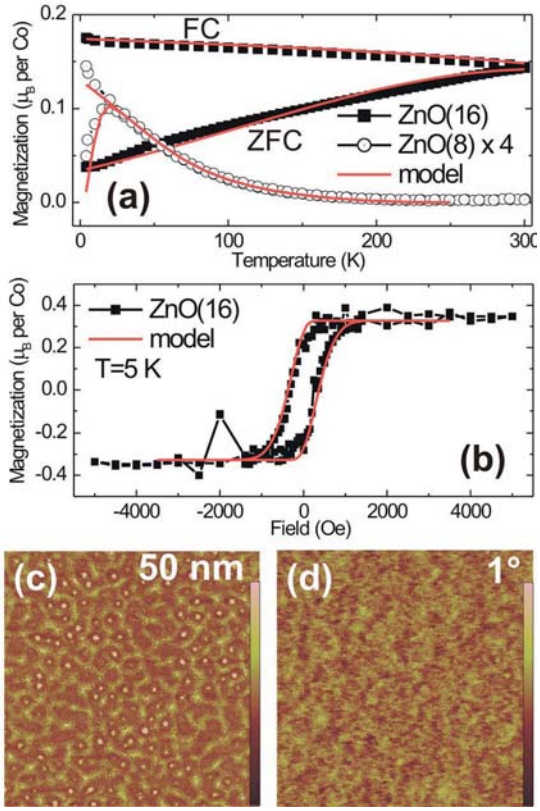

FIG. 1. (Color online) (a) ZFC/FC curves recorded at 100 Oe using SQUID for ZnO(8) and ZnO(16). The curve for ZnO(8) was enlarged for better visibility. The Preisach model is displayed as red full lines. In (a) a clear superparamagnetic behavior can be observed with a magnetization maximum at $T_{max} \sim 25$ K for ZnO(8). For ZnO(16) the thermomagnetic irreversibility occurs above 300 K. (b) *M-H* curve for ZnO(16) at 5 K. For all curves the linear background has been subtracted. Figure 1(c) surface topography of ZnO(16) investigated by AFM. Figure 1(d) shows the corresponding ferromagnetic contrast observed by MFM. The sizes of the micrographs are 10×10 μm^2.

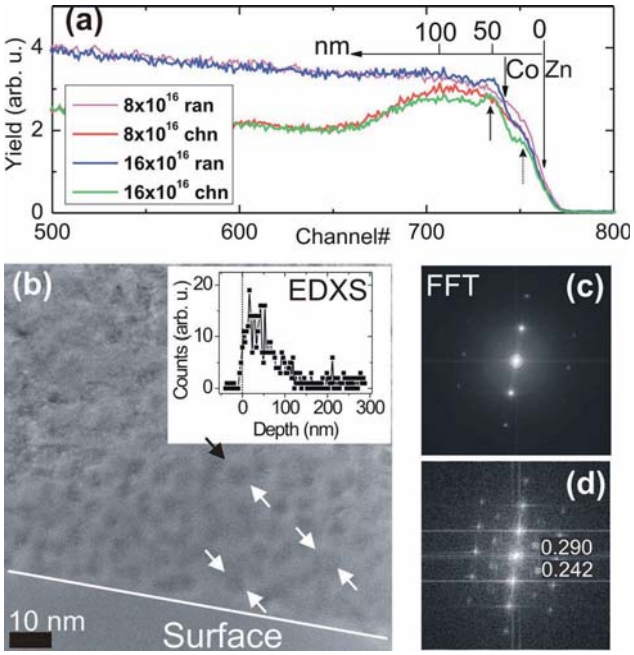

FIG. 2. (Color online) (a) RBS/C measurement for ZnO(8) and ZnO(16) which are implanted with 8 and 16×10^{16} Co^+/cm^2, respectively. The depth scale for ZnO is indicated. The vertical lines denote the energy of He scattered by Zn and Co at the surface. The full and dotted arrows indicate a bump resulting from the implanted Co and the surface damage peak, respectively. (b) TEM micrograph of ZnO(16). Heavy disorder and even amorphous areas are visible close to the surface. The dark contrast in the amorphous dominated region (arrows) indicates low crystalline areas. The inset shows the EDXS profile of Co measured using TEM. The beam diameter was approximately 2 nm. (c) Amorphous rings in the FFT of a similar but thicker cross section in defocus. (d) FFT of a part of the near surface region containing Zn(or Co)Co_2O_4 precipitates. Net-plane distances are indicated.

nanoparticles would, on the other hand, be easily detectable[11] at a high amount of 2×10^{16} Co^0/cm^2, i.e., 2 $\mu g/cm^2$ of metallic Co with a magnetization of $1.6\mu_B$/atom (again the resputtered Co ions are taken into account). Thus, the superparamagnetic nanoclusters are either wurtzite with similar lattice parameters as ZnO or structurally highly disordered. The latter can be expected from the large fluence implanted. Structural disorder due to ion implantation in ZnO was described in detail by Kucheyev *et al.*[7] At Au fluences as large as 3×10^{16} cm^{-2}, the ZnO crystals are heavily disordered, but no amorphous phase was detected. Concerning the energy used in Ref. 7 and the different masses of Au and Co, the maximum total displacements per atom are half as for our ZnO(16). For a structure and composition analysis of both samples, we performed Rutherford backscattering/channeling (RBS/C) experiments using a primary energy of 1.7 MeV. Transmission electron microscopy (TEM) using a FEI Titan machine equipped with an energy dispersive x-ray spectrometer (EDXS) was applied only to ZnO(16) (Fig. 2). The main observations using these methods are as follows.

- First, heavy disorder of the crystalline matrix is reflected by a broad bulk damage peak extending from 50 to 150 nm below the surface [Fig. 2(a)]. The bulk channeling reflects the maximum disorder in the crystals and is similar (saturated) for both fluences. As in Ref. 7, a damage peak close to the surface can be detected (dotted arrow). As observed by TEM, the implanted film close to the surface [Fig. 2(b)] is a mixture of a crystalline dominated area and an amorphous dominated area. The crystalline dominated area is basically wurtzite but structurally disordered due to dislocations and precipitations (see below). The amorphous phase can be observed either by focusing on a very thin part of the specimen [Fig. 2(b)] or as rings in the fast Fourier transform (FFT) [Fig. 2(c)]. The rings appear under appropriate defocusing of the electron beam. They are not present for crystals with a long range order, such as single crystalline Si. Note that the amorphous dominated area contains low crystalline cores of only ~4 nm size, which is nearly not dispersed. They basically exhibit a similar crystalline orientation like the substrate, and they are surrounded by interconnected amorphous shells [Fig. 2(b)].
- Second, the maximum Co to Zn relation for ZnO(16) indicated by the full arrow in Fig. 2(a) and derived from grazing incidence RBS (not shown) amounts to 0.33 (10). The maximum ratio between Co and Zn derived by the TRIDYN (Ref. 8) code amounts to 0.37 for ZnO(8) and 0.62 for ZnO(16). This value is significantly larger than the one found by RBS. This implicates diffusion of Co toward the ZnO bulk. The latter was confirmed by using EDXS [inset in Fig. 2(b)]. The thickness of the Co^+ implanted layer

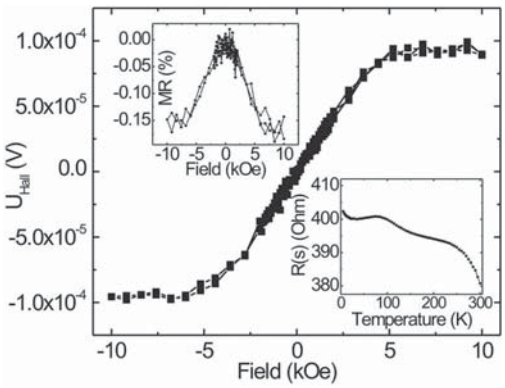

FIG. 3. AHE of the 16×10^{16} Co^{+}/cm^{2} implanted sample ZnO(16) recorded at a temperature of 5 K. The left inset shows the corresponding MR effect. The right inset shows the evolution of sheet resistance $R(s)$ with temperature. The magnetic field was applied perpendicular to the film.

approximated by the full width at half maximum amounts to 75 nm as compared to 45 nm as derived by TRIDYN.

- Third, stoichiometric disorder is indicated. EDXS point measurements at distances of 25 and 50 nm from the surface (not shown) reveal two kinds of O:(Zn+Co) ratios. The first equals unity proofing Zn and Co to be mainly in the 2+ state. The second—which occurs rather sporadically—exceeds unity significantly. Correspondingly, nanoscale regions with crystalline superstructure [FFT in Fig. 2(d)] sporadically occur. Their net-plane distances of 0.290 and 0.242 nm can be assigned to the (220) and (311) Miller indices of Zn(or Co)Co_2O_4. They nearly correspond to those of the bulk materials.[12] We found fixed orientation relationships of [111]‖ZnO[001] and (110)‖ZnO(110) as well as [111]‖ZnO[001] and (112)‖ZnO(110). Streaklike shapes of the spots indicate a distribution of the lattice parameters.

The surface layer of the otherwise insulating ZnO single crystals becomes *n*-type conducting after implantation. In our case, ZnO(16) exhibits anomalous Hall effect (AHE), as shown in Fig. 3. The saturation field amounts to ~6 kOe for 5 K. It persists up to room temperature (not shown) and implicates charge carrier spin polarization. The magnetoresistance (MR) effect is negative, amounting to −0.15% at 10 kOe and 5 K (left inset in Fig. 3). The room-temperature resistivity of ZnO(16) amounts to 2.4×10^{-3} Ω cm if a film thickness of 75 nm is assumed. For a metallic Co film, it is much lower, i.e., 6×10^{-6} Ω cm.[13] The latter rules out the presence of a pure metallic film. The temperature dependence of the sheet resistance $R(s)$ (Fig. 3, right inset) hints to different transport mechanisms inside the material with mostly semiconducting behavior, indicating a multiphase system. Especially, at around 80 K there is a pronounced change in the slope. The room-temperature charge carrier concentration of ZnO(16) is 1.3×10^{21} cm^{-3}, assuming a thickness of 75 nm.

In conclusion, high fluence Co^{+} ion implantation into ZnO single crystals leads to the formation of superparamagnetic clusters consisting of Zn, Co, and O. We relate them to nanosized regions consisting of low crystalline cores of 4 nm diameter and interconnected amorphous shells created by the ion beam impact. This secondary phase occurs simultaneously with areas of wurtzite as well as spinel structures. Crystalline $Zn_{1-x}Co_xO$ and Zn(or Co)Co_2O_4 cannot account for the pronounced ferromagnetic signal since the former is paramagnetic and the latter occurs only sporadically. Thus, relating the structural to the magnetic properties, a likely mechanism is ferromagnetic 3*d* exchange fostered by the crystalline disorder. Suppression of antiferromagnetic coupling, nanoscale dimensions of the clusters, or stoichiometric disorder might be relevant to the magnetic ordering. In the future it has to be investigated whether fully amorphous regions or such with residual crystalline relations are responsible for the signal. As an outlook, following Ref. 6, a continuous fully amorphous phase cannot account for ferromagnetism in NiO. Moreover, for disordered ferromagnetic phases in other DMSs,[14] also an increase in magnetization with the formation of crystalline/amorphous nanostructures has been found. The implanted sheet shows pronounced AHE, which is saturated at low field, giving hope for applicability in spintronics.

A.S. wants to thank the Deutsche Forschungsgemeinschaft (DFG) (Project No. PO1275/2-1, “SEMAN” and S.Z., Q.X., and H.S. would like to thank the Bundesministerium für Bildung und Forschung (Grant No. FKZ03N8708) for funding.

[1] K. Sato and H. Katayama-Yoshida, Semicond. Sci. Technol. **17**, 367 (2002).
[2] A. Ney, K. Ollefs, S. Ye, T. Kammermeier, V. Ney, T. C. Kaspar, S. A. Chambers, F. Wilhelm, and A. Rogalev, Phys. Rev. Lett. **100**, 157201 (2008).
[3] T. Kaneyoshi, *Introduction to Amorphous Magnets* (World Scientific, Singapore, 1992).
[4] D. P. Dutta, G. Sharma, P. K. Manna, A. K. Tyagi, and S. M. Yusuf, Nanotechnology **19**, 245609 (2008).
[5] C. Sudakar, P. Kharel, G. Lawes, R. Suryanarayanan, R. Naik, and V. M. Naik, Appl. Phys. Lett. **92**, 062501 (2008).
[6] B. Yi, J. Ding, Y. P. Feng, G. W. Peng, G. M. Chow, Y. Kawazoe, B. H. Liu, J. H. Yin, and S. Thongmee, Phys. Rev. B **76**, 224402 (2007).
[7] S. O. Kucheyev, J. S. Williams, C. Jagadish, J. Zou, C. Evans, A. J. Nelson, and A. V. Hamza, Phys. Rev. B **67**, 094115 (2003).
[8] W. Möller and W. Eckstein, Nucl. Instrum. Methods Phys. Res. B **2**, 814 (1984).
[9] T. Song, R. M. Roshko, and E. Dan Dahlberg, J. Phys.: Condens. Matter **13**, 3443 (2001).
[10] T. M. Børseth, B. G. Svensson, and A. Yu. Kuznetsov, Phys. Scr. **T126**, 10 (2006).
[11] S. Zhou, K. Potzger, G. Talut, J. von Borany, W. Skorupa, M. Helm, and J. Fassbender, J. Appl. Phys. **103**, 07D530 (2008).
[12] International Centre for Diffraction Data, Powder-Diffraction File No. 00-023-1390.
[13] I. Bakonyi, E. Toth Kadar, J. Toth, L. F. Kiss, L. Pogany, A. Cziraki, C. Ulhaq-Bouillet, V. Pierron-Bohnes, A. Dinia, B. Arnold, and K. Wetzig, Europhys. Lett. **58**, 408 (2002).
[14] A. Verna, L. Ottaviano, M. Passacantando, S. Santucci, P. Picozzi, F. D’Orazio, F. Lucari, M. De Biase, R. Gunnella, M. Berti, A. Gasparotto, G. Impellizzeri, and F. Priolo, Phys. Rev. B **74**, 085204 (2006).

APPLIED PHYSICS LETTERS **93**, 232507 (2008)

Room temperature ferromagnetism in carbon-implanted ZnO

Shengqiang Zhou,[1,a)] Qingyu Xu,[1,2] Kay Potzger,[1] Georg Talut,[1] Rainer Grötzschel, Jürgen Fassbender,[1] Mykola Vinnichenko,[1] Jörg Grenzer,[1] Manfred Helm,[1] Holger Hochmuth,[3] Michael Lorenz,[3] Marius Grundmann,[3] and Heidemarie Schmidt[1]
[1]*Institut für Ionenstrahlphysik und Materialforschung, Forschungszentrum Dresden-Rossendorf e.V., Bautzner Landstraße 128, 01328 Dresden, Germany*
[2]*Department of Physics, Southeast University, Nanjing 211189, People's Republic of China*
[3]*Institut für Experimentelle Physik II, Universität Leipzig, Linnéstraße 5, 04103 Leipzig, Germany*

(Received 2 October 2008; accepted 19 November 2008; published online 12 December 2008)

Unexpected ferromagnetism has been observed in carbon doped ZnO films grown by pulsed laser deposition [H. Pan *et al.*, Phys. Rev. Lett. **99**, 127201 (2007)]. In this letter, we introduce carbon into ZnO films by ion implantation. Room temperature ferromagnetism has been observed. Our analysis demonstrates that (1) C-doped ferromagnetic ZnO can be achieved by an alternative method, i.e., ion implantation, and (2) the chemical involvement of carbon in the ferromagnetism is indirectly proven. © *2008 American Institute of Physics*. [DOI: 10.1063/1.3048076]

The practical application of diluted magnetic semiconductors (DMSs) in spintronics requires the DMS to exhibit ferromagnetism above room temperature. After the prediction that a Curie temperature higher than room temperature can be achieved by transition metal (TM) doping, ZnO has been intensively studied.[1,2] Room temperature ferromagnetism has been reported by many researchers for 3*d* TM doped ZnO.[3–5] However, the observed ferromagnetism is always rather weak and the detected magnetization might arise from ferromagnetic impurities.[6,7] Another source for weak ferromagnetic signals are intrinsic defect complexes which occur in ZnO of low crystalline quality, e.g., if grown under N_2 atmosphere[8] or if vacuum annealed.[9] Such ferromagnetic defects can also be produced by Fe or Ar ion beams.[9,10]

Despite such drawbacks, Pan *et al.*[11] reported strong room temperature ferromagnetism in C-doped ZnO films grown by pulsed laser deposition (PLD). Together with the first-principles calculations, evidence is given that carbon ions substitute for oxygen and their *p*-orbits contribute the local moments. Since carbon is approximately five times lighter than TM, it can be incorporated into ZnO by ion implantation while much less defects are created.[12] Recently, the equal-term applicability of thin-film growth and carbon ion implantation has been demonstrated for the ferromagnetic semiconductor $C:Mn_5Si_3$.[13] We utilized various techniques to characterize the structural and magnetic properties of the C-implanted ZnO films with different C concentrations as well as of a Ne-implanted ZnO and a C-implanted Ge reference samples. The aim is to check whether ferromagnetic ZnO can be realized by C implantation and whether carbon or indeed defects play the active role in generating the observed ferromagnetism.

260 nm thick ZnO films were grown from a ZnO ceramic target on 10×10 mm^2 *a*-plane sapphire substrates by PLD using a KrF excimer laser in O_2 atmosphere (0.2 Pa) with a substrate temperature T_s of 715 °C and subsequently implanted. The TRIM code was used to simulate the depth dependent distribution of implanted C in the ZnO films.[14] In order to obtain a boxlike C distribution in the ZnO films, four different energies with different fluences of C were implanted in the same film at room temperature. For instance, for 1 at. % C-doped ZnO, 70, 35, 17.5, and 8.8 keV with fluences of 8.2×10^{15}, 3.28×10^{15}, 9.84×10^{14}, and 9.84×10^{14} cm^{-2} were applied, respectively. As comparison, Ne ions were implanted with the same energy choice but with fluences of 16.4×10^{15}, 6.56×10^{15}, 1.97×10^{15}, and 1.97×10^{15} cm^{-2}. Additionally, in order to exclude the possible contamination of carbon beam a Ge wafer was implanted with carbon at the same implanter with ion energies of 70 and 35 keV and fluences of 4.1×10^{16} and 1.6×10^{16} cm^{-2}, respectively. Compared with the C-fluence series, the middle fluence for Ne was chosen to produce a mild amount of defects, while the largest C fluence for the Ge sample was used to receive the largest amount of contamination if there was. The magnetization M versus temperature T from 5 to 300 K and versus magnetic field H was measured with a superconducting quantum interference device magnetometer with the magnetic field applied in the film plane. All samples were investigated using Rutherford backscattering/channeling (RBS/C) spectrometry to check the defects induced by ion implantation. The crystal lattice disorder upon implantation is quantified by the parameter χ_{min}, which is the ratio of the backscattering yield at channeling condition to that at random beam incidence. Here χ_{min} is given for the Zn signal. The crystal structure of the films was probed by x-ray diffraction (XRD) θ-2θ scans using a Cu $K\alpha$ source.

Magnetic properties of the pure ZnO, C- and Ne-implanted ZnO films as well as a C-implanted Ge wafer were investigated. Figure 1 shows the *M*-*H* curves at 5 K of virgin ZnO, Ne-implanted, and 5 at. % C-implanted ZnO films with the area of 1 cm^2 at 5 K. For the virgin and Ne-implanted ZnO film, only a linear diamagnetic signal is observed at 5 K. After implantation with 5 at. % C, an overlap of *M*-*H* hysteresis and the diamagnetic signal already probed on unimplanted ZnO is observed at 5 K. The inset of Fig. 1 displays the *M*-*H* curve measured at 4 K for C-implanted Ge, which exhibits only diamagnetism and no difference compared with the virgin Ge. This observation confirms the noncontamination of the carbon beam by 3*d* TMs.

We subtracted the diamagnetic contribution determined from the high-field linear part of *M*-*H* loops to get the fer-

a)Electronic mail: s.zhou@fzd.de.

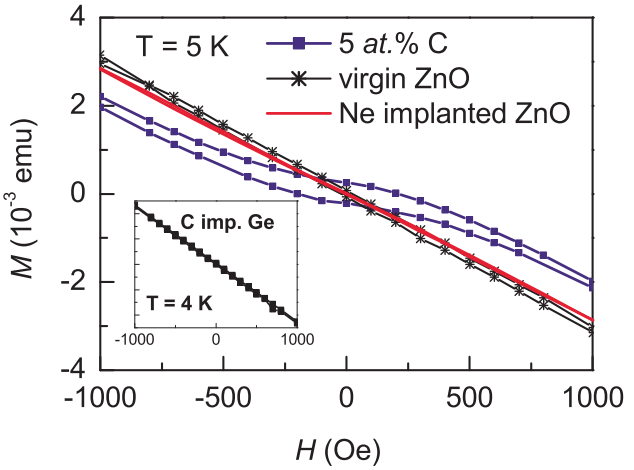

FIG. 1. (Color online) The *M-H* curves measured at 5 K for virgin, Ne-, and 5 at. % C-implanted ZnO with the same sample size of 1 cm^2 and mass of 200 mg. The inset displays the *M-H* curve at 4 K for C-implanted Ge, which exhibits only diamagnetism. Every *M-H* curve was measured with the field up to 8000 Oe, but only a zoom of the low-field part is shown.

romagnetic magnetization of the C-implanted films. Figure 2(a) shows the *M-H* curves for two selected samples, 1 and 5 at. % C-implanted ZnO films, at 5 and 300 K. A clear hysteresis loop can be observed, indicating the ferromagnetic properties. The concentration-dependent saturation magnetization M_s has been plotted in Figs. 3(d) and 3(e) being normalized by the carbon concentration in units of μ_B/C or being normalized in units of 10^{-5} emu per sample with the area of 1 cm^2. The saturation magnetization of 1 at. % C-implanted ZnO is about 0.24 μ_B/C and decreases to about 0.06 μ_B/C for 5 at. % C-implanted ZnO. The hysteresis loop can also be observed at 300 K, as can be seen exemplarily in the *M-H* curve for 5 at. % C-implanted ZnO in the inset of Fig. 2(a), indicating that the Curie temperature is

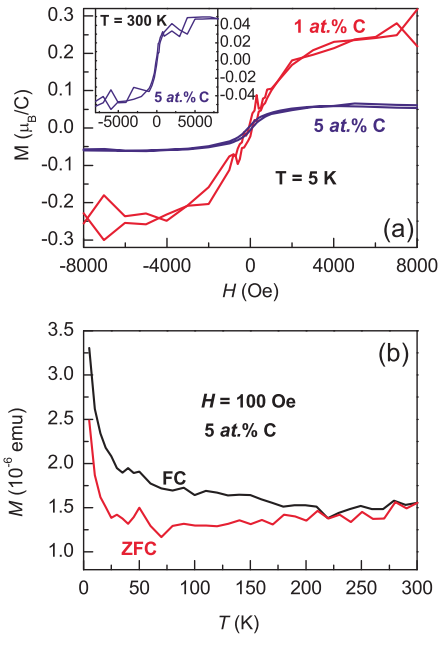

FIG. 2. (Color online) (a) The *M-H* curves measured at 5 K for 1 and 5 at. % C-doped ZnO films. The inset shows the *M-H* curve for the 5 at. % C-doped ZnO film at 300 K. (b) The ZFC and FC *M-T* curves for the 5 at. % C-doped ZnO film.

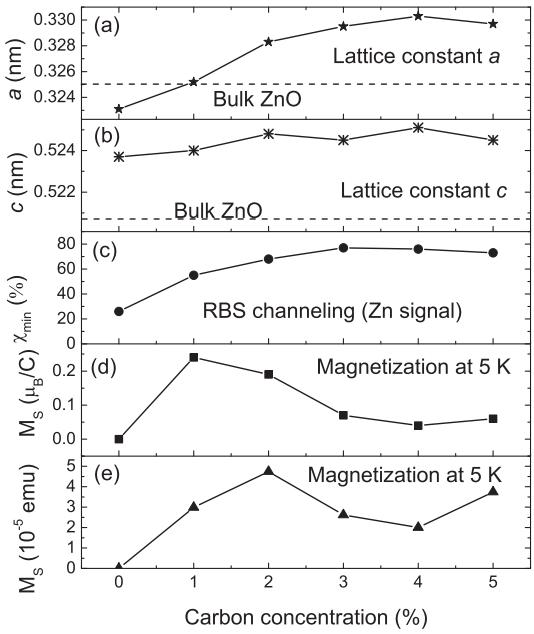

FIG. 3. Carbon-concentration-dependent structural and magnetic properties of C-implanted ZnO films. No scaling relation between defects and magnetization can be found.

above room temperature. Figure 2(b) shows the field cooled (FC) and zero field cooled (ZFC) curve for 5 at. % implanted ZnO measured in an applied field of 100 Oe. Similar FC and ZFC curves were also observed in x at. % C-implanted ZnO (x=1,2,3,4). The separation between the FC and ZFC curves further demonstrates the ferromagnetic properties of C-implanted ZnO. It must be noted that the FC curve was measured after the ZFC curve; the magnetization was measured with FC from 300 to 5 K under 100 Oe. Thus the separation between ZFC and FC disappears at 300 K. The real Curie temperature can be assumed to be higher than room temperature, which is also supported by the slight decrease in saturation magnetization at 300 K, as shown in the inset of Fig. 2(a). In contrast, for the virgin and Ne-implanted ZnO films, only a linear diamagnetic signal is found at 5 K (Fig. 1). Thus, purely defect-induced ferromagnetism can be excluded. Further support for the exclusion of ferromagnetic defects can be found by annealing. The 4 at. % C-implanted sample was annealed in air for 2 h at 400 °C.[10] After annealing, the sample magnetization is not significantly changed, but the coercivity is increased from ~100 to ~250 Oe. Thus, we can exclude the purely defect-induced ferromagnetism since in such case the saturation magnetization should significantly drop with postannealing.[10]

No impurity phases were observed in the θ-2θ XRD patterns of the unimplanted and C-implanted wurtzite ZnO (not shown). However, besides the (002) peak of ZnO, the (100) peak can also be observed in virgin ZnO films. This indicates the coexistence of (001) and (100) textured grains in the films. After C implantation, the (100) peak position shifts significantly to smaller angles. The lattice constants calculated from the position of ZnO (100) and (002) peaks are summarized in Figs. 3(a) and 3(b). The a-lattice constant of the (100) oriented grains gradually increases with increasing C concentration, while the c-lattice constant of the (001) oriented grains only slightly increases after C implantation

and reaches an average value of 0.525 nm at larger C concentrations. As the ionic radius of C^{4-} (0.260 nm) is much larger than that of O^{2-} (0.140 nm),[15] the substitution of O by C will expand the lattice. However, the expansion of the ZnO lattice might also originate from C atoms located at interstitial sites or from defects induced by ion implantation. In Fig. 3(c), the minimum yield of RBS/C, $\chi_{\min}$ of the Zn signal, is shown as a function of carbon concentration. For the virgin sample, $\chi_{\min}$ is around 26%, which is acceptable considering the two kinds of ZnO crystallite orientation. With increasing implantation fluences, $\chi_{\min}$ gradually increases, indicating more defects generated inside the ZnO matrix. However, ZnO is an irradiation-hard material and still shows the channeling effect ($\chi_{\min}$ of 73%) after the largest fluence implantation. In order to understand the observed ferromagnetism, all the measured structural and magnetic parameters are compared in Fig. 3. There is a scaling effect between lattice expansion and RBS channeling $\chi_{\min}$: both parameters increase gradually with increasing carbon concentration. This proves that in the region of larger fluences, lattice expansion is induced rather by defects than by carbon substitution. For ferromagnetism induced by substitutional carbon the maximum magnetization is thus expected for fluences/concentrations where its crystalline neighborhood is still intact, i.e., below disorder saturation at 3% carbon concentration [Fig. 3(c)]. Exactly this is what we observe, i.e., both the normalized saturation magnetizations [Figs. 3(d) and 3(e)] reach their maximum value for 1 and 2 at. % carbon, respectively. It must be noted that the saturation magnetic moment per carbon (highest value of 0.24 μ_B/C for 1 at. % C-implanted ZnO at 5 K) is much smaller than the theoretically predicted value of 2.02 μ_B/C and the experimentally reported value of 2.5 μ_B/C.[11] We relate this behavior to nonuniform distribution of the C ions inside the ZnO host lattice and thus a large number of magnetically inactive C ions. The origin of the ferromagnetic signal must be related to the chemical presence of C (Ref. 11) and not to implantation induced defects since the Ne-implanted sample is diamagnetic.

A measurement confirming the substitution of carbon is surely helpful to understand the ferromagnetic coupling mechanism. Channeling RBS and particle induced x-ray emission can probe the lattice location of heavy elements,[16,17] while channeling nuclear reaction analysis (NRA) would be suitable for the lattice location of light element, e.g., C.[18] We performed channeling NRA using the $^{12}C(d,p)^{13}C$ reaction. Implanted carbon can be easily detected, but no channeling effect can be found. This is due to the fact that the applicability of channeling techniques depends on the crystalline quality. For our C-implanted ZnO, the $\chi_{\min}$ of the Zn signal is above 50%. The maximum substitution fraction of C is around 12% (calculated by 0.24 μ_B/2.02 μ_B). After considering these two facts the channeling effect for C becomes too weak to be detected by NRA.

In summary, 1–5 at. % C were implanted into the ZnO films on *a*-plane sapphire substrates prepared by PLD. In contrast to the virgin ZnO, the Ne-implanted ZnO, and the C-implanted Ge reference samples, clear ferromagnetic hysteresis loops have been observed in all C-implanted ZnO films up to 300 K, indicating a Curie temperature higher than room temperature. The observed ferromagnetism must be related to the chemical involvement of carbon. A saturation magnetic moment of 0.24 μ_B/C at 5 K is observed for the 1 at. % C-implanted ZnO film and it decreases with increasing carbon concentration. The experiments clearly show that the C-induced ferromagnetism in ZnO can be achieved by different preparation methods. Optimal implantation and postannealing treatments are needed to improve the effective substitution of C on O sites.

This work is partially (S.Z., Q.X., H.H., and H.S.) supported by BMBF (Grant Nos. FKZ03N8708 and CHN 05/010). Q.X. acknowledges the National Natural Science Foundation of China (Contract No. 50802041). The authors would like to thank G. Ramm for the PLD target preparation.

[1] T. Dietl, H. Ohno, F. Matsukura, J. Cibert, and D. Ferrand, Science **287**, 1019 (2000).
[2] K. Sato and H. Katayama-Yoshida, Jpn. J. Appl. Phys., Part 2 **40**, L334 (2001).
[3] Q. Xu, H. Schmidt, L. Hartmann, H. Hochmuth, M. Lorenz, A. Setzer, P. Esquinazi, C. Meinecke, and M. Grundmann, Appl. Phys. Lett. **91**, 092503 (2007).
[4] K. R. Kittilstved, D. A. Schwartz, A. C. Tuan, S. M. Heald, S. A. Chambers, and D. R. Gamelin, Phys. Rev. Lett. **97**, 037203 (2006).
[5] A. J. Behan, A. Mokhtari, H. J. Blythe, D. Score, X.-H. Xu, J. R. Neal, A. M. Fox, and G. A. Gehring, Phys. Rev. Lett. **100**, 047206 (2008).
[6] T. C. Kaspar, T. Droubay, S. M. Heald, M. H. Engelhard, P. Nachimuthu, and S. A. Chambers, Phys. Rev. B **77**, 201303 (2008).
[7] S. Zhou, K. Potzger, J. von Borany, R. Grtzschel, W. Skorupa, M. Helm, and J. Fassbender, Phys. Rev. B **77**, 035209 (2008).
[8] Q. Xu, H. Schmidt, S. Zhou, K. Potzger, M. Helm, H. Hochmuth, M. Lorenz, A. Setzer, P. Esquinazi, C. Meinecke, and M. Grundmann, Appl. Phys. Lett. **92**, 082508 (2008).
[9] S. Zhou, K. Potzger, G. Talut, H. Reuther, K. Kuepper, J. Grenzer, Q. Xu, A. Mücklich, M. Helm, J. Fassbender, and E. Arenholz, J. Phys. D: Appl. Phys. **41**, 105011 (2008).
[10] R. P. Borges, R. C. da Silva, S. Magalhaes, M. M. Cruz, M. Godinho, and J. Phys.: Condens. Matter **19**, 476207 (2007).
[11] H. Pan, J. B. Yi, L. Shen, R. Q. Wu, J. H. Yang, J. Y. Jin, Y. P. Feng, J. Ding, L. H. Van, and J. H. Yin, Phys. Rev. Lett. **99**, 127201 (2007).
[12] J. Fassbender and J. McCord, J. Magn. Magn. Mater. **320**, 579 (2008).
[13] C. Sürgers, K. Potzger, T. Strache, W. Möller, G. Fischer, N. Joshi, and H. v. Löhneysen, Appl. Phys. Lett. **93**, 062503 (2008).
[14] J. Ziegler, J. Biersack, and U. Littmark, *The Stopping and Range of Ions in Matter* (Pergamon, New York, 1985).
[15] http://chemed.chem.purdue.edu/genchem/topicreview/bp/ch7/size.html.
[16] E. Alves, E. Rita, U. Wahl, J. G. Correia, T. Monteiro, J. Soares, and C. Boemare, Nucl. Instrum. Methods Phys. Res. B **206**, 1047 (2003).
[17] T. Monteiro, C. Boemare, M. J. Soares, E. Rita, and E. Alves, J. Appl. Phys. **93**, 8995 (2003).
[18] K. Kuriyama, Y. Mizuki, H. Sano, A. Onoue, M. Hasegawa, and I. Sakamoto, Solid State Commun. **135**, 99 (2005).

APPLIED PHYSICS LETTERS **93**, 151903 (2008)

Buried melting in germanium implanted silicon by millisecond flash lamp annealing

Matthias Voelskow,[1,a)] Rossen Yankov,[1] Wolfgang Skorupa,[1] Jörg Pezoldt,[2] and Thomas Kups[3]
[1]*Institute of Ion Beam Physics and Materials Research, Forschungszentrum Dresden-Rossendorf, P.O. Box 510119, 01314 Dresden, Germany*
[2]*Nanotechnology, Institute of Micro- and Nanotechnologies, TU Ilmenau, P.O. Box 100565, 98684 Ilmenau, Germany*
[3]*Materials for Electronics, Institute of Micro- and Nanotechnologies, TU Ilmenau, P.O. Box 100565, 98684 Ilmenau, Germany*

(Received 17 July 2008; accepted 12 September 2008; published online 13 October 2008)

Flash lamp annealing in the millisecond range has been used to induce buried melting in silicon. For this purpose high dose high-energy germanium implantation has been employed to lower the melting temperature of silicon in a predetermined depth region. Subsequent flash lamp treatment at high energy densities leads to local melting of the germanium rich layer. The thickness of the molten layer has been found to depend on the irradiation energy density. During the cool-down period, epitaxial crystallization takes place resulting in a largely defect-free layer. © *2008 American Institute of Physics*. [DOI: 10.1063/1.2993332]

Doping of semiconductors by ion implantation is generally associated with the formation of Gaussian-like concentration/depth profiles. Because of the range straggling of the implanted ions, it is practically impossible to form a steep implant profile at a predetermined depth. Moreover, the range straggle increases with the increasing ion energy, thereby producing progressively broader implant profiles. Postimplantation annealing brings about additional profile broadening because of the dopant diffusion. Although dopant diffusion in the solid phase may be minimized by using rapid thermal annealing methods,[1,2] the range straggle remains a major limiting factor in the formation of steep buried profiles.

Basically, the use of a laser for surface melting followed by dopant segregation may lead to the formation of pronounced dopant peaks.[3,4] However, the laser efficiency is low, the uniformity of processing is poor, and moreover, the resulting dopant peak will be positioned at the surface. In the standard situation, melting always starts from the surface independently of the annealing method used. It would be of great practical importance to be able to initiate controllable melting at a certain depth beneath the surface. Subsequent segregation of the previously implanted dopant species would lead to the formation of a sharp buried dopant profile.

In this work we propose an approach in achieving localized buried melting at a predetermined depth as the basis for the formation of either a pronounced dopant segregation peak or a homogeneous plateaulike dopant distribution. More specifically, we have used Ge ion implantation to lower the melting temperature of the implanted zone,[5] and subsequent flash lamp annealing (FLA) to selectively melt this zone.

FLA is a process which enables semiconductor materials to be heat treated and cooled for times in the millisecond range. In this sense, FLA can be viewed as an ultrarapid thermal processing (RTP) technique differing from the standard RTP primarily by the timescale in which the radiant energy incident on the wafer is delivered (milliseconds versus seconds). The great advantage of the flash lamp system over the traditional tungsten filament or quartz halogen lamp based versions is that the former provides much steeper heating/cooling ramp rates and lower thermal budgets. The basic issues of the millisecond heat treatment are discussed in detail in Ref 6.

To produce a buried layer of a reduced melting temperature, (100)-oriented Si wafers were implanted with 190 keV Ge ions to a dose of 5×10^{17} cm^{-2}. The implantation was carried out at a substrate temperature of 400 °C to avoid amorphization of the implanted layer as well as any spontaneous crystallization during subsequent annealing. Flash lamp annealing was carried out using the Rossendorf flash lamp apparatus. The system consists of a process chamber, an upper bank of 12 xenon lamps, a wafer holder, a lower bank of halogen lamps allowing the wafer to be preheated to a selected intermediate temperature, and an aluminum reflector behind each bank of lamps. Wafer preheating (typically to 750 °C) is necessary to uniformly heat the entire wafer to a certain intermediate temperature, thus minimizing the undesirable thermally induced stresses arising from the momentary temperature elevation. The wafer rested on special quartz holders thereby reducing heat losses and allowing for uniform heating. The duration of the flash was 20 ms. The maximum energy density of the light pulse at the sample surface was 155 J cm^{-2}, which is sufficient to heat the substrate to a temperature above the Si melting point. A detailed description of the experimental setup is given elsewhere.[7]

After FLA, the resulting Ge profiles were characterized by Rutherford backscattering spectrometry (RBS), and the data were processed using the RUMP computer code.[8,9] Cross-sectional transmission electron microscopy (XTEM) was undertaken to study the defect structure in both the as-implanted and the annealed samples.

Figure 1 shows Ge profiles after FLA at different energy densities in comparison with the as-implanted Ge distribution. According to stopping and range of ions in matter

a)Electronic mail: m.voelskow@fzd.de.

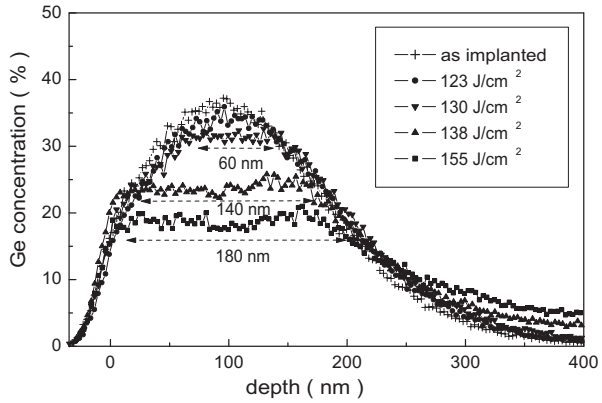

FIG. 1. Ge depth profiles derived from random RBS spectra for Si samples implanted with 190 keV, 5×10^{17} cm^{-2} Ge ions at 400 °C before and after 20 ms FLA at different light energy densities. The nominal width of the molten zone is also shown.

simulations,[10] the Ge implant profile peaks at 135 nm and has a full width at half maximum of about 89 nm. The actual measured Ge distribution, however, peaks at about 100 nm due to the effect of sputtering by the high dose implant.

As far as the shape of the Ge profiles after FLA is concerned, no change can be observed up to an energy density of 123 J cm^{-2}. However, a further increase in the energy density to 130 J cm^{-2} results in a specific transformation of the Ge profile. While the flanks of the distributions remain much the same, the peak of the profile broadens and moves to lower concentrations forming a well-defined plateau. The observed modification cannot be explained by solid-state diffusion, but may rather be attributed to the melting process that has occurred in the region of maximum Ge concentration. Further increasing FLA energy density results in the plateau becoming broader and finally reaching the surface at 138 J cm^{-2}. The width of the respective molten zones is given in Fig. 1.

Figure 2 shows TEM micrographs of the Ge implanted specimens before [Fig. 2(a)] and after [Figs. 2(b) and 2(c)] FLA at 130 and 155 J cm^{-2}, respectively. The as-implanted sample [Fig. 2(a)] exhibits a defect structure typical of a high dose ion implanted material, with the defect-rich region extending from the surface to a depth of about 500 nm. Individual defects are not seen under the magnification used. As determined by additional RBS channeling measurements (not shown) the defect level in the implanted region is well below the amorphization threshold, evidently because of the elevated substrate temperature during implantation.

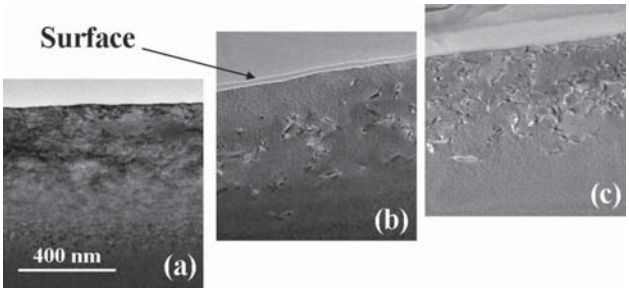

FIG. 2. (a) TEM micrographs of high-dose Ge-implanted Si after implantation, (b) FLA at 130, and (c) 155 J cm^{-2}.

Figure 2(b) shows the defect structure after FLA at 130 J cm^{-2}. The near-surface region is of low defect density while numerous linear defects of a typical length of 5 to 20 nm are seen over the depth range of 130 to 450 nm. They are located perpendicular to the (112) direction, with an angle of 70.5° between the defects corresponding to the angle between the (111) lattice planes in (100) direction. Correlating the RBS data with the TEM results for the 130 J cm^{-2} sample reveals three distinct depth zones.

The first zone extends from the surface to about 60 nm and remains solid during the FLA treatment as confirmed by the unchanged near surface part of the Ge profile over this region. The second zone is located at a depth of 60 to 130 nm and corresponds to the flat-topped portion of the Ge profiles. This zone has undergone melting and solidification resulting in an almost defect free recrystallized region. The third zone spans the depth range of 130 to 450 nm and is characterized by a relatively high defect density, presumably because of the high Ge concentration and the attendant strain. The respective portion of the RBS spectra remains unchanged, which implies that this zone has similarly not been molten during FLA. The observed high defect density may be related to the relaxation of the mechanical stress in this region due to the high Ge concentration. In contrast, relaxation within the molten region where the Ge concentration is even higher has occurred via liquid phase crystallization, which in turn has enabled the crystalline material to regrow in a largely defect-free manner. The most important finding for the 130 J cm^{-2} flashed sample is that the molten Ge rich layer crystallizes epitaxially using the thin solid near-surface region as a practically defect-free seed. Unlike this region, the zone beneath the lower liquid/solid interface (i.e., the one adjacent to the molten Ge-rich layer) contains high-density linear defects of a mean length of 5 to 20 nm. If crystallization had occurred starting from this interface, then defects of high density would have formed in the recrystallized layer, and these would have been easily detected by TEM.

The TEM micrograph of the sample annealed at 155 J cm^{-2} [see Fig. 2(c)] shows that at this highest energy density a continuous defective layer has been formed, which extends from the surface down to a depth of 500 nm. The layer contains numerous linear defects but, in comparison to the lower energy density case, these are of a smaller mean length of 5 to 10 nm. In contrast to the lower energy density situation, it is evident that the whole surface layer has now been molten and, accordingly, the crystallization process has started from the lower liquid/solid interface because of the lack of a seed at the surface. The high defect density at the lower flank of the Ge implant profile, however, gives rise to the poor crystalline quality of the crystallized layer as confirmed by the micrograph in Fig. 2(c).

The XTEM images also reveal that there is no noticeable change in the surface quality after implantation and, more significantly, after buried melting. The surface in all samples shows a roughness of 5 to 10 nm, implying that it is practically flat.

Referring back to Fig. 1 and taking into account the TEM results, one may infer that the observed tail in the Ge profiles at larger depths (see Fig. 1) is associated with the well-known faceted liquid/solid interface during the rapid melting of the single-crystal material.[11] Because of the faceted nature of the interface and the much larger diameter of the RBS beam spot compared with the characteristic size of

the faceted structure, one observes in practice a gradual transition from a molten to a nonmolten bulk region, and this is the reason for the elevation in the Ge profiles at larger depths. Optimized implantation and FLA conditions will certainly enable one to minimize the faceting of the lower liquid/solid interface.

In conclusion, we have demonstrated the possibility of achieving buried melting in Si during pulsed short-time heat treatment at moderate energy densities (130 J cm^{-2}) by introducing a previously created layer of a reduced melting temperature containing ion implanted Ge. At sufficiently high doses and energies, the Ge atoms will lower locally the melting temperature in the implanted Si region by tens of degrees. In this way, melting starts at a predetermined depth, is confined to the Ge-implanted zone, and proceeds in a controllable manner as distinct from the standard case where melting starts unavoidably from the surface. A practically useful consequence of this process is that the ingrowth of defects from the defect-rich lower solid/liquid interface is prevented.

The process of buried melting by introducing Ge would similarly be helpful for the formation of strained Si structures. Once the buried layer is molten, the layer system would undergo considerable relaxation. Cooling down the structure would result in epitaxial crystallization of the molten layer. However, a further cool down of the solidified system would induce high tensile stresses in the upper Si layer because of the much higher expansion coefficient of pure Si compared to that of the SiGe alloy. As is well known, a high tensile stress in Si leads to increased carrier mobility and may be used for the fabrication of advanced devices.

We would like to thank W. Anwand and T. Schumann for performing the flash lamp annealing experiments, G. Winkler for the Ge ion implantation, and E. Remdt for TEM sample preparation.

[1]W. Lerch, S. Paul, J. Niess, S. McCoy, J. Gelpey, F. Cristiano, S. Boninelli, O. Marcelot, P. F. Fazzini, and R. Duffy, ECS Trans. **3**(2), 77 (2006).
[2]W. Skorupa, T. Gebel, R. A. Yankov, S. Paul, W. Lerch, D. F. Downey, and E. A. Arevalo, J. Electrochem. Soc. **152**, G436 (2005).
[3]D. Hoonhout and F.W. Saris, Phys. Lett. **74A**, 253 (1979).
[4]J.-N. Gillet, J.-Y. Degorce, and M. Meunier, Appl. Phys. Lett. **86**, 222104 (2005).
[5]R. W. Olesinski and G. J. Abbaschian, Bull. Alloy Phase Diagrams **5**, 180 (1984).
[6]R. A. McMahon, M. P. Smith, K. A. Seffen, M. Voelskow, W. Anwand, and W. Skorupa, Vacuum **81**, 1301 (2007).
[7]W. Skorupa, W. Anwand, D. Panknin, M. Voelskow, R. A. Yankov, and T. Gebel, Vacuum **78**, 673 (2005).
[8]L. R. Doolittle, Nucl. Instrum. Methods Phys. Res. B **15**, 227 (1986).
[9]See www.genplot.com for RBS spectra simulation.
[10]See www.srim.org.
[11]M. Voelskow, M. Smith, W. Skorupa, and R. McMahon, Appl. Phys. Lett. **87**, 241901 (2005).

APPLIED PHYSICS LETTERS **93**, 161907 (2008)

Efficient oxygen gettering in Si by coimplantation of hydrogen and helium

Xin Ou,[1] Reinhard Kögler,[1,a)] Arndt Mücklich,[1] Wolfgang Skorupa,[1] Wolfhard Möller,[1] Xi Wang,[2] Jürgen W. Gerlach,[3] and Bernd Rauschenbach[3]
[1]*Forschungszentrum Rossendorf, PF 510119, D-01314 Dresden, Germany*
[2]*Shanghai Institute of Microsystem and Information Technology, Chinese Academy of Sciences, Shanghai 20050, People's Republic of China*
[3]*Leibniz-Institut für Oberflächenmodifizierung, Permoserstrasse 15, D-04318 Leipzig, Germany*

(Received 15 August 2008; accepted 2 October 2008; published online 21 October 2008)

Hydrogen preimplantation performed in addition to helium implantation efficiently shrinks the width of the gettering layer in Si and increases the empty volume fraction as well as the internal surface area per unit volume. The gettering efficiency for oxygen is significantly enhanced compared to the single helium implantation, and the helium implantation dose can be strongly reduced. The gas-filled bubble layer induced by the coimplantation of hydrogen and helium has the highest gettering efficiency for the oxygen accumulation. Direct evidence for oxygen gettering at the internal wall of the cavity is demonstrated by cross-sectional transmission electron microscopy. © *2008 American Institute of Physics*. [DOI: 10.1063/1.3005595]

Gettering processes are an important tool for the accumulation of extrinsic impurities away from the device region at the predefined gettering sites. Helium or hydrogen ion implantation induced cavity formation in silicon is a well established and efficient method to trap impurities.[1,2] In the silicon-on-insulator (SOI) substrate fabrication the coimplantation of hydrogen and helium improves the "smart-cut" process by reducing the necessary ion dose.[3] The cavities found in a very narrow layer show an increased empty volume fraction and a higher internal surface per volume, which are considered as two critical parameters for the gettering process.[4–6] Moreover, the total ion dose to create a stable gettering layer is significantly reduced by coimplantation of hydrogen and helium.[7] One application for such a narrow cavity layer is to serve as an oxygen gettering layer at the early stage of the separation-by-implanted-oxygen (SIMOX) technology which is used for the fabrication of SOI substrates by implanting high doses of oxygen and subsequent high temperature annealing.[8] In this study, we demonstrate that the thickness of the cavity layer induced by helium implantation can be substantially reduced by adding a small dose of hydrogen before. In order to reduce the oxygen dose necessary for the continuous buried oxide layer, the accumulation of the implanted oxygen in a narrow layer is very critical, as the thickness of the gettering layer defines the final thickness of the oxide layer. The efficiency of oxygen gettering is compared for the coimplantation of hydrogen and helium and for the single helium implantation and the reference with only oxygen implantation, as well as for an empty cavity or a gas-filled bubble.

Si (100) wafers were preimplanted at room temperature with 40 keV H^+ to 4×10^{15} cm^{-2} followed by 45 keV He^+ to 1×10^{16} cm^{-2} or by 45 keV He^+ to 4×10^{16} cm^{-2} only. The threshold dose for the cavity layer formation by single He^+ implantation in Si is around 1×10^{16} cm^{-2} at the present energy, and a cavity layer for reliable gettering requires a He^+ ion dose of $(4-5)\times10^{16}$ cm^{-2}.[4,9] The significantly lower He^+ ion dose used in the coimplantation prevents exfoliation and blistering in silicon. O^+ ion implantation at 550 °C was performed with 160 keV to a dose of 1×10^{17} cm^{-2}. Implantation energies were chosen according to TRIM calculations[10] in order to guarantee maximum implantation profile overlap. The introduction of the oxygen gettering layer was carried out in two approaches. One was to form a gas-free cavity layer after the hydrogen and/or helium implantation by a preannealing at 1000 °C for 1 h before the oxygen implantation. This preannealing results in the outdiffusion of hydrogen and helium.[4] Alternatively, without the preannealing, a layer of gas-filled microbubbles is formed. The final annealing for oxygen gettering was performed at 1150 °C for 2 h in an atmosphere containing Ar and O_2 in the ratio $Ar/O_2 = 100/5$. The oxygen depth distribution was analyzed by means of time-of-flight secondary ion mass spectrometry (TOF-SIMS) and the sample morphology was investigated by cross-section transmission electron microscopy (XTEM).

Figure 1 shows the effect of an additional hydrogen implantation on a cavity layer induced by helium implantation. A well defined cavity layer is formed by single helium implantation with the thickness of 130 nm. The total empty volume fraction of 10% and the internal surface of 2.8×10^5 cm^2/cm^3 inside the layer were estimated from XTEM images examined for a constant thickness of 57 nm [Fig. 1(a)]. The coimplantation generated a cavity layer [Fig. 1(b)] with the thickness as narrow as 50 nm at a depth position in correspondence with the depth of the platelet defects induced by single hydrogen implantation at 40 keV. This reduction in the thickness of the cavity layer exclusively results from the hydrogen implantation, not from the decreased helium dose. The total empty volume fraction and the internal surface per unit volume of this cavity layer in Fig. 1(b) are higher than those of the cavity layer in Fig. 1(a) by factors of 2 and 1.1, respectively. To achieve a continuous buried oxide layer in the existing cavity layer, the oxygen dose necessary to form an oxide layer of the same thickness as the gettering layer is about 6×10^{17} cm^{-2} for the cavity layer in Fig. 1(a), while it is only 2×10^{17} cm^{-2} for the narrow cavity layer in Fig. 1(b).[11] As demonstrated by Fig. 2 the maximum oxygen concentration of the bubble layer induced by coimplantation is two times higher than for the single helium implantation and

a)Electronic mail: Koegler@fzd.de.

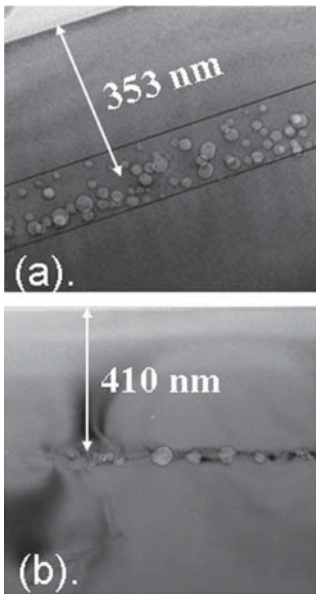

FIG. 1. XTEM images in underfocus mode of the cavity layer in Si induced by single He implantation to a dose of 4×10^{16} cm^{-2} (a) and induced by coimplantation of H to 4×10^{15} cm^{-2} and He to 1×10^{16} cm^{-2} (b). Annealing was performed at 1000 °C for 1 h.

four times higher than in the reference sample. The bubble layer is more efficient in oxygen gettering than the cavity layer and the coimplantation is more efficient than the single helium implantation. Figure 3 compares the oxygen profile and the distribution of the SiO_2 precipitates for the coimplanted bubble layer and the reference sample. The distribution of SiO_2 precipitates is changed already for annealing at 1150 °C. A sharp band of SiO_2 precipitates is formed in one layer with a thickness of only 16 nm [Fig. 3(b)] in addition to the broad oxygen background which is similar in shape as for the reference sample. These are preferable conditions for the coalescence of separate precipitates to a continuous oxide layer by annealing at even higher temperatures as usually applied in SIMOX processing.[11] Figure 4 gives the evidence that under the present conditions, oxide formation begins directly at the internal {111} and {100} surface facets of the preformed cavity. This decoration of the inner cavity surface has not been directly observed in former experiments which introduced the cavity by single helium or hydrogen

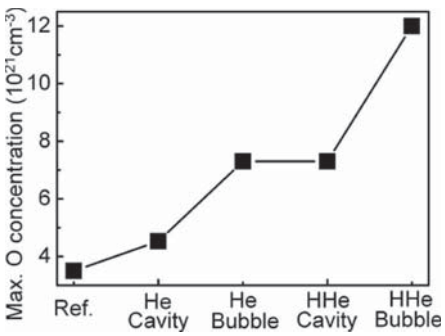

FIG. 2. Comparison of the maximum oxygen concentrations (measured by TOF-SIMS) accumulated by different gettering layers after the oxygen implantation to a dose of 1×10^{17} cm^{-2} and annealing at 1150 °C for 2 h. The He cavity or bubble layer was formed by single He implantation to a dose of 4×10^{16} cm^{-2}, while the HHe cavity or bubble layer was formed by coimplantation of H to 4×10^{15} cm^{-2} and He to 1×10^{16} cm^{-2}.

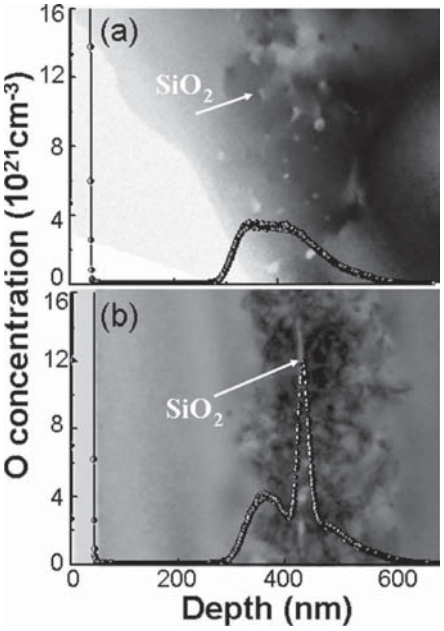

FIG. 3. XTEM micrographs showing the distribution of SiO_2 precipitates (bright dots) in the reference sample (a) and in the sample with a bubble layer induced by coimplantation of H and He (b) as described in Fig. 2. The corresponding oxygen profiles measured by TOF-SIMS are inserted with the same depth scale as the XTEM images.

implantation.[2,12] The oxidation proceeds from the facetted surface into the silicon substrate leaving the empty volume inside with a spherical shape due to the isotropic surface free energy of the amorphous oxide. Volume expansion (by a factor of 2.27) generated by the SiO_2 formation leads to the shrinkage of the empty volume. The cavities are expected to disappear for annealing at higher temperatures. Assuming an equal amount of empty volume in the cavities and bubbles, the bubbles exhibit much more internal surface due to their significantly higher density and smaller size (they could not be observed by XTEM), and therefore bubbles are more efficient for oxygen gettering. The coalescence of the oxide precipitates results in a buried layer parallel to the surface in Si (100) as the oxidation velocity in the [111] direction is higher than that in the [100] direction.[13]

Even though gettering of oxygen in silicon by cavities or microbubbles is demonstrated in this study, also other impurities in semiconductor processing may be gettered in the same way. This especially holds for impurities, for instance,

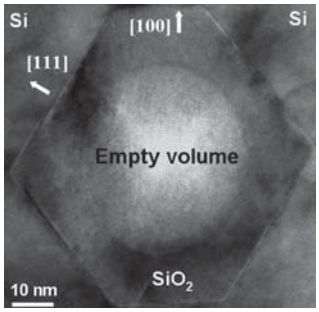

FIG. 4. XTEM micrograph showing the direct evidence of oxide formation at the internal wall of a cavity formed by H (4×10^{15} cm^{-2}) plus He (1×10^{16} cm^{-2}) implantation and annealing at 1000 °C for 1 h. Oxygen was subsequently implanted to a dose of 1×10^{17} cm^{-2}. The thermal treatment was performed at 1150 °C for 2 h.

Au and Cu,[6,9,14,15] which are known to be trapped directly at the internal surface of the cavity.

To summarize, an excellent gettering layer for trapping of oxygen in silicon is formed by coimplantation of hydrogen and helium. A twofold trapping mechanism results in a very narrow and efficient gettering layer. Helium is trapped by hydrogen induced platelet defects, and the helium bubbles are nucleation sites for SiO_2 precipitation. The oxidation has been demonstrated to occur directly at the internal wall of the cavity or bubble.

[1]S. M. Myers, M. Seibt, and W. Schröter, J. Appl. Phys. **88**, 3795 (2000).
[2]J. S. Wiliams, M. C. Ridgway, M. J. Conway, J. Wong-Leung, X. F. Zhu, M. Petravic, F. Fortuna, M.-O. Ruault, H. Bernas, A. Kinomura, Y. Nakano, and Y. Hayashi, Nucl. Instrum. Methods Phys. Res. B **178**, 33 (2001).
[3]A. Agarwal, T. E. Haynes, V. C. Venezia, O. W. Holland, and D. J. Eaglesham, Appl. Phys. Lett. **72**, 1086 (1998).
[4]V. Raineri, M. Saggio, and E. Rimini, J. Mater. Res. **15**, 1449 (2000).
[5]J. W. Medernach, T. A. Hill, S. M. Myer, and T. J. Headley, J. Electrochem. Soc. **143**, 725 (1996).
[6]J. Wong-Leung, E. Nygren, and J. S. Wiliams, Appl. Phys. Lett. **67**, 416 (1995).
[7]G. Gaudin, F. Cayrel, C. Bongiorno, R. Jérisian, V. Raineri, and D. Alquier, Solid State Phenom. **108**, 309 (2005).
[8]*SIMOX*, edited by M. J. Anc (Institution of Electrical Engineers, Stevenage Herts., UK, 2004).
[9]D. M. Follstaedt, S. M. Myers, G. A. Peersen, and J. W. Medernach, J. Electron. Mater. **25**, 151 (1996).
[10]J. F. Ziegler, J. P. Biersack, and U. Littmark, *The Stopping and Ranges of Ions in Solids*, edited by J. F. Ziegler (Pergamon, New York, 1985), Vol. 1.
[11]R. Kögler, X. Ou, W. Skorupa, and W. Möller, Appl. Phys. Lett. **92**, 181906 (2008).
[12]V. M. Vishnyakov, S. E. Donnelly, and G. Carter, J. Appl. Phys. **94**, 238 (2003).
[13]H. Iikawa, M. Nakao, and K. Izumi, J. Mater. Res. **19**, 3607 (2004).
[14]J. Wong-Leung, C. E. Ascheron, M. Petravic, R. G. Elliman, and J. S. Wiliams, Appl. Phys. Lett. **66**, 1231 (1995).
[15]S. M. Myers and D. M. Follstaedt, J. Appl. Phys. **79**, 1337 (1996).

APPLIED PHYSICS LETTERS **92**, 181906 (2008)

The origin of the energy-dose window in separation-by-implanted-oxygen materials processing

R. Kögler,[a] Xin Ou, W. Skorupa, and W. Möller
Forschungszentrum Dresden-Rossendorf, PF 510119, D-01314 Dresden, Germany

(Received 25 March 2008; accepted 8 April 2008; published online 7 May 2008)

The energy-dose (ED) window (so called Izumi window) for the formation of a perfect planar and homogeneous buried oxide layer in silicon using ion implantation is controlled by the interaction of excess radiation defects and the local oxygen concentration. The ED window is defined by an appropriate correlation between the distribution of implantation-induced excess defects and the position of the finally formed oxide layer. A quantitative relation is established on the basis of collisional computer simulations. The findings are discussed in terms of oxide precipitation under the influence of defects. © *2008 American Institute of Physics*. [DOI: 10.1063/1.2917582]

The separation-by-implantated-oxygen (SIMOX) process is one of the well established techniques to fabricate silicon-on-insulator (SOI) material.[1] The process consists of a high-dose O implantation at temperatures $T \geqslant 500$ °C and a long-term annealing at temperatures $T \geqslant 1300$ °C resulting in a buried oxide layer with box-shaped O profile (BOX). However, the required very high ion dose does not only present an economic problem but also introduces a high level of implantation defects into the top Si layer. Consequently, numerous investigations were performed in order to reduce the oxygen dose. The state-of-the-art of SIMOX processing employs defect engineering, as, e.g., internal oxidation (ITOX).[2–4] The experimental results also revealed an energy-dose (ED) window[5] within which a planar continuous buried oxide layer is achieved with excellent SOI material properties.[6–8] For a lower oxygen dose, the layer is mostly not continuous and consists of isolated oxide precipitates. For a higher oxygen dose, a continuous but inhomogeneous oxide layer is formed including silicon islands. The origin of the ED window is not yet explained by theoretical modeling.[9–11] In this study the implantation-induced excess of vacancies V_{ex} or of interstitials I_{ex} is supposed to be the cause of the ED window. Such excess defects are generated and accumulated during implantation by spatial separation of Frenkel defect pairs and survive the implantation at enhanced temperature.[12]

Figure 1 shows the O profile and the corresponding distributions of V_{ex} and I_{ex} for 150 keV O ion implantation. Following the concept of Holland *et al.*,[12] the profiles in this study were calculated by full cascade simulations using the computer code transport of ions in matter (TRIM).[13,14] The indicated position x_J is the depth where the defect distribution changes from excess of vacancies to interstitials. BOX formation requires the redistribution of the implanted oxygen from outside into the BOX region. The hatched area in Fig. 1 shows the BOX after complete O redistribution centered at the O profile peak. The Si/SiO_2 interface is marked at the position x_B. O redistribution against the concentration gradient proceeds by coarsening or Ostwald ripening.[9–11] Any implanted oxygen dose Φ_O results in a BOX of corresponding thickness $d_B = \Phi_O / c_{OX}$, where c_{OX} is the O concentration in SiO_2 (e.g., $d_B = 22.5$ nm for $\Phi_O = 1 \times 10^{17}$ cm^{-2}). However, as indicated by the ED window, there is also another factor restricting the O redistribution process. SiO_2 precipitate formation in Si results in significant volume expansion by the factor 2.27. Thus, the presence of vacancies or vacancy clusters enhances the precipitate growth rate and, hence, the O redistribution, whereas, it is restrained by interstitials.

The calculated O profiles and their corresponding BOX position were compared to the depth distributions of excess defects (V_{ex}, I_{ex}) for different implantation parameters. The depth position x_J is fixed by the ion energy, whereas the position x_B varies with ion dose. There is just one ion dose for which x_J is in agreement with x_B, as demonstrated in Fig. 1. The calculations performed for the implantation parameters of ED window implants taken from Ref. 7 revealed that these implants always fulfill the condition $x_J = x_B$. Two examples of calculations for ED window implants are shown in Fig. 2 in linear scale. Figure 2 also demonstrates that there is a secondary relation which is approximately valid for O implantation in the ED window: $c_O(x_J) = c_C = 1.9(\pm 0.12) \times 10^{22}$ cm^{-3}, where $c_O(x_J)$ is the O concentration at x_J. Both relations determine the ED window: (i) $x_J = x_B$ and (ii) $c_O(x_J) = c_C = 1.9 \times 10^{22}$ cm^{-3}.

The first relation (i) can be explained by the rapid decrease in oxide precipitate growth rate at x_J due to the change

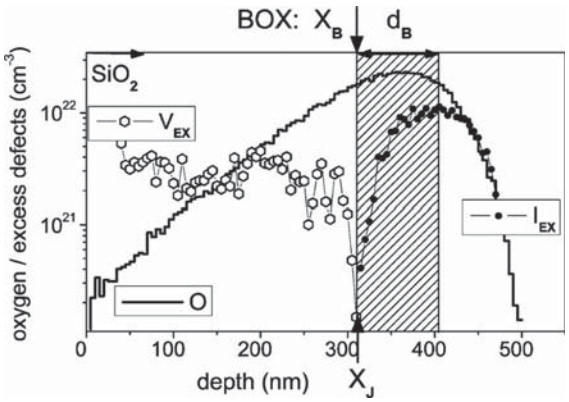

FIG. 1. Calculated depth profiles of oxygen and the corresponding distributions of excess vacancies V_{ex} and excess interstitials I_{ex} are shown for silicon implanted with 150 keV to 4.1×10^{17} O cm^{-2} (dose in the ED window). The abrupt junction from V_{ex} to I_{ex} is marked by x_J. The position x_B indicates the Si/SiO_2 interface of the finally formed buried oxide layer (hatched area =BOX) and d_B is the thickness of the BOX.

[a]Electronic mail: r.koegler@fzd.de.

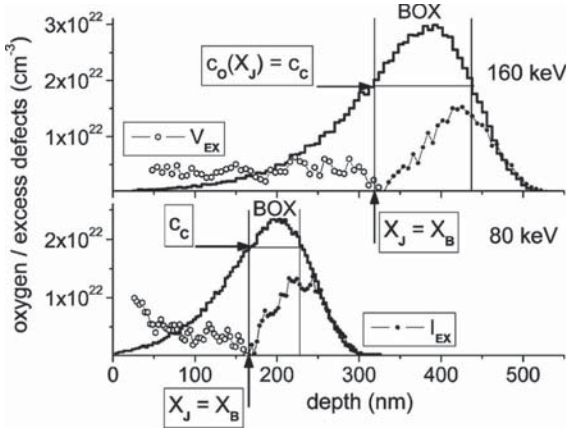

FIG. 2. Oxygen depth profiles and the profiles of excess vacancies V_{ex} and excess interstitials I_{ex} for oxygen implants in the ED window into silicon. Calculations were performed for implantation with ion energies of 80 and 160 keV to doses of 3×10^{17} and 5.3×10^{17} O cm^{-2}, respectively. These implantation parameters according to the ED data given in Ref. 7 satisfy the relation $x_J=x_B$. The corresponding position of the BOX is indicated. The arrows show the O concentration level at x_J which is approximately constant for all ED window implantations: $c_O(x_J)=c_C=$const.

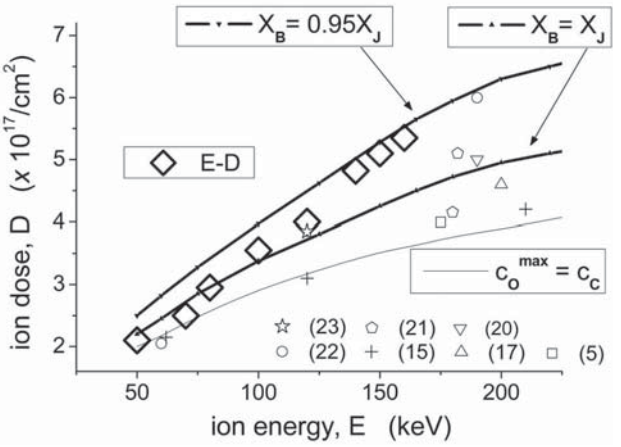

FIG. 3. Comparison of the calculated ED window with experimental results. The thin curve below shows the oxygen dose required for a maximum O concentration of $c_O^{max}=1.9\times10^{22}$ cm^{-3}. The ED window is the distance between both thick lines which were calculated for the conditions $x_B=x_J$ and $x_B=0.95x_J$. Experimental results for the ED window (rhombs) are taken from Ref. 7. Other experimental data are also included. Figures in brackets indicate the references.

of the defect type. The slow down of the precipitate growth at x_J results in a discontinuity of the process of O redistribution toward the maximum of oxygen concentration. Therefore, large precipitates may grow in the vacancy-dominated region by accumulation of oxygen which does not pass down. The parity $x_J=x_B$ is the "best choice" for O redistribution resulting in a narrow oxide layer without discontinuity. Large precipitates eventually formed in the region outside the BOX, can hardly be resolved. Such precipitates are mainly arranged in one layer in addition to the precipitates in the BOX region. A double layer of precipitates was frequently observed for low dose O implantation.[15–17] Furthermore, the region in front of the mean projected ion range in Si is known for gettering of impurities by excess vacancy clusters.[18,19] The second relation (ii) defines a particular O concentration c_C (see Fig. 2). The volume fraction of SiO_2 corresponding to c_C is very high ($\approx$50%). Therefore, the precipitates are in immediate vicinity. For a marginally higher volume fraction of 52%, spherical precipitates of arbitrary size would be in direct contact. At such high density precipitates rather grow by coalescence than by coarsening. Large-size precipitates are rapidly formed by coalescence. The O concentration c_C may be a threshold between depth regions dominated by coarsening (below c_C) and by coalescence (above c_C). For ED window implants, the region dominated by coalescence (the "core" region of precipitate growth) coincides with the BOX region.

Calculated ED data are presented in Fig. 3 together with experimental results. The thin line shows the minimum O dose to reach a maximum concentration of $c_C=1.9\times10^{22}$ cm^{-3} in the as-implanted profile. Two thick lines represent combinations of ion energy and dose for which the Si/SiO_2 interface of the BOX is at $x_B=x_J$ and at $x_B=0.95x_J$. In addition, the relation $c_O(x_B)=c_C$ is satisfied. The curves are slightly smoothed. A small shift of x_B toward a position of about 5% shallower than x_J is inside the margin of deviation of data in the Monte Carlo simulations[14] (see Fig. 2). The gap between the curves reflects the statistical character of ion implantation and the range between them is supposed to be the calculated ED window region.

For ion energies below 75 keV, the ED window is overestimated. This might be due to enhanced annihilation of defects at the nearby surface. As the energy decreases, an increasing fraction of the generated excess vacancies is located close to the surface (visible in Fig. 2). Notice that the amount of excess vacancies generated in O implantation is always about 0.2 per O ion. For comparison, other experimental data are also indicated in Fig. 3. Some of them fall below the ED window. The relatively large scattering of the experimental data[5,7,15,17,20–23] is probably due to variations of the process parameters resulting in different kinds of defect engineering. Appropriate experiments[5,24] made use of extreme long-term annealing (very slow temperature ramping) and/or of a foreign O source (ITOX). Such techniques may change the implantation-induced defect state and were not considered in the present model.

To summarize, the ED window indicates that implantation-induced defects control the O redistribution during high-temperature annealing in SIMOX processing. The ED window is determined by the relations $x_B=x_J$ and $c_O(x_B=x_J)=c_C=1.9\times10^{22}$ cm^{-3}. Moreover, the effect of implantation defects demonstrates that appropriate defect annealing or smart defect engineering can overcome the ED window in order to further reduce the required O dose.

[1]See: SIMOX, edited by Maria J. Anc (The Institution of Electrical Engineers, Stevenage Herts, UK, 2004).
[2]Y. Takahashi, T. Ishiyama, and M. Tabe, Appl. Phys. Lett. **65**, 2987 (1994).
[3]S. Nakashima, T. Katayama, Y. Miyamura, A. Matsuzaki, M. Kataoka, D. Ebi, M. Imai, K. Izumi, and N. Ohwada, J. Electrochem. Soc. **143**, 244 (1996).
[4]A. Matsumura, I. Hamaguchi, K. Kawamura, T. Sasaki, S. Takayama, and Y. Nagatake, Microelectron. Eng. **66**, 400 (2003).
[5]S. Nakashima and K. Izumi, J. Mater. Res. **8**, 523 (1993).
[6]M. Chen, J. Chen, W. Zheng, L. Li, H. C. Mu, Z. X. Lin, Y. H. Yu, X. Wang, and G. Y. Wang, J. Vac. Sci. Technol. B **19**, 337 (2001).
[7]M. Chen, X. Wang, J. Chen, Y. Dong, W. Yi, X. Liu, and X. Wang, J. Vac. Sci. Technol. B **21**, 2001 (2003).
[8]M. Chen, X. Wang, J. Chen, Y. Dong, X. Liu, Y. Yu, and X. Wang, Appl. Phys. Lett. **80**, 880 (2002).
[9]S. Reiss and K.-H. Heinig, Nucl. Instrum. Methods Phys. Res. B **84**, 229 (1994).

[10]S. Reiss and K.-H. Heinig, Nucl. Instrum. Methods Phys. Res. B **112**, 223 (1996).
[11]S. Strobel, S. Reiss, K.-H. Heinig, and W. Möller, Radiat. Eff. Defects Solids **141**, 99 (1997).
[12]O. W. Holland, L. Xie, B. Nielson, and D. S. Zhou, J. Electron. Mater. **25**, 99 (1996).
[13]J. Biersack and L. G. Haggmark, Nucl. Instrum. Methods **174**, 257 (1980).
[14]R. Kögler, A. Peeva, J. Kaschny, W. Skorupa, and H. Hutter, Nucl. Instrum. Methods Phys. Res. B **186**, 298 (2002).
[15]M. Tamura, M. Ishimaru, K. Hinode, K. Tokiguchi, H. Seki, and H. Mori, Jpn. J. Appl. Phys., Part 1 **45**, 7592 (2006).
[16]H. Ono and A. Ogura, J. Appl. Phys. **87**, 7782 (2000).
[17]S. Bagchi, S. J. Krause, and P. Roitman, Appl. Phys. Lett. **71**, 2136 (1997).
[18]A. Peeva, R. Kögler, and W. Skorupa, Nucl. Instrum. Methods Phys. Res. B **206**, 71 (2003).
[19]A. Peeva, R. Kögler, W. Skorupa, J. S. Christensen, and A. Y. Kuznetsov, J. Appl. Phys. **95**, 4738 (2004).
[20]Y. Tan, B. Johnson, S. Seraphin, J. Jiao, M. J. Anc, and L. P. Allen, J. Mater. Sci.: Mater. Electron. **12**, 537 (2001).
[21]H. Iikawa, M. Nakao, and K. Izumi, J. Mater. Res. **19**, 3607 (2004).
[22]J. Jiao, B. Johnson, S. Seraphin, M. J. Anc, R. P. Dolan, and B. F. Cordts, Mater. Sci. Eng., B **72**, 150 (2000).
[23]A. Auberton-Herve, A. Wittkower, and B. Aspar, Nucl. Instrum. Methods Phys. Res. B **96**, 420 (1995).
[24]A. Ogura, Jpn. J. Appl. Phys., Part 2 **40**, L1075 (2001).

APPLIED PHYSICS LETTERS **93**, 071908 (2008)

Blue and red electroluminescence of Europium-implanted metal-oxide-semiconductor structures as a probe for the dynamics of microstructure

L. Rebohle,[a] J. Lehmann, S. Prucnal, A. Kanjilal, A. Nazarov,[b] I. Tyagulskii,[b] W. Skorupa, and M. Helm
Institute of Ion Beam Physics and Materials Research, Forschungszentrum Dresden Rossendorf, POB 510119, D-01314, Germany

(Received 4 June 2008; accepted 2 July 2008; published online 22 August 2008)

The strong blue and red electroluminescence from Eu-implanted SiO_2 layers were investigated as a function of implantation and annealing conditions. It is shown that the red electroluminescence assigned to Eu^{3+} ions is favored by low Eu concentrations, low annealing temperatures, and short annealing times. Based on a more quantitative analysis of the electroluminescence spectra this preference is explained by a shorter supply of oxygen for higher Eu concentrations and the growth of Europium or Europium oxide clusters with increasing annealing temperatures and annealing times. The correlation between electroluminescence and microstructure is supported by transmission electron microscopy investigations and demonstrates that the electroluminescence of Eu-implanted SiO_2 layers can serve as a probe for the microstructural development in the active layer of the light emitter. © *2008 American Institute of Physics*. [DOI: 10.1063/1.2964176]

Light emission from Si is a top issue of current research due to the numerous application fields in optoelectronics, photonics, and sensor technology. Although Si-based light emitters are very attractive and despite the intense research in the last two decades, a sufficiently efficient, electrically driven Si-based light emitter is not yet available. Among the different approaches, rare-earth implanted SiO_2 layers are very promising candidates.[1–3] So we were able to demonstrate strong electroluminescence (EL) from metal-oxide-semiconductor based light emitting diodes (MOSLEDs) doped with Er^{3+},[4] Eu^{3+},[5] Tb^{3+},[6] Ce^{3+},[7] and Gd^{3+} ions.[8] Although in the case of Tb an external quantum efficiency of up to 15% was reached[6] and the lifetime of the devices was improved by more than three orders of magnitude,[9] the MOSLEDs still have deficiencies in terms of efficiency and lifetime if compared with III-IV light emitters or organic LEDs. To overcome these deficiencies the insight into the dynamic processes on a microstructural scale within the light emitter during fabrication and operation is essential. Eu-implanted SiO_2 layers have a lower efficiency than those implanted with Tb, but the existence of two oxidation states, which can be traced indirectly by EL measurements, is a good probe for ongoing processes within the oxide layer.

In this work we investigate the complex dependence of the EL spectrum of Eu-implanted SiO_2 layers on the implantation and annealing conditions. It is shown that the red EL assigned to Eu^{3+} ions is favored by low Eu concentrations, low annealing temperatures, and short annealing times. Based on a more quantitative analysis of the spectra the underlying microstructural processes within the oxide layer will be discussed.

The Eu-implanted MOS structures were fabricated by local oxidation of silicon with 100 nm thick thermally grown SiO_2 on {100} oriented *n*-type silicon wafers. The 100 keV implantation resulted in an Eu profile with a maximum Eu concentration between 0.05% and 6% in the middle of the oxide layer. The samples were subjected to flash lamp annealing (FLA) for 20 ms, rapid thermal annealing (RTA) for 6 s or furnace annealing (FA) for 30 min in nitrogen at temperatures between 900 and 1100 °C. The structure is finally supplied with a SiON protection layer, a transparent front contact made of indium-tin oxide, and a rear contact made of aluminum. For EL measurements a constant injection current of 5 μA at voltages between 140 and 160 V was applied to circular dots with a diameter of 300 μm. The EL spectrum was recorded at room temperature (RT) with a monochromator (Jobin Yvon Triax 320) and a photomultiplier (Hamamatsu H7732-10). The EL decay time was measured by a multichannel scaler (Stanford Research System SR430) under constant voltage pulses. Furthermore, the microstructure of the Eu-implanted SiO_2 layers was analyzed by means of transmission electron microscopy (TEM) with a FEI-Titan instrument.

Figure 1 exhibits the EL spectrum of Eu-implanted MOS devices annealed with RTA at 1000 °C for various Eu concentrations. The spectra consist of a broad EL band in the blue green and at least three EL lines in the red spectral region, which are assigned to Eu^{2+} and Eu^{3+} ions, respectively. The emission of the Eu^{3+} ions is caused by $4f$-intrashell transitions from the $^5D_0$ level to some ^7F_J sublevels, which are indicated in Fig. 1, according to Ref. 10. Since the $4f$ shell is well screened from the chemical environment, these transitions are relatively sharp. However, as the chemical environment strongly varies in the amorphous SiO_2 network, the lines are broader than those usually reported for crystalline matrices.[10] In contrast to this the transition in the Eu^{2+} ion involves an electron that transits from the electronic $5d$ level to the $4f$ shell. As the $5d$ level is much less screened from the chemical environment, the corresponding EL emission is broad, reflecting the variation in the local chemical environment of the Eu^{2+} ion. Furthermore,

[a]Author to whom correspondence should be addressed. Electronic mail: l.rebohle@fzd.de.
[b]Also at Lashkaryov Institute of Semiconductor Physics, National Academy of Sciences of Ukraine, Prospect Nauky 45, 03028 Kiev, Ukraine.

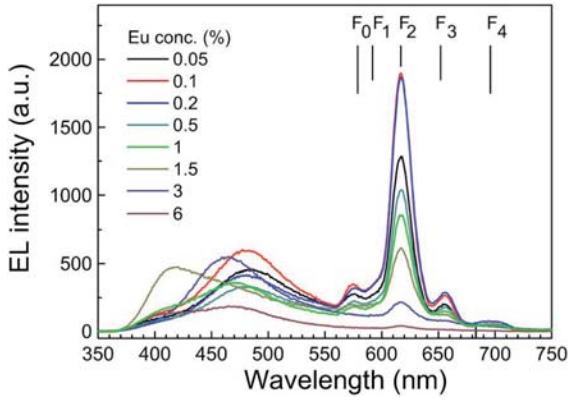

FIG. 1. (Color online) EL spectrum of Eu-implanted MOS devices annealed with RTA at 1000 °C for various Eu concentrations and under an injection current of 5 μA. The black solid lines indicate the position of the $^5D_0$-^7F_J lines ($0 \leqslant J \leqslant 4$) according to Ref. 10.

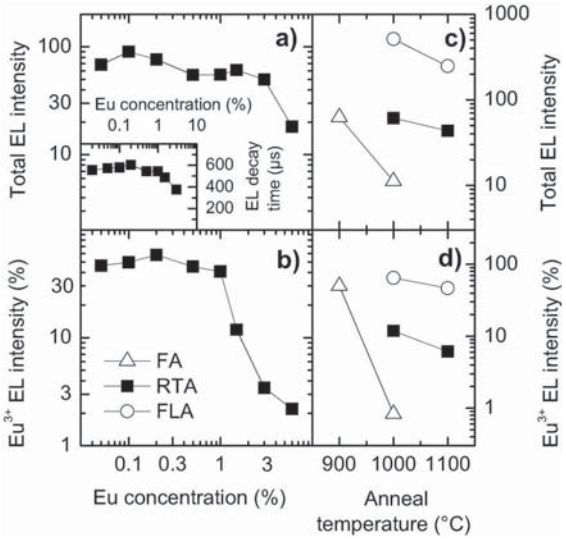

FIG. 2. The dependence of the total EL intensity [(a) and (c)] and the relative intensity of the Eu^{3+} emission in percent [(b) and (d)] of MOS structures on Eu concentrations [(a) and (b)] for RTA at 1000 °C and on annealing [(c) and (d)] for an Eu concentration of 1.5%. The inset shows the EL decay time of the $^5D_0$-$^7F_2$ line for RTA at 1000 °C.

$4f$-intrashell transitions are dipole forbidden resulting in a long decay time for the radiative relaxation, which is not the case for the blue $5d$-$4f$ transition. Consequently, an EL decay time between 350 and 700 μs for the $^5D_0$-$^7F_2$ line and a decay time shorter than 17 μs for the blue EL band is measured. In the latter case the measured decay time was limited by the edge steepness of the voltage pulses we applied to the devices during EL decay time measurements. As can be seen in Fig. 1, the ratio between the blue and red EL emission as well as the detailed structure of the blue-green EL strongly depend on the Eu concentration. For a deeper insight a peak fit analysis of the EL spectra was performed where the EL of the Eu^{3+} ions is modeled by five Gaussian peaks in correspondence to the possible transitions $^5D_0$-^7F_J with $0 \leqslant J \leqslant 4$. An additional Gaussian peak is used in order to consider the asymmetry of the $^5D_0$-$^7F_2$ line. The sum of these peak areas is assumed to represent the EL intensity of the Eu^{3+} ions, and is called the red EL in the following. All other Gaussian peaks are considered to be caused by either Eu^{2+} ions or Si-related defects. It should be noted that the peak positions of the Eu^{3+} peaks are always close to the positions reported in Ref. 10 and that the $^5D_0$-$^7F_2$ line always contains more than 70% of the red EL.

Figure 2 shows the total EL intensity [(a) and (c)] and the relative intensity of the Eu^{3+} emission in percent [(b) and (d)] for MOS structures for different Eu concentrations [(a) and (b)] and different thermal treatments [(c) and (d)]. There the relative intensity of the Eu^{3+} emission is defined as the percentage of the red on the total EL intensity. Whereas there is a smooth decrease in the total EL intensity with Eu concentration (a), the relative intensity of the red EL varies between 0.4 and 0.6 for small concentrations and shows a strong decrease for concentrations higher than 1% (b). The inset of Fig. 2(a) displays the EL decay time of the $^5D_0$-$^7F_2$ line. Furthermore, within one type of annealing both the total EL and the relative intensity of the Eu^{3+} emission decrease with increasing annealing temperature [(c) and (d)]. For a fixed annealing temperature a similar tendency can be observed: a decrease in the total EL and the relative Eu^{3+} intensity with increasing annealing time.

To understand the quenching of the red EL it is necessary to have a closer look to the microstructure of the SiO_2 layer as there are at least three different processes involved. First, during implantation Si and oxygen are released from the SiO_2 network either by nuclear collisions or by electronic energy deposition leading to bond breaking. In the following phase of annealing the released oxygen can be either reintegrated in the SiO_2 network or can be used to oxidize Eu. The formation enthalpy at RT for EuO, Eu_2O_3, and SiO_2 is in the order of -565 kJ mol^{-1},[11] -1650 kJ mol^{-1} (that is -825 kJ mol^{-1} per Eu atom)[12] and -910 kJ mol^{-1},[13] respectively. Although SiO_2 has the lowest value, it has also the highest demand on oxygen per reactant (Si or Eu). Indeed, there will be a competition for oxygen leading also to a local excess of Si that in turn triggers the formation of oxygen deficiency centers (ODCs). The ODCs are known to be efficient luminescence centers in the blue,[14,15] which can give a contribution to the total EL intensity. This process becomes more intense with increasing implantation dose, and as a consequence the relative Eu^{3+} intensity decreases with increasing Eu concentration. However, Tb-implanted and Gd-implanted SiO_2 layers that were prepared with similar parameters show either no or only a weak EL in the blue green,[6,8] which leads to the conclusion that the complex dynamics in the blue-green spectral region is mainly due to Eu.

The second quenching process is the preference of EuO compared to Eu_2O_3. Although the formation enthalpy of Eu_2O_3 (Eu^{3+} configuration) is higher than that of EuO (Eu^{2+} configuration), the supply of oxygen that is available for the oxidation of Eu determines whether EuO or Eu_2O_3 dominates. At low Eu concentrations a single Eu atom will find enough oxygen in its local environment to achieve a Eu_2O_3 configuration. With increasing Eu concentration the average distance between neighboring Eu ions decreases, and a competition of the Eu ions for oxygen starts which finally will shift the weight from Eu^{3+} to Eu^{2+} for high Eu concentrations. For RTA at 1000 °C the EL decay time of the $^5D_0$-$^7F_2$ line drops down continuously from 606 μs for 0.2% Eu to 375 μs for 3% Eu. The intensity of the red EL decreases in a similar way, but is stronger than implied by the ratio of the corresponding EL decay times. Thus the EL quenching caused by additional nonradiative relaxation processes of ex-

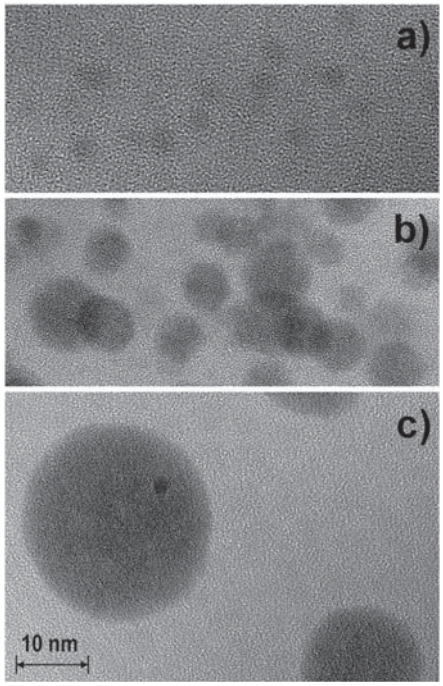

FIG. 3. Bright field cross section TEM images showing Eu/Eu oxide clusters in the SiO_2 layer for 1.5% Eu and annealed at 1000 °C by FLA (a), RTA (b), and FA (c). All images have the same magnification.

cited Eu^{3+} ions will give a minor contribution to the total quenching only.

The third development to be considered is the formation and the subsequent ripening of Eu/Eu oxide clusters. In Fig. 3 the development of these clusters is shown for an annealing temperature of 1000 °C. After FLA 20 ms only small amorphous Eu/Eu oxide clusters with diameters between 2 and 3 nm are observed. Whereas the amorphous clusters enlarge to diameters between 7 and 9 nm for RTA 6 s, huge and partly crystallized clusters with sizes around 25 nm can be found for FA 30 min. An analogous behavior is observed for the temperature dependence (not shown), so that a clear increase in the cluster size with increasing annealing temperature and time can be asserted. Because of the higher dielectric constant of Eu oxide[16] compared with SiO_2 and the continuity of the dielectric displacement, the electric field within an Eu oxide cluster is lower than in the SiO_2 matrix. Lower electric fields are not high enough to accelerate electrons to energies needed for the excitation of Eu ions, for which reason Eu ions inside a cluster are assumed to be optically inactive. Hot electrons moving in the conduction band of SiO_2 are able to excite Eu ions that are located at the surface of an Eu/Eu oxide cluster only. With increasing cluster size the fraction of Eu ions located at the cluster surface will decrease, and in turn a decrease in the total EL intensity with increasing annealing temperature time, namely, in the order FLA, RTA, and FA, is expected. Indeed, such a behavior is observed in Fig. 2(c). Moreover, because of the high Eu concentration within and on the surface of the clusters Eu will predominantly occur in the divalent stage. So if more and more Eu atoms are bound in clusters the weight will shift more and more to the blue EL. Finally, a certain fraction of Eu will diffuse toward the interfaces of the SiO_2 layer under long-time annealing (not shown) and cannot be excited electrically anymore. It has to be noted that the question, whether the clusters consists of Eu, Eu_2O_3 or EuO_x with $0<x<1.5$, is still under investigation. However, on the basis of the thermodynamic properties of Eu and its oxide we assess that the formation of Eu oxide clusters are more probable than that of Eu clusters.

In summary we have demonstrated that Eu-implanted SiO_2 layers exhibit a strong EL that is both due to the emission from Eu^{2+} and Eu^{3+} states. The red EL due to Eu^{3+} ions is favored by low Eu concentrations, lower annealing temperatures, and shorter annealing times. The increase in the blue portion of the EL with larger Eu concentrations, annealing temperatures, and annealing times is accompanied by a reduction in the total EL intensity. Although not all details are known, this behavior can be well explained by a shorter supply of oxygen for higher Eu concentrations and the growth of Eu/Eu oxide clusters with increasing anneal temperatures and times.

The authors would like to thank A. Dahmen of the Forschungszentrum Jülich and the Rossendorf Implantation Group for ion implantation and H. Felsmann, C. Neisser, and G. Schnabel for their careful semiconductor preparation work.

[1]C. Buchal, S. Wang, F. Lu, R. Carius, and S. Coffa, Nucl. Instrum. Methods Phys. Res. B **190**, 40 (2002).
[2]A. Irrera, M. Miritello, D. Pacifici, G. Franz, F. Priolo, F. Iacona, D. Sanfilippo, G. Di Stefano, and P. G. Fallica, Nucl. Instrum. Methods Phys. Res. B **216**, 222 (2004).
[3]F. Priolo, C. D. Presti, G. Franzò, A. Irrera, I. Crupi, F. Iacona, G. Di Stefano, A. Piana, D. Sanfilippo, and P. G. Fallica, Phys. Rev. B **73**, 113302 (2006).
[4]J. M. Sun, W. Skorupa, T. Dekorsy, M. Helm, and A. M. Nazarov, Opt. Mater. (Amsterdam, Neth.) **27**, 1050 (2005).
[5]S. Prucnal, J. M. Sun, W. Skorupa, and M. Helm, Appl. Phys. Lett. **90**, 181121 (2007).
[6]J. M. Sun, W. Skorupa, T. Dekorsy, M. Helm, L. Rebohle, and T. Gebel, J. Appl. Phys. **97**, 123513 (2005).
[7]J. M. Sun, S. Prucnal, W. Skorupa, M. Helm, L. Rebohle, and T. Gebel, Appl. Phys. Lett. **89**, 091908 (2006).
[8]J. M. Sun, S. Prucnal, W. Skorupa, T. Dekorsy, A. Mücklich, M. Helm, L. Rebohle, and T. Gebel, J. Appl. Phys. **99**, 103102 (2006).
[9]J. M. Sun, L. Rebohle, S. Prucnal, M. Helm, and W. Skorupa, Appl. Phys. Lett. **92**, 071103 (2008).
[10]G. H. Dieke, *Spectra and Energy Levels of Rare Earth Ions in Crystals* (Interscience, New York, 1968).
[11]E. J. Huber and C. E. Holley, J. Chem. Thermodyn. **1**, 301 (1969).
[12]G. C. Fitzgibbon, E. J. Huber, and C. E. Holley, J. Chem. Thermodyn. **4**, 349 (1972).
[13]M. Nagamori, J.-A. Boivin, and A. Claveau, J. Neurosci. Res. **189**, 270 (1995).
[14]L. Rebohle, J. von Borany, H. Fröb, and W. Skorupa, Appl. Phys. B: Lasers Opt. **70**, 1 (2000).
[15]A. N. Trukhin, M. Goldberg, J. Jansons, H.-J. Fitting, and I. A. Tale, J. Non-Cryst. Solids **223**, 114 (1998).
[16]H. Nakane, A. Noya, S. Kuriki, and G. Matsumoto, Thin Solid Films **59**, 291 (1979).

APPLIED PHYSICS LETTERS **92**, 071103 (2008)

Giant stability enhancement of rare-earth implanted SiO_2 light emitting devices by an additional SiON protection layer

J. M. Sun,[a] L. Rebohle,[b] S. Prucnal, M. Helm, and W. Skorupa
Institute of Ion Beam Physics and Materials Research, Forschungszentrum Dresden Rossendorf, P.O. Box 510119, Dresden D-01314, Germany

(Received 20 December 2007; accepted 24 January 2008; published online 20 February 2008)

The electrical stability of rare-earth implanted SiO_2 light emitting devices was improved by using a SiON dielectric buffer layer in an indium tin oxide/SiON/SiO_2:Tb/Si device structure. At the expense of a small increase of the electroluminescence threshold voltage, a large increase of the breakdown electric field from 7.5 to 10.5 MV/cm was obtained in the SiO_2:Tb layer, and the maximum injection current density was increased by three orders of magnitude from 4 mA/cm^2 to 4 A/cm^2. The operation time of the electroluminescence devices was increased by more than three orders of magnitude at an injection current density of ~4 mA/cm^2. Our experimental results are consistent with a theoretical model proposed for designing a stable and efficient thin-film light emitting device containing double-stacked dielectric layers. © *2008 American Institute of Physics*. [DOI: 10.1063/1.2870203]

Optoelectronics based on Si offers the opportunity to achieve higher data transfer rates and higher integration densities at very low costs.[1] However, the electrically driven, Si-based light emitter which is a key component of a complete photonic circuit is hard to realize. One of the most promising approach is the incorporation of luminescence centers into a SiO_2 matrix, as it was successfully demonstrated for Si nanoclusters,[2,3] Si nanoclusters codoped with Er ions[4,5] and different rare-earth ions.[6] Recently, we have demonstrated efficient electroluminescence (EL) from Ge-implanted SiO_2 layers[7] and metal-oxide-semiconductor based light emitting diodes (MOSLEDs) doped with Er^{3+},[8] Eu^{3+},[9] Tb^{3+},[10] Ce^{3+},[11] and Gd^{3+}.[12]

These MOSLEDs typically reach high external quantum efficiencies between 1% and 16%.[11–15] The efficient EL from MOSLEDs is obtained by impact excitation of the luminescent centers with energetic hot electrons in the SiO_2 matrix. For Fowler–Nordheim (FN) injection and sufficient acceleration of the electrons in the conduction band of the SiO_2 layer, the MOSLEDs are often operated under unstable prebreakdown conditions with the electric field in the SiO_2 layers above 7.5 MV/cm. Irreversible degradation of the EL intensity under constant-current FN injection was also observed due to charge trapping in the oxide layers.[13] These electrical instabilities cause a short lifetime of the MOSLEDs Castagna *et al.*[6] proposed a Si-rich SiO_2 matrix as the amorphous silicon network or silicon clusters in the SiO_2 layers allow the emission of more electrons from traps by the Poole–Frenkel (PF) mechanism under lower electric fields and a better electrical stability. However, the excess Si in SiO_2 causes a strong decrease of the EL efficiency due to the reduction of the average energy of the hot electrons through the PF and tunneling transport. Sun *et al.*[14] proposed an alternative solution by stacking the SiO_2 light emitting layer with a high-k dielectric Ta_2O_5 buffer layer. Stable electroluminescence from a magnetron sputtered SiO_2 layer and Si/SiO_2 superlattices[15] was observed in indium tin oxide (ITO)/Ta_2O_5/SiO_2/Al multiple layered structures.

In this paper, the electrical stability of Tb-doped MOSLEDs is studied by stacking the SiO_2:Tb layer with a SiON dielectric buffer layer. By changing the thickness ratio of the SiO_2/SiON layers, the slope of the current-voltage (I-V) and EL intensity–voltage (EL-V) characteristics is modified. The maximum breakdown electric field, the injection current density, and the operation life time of EL devices are strongly increased without a reduction of the quantum efficiency of the EL. This concept is also applicable for devices doped with other rare-earth elements.

The MOS structures were fabricated by local oxidation of silicon with thermally grown SiO_2 (dry oxidation at 1050 °C) on 4 in. {100} n-type silicon wafers. Tb^+ ions were implanted in such a way that the Tb profile is located at the middle of the oxide layer with a peak atomic concentration of 2%. After furnace annealing at 900 °C in flowing N_2 for 30 min, a SiON layer with a thickness of 30–200 nm was deposited on the SiO_2:Tb layer by plasma-enhanced chemical vapor deposition, followed by the same annealing process. Two sets of double-stacked MOSLED structures were produced: in one set, the thickness of the SiO_2:Tb layers is constant at 50 nm and the SiON layer thickness is varied from 30 to 200 nm, whereas in the other one, the SiO_2:Tb layer thickness is varied from 30 to 70 nm with a constant SiON layer thickness of 100 nm. The gate electrode is a 100 nm thick transparent ITO layer.

EL spectra were measured on a MOSLED structure with a circular ITO electrode of 500 μm diameter at a constant current supplied by a source meter with a positive bias at the gate. The EL signal was recorded at room temperature with a monochromator and a photomultiplier.

Figure 1 shows capacitance-voltage (C-V) characteristics of the ITO/SiON/SiO_2:Tb/n-type Si MOSLEDs for a SiO_2:Tb thickness of 50 nm and a SiON layer thickness which varies from 30 to 200 nm. With increasing SiON layer thickness, the capacitance of the MOS devices decreases and the flatband voltage shifts to negative values. This reveals that the SiON layers contain positive charges. The reciprocal of the total saturated capacitance can be expressed as

[a]Present address: Key Laboratory of Weak Light Nonlinear Photonics (Nankai University, Tianjin 300457), Ministry of Edication, China.
[b]Author to whom correspondence should be addressed. Electronic mail: l.rebohle@fzd.de.

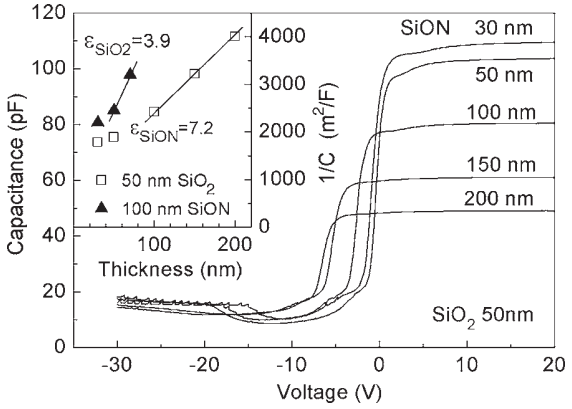

FIG. 1. *C-V* characteristics of the MOSLED with a SiO_2 thickness of 50 nm and different SiON thicknesses. The inset is the reciprocal of the capacitance as a function of the thickness of the SiO_2 (solid triangles) and SiON (open rectangles) layers, respectively, where the dielectric constants of the SiO_2 and SiON layers are calculated from the slopes of the curves.

$$\frac{1}{C}=\frac{1}{C_{\mathrm{SiO_2}}}+\frac{1}{C_{\mathrm{SiON}}}=\frac{d_{\mathrm{SiO_2}}}{\varepsilon_0\varepsilon_{\mathrm{SiO_2}}}+\frac{d_{\mathrm{SiON}}}{\varepsilon_0\varepsilon_{\mathrm{SiON}}}. \quad (1)$$

Here, C is the total capacitance, ε_0 is the dielectric constant of the vacuum, $C_{\mathrm{SiO_2}}$, $d_{\mathrm{SiO_2}}$, and $\varepsilon_{\mathrm{SiO_2}}$ and C_{SiON}, d_{SiON}, and $\varepsilon_{\mathrm{SiON}}$ are the capacitance, thickness, and relative dielectric constant of the SiO_2:Tb and the SiON layers, respectively. The inset plots $1/C$, as a function of $d_{\mathrm{SiO_2}}$ and d_{SiON} for the two sets of samples with SiON and SiO_2 layer thicknesses of 100 and 50 nm, respectively. The relative dielectric constants of the SiO_2 and the SiON layers are determined to be 3.9 and 7.2 by the slope of the $1/C$ versus $d_{\mathrm{SiO_2}}$, and $1/C$ versus d_{SiON}, respectively, as shown in the inset. Because of a thin transition layer between SiO_2 and SiON, only thicker SiO_2 and SiON layers were considered for the determination of the dielectric constants.

Figure 2 shows the *I-V* (a), EL-*V* (b), and EL-*I* (c) characteristics of the MOSLEDs with a constant SiO_2:Tb thickness of 50 nm and different SiON layer thicknesses. The EL intensity was measured by monitoring the peak of the $^5D_4$-$^7F_5$ transition from the Tb^{3+} ions at 541 nm.[10] The threshold voltages of the EL devices are equal to the applied voltage for the onset of the FN injection of hot electrons from the Si substrate into the conduction band of the SiO_2 layer. This shows that the EL from the Tb^{3+} is excited by hot electrons from the conduction band of the SiO_2 matrix. For MOSLEDs containing only a SiO_2:Tb layer, the maximum current is limited to 4 mA/cm^2 due to the destructive avalanche breakdown of the single SiO_2:Tb layer at an electric field above 7.5 MV/cm (not shown). By stacking the SiO_2:Tb luminescent layer with a SiON layer, the maximum injection current density at breakdown is increased up to 4 A/cm^2. With increasing SiON layer thickness, the slopes of the *I-V* and EL-*V* curves decrease, and the voltage range between the EL threshold and the breakdown of the devices increases. Despite the considerable change of the *I-V* and EL-*V* characteristics, the EL intensity–current characteristics in Fig. 2(c) do not change significantly with varying the thickness of the SiON layer. Under optimum fabrication and excitation conditions, the devices can have an external quantum efficiency up to 15% which is equivalent to a power efficiency of about 0.3%.[10]

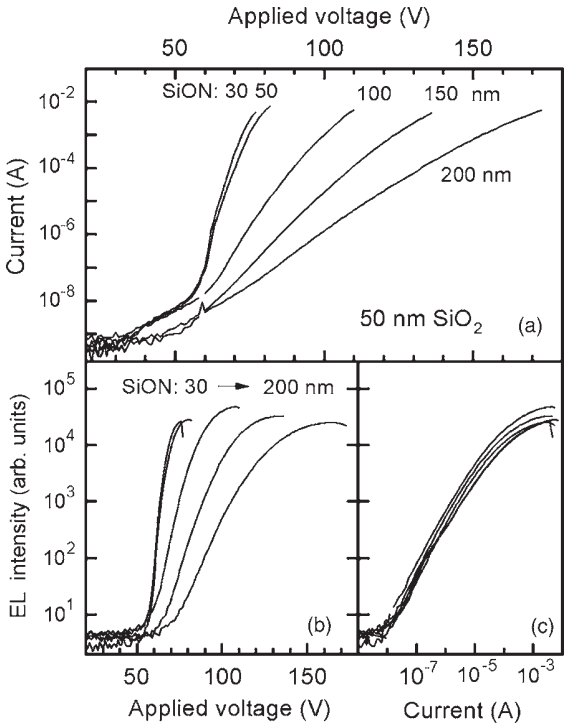

FIG. 2. The dependence of the current (a) and the EL intensity (b) on the applied voltage for the MOSLED with a SiO_2 thickness of 50 nm and different SiON thicknesses. The diagram (c) shows the EL intensity vs the current for different SiON thicknesses.

Figure 3 shows the EL threshold voltage V_{th} and the breakdown voltage V_B at a fixed SiON layer thickness of 100 nm (a) and a fixed SiO_2:Tb layer thickness of 50 nm (b). V_B is defined at a current density of 4 A/cm^2 when a destructive breakdown of the MOSLEDs occurs. V_{th} increases strongly with increasing SiO_2:Tb thickness, but it changes only slightly with increasing SiON layer thickness.

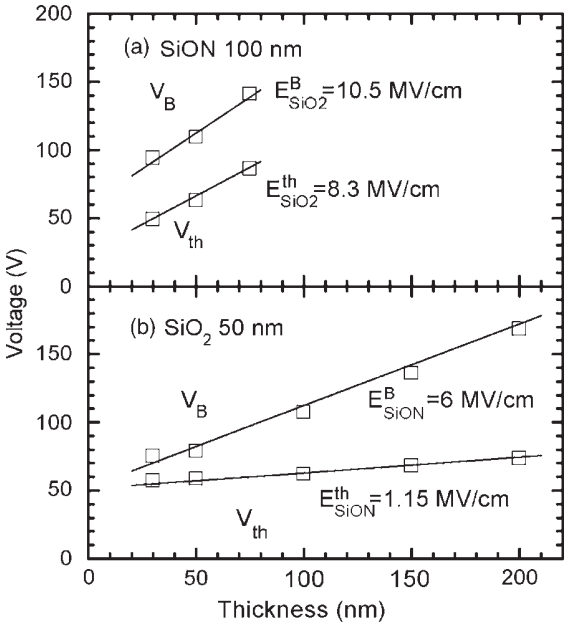

FIG. 3. The EL threshold voltages V_{th} and the breakdown voltages V_B of the MOSLEDs with different SiO_2 (a) and SiON thicknesses (b). The slope of the linear fits (black lines) indicates the threshold electric field E^{th} for EL and the breakdown electric field E^B in the SiO_2 and SiON layers, respectively.

The threshold electric field of EL in the SiO_2 layer $E^{th}_{SiO_2}$ is determined to be 8.3 MV/cm from the slope of V_{th} as a function of the SiO_2 layer thickness which is larger than the breakdown electric field of 7.5 MV/cm for MOS capacitors containing one single SiO_2:Tb layer. However, the electric field in the stacked SiON layer at the EL threshold E^{th}_{SiON} is only 1.15 MV/cm, which is far below the breakdown field of the SiON layer E^{B}_{SiON} of ~6.0 MV/cm. Therefore, the SiO_2/SiON stacked layers do not break down since the SiON layer acts as a current limiter. In the stacked structures, the V_B rises strongly with increasing SiON layer thickness. The electric field in the SiO_2 layer at breakdown $E^{B}_{SiO_2}$ is determined to be increased up to ~10.5 MV/cm.

In order to study the electrical stability of the MOSLEDs, the devices are stressed at a constant injection current of 3 μA until the breakdown. The time to breakdown under such conditions is called the operation time in the following. We find that the maximum operation time of the MOSLEDs is strongly increased to values above 25 000 s when a thin SiON layer is deposited on the top of the active SiO_2:Tb layers whose thickness is at least twice as much as those of the SiO_2:Tb layers. This is three orders of magnitude longer than the typical average operation time (<20 s) of the MOSLEDs with a single SiO_2:Tb layer. The best values for the operation time were observed for a thickness ratio of the SiO_2:Tb/SiON layers around 0.2–0.3.

For a MOS capacitor containing a single SiO_2:Tb layer, the devices do normally break down after a few seconds. The reason is that under constant voltage, a strong multiplication of hot electrons in SiO_2 at high electric fields causes a rapid increase of the current, leading to a destructive avalanche breakdown of the device. In contrast, in SiO_2/SiON stacked dielectric films, since the SiON layer has a larger dielectric constant and a larger conductivity than SiO_2, when the electric field in the SiO_2 layer exceeds $E^{th}_{SiO_2}$, the electric field in the SiON layer is still lower than its breakdown value, as shown in Fig. 3. The SiON layer acts as a current limiter which restricts the rapid increase of the current flow through the stacked SiO_2/SiON films. After the SiO_2 layer becomes conductive due to FN injection, the electric field in the SiO_2 layer increases with the current limited by the SiON layer, while the voltage across the SiON buffer layer increases until the SiON layer breaks down with increasing the applied voltage. Therefore, the breakdown voltage of the SiO_2/SiON stacked dielectric layers increases with increasing thickness of the stacked SiON buffer layer.

If E^{B}_{SiON} denotes the breakdown field of the SiON layer, the breakdown voltage across a single SiON layer should be larger than the overall applied voltage across the MOSLEDs; this means $E^{B}_{SiON} d_{SiO_2} \geqslant E^{B}_{SiO_2} d_{SiO_2} + E_{SiON} d_{SiON}$ in order to effectively suppress the locally dielectric breakdown during EL operation in MOSLEDs. E_{SiON} can be calculated by the continuity of the electric displacement at the interface of the SiO_2/SiON, assuming that the two layers are ideal dielectric layers. This leads to $\varepsilon_{SiO_2} E^{B}_{SiO_2} \approx \varepsilon_{SiON} E_{SiON}$ with $E^{B}_{SiO_2}$ and E_{SiON} the electric fields in the SiO_2 and SiON layers. Finally, the thickness ratio of SiO_2/SiON layers, d_{SiO_2}/d_{SiON}, designed for stable operation of the MOSLEDs is given as follows:

$$\frac{d_{SiO_2}}{d_{SiON}} \leqslant \frac{E^{B}_{SiON}}{E^{B}_{SiO_2}} - \frac{\varepsilon_{SiO_2}}{\varepsilon_{SiON}}. \tag{2}$$

For our SiO_2:Tb/SiON stacked MOSLED system, $\varepsilon_{SiO_2}=3.9$, $\varepsilon_{SiON}=7.2$, $E^{B}_{SiO_2}=8.3$ MV/cm, and $E^{B}_{SiON}=6$ MV/cm are determined from our experimental results resulting in $d_{SiO_2}/d_{SiON} \leqslant 0.18$. This is consistent with our experimental results, where the MOSLEDs with a ratio of d_{SiO_2}/d_{SiON} close to 0.2–0.3 have the longest lifetime. Equation (2) shows that a further increase of the electrical stability of the MOSLEDs is favorable by using a high-ε dielectric buffer layer with a larger dielectric constant and a higher breakdown field than SiON, such as Ta_2O_5, HfO_2, ZrO_2, or TiO_2.

In summary, we have demonstrated that the electrical stability of rare-earth doped MOSLEDs is improved by stacking active SiO_2 layers with a SiON dielectric buffer layer against avalanche breakdown. This has been demonstrated explicitly with a Tb-doped structure emitting in the green. It is demonstrated that the maximum breakdown electric field, the injection current density, and the operation lifetime of MOSLEDs are strongly increased with decreasing the thickness ratio of the stacked SiO_2/SiON layers without causing a reduction of the EL quantum efficiency.

The authors would like to thank J. Winkler and F. Ludewig for the ion implantation, Dr. B. Schmidt, H. Felsmann, C. Neisser, and G. Schnabel for the processing of the MOS structures.

[1] S. Ossicini, L. Pavesi, and F. Priolo, *Light Emitting Silicon for Microphotonics*, Springer Tracts in Modern Physics Vol. 194 (Springer, New York, 2003).
[2] L. Pavesi, L. Dal Negro, C. Mazzoleni, G. Franzò, and F. Priolo, Nature (London) **408**, 440 (2000).
[3] R. J. Walters, G. I. Bourianoff, and H. A. Atwater, Nat. Mater. **4**, 143 (2005).
[4] A. Polman, Nat. Mater. **1**, 10 (2002).
[5] F. Iacona, D. Pacifici, A. Irrera, M. Miritello, G. Franzò, F. Priolo, D. Sanfilippo, G. Di Stefano, and P. G. Fallica, Appl. Phys. Lett. **81**, 3242 (2002).
[6] M. E. Castagna, S. Coffa, M. Monaco, A. Muscara, L. Caristia, S. Lorenti, and A. Messina, Mater. Sci. Eng., B **105**, 83 (2003).
[7] L. Rebohle, J. von Borany, R. A. Yankov, W. Skorupa, I. E. Tyschenko, H. Fröb, and K. Leo, Appl. Phys. Lett. **71**, 2809 (1997).
[8] J. M. Sun, W. Skorupa, T. Dekorsy, M. Helm, and A. M. Nazarov, Opt. Mater. (Amsterdam, Neth.) **27**, 1050 (2005).
[9] S. Prucnal, J. M. Sun, W. Skorupa, and M. Helm, Appl. Phys. Lett. **90**, 181121 (2007).
[10] J. M. Sun, W. Skorupa, T. Dekorsy, M. Helm, L. Rebohle, and T. Gebel, J. Appl. Phys. **97**, 123513 (2005).
[11] J. M. Sun, S. Prucnal, W. Skorupa, M. Helm, L. Rebohle, and T. Gebel, Appl. Phys. Lett. **89**, 091908 (2006).
[12] J. M. Sun, W. Skorupa, T. Dekorsy, M. Helm, L. Rebohle, and T. Gebel, Appl. Phys. Lett. **85**, 3387 (2004).
[13] S. Prucnal, J. M. Sun, H. Reuther, W. Skorupa, and Ch. Buchal, Electrochem. Solid-State Lett. **10**, J30 (2007).
[14] J. M. Sun, G. Z. Zhong, X. W. Fan, G. Z. Fu, and C. W. Zheng, J. Non-Cryst. Solids **212**, 192 (1997).
[15] J. M. Sun, G. Z. Zhong, and X. W. Fan, Chinese J. Luminescence **21**, 24 (2000).

APPLIED PHYSICS LETTERS **92**, 051104 (2008)

Two-color pump-probe studies of intraminiband relaxation in doped GaAs/AlGaAs superlattices

D. Stehr,[a] M. Wagner, H. Schneider, and M. Helm
Institute of Ion Beam Physics and Materials Research, Forschungszentrum Dresden-Rossendorf, P.O. Box 510119, 01314 Dresden, Germany

A. M. Andrews, T. Roch, and G. Strasser
Institut für Festkörperelektronik, TU Wien, Floragasse 7, 1040 Wien, Austria

(Received 14 November 2007; accepted 14 January 2008; published online 5 February 2008)

The miniband relaxation dynamics of electrons in doped GaAs/AlGaAs superlattices are investigated by two-color infrared pump-probe experiments. By this technique, we are able to separate the different contributions from inter- and intraminiband relaxations to the transient behavior after an ultrafast excitation. In particular, the intraminiband relaxation is studied for different miniband widths below and above the optical phonon energy of GaAs. For minibands wider than this critical value, we find fast relaxation, nearly constant for different excitation intensities, whereas for narrow minibands, a strong temperature and intensity dependence of the relaxation is found. The results are in good agreement with previously published Monte Carlo simulations. © *2008 American Institute of Physics*. [DOI: 10.1063/1.2840159]

The dynamic behavior of electrons in semiconductors and their heterostructures is of crucial importance for many of their optoelectronic applications.[1] Most prominently, intersubband relaxation processes are directly incorporated into the design of quantum cascade lasers[2–4] (QCLs) and quantum well infrared photodetectors.[5] Along with further development of such devices, a detailed understanding of the intersubband relaxation in quantum well structures has been obtained.[6] Yet, only recently, the relaxation behavior in semiconductor superlattices (SLs) has been experimentally studied.[7] The obtained results were in good agreement with the Monte Carlo calculations where the interminiband relaxation and a stationary electron distribution function were modeled.[8] Also demonstrated was the redistribution of electrons within the entire mini-Brillouin zone caused by thermalization—leading to strong absorption changes that allow one to monitor the electron temperature dynamically on a picosecond timescale. However, these signals were a mixture of bleaching, inter-, and intraminiband relaxation components due to the nature of the single-color pump-probe experiments.

In this letter, we present two-color pump-probe transmission measurements on doped GaAs/$Al_{0.3}Ga_{0.7}As$ superlattices using the infrared free-electron laser (FEL) at the Forschungszentrum Dresden-Rossendorf in combination with a synchronized table-top broadband infrared light source. We observe the transient relaxation between and *within* the respective minibands giving a deeper insight into the relaxation channels after an ultrafast excitation. Two samples, having a lower-miniband width below and above the longitudinal optical (LO) phonon energy of 36 meV, respectively, are investigated.

Samples SL1 (SL2) were grown by molecular beam epitaxy on semi-insulating GaAs substrates. They consist of 300 periods of 7.7 (6.8) nm thick quantum wells and 2.1 (1.1) nm thick barriers. The wells are doped in the central (4 nm) resulting in an areal density of $6\ (4)\times10^{10}$ cm^{-2}/period. The widths of the lower miniband are 25 meV for SL1 and 45 meV for SL2, respectively. The linear interminiband absorption spectrum, measured on sample SL1 with 38° polished facets and one total internal reflection, is shown in Fig. 1 for different temperatures. At high temperature, the spectra reflect the van Hove singularities of the joint density of states at the center and the edge of the mini-Brillouin zone, while at low temperature, they are dominated by impurity transitions.[9] Also shown in Fig. 1 is the wavelength configuration of the two-color pump-probe experiment.

The scope of the experiments is to distinguish between the different relaxation channels for electrons that have been excited to the upper miniband at $k_z=0$. As indicated by the arrows in the inset of Fig. 1, apart from thermalization, there are primarily two different relaxation possibilities: i.e., relaxation back to the ground miniband (interminiband relaxation) and relaxation within the upper miniband toward $k_z=\pi/d$.

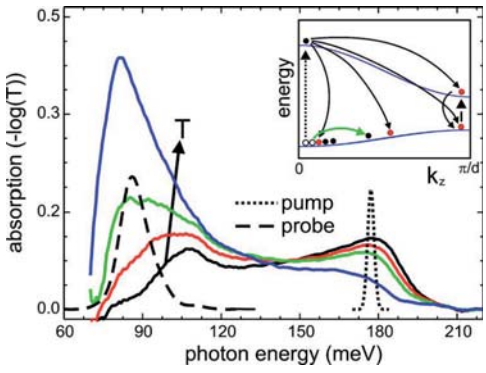

FIG. 1. (Color online) Experimental infrared absorption spectrum of sample SL1 at temperatures of 4 K (solid black), 50 K (red), 100 K (green), and 300 K (blue). The cutoff at 70 meV is due to the detector employed in the measurement. Also shown are the spectra of the pump (dotted) and probe (dashed) pulses. The inset illustrates the k_z position of the infrared pulses and possible relaxation processes within the mini-Brillouin zone (black arrows) as well as heating effects (green arrow).

[a]Electronic mail: d.stehr@fzd.de.

The latter is regarded as *intraminiband* relaxation. After thermalization and relaxation toward the ground miniband, also the relaxation within the lower miniband can be studied. In this letter, we mainly investigate the relaxation within the ground miniband by a two-color pump-probe approach, allowing to clearly identify the contributing mechanisms without the signals being mixed with bleaching components as observed in single-color experiments.[7]

To this end, the FEL was tuned to the transition at $k_z=0$ for all experiments, being around 7 μm for sample SL1 and 4.5 μm for sample SL2, respectively. The pulse length of the FEL was 1.5 ps. The probe beam is tuned to monitor the transient absorption around the zone-edge transition ($k_z=\pi/d$), shown as the dashed line in Fig. 1. The probe beam is obtained by phase-matched difference frequency generation[10,11] (DFG) of 10 fs optical pulses delivered by a Ti:Sa oscillator that is actively synchronized to the master clock of the accelerator driving the FEL.[12] The timing jitter between the two lasers was between 1 and 2 ps. GaSe is chosen as nonlinear crystal for the DFG, allowing the generation of broadband[13] infrared pulses, tunable in the range from 8 to 20 μm. Since these pulses are generated directly from a Ti:Sa oscillator running at 78 MHz, in combination with the 13 MHz FEL, this setup allows for very sensitive transmission measurements.

For the time-resolved experiments, both pump and probe were focused noncollinearly onto the sample using a 10 cm focal-length off-axis parabolic mirror, taking care that the focal spot of the pump was larger than that of the probe. Behind the sample, the transmitted probe beam was detected with a LN_2 cooled mercury-cadmium telluride (MCT) detector. The time delay of the probe pulse was achieved by using a mechanical delay line. Since in our case the FEL pulses and the probe pulses are spectrally well separated, we insert a suitable edge filter in front of the detector, which reduces noise due to scattered pump light. The sensitivity can be enhanced by placing a mechanical chopper into the FEL beam path and using a lock-in amplifier, giving the transient transmission change of the probe pulse. A major benefit of this method is that the redundant probe pulses that do not coincide with the pump pulses are filtered out. Consequently, since we are using a slow MCT detector that measures the time-integrated probe signal, the obtained change of transmission has to be multiplied by six, resulting in the absolute transmission change ΔT. The maximum pulse energy used for excitation was 100 nJ, corresponding to a peak intensity of 100 MW/cm^2, taking the sample geometry and attenuation of the cryostat windows into account. Under these conditions, the lattice temperature of the samples increases by a few kelvin.

We start first with the transient behavior of sample SL1 which is analyzed at $T=4$ K for different pump intensities and also at room temperature. The experimental results are shown in Fig. 2. From there, we find that after the strong excitation with the FEL pulse at $k_z=0$, the transmission at $k_z=\pi/d$ drastically drops (i.e., induced absorption) and recovers on a timescale of several tens of picoseconds. This behavior can be attributed to the heat up of the entire electron gas, leading to thermally activated population of the lower miniband at $k_z=\pi/d$, where strong absorption is found according to the linear absorption spectra (see Fig. 1). We find that the recovery is not a single exponential curve, and the initial decay within 50 ps depends strongly on the pump

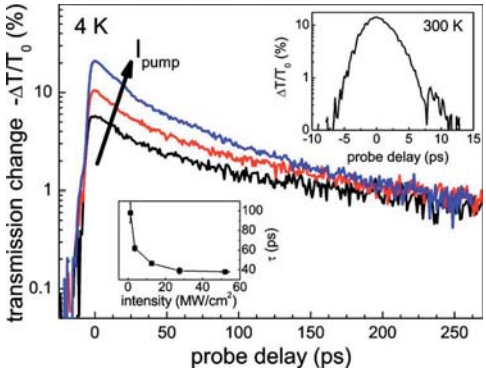

FIG. 2. (Color online) Transmission changes of sample SL1 at $T=4$ K for pump intensities of 3.8 (black), 12.6 (red), and 52 (blue) MW/cm^2. The lower inset shows the recovery times by extracting the time when the transmission decrease has dropped to $1/e$ of its highest value. The upper inset shows the transmission change at 300 K at a pump intensity of 80 MW/cm^2.

intensity. This decay time drops from 100 to 40 ps for the highest pump intensity (see lower inset of Fig. 2). However, around a probe delay of about 200 ps, we find that the curves merge. Similar behavior has been observed in far-infrared pump-probe experiments on wide quantum wells where the subband spacing was lower than the energy of one LO phonon.[14] The intensity dependence on the intersubband relaxation in these experiments could be reproduced by the Monte Carlo simulations that were able to identify the most efficient scattering mechanisms regarding the heat up of the electron gas as well as its cooling:[15] while electron-electron and electron-impurity scatterings were found to be responsible for the heat up of the electron gas, LO-phonon scattering dominates the dissipation of the electron energy to the lattice, *although* the respective subband spacing is smaller than the LO-phonon energy. This is due to electrons within the high-energy tail of the Fermi-Dirac distribution. Since only those electrons that are above 36 meV can contribute to the cooling of the system, the cooling rate will decrease during the entire process. Note that this results in a nonexponential decay of the subband population,[15] which is also clearly observed in our experiment. Additionally, it was demonstrated that LO-phonon scattering remains the leading cooling mechanism throughout the first 500 ps from where acoustic phonon scattering dominates.[15] Comparing these findings with our data, we can conclude that also in the intraminiband relaxation, LO-phonon scattering has the largest contribution.

Let us turn to the result at $T=300$ K. Instead of a transmission decrease, we now observe a *positive* transmission change on a fast timescale, i.e., the signal rises and falls within a few picoseconds (see upper inset of Fig. 2). At 300 K, heating effects on the electron gas are expected to be much smaller, since the Fermi-Dirac distribution function will not change its shape as drastically as for 4 K, which leads to smaller heating-induced population changes within the lower miniband. In this regime, other processes that lead to a transmission increase become observable in our experiment: here, the signal corresponds to relaxation of a fraction of the excited electrons within the *upper* miniband from $k_z=0$ to $k_z=\pi/d$. Once electrons are populating the upper miniband at $k_z=\pi/d$, they will decrease the initially strong absorption by either the Pauli blocking or by stimulated

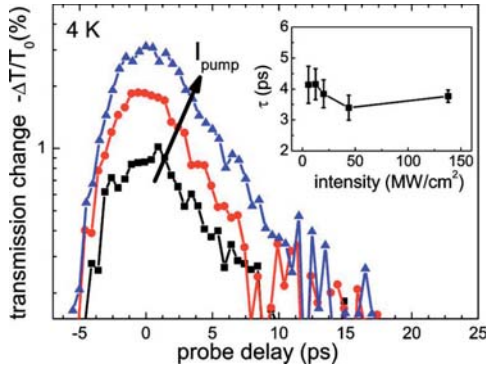

FIG. 3. (Color online) Transmission changes of sample SL2 at $T=4$ K for pump intensities of 12.5 (black), 43.9 (red), and 138 (blue) MW/cm^2. The inset shows the extracted recovery times from an exponential fit to the data.

emission, the latter being an important process in SL-QCLs. Due to the larger width (80 meV) of the upper miniband in SL-QCLs, this relaxation time (representing the rise time of the observed signal) is expected to be on the order of 1 ps or less (for comparison, see Ref. 8). Since this timescale is below the timing jitter between the two involved laser sources, we cannot extract the relaxation time reliably. The decay of the signal then corresponds to the *interminiband* relaxation back to the ground miniband. The observed decay time is in good agreement to our previously reported data, obtained by single-color experiments.[7] Note that this process is also present at low temperatures, however, it cannot overcome the heating that has a much stronger, opposite effect on the transmission. In fact, we observed a slight reduction of the heat-induced absorption at high pump intensities, which indicates the presence of these two competing mechanisms at low temperatures (not shown).

A major reason for the lack of a positive transmission change at low temperature is of course the fact that relaxation within the lower miniband is substantially slower than the respective interminiband relaxation, resulting in a balance of populations at $k_z=\pi/d$ that induces absorption instead of stimulated emission. To further investigate the relaxation within the lower miniband, we studied also a sample exhibiting a wide lower miniband (45 meV, well above the LO-phonon energy), where the relaxation is expected to be much faster. Transmission measurements showed a strong temperature dependence of the $k_z=\pi/d$ transition with its onset at around 100 K due to thermal occupation. This structure is similar to the lasing region of SL QCLs. However, instead of electrically injecting carriers directly at $k_z=\pi/d$, carriers are excited at the $k_z=0$ transition, now being at 4.5 μm. Due to the nature of an optically pumped system, we are not able to directly excite electrons from the bottom of the lower miniband (at $k_z=0$) to the bottom of the upper miniband (at $k_z=\pi/d$). The transmission of the probe pulse was recorded at $T=4$ K for different pump intensities, as shown in Fig. 3. Interestingly, in contrast to similar experiments on double quantum well structures,[16] the transients always show decreased transmission for all applied intensities, but now decaying on a much faster timescale than in the previous sample. Thus, although the lower-miniband width is larger than the LO-phonon energy, the heat up of the electron gas has still a larger contribution to our signal than the transfer of electrons within the upper miniband from $k_z=0$ to $k_z=\pi/d$. In our data, however, we find that the cooling of the electron gas is now much faster and nearly intensity independent (see inset of Fig. 3) due to the larger width of the lower miniband, allowing direct and efficient relaxation to the bottom of the lower miniband by LO-phonon scattering. The reason why we do not observe a positive transmission change might be that in such a strongly coupled superlattice, the oscillator strength at $k_z=0$ is very small (≈ 0.1),[17] requiring very high pump intensities to saturate the transition in order to get a large number of excited electrons that could contribute to stimulated emission. Unfortunately, the pump intensity could not be increased further in our experiments.

In conclusion, we have studied the intraminiband relaxation within the lower and upper minibands of doped superlattices using a sensitive two-color infrared pump-probe technique. For further investigation, it is desirable to perform detailed Monte Carlo simulation of optically pumped superlattices, allowing a better understanding of the competing processes—in particular, in the dynamics observed in the wide-miniband sample. These simulations are planned for the near future.

We thank S. Winnerl and W. Seidel for friendly collaboration as well as P. Michel and the FELBE team for their dedicated support.

[1] J. Shah, *Ultrafast Spectroscopy of Semiconductors and Semiconductor Nanostructures* (Springer, Berlin, 1999).
[2] C. Sirtori and R. Teissier, in *Intersubband Transitions in Quantum Structures*, edited by R. Paiella (McGraw-Hill, New York, 2006), Chap. 1, pp. 1–44.
[3] M. S. Vitiello, G. Scamarcio, V. Spagnolo, B. S. Williams, S. Kumar, Q. Hu, and J. L. Reno, Appl. Phys. Lett. **86**, 111115 (2005).
[4] M. Troccoli, G. Scamarcio, V. Spagnolo, A. Tredicucci, C. Gmachl, F. Capasso, D. L. Sivco, A. Y. Cho, and M. Striccoli, Appl. Phys. Lett. **77**, 1088 (2000).
[5] H. Schneider and H. C. Liu, *Quantum Well Infrared Photodetectors: Physics and Applications*, Springer Series in Optical Sciences Vol. 126 (Springer, Heidelberg, 2006).
[6] T. Elsaesser and M. Woerner, Phys. Rep. **321**, 253 (1999).
[7] D. Stehr, S. Winnerl, M. Helm, T. Dekorsy, T. Roch, and G. Strasser, Appl. Phys. Lett. **88**, 151108 (2006).
[8] F. Compagnone, A. DiCarlo, and P. Lugli, Appl. Phys. Lett. **80**, 920 (2002); S. Tortora, F. Compagnone, A. DiCarlo, and P. Lugli, Physica E (Amsterdam) **7**, 20 (2000).
[9] D. Stehr, M. Helm, C. Metzner, and M. C. Wanke, Phys. Rev. B **74**, 085311 (2006). Note that the impurity nature of the transitions at low temperature is not expected to change the dynamics observed in this experiment, since the excited impurity band largely overlaps with the excited miniband. Additionally, the elevated temperature of the excited electrons ensures that they are present mainly in the miniband rather than in the impurity band.
[10] R. A. Kaindl, F. Eickemeyer, M. Woerner, and T. Elsaesser, Appl. Phys. Lett. **75**, 1060 (1999).
[11] R. Huber, A. Brodschelm, F. Tauser, and A. Leitenstorfer, Appl. Phys. Lett. **76**, 3191 (2000).
[12] G. M. H. Knippels, M. J. van de Pol, H. P. M. Pellemans, P. C. M. Planken, and A. F. G. van der Meer, Opt. Lett. **23**, 1754 (1998).
[13] The spectral width depends strongly on the crystal length. In this work, a 200 μm thick GaSe crystal was chosen, resulting in a full width at half maximum of 2.8 μm at a center wavelength of 15 μm.
[14] B. N. Murdin, W. Heiss, C. J. G. M. Langerak, S.-C. Lee, I. Galbraith, G. Strasser, E. Gornik, M. Helm, and C. R. Pidgeon, Phys. Rev. B **55**, 5171 (1997).
[15] M. Dür, S. M. Goodnick, and P. Lugli, Phys. Rev. B **54**, 17794 (1996).
[16] O. Gauthier-Lafaye, S. Sauvage, P. Boucaud, F. H. Julien, R. Prazeres, F. Glotin, J.-M. Ortega, V. Thierry-Mieg, and R. Planel, Appl. Phys. Lett. **70**, 3197 (1997).
[17] M. Helm, Semicond. Sci. Technol. **10**, 557 (1995).

APPLIED PHYSICS LETTERS **93**, 101102 (2008)

Terahertz emission from a large-area GaInAsN emitter

Falk Peter,[1,a)] Stephan Winnerl,[1] Harald Schneider,[1] Manfred Helm,[1] and Klaus Köhler[2]
[1]*Institute of Ion Beam Physics and Materials Research, Forschungszentrum Dresden Rossendorf, P.O. Box 510119, 01314 Dresden, Germany*
[2]*Fraunhofer-Institute for Applied Solid State Physics, 79108 Freiburg, Germany*

(Received 25 July 2008; accepted 18 August 2008; published online 8 September 2008)

A large-area interdigitated terahertz emitter based on molecular-beam epitaxy grown GaInAsN with an additional AlGaAs heterostructure is investigated as a terahertz source for excitation wavelengths between 1.1 and 1.5 μm. The optical and electrical properties of the emitter material exhibit absorption up to a wavelength of 1.5 μm and have a resistivity of 550 kΩ cm. Terahertz waves were detected by electro-optical sampling with a bandwidth exceeding 2 THz. Best performance is found for excitation wavelengths below 1.35 μm. Furthermore the emission properties for several excitation powers are investigated, showing a linear increase in terahertz emission. © *2008 American Institute of Physics*. [DOI: 10.1063/1.2978398]

Photoconductive (PC) antennas are key elements of many terahertz systems. Over the past years, significant improvements in emitter efficiency have been achieved by large-area emitters based on GaAs with interdigitated electrodes.[1,2] These structures prevent carrier excitation in every second spacing by additional metallization[1,2] or by etching of the substrate.[3,4] Hereby the excited elementary terahertz waves interfere constructively in the far field. These emitter designs combine the advantages of high bias fields and large active areas. Furthermore detection with elements with similar electrode geometry based on GaAs substrates with subpicosecond carrier lifetimes and resistivity in the 10^6 Ω cm range has been demonstrated.[5,6] The availability of low-cost, stable, and compact fiber lasers has stimulated research on PC antennas based on substrates that allow interband excitation with wavelengths up to 1.55 μm. The challenge is to find small-gap materials with photoexcited carriers with high resistivities and short lifetimes.[7] Low-temperature-grown GaInAs and ion-irradiated GaInAs, both grown lattice matched on InP, have been used as substrate materials for dipole emitter antennas.[8,9] However, the resistivity of these materials is still too low for large-area emitters with interdigitated electrodes.

In this letter we discuss such large-area emitters based on 1000 nm quaternary $Ga_{0.89}In_{0.11}As_{0.96}N_{0.04}$ on (001) semi-insulating (SI) GaAs grown in a Varian Gen II modular molecular-beam epitaxy (MBE) system using Al, Ga, In, and As solid sources and a rf nitrogen plasma source. The optimum growth temperature, which depends on the In content of the structure, was in the range of 530–580 °C.[10]

GaInAsN based emitters show efficient terahertz emission for excitation wavelengths up to 1.35 μm. While the indium lowers the bandgap, the nitrogen reduces lattice strains, resulting in a nearly lattice matched compound. Further optimization is achieved by an additional $Al_{0.3}Ga_{0.7}As$/GaAs heterostructure layer (60 nm AlGaAs and 5 nm GaAs) as barrier on top, resulting in a higher resistivity of the substrate.

We compare the optical and electrical properties of the MBE grown substrate materials. As reference we compare the terahertz performance of SI-GaAs at 800 nm with the best MBE grown material.

The active area of the processed emitter is 1×1 mm^2. The interdigitated metallization consists of 5 μm wide metal stripes with 5 μm spacing. A second gold layer separated from the first one by a Si_3N_4 layer blocks the excitation in every second spacing.

For our experiments we used an optical parametric oscillator (OPO) which is driven by a mode-locked femtosecond Ti:sapphire laser with a central wavelength of 820 nm, a pulse duration of 80 fs, and a repetition rate of 78 MHz. The signal beam of the OPO is tunable between 1.1 and 1.5 μm. The pulse width is in the order of 250 fs. While the signal from the OPO excites the emitter, a small part of the 820 nm beam is split off before entering the OPO and is used for electro-optic sampling in a 1 mm thick (110) oriented ZnTe crystal. The emitter is driven with a bias of 15 V. The terahertz signal and the sampling beam are combined by a tin doped indium oxide coated mirror and focused on the ZnTe crystal by a pair of off-axis parabolic mirrors. The transmitted sampling beam was separated in its vertical and horizontal components by a polarization sensitive beamsplitter cube. Balanced detection is performed using two photodiodes and a quarter-wave-plate. The change of this balanced signal is proportional to the terahertz field reaching the ZnTe crystal

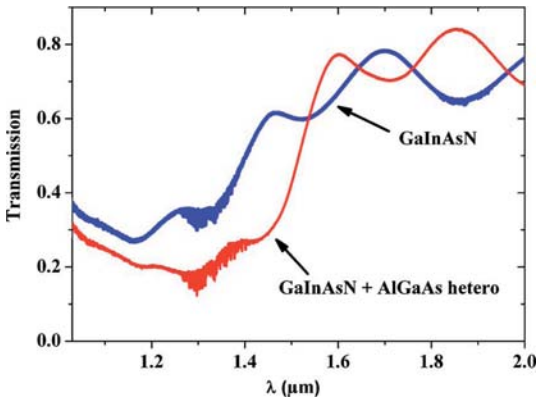

FIG. 1. (Color online) Transmission spectra of the emitters for different substrate materials: GaInAsN (blue) and GaInAsN with AlGaAs heterostructure (red).

[a)]Electronic mail: f.peter@fzd.de.

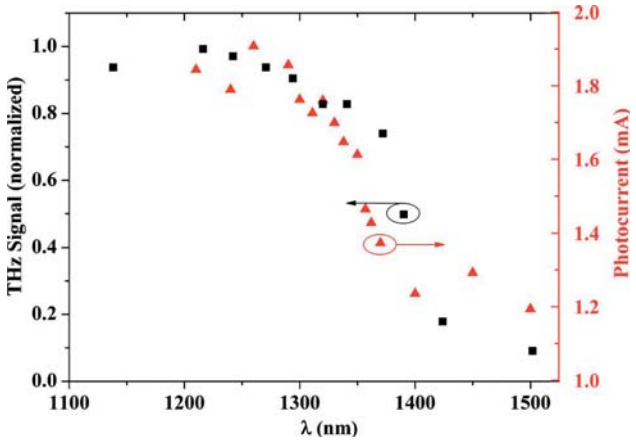

FIG. 2. (Color online) Terahertz signal and photocurrent vs excitation wavelength (black squares and red triangles, respectively) of the GaInAsN device with AlGaAs heterostructure at a 25 mW excitation power.

as described in Ref. 11. To prevent water absorption, the whole setup is purged with dry nitrogen. Temporal resolution is achieved by mechanical delay of the sampling beam.

Figure 1 shows the transmission spectra of the emitters with different MBE grown layers on SI-GaAs. The large oscillations are due to Fabry-Perot oscillations on the Si_3N_4 layer of the device; the smaller ones are from water absorption. The blue curve corresponds to the spectrum for the GaInAsN without and the red to the sample with AlGaAs/GaAs heterostructure. Both substrates show a strong absorption below 1.4 and 1.5 μm, respectively. This step in the transmission spectra is linked to the bandgap[12] and therefore to the excitation of free carriers in the substrate. The resistivity in the GaInAsN substrate is only 150 Ω cm. The absorption coefficient in the GaInAsN substrate with AlGaAs barrier at a 1.3 μm wavelength is 1.5×10^4 cm^{-1}, which is comparable to the absorption coefficient for SI-GaAs at 800 nm. The GaInAsN device with AlGaAs heterostructure shows a resistivity of 500 kΩ cm, which is almost three orders of magnitude higher than previously reported for high resistivity GaInAs material grown on InP substrate.[13] After processing the interdigitated electrodes, the whole device resistance is 280 kΩ, enabling a high bias field of up to 60 kV/cm. Therefore we investigate the terahertz emission from emitters which are fabricated on the GaInAsN/AlGaAs substrate.

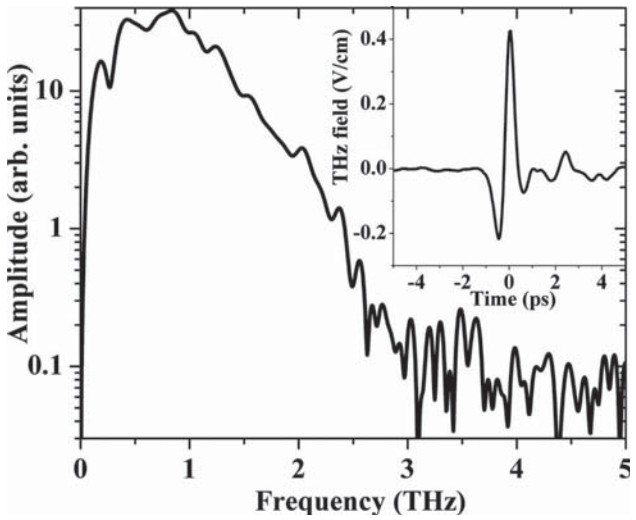

FIG. 3. Terahertz spectrum obtained by Fourier transformation of time-domain data as shown in the inset. The emitter was excited at 1.3 μm and 50 mW average power.

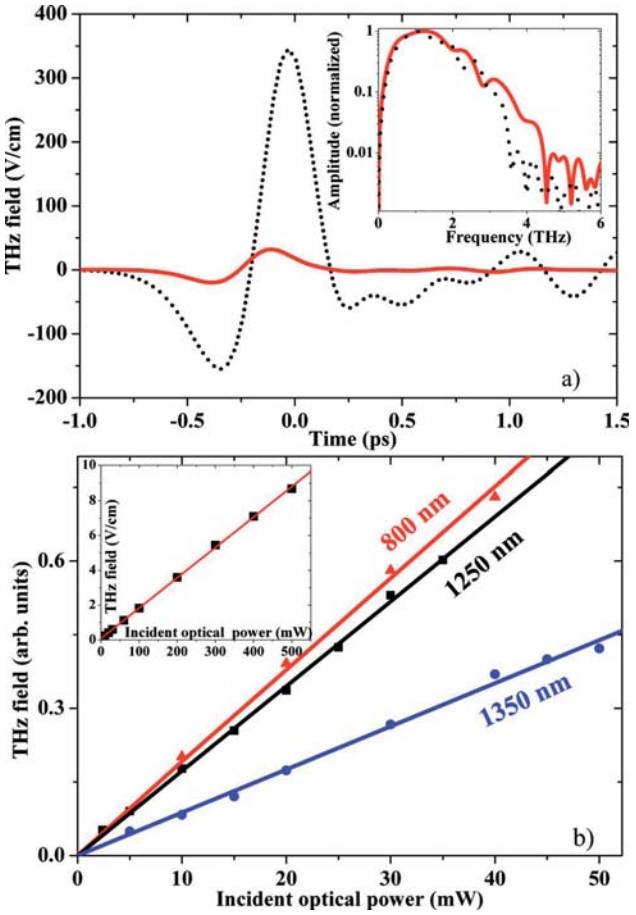

FIG. 4. (Color online) (a) Terahertz transient of a SI-GaAs emitter (black dotted) in comparison to a GaInAsN/AlGaAs emitter (red solid) excited at 800 nm. The inset shows the Fourier transformed spectra obtained from time-domain data. (b) Terahertz field from the GaInAsN/AlGaAs emitter as a function of excitation power for 800, 1250, and 1350 nm (red triangles, black squares, and blue circles respectively). Solid lines are fits to the experimental data. The inset shows higher optical excitation powers reached at 800 nm.

Figure 2 shows the dependency of the terahertz signal on the excitation wavelength while keeping the excitation power constant. Between 1.1 and 1.34 μm the terahertz emission remains constant. For excitation wavelengths above 1.4 μm the signals are about five times smaller as compared to the shorter wavelength. This is consistent with the dependency in the measured photocurrents of the emitter. Based on the transmission spectra in Fig. 1 where absorption is observed up to an excitation wavelength of 1.5 μm, we would expect the decrease in terahertz emission at longer excitation wavelengths. We attribute this to the lower mobility of the electrons due the modified band structure in $GaInAs_{1-x}N_x$.[14,15]

Figure 3 displays the Fourier transform amplitude of the temporal waveform, which is also shown in the inset. The spectral maximum is around 1 THz and the usable bandwidth exceeds 2 THz. The terahertz transient is measured with lock-in technique and has a signal to noise ratio of 400 with a 100 ms lock-in time constant. The bandwidth of the emit-

ted terahertz radiation is limited by the pulse duration of the OPO. For a 250 fs pulse the bandwidth is limited to about 2 THz.

Figure 4(a) shows a comparison between a normal SI-GaAs emitter and the GaInAsN/AlGaAs emitter at 800 nm excited with a 500 mW optical power and an 80 fs pulse duration and focused to a spot of 300 μm. For SI-GaAs the signal is eight times higher than that for GaInAsN/AlGaAs. In principle the emitted terahertz field is proportional to the mobility times the excited carrier density. Since the number of excited carriers at 800 nm in GaInAsN/AlGaAs is at least equal to that in SI-GaAs, we conclude from our data that the mobility in GaInAsN/AlGaAs is at least a factor of 8 lower than in SI-GaAs (6000 $cm^2\ V^{-1}\ s^{-1}$). The inset shows the spectra obtained from a Fourier transform of the time-domain data. The bandwidth exceeds 3 THz, which is consistent with the assumption that the long pulse duration of the OPO (250 fs) limits the terahertz bandwidth at excitations above 1 μm.

Figure 4(b) shows the terahertz signal versus excitation power for 800, 1250, and 1350 nm wavelengths. For the whole optical power range of the OPO up to a fluence of 1 $\mu J/cm^2$ we observe a linear dependence of the emitted terahertz field. The inset shows even higher optical powers obtained from direct excitation by the Ti:sapphire laser at 800 nm and up to 500 mW, corresponding to a carrier density of 10^{17} cm^{-3}. This behavior is in contrast to low-temperature-grown GaInAs emitters on InP with smaller active areas operating at 1.56 μm, where saturation behavior already occurs at a few milliwatt optical excitation power.[9]

In conclusion, we have demonstrated a large-area PC terahertz source operating at excitation wavelengths up to 1.5 μm, while best performance is achieved for wavelengths below 1.35 μm. A high resistivity substrate, which is a key prerequisite for a large-area device, can be realized by MBE grown GaInAsN on GaAs with an additional AlGaAs heterostructure. Based on the scalability of the device, no saturation behavior over the available range of excitation powers was observed. The limited bandwidth of the emitted terahertz radiation of 2 THz is attributed to the relatively large pulse duration of the OPO. Further optimization of the balance between the high resistivity and high mobility of the substrate material should increase the performance in bandwidth and excitation wavelength toward the 1.55 μm range. In addition the presented device shows an interesting opportunity for fiber lasers operating around 1.1 μm, as described in Ref. 16.

The authors are grateful to H. Felsmann for sample preparation and A. Dreyhaupt for his support and discussion. Research was conducted in the scope of GDRE: "Semiconductor sources and detectors of THz frequencies."

[1] A. Dreyhaupt, S. Winnerl, T. Dekorsy, and M. Helm, Appl. Phys. Lett. **86**, 121114 (2005).
[2] A. Dreyhaupt, S. Winnerl, M. Helm, and T. Dekorsy, Opt. Lett. **31**, 1546 (2006).
[3] M. Awad, M. Nagel, and H. Kurz, Appl. Phys. Lett. **91**, 181124 (2007).
[4] G. P. Acuna, F. F. Buersgens, C. Lang, M. Handloser, A. Guggenmos, and R. Kersting, Electron. Lett. **44**, 229 (2008).
[5] F. Peter, S. Winnerl, S. Nitsche, A. Dreyhaupt, H. Schneider, and M. Helm, Appl. Phys. Lett. **91**, 081109 (2007).
[6] S. Winnerl, F. Peter, A. Dreyhaupt, B. Zimmermann, M. Wagner, H. Schneider, M. Helm, and K. Köhler, IEEE J. Sel. Top. Quantum Electron. **14**, 449 (2008).
[7] H. Künzel, J. Böttcher, R. Gibis, and G. Urmann, Appl. Phys. Lett. **61**, 1347 (1992).
[8] M. Suzuki and M. Tonouchi, Appl. Phys. Lett. **86**, 163504 (2005).
[9] A. Takazato, M. Kamakura, T. Matsui, J. Kitagawa, and Y. Kadoya, Appl. Phys. Lett. **91**, 011102 (2007).
[10] K. Köhler, J. Wagner, P. Ganser, D. Serries, T. Geppert, M. Maier, and L. Kirste, J. Phys.: Condens. Matter **16**, S2995 (2004).
[11] Q. Wu and X. C. Zhang, Appl. Phys. Lett. **68**, 1604 (1996).
[12] B. K. Ridley, *Quantum Processes in Semiconductors* (Oxford University Press, Oxford, 1999), pp. 218–231.
[13] A. Takazato, M. Kamakura, T. Matsui, J. Kitagawa, and Y. Kadoya, Appl. Phys. Lett. **90**, 101119 (2007).
[14] W. Shan, W. Walukiewicz, J. W. Ager III, E. E. Haller, J. F. Geisz, D. J. Friedman, J. M. Olson, and S. R. Kurtz, J. Appl. Phys. **86**, 2349 (1999).
[15] S. Fahy and E. P. O'Reilly, Appl. Phys. Lett. **83**, 3731 (2003).
[16] G. Matthäus, T. Schreiber, J. Limpert, S. Nolte, G. Torosyan, R. Beigang, S. Riehemann, G. Notni, and A. Tünnermann, Opt. Commun. **261**, 114 (2006).

APPLIED PHYSICS LETTERS **93**, 101114 (2008)

Room-temperature midinfrared two-photon photodetector

H. Schneider,[1,a] H. C. Liu,[2] S. Winnerl,[1] O. Drachenko,[1] M. Helm,[1] and J. Faist[3]
[1]*Forschungszentrum Dresden Rossendorf, Institute of Ion Beam Physics and Materials Research, P.O. Box 510119, 01314 Dresden, Germany*
[2]*Institute for Microstructural Sciences, National Research Council, Ottawa K1A 0R6, Canada*
[3]*ETH Zürich, Institute for Quantum Electronics, 8093 Zürich, Switzerland*

(Received 26 June 2008; accepted 14 August 2008; published online 12 September 2008)

We report on a two-photon detector based on resonantly enhanced nonlinear absorption between subbands in InGaAs/InAlAs quantum wells and demonstrate its use as a quadratic autocorrelator for midinfrared pulses. Modified device design allows for device operation at room temperature, which is crucial for applications in practical systems. © *2008 American Institute of Physics*.
[DOI: 10.1063/1.2977864]

Various recent innovations have turned midinfrared and terahertz optoelectronics into a rapidly growing field with significant importance for applications including surveillance technology,[1] chemical sensing,[2,3] and infrared data links.[4–6] Intersubband transitions in quantum wells (QWs) have led to the development of quantum well infrared photodetectors (QWIPs),[7] now providing a mature technology for thermal imaging applications, and a variety of systems with increasing complexity and performance has been developed in the past years (see, e.g., Refs. 8 and 9). Another important device based on intersubband transitions is the quantum cascade laser[10,11] capable of cw operation at room temperature.[12] For this device, various modes of pulsed operation, including self-pulsations,[13] coherent instabilities,[14,15] and modelocking,[16] have been demonstrated recently. Additional midinfrared and terahertz radiation sources that became available in recent years use frequency conversion of visible or near-infrared lasers, mostly diode lasers and Ti:sapphire lasers, with pulse widths down to a few tens of femtoseconds. This frequency conversion is typically achieved via nonlinear optical processes including difference frequency generation[17] and optical parametric oscillation.[18] In most cases, the intensity of these novel light emitters is rather weak. Therefore, dynamic characterization of such radiation can be highly involved since this task generally relies on rather inefficient crystal materials where nonlinear effects only become significant at high intensity. Innovative detection concepts are required in order to achieve subpicosecond time resolution also for weak signals.

We have recently demonstrated a quadratic two-photon detector designed for wavelengths in the third atmospheric window at $8-12\ \mu$m. Huge optical nonlinearity, six orders of magnitude stronger than for bulk crystals, is induced by an artificial three-level system realized by subbands in a semiconductor QW. In this way, excellent sensitivity has been achieved for quadratic detection of incident radiation, with nonlinear optical signals appearing at power densities as low as $0.1\ \mathrm{W/cm^2}$.[19] The device has successfully been applied in an ultrasensitive interferometric autocorrelator for the characterization of midinfrared pulses from frequency-converted radiation,[19] free-electron lasers (FELs),[20] and quantum cascade lasers.[14–16] In addition, this approach has been exploited for investigating the dynamics of intersubband transitions.[21] In these studies, operation as a quadratic detector was limited to cryogenic temperatures where thermal occupation of the intermediate subband was low enough to avoid any linear signal. For possible application in any practical system, e.g., for midinfrared free-space data transmission,[4,22] room-temperature operation would be crucial.

In this letter, we report a $Ga_{0.47}In_{0.53}As/Al_{0.48}In_{0.52}As$ two-photon QWIP with true quadratic detection at room temperature.

Our detector scheme employs three energetically equidistant electronic states $|1\rangle$, $|2\rangle$, and $|3\rangle$. States $|1\rangle$ and $|2\rangle$ are bound in the QW, whereas state $|3\rangle$ is a resonance located in the continuum above the QW as shown in the inset of Fig. 1(a). The energy spacing between the subbands is matched to the photon energy of the radiation of interest by choosing appropriate well thicknesses and material compositions. Applying an external electric field across such a structure, the carriers excited into the continuum are swept out of the QW, thus creating a photocurrent in the external circuit. For detection at wavelengths around $5.5\ \mu$m, we use 6.2 nm thick $Ga_{0.47}In_{0.53}As$ QWs sandwiched between $Al_{0.48}In_{0.52}As$ barriers and grown by molecular beam epitaxy on a semi-insulating InP substrate. Using these material parameters, we have fabricated a detector structure comprising $N=60$ such QWs separated by 45 nm barriers. Each InGaAs well is n-doped with Si to an electron concentration of $4\times10^{11}\ \mathrm{cm^{-2}}$. The active region is sandwiched between n-type InGaAs contact layers of 300 and 600 nm thickness at the top and substrate sides, respectively. Mesa diodes with metal contacts were fabricated using standard optical lithography and wet-chemical etching.

Figure 1 summarizes the spectral characteristics of the device. The spectral dependence of the optical transition from subband $|1\rangle$ into subband $|2\rangle$ in Fig. 1(a) is obtained through standard intersubband absorption measurements, which have been conducted at room temperature in a Brewster-angle geometry at an external (internal) angle of about 73° (17°) with respect to the surface normal.[7] The spectrum is obtained at a temperature of 81 K using a Fourier-transform infrared spectrometer with p-polarized infrared radiation. The spectrum shows evidence of a strong intersubband transition between the lowest two subbands (as shown in the inset) at $5.48\ \mu$m, corresponding to an intersubband energy of 226 meV. Some additional weaker oscil-

[a]Author to whom correspondence should be addressed. Electronic mail: h.schneider@fzd.de.

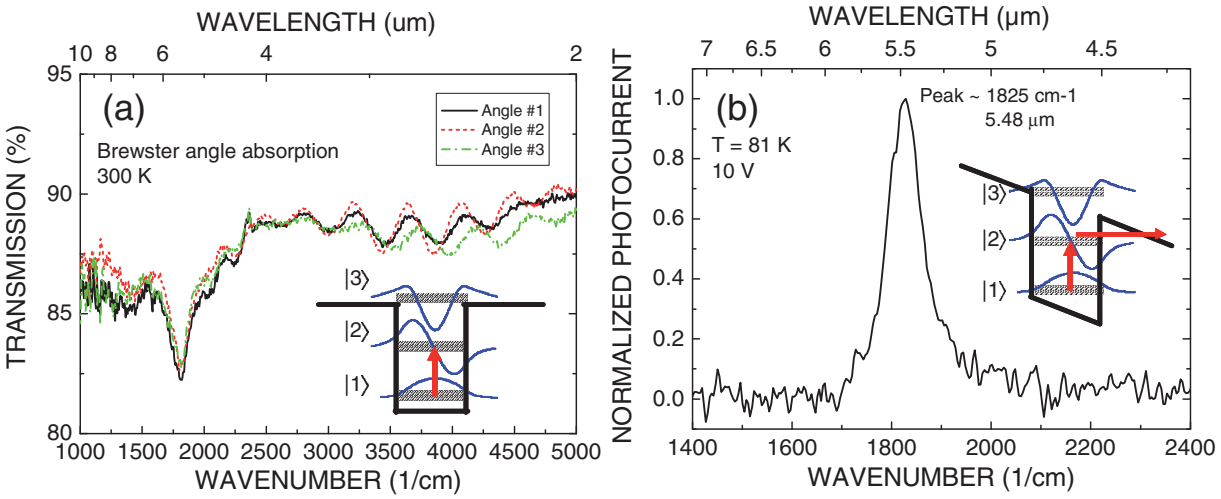

FIG. 1. (Color online) (a) Transmission spectra at three different angles around the Brewster angle and (b) normalized linear photocurrent spectrum of the two-photon QWIP. Insets: band diagrams for (a) intersubband absorption and (b) linear photodetection.

lations are attributed to Fabry–Pérot resonances of the epitaxial layer. As shown in Fig. 1(b), this transition is also observed in photocurrent measurements under high bias (10 V). At these fields, electrons excited into subband $|2\rangle$ gain a finite probability to escape from the QWs due to field-induced lowering of the AlInAs barriers [see inset of Fig. 1(b)].

The quadratic behavior of the photocurrent at much lower bias of 2 V becomes evident from Fig. 2, where we have plotted the photocurrent I versus the incident power P of the FEL running at 5.4 μm. At 300 K, the photocurrent exhibits quadratic power dependence up to about 5 mW average power followed by a saturation behavior. The latter is well described by an analytical expression of the form[20]

$$I = (RP + SP^2)W\left(\frac{I_{\text{sat}}}{RP + SP^2}\right), \tag{1}$$

where R corresponds to the linear and S to the quadratic contribution to the photocurrent and W is Lambert's W-function.[23] This expression originates from a transport model, which is based on the approximations that the photoconductive gain depends linearly and the dark current exponentially on the local electric field inside the active region.[20] Setting $R=0$, Eq. (1) yields excellent agreement with the measured intensity dependence for $T=297$ and 260 K, indicating purely quadratic detection (see Fig. 2). We also repeated the experiment at 335 K, where higher photocurrent was observed due to the additional presence of a linear photocurrent contribution (i.e., $R>0$). The linear component is caused by thermal population of the intermediate subband.[19,20]

We now apply the detector to characterize the time structure of midinfrared pulses from the FEL "FELBE" in Dresden that produces a continuous picosecond pulse train at 13 MHz repetition rate. A standard approach employed for this purpose is the autocorrelation measurement. Here a Michelson-interferometer configuration is used to split the pulse into two parts separated by a variable time delay Δt. If the measured time-integrated signal is proportional to the square of the optical power, simultaneous incidence of the two pulses ($\Delta t \approx 0$) results in a higher signal than sequential illumination. The dependence of the signal on Δt can thus be used to determine the pulse duration. For collinear illumination, the interference between the pulses contains additional information associated with the relative phase between the pulses (interferometric autocorrelation). The required quadratic power law detection system is directly obtained by using a two-photon detector rather than using second harmonic generation in a nonlinear crystal together with a linear detector.

Figure 3(a) shows an autocorrelation trace measured at room temperature. From the width of the autocorrelation trace (3.7 ps full width at half maximum), the FEL pulsewidth is estimated to be 2.6 ps. The ratio between the maximum of the interferometric autocorrelation at zero delay and the signal at large delay amounts to about 6 (about 2.1 for intensity autocorrelation), which is somewhat less than the ideal value of 8 (3), the deviation being attributed to the onset of saturation effects.[20] Intensity autocorrelation is obtained here via numerical filtering of the fringes.[20] Interferometric autocorrelation fringes are shown in Fig. 3(b) on an expanded scale. The observed $(1-\cos)^2$ shape of the fringes is characteristic for quadratic autocorrelation.

In conclusion, two-photon detectors based on resonant optical transitions between three energetically equidistant

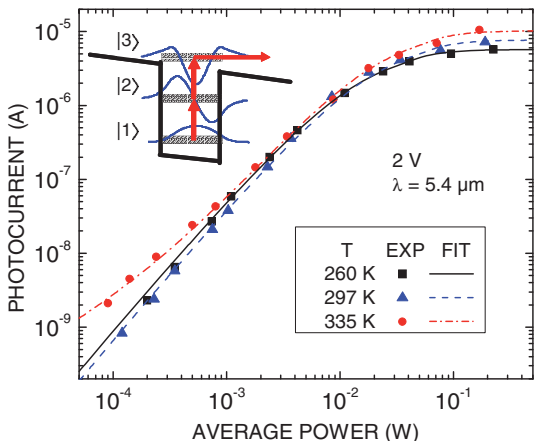

FIG. 2. (Color online) Measured and simulated intensity dependence of the photocurrent on different temperatures as indicated. Inset: band diagram for device operation as the quadratic detector.

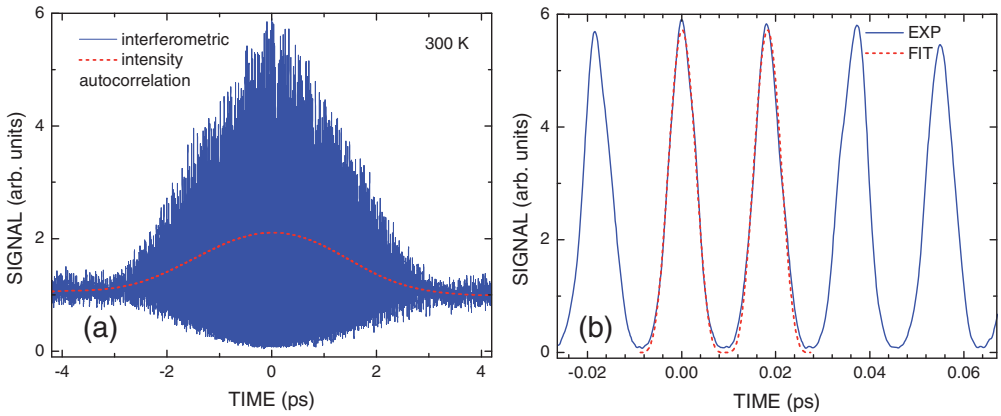

FIG. 3. (Color online) Room-temperature interferometric and intensity autocorrelation (a) of the two-photon QWIP at 2 V bias, and autocorrelation fringes (b) with $(1-\cos)^2$ fit.

subbands allow us to study quadratic autocorrelation at room temperature. The present demonstration of room-temperature operation is expected to make substantial impact on the characterization and development of novel radiation sources in the thermal infrared and terahertz regimes. Further improvements may open up applications in autocorrelating very weak signals in studying coherence, ultimately autocorrelating a blackbody source for fundamental research.

The authors are grateful to M. Giovannini (University of Neuchatel, Switzerland) for epitaxial growth and to H. Luo and C. Y. Song (NRC Ottawa, Canada) for device fabrication and characterization.

[1]E. L. Dereniak and G. D. Boreman, *Infrared Detectors and Systems* (Wiley, New York, 1996).
[2]D. Weidmann, F. K. Tittel, T. Aellen, M. Beck, D. Hofstetter, J. Faist, and S. Blaser, Appl. Phys. B: Lasers Opt. **79**, 907 (2004).
[3]M. T. McCulloch, N. Langford, and G. Duxbury, Appl. Opt. **44**, 2887 (2005).
[4]F. Capasso, R. Paiella, R. Martini, R. Colombelli, C. Gmachl, T. L. Myers, M. S. Taubman, R. M. Williams, C. G. Bethea, K. Unterrainer, H. Y. Hwang, D. L. Sivco, A. Y. Cho, A. M. Sergent, H. C. Liu, and E. A. Whittaker, IEEE J. Quantum Electron. **38**, 511 (2002).
[5]A. Neogi, in *Intersubband Transitions in Quantum Structures*, edited by R. Paiella (McGraw-Hill, New York, 2006), pp. 389–425.
[6]S. S. Dhillon, C. Sirtori, J. Alton, S. Barbieri, A. de Rossi, H. E. Beere, and D. A. Ritchie, Nat. Photonics **1**, 411 (2007).
[7]H. Schneider and H. C. Liu, *Quantum Well Infrared Photodetectors: Physics and Applications* (Springer, Heidelberg, 2007).
[8]S. D. Gunapala, S. V. Bandara, J. K. Liu, J. M. Mumolo, C. J. Hill, S. B. Rafol, D. Salazar, J. Woolaway, P. D. LeVan, and M. Z. Tidrow, Infrared Phys. Technol. **50**, 217 (2007).
[9]H. Schneider, T. Maier, J. Fleissner, M. Walther, P. Koidl, G. Weimann, W. Cabanski, M. Finck, P. Menger, W. Rode, and J. Ziegler, Electron. Lett. **40**, 831 (2004).
[10]J. Faist, F. Capasso, D. L. Sivco, C. Sirtori, A. L. Hutchinson, and A. Y. Cho, Science **264**, 553 (1994).
[11]C. Sirtori and R. Teissier, in *Intersubband Transitions in Quantum Structures*, edited by R. Paiella (McGraw-Hill, New York, 2006), pp. 1–44.
[12]M. Beck, D. Hofstetter, T. Aellen, J. Faist, U. Oesterle, M. Ilegems, E. Gini, and H. Melchior, Science **295**, 301 (2002).
[13]R. Paiella, F. Capasso, C. Gmachl, D. L. Sivco, J. N. Baillargeon, A. L. Hutchinson, A. Y. Cho, and H. C. Liu, Science **290**, 1739 (2000).
[14]C. Y. Wang, L. Diehl, A. Gordon, C. Jirauschek, F. X. Kärtner, A. Belyanin, D. Bour, S. Corzine, G. Höfler, M. Troccoli, J. Faist, and F. Capasso, Phys. Rev. A **75**, 031802(R) (2007).
[15]A. Gordon, C. Y. Wang, L. Diehl, F. X. Kärtner, A. Belyanin, D. Bour, S. Corzine, G. Höfler, H. C. Liu, H. Schneider, T. Maier, M. Troccoli, J. Faist, and F. Capasso, Phys. Rev. A **77**, 053804 (2008).
[16]C. Y. Wang, L. Kuznetsova, L. Diehl, F. Kärtner, M. A. Belkin, H. Schneider, H. C. Liu, and F. Capasso, Technical Digest of CLEO 2008, 2008 (unpublished), Paper No. CPDA11.
[17]S. Ehret and H. Schneider, Appl. Phys. B: Lasers Opt. **66**, 27 (1998).
[18]S. Chandra, T. H. Allik, G. Catella, R. Utano, and J. A. Hutchinson, Appl. Phys. Lett. **71**, 584 (1997).
[19]H. Schneider, T. Maier, H. C. Liu, M. Walther, and P. Koidl, Opt. Lett. **30**, 287 (2005).
[20]H. Schneider, O. Drachenko, S. Winnerl, M. Helm, and M. Walther, Appl. Phys. Lett. **89**, 133508 (2006).
[21]H. Schneider, T. Maier, M. Walther, and H. C. Liu, Appl. Phys. Lett. **91**, 191116 (2007).
[22]R. Martini, C. Bethea, F. Capasso, C. Gmachl, R. Paiella, E. A. Whittaker, H. Y. Hwang, D. L. Sivco, J. N. Baillargeon, and A. Y. Cho, Electron. Lett. **38**, 181 (2002).
[23]B. Hayes, Am. Sci. **93**, 104 (2005).

Statistics

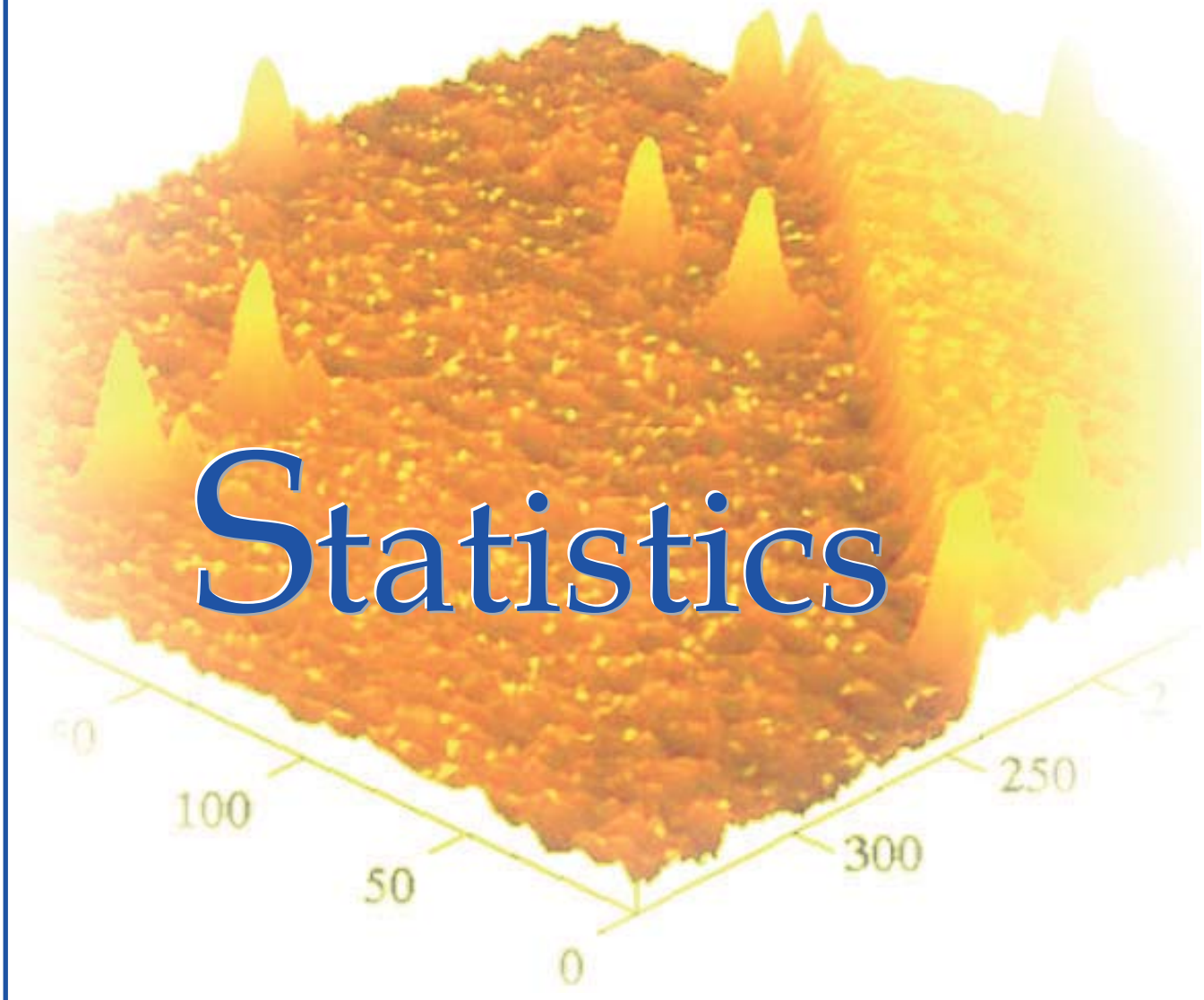

Publications

Ion-Solid-Interaction

1. Bischoff, L.
Application of mass-separated focused ion beams in nano-technology
Nuclear Instruments and Methods in Physics Research B ***266****, 1846 (2008).*

2. Carbone, D.; Alejandro, A.; Raul, G.; Facsko, S.; Plantevin, O.; Metzger, T. H.
Early stage of ripple formation on Ge (001) surfaces under near-normal ion beam sputtering
Nanotechnology ***19****, 035304 (2008).*

3. Chini, T. K.; Datta, P. D.; Facsko, S.; Mücklich, A.
Room temperature photoluminescence from the amorphous Si structure generated under keV Ar-ion-induced surface rippling condition
Applied Physics Letters ***92****, 101919 (2008).*

4. El-Said, A. S.; Heller, R.; Meissl, W.; Ritter, R.; Facsko, S.; Lemell, C.; Solleder, B.; Gebeshuber, I. C.; Betz, G.; Toulemonde, M.; Möller, W.; Burgdörfer, J.; Aumayr, F.
Creation of nanohillocks on CaF_2 surfaces by single slow highly charged ions
Physical Review Letters ***100****, 237601 (2008).*

5. Güttler, D.; Möller, W.
The influence of non-uniform target poisoning on the energy distributions of atoms sputtered in a reactive DC magnetron discharge
Plasma Sources Science & Technology ***17****, 025016 (2008).*

6. Heller, R.; Facsko, S.; Wilhelm, R.; Möller, W.
Defect mediated desorption of the KBr(001) surface induced by single highly charged ion impact
Physical Review Letters ***101****, 096102 (2008).*

7. Mahieu, S.; Leroy, W. P.; Depla, D.; Schreiber, S.; Möller, W.
Noble gas retention in the target during rotating cylindrical magnetron sputtering
Applied Physics Letters ***93****, 061501 (2008).*

Thin Films

8. Abrasonis, G.; Berndt, M.; Krause, M.; Küpper, K.; Munnik, F.; Kolitsch, A.; Möller, W.
Soft X-ray absorption and emission spectroscopic investigation of carbon and carbon:transition metal composite films
Journal of Physical Chemistry C ***112****, 17161 (2008).*

9. Abrasonis, G.; Scheinost, A. C.; Zhou, S.; Torres, R.; Gago, R.; Jimenez, I.; Küpper, K.; Potzger, K.; Krause, M.; Kolitsch, A.; Möller, W.; Bartkowski, S.; Neumann, M.; Gareev, R. R.
X-ray spectroscopic and magnetic investigation of C:Ni nanocomposite films grown by ion beam cosputtering
Journal of Physical Chemistry C ***112****, 12628 (2008).*

10. Cizek, J.; Prochazka, I.; Vlach, M.; Zaludova, N.; Danis, S.; Dobron, P.; Chmelik, F.; Brauer, G.; Anwand, W.; Mücklich, A.; Nikitin, E.; Gemma, R.; Kirchheim, R.; Pundt, A.
Hydrogen-induced buckling of Pd films studied by positron annihilation
Applied Surface Science ***255****, 241 (2008).*

11. Dezelah, Ch. L.; Niinistö, J.; Kukli, K.; Munnik, F.; Lu, J.; Ritala, M.; Leskelä, M.; Niinistö, L.
The atomic layer deposition of HfO_2 and ZrO_2 using advanced metallocene precursors and H_2O as an oxidant
Chemical Vapor Deposition ***14****, 358 (2008).*

12. Donchev, A.; Richter, E.; Schütze, M.; Yankov, R.
Improving the oxidation resistance of TiAl alloys with fluorine
Journal of Alloys and Compounds ***452****, 7 (2008).*

13. Gohier, A.; Point, S.; Djouadi, M. A.; Granier, A.; Minea, T. M.; Kreißig, U.; Abrasonis, G.; Kolitsch, A.; Möller, W.
ERDA and structural characterization of oriented multiwalled carbon nanotubes
Journal of Physical Chemistry C ***111****, 10353 (2008).*

14. Hämäläinen, J.; Kemell, M.; Munnik, F.; Kreißig, U.; Ritala, M.; Leskelä, M.
Atomic layer deposition of iridium oxide thin films from $Ir(acac)_3$ and ozone
Chemistry of Materials ***20****, 2903 (2008).*

15. Hämäläinen, J.; Munnik, F.; Ritala, M.; Leskelä, M.
Atomic layer deposition of platinum oxide and metallic platinum thin films from $Pt(acac)_2$ and ozone
Chemistry of Materials ***20****, 6840 (2008).*

16. Hofmann, M.; Kambor, S.; Schmidt, C.; Grambole, D.; Rentsch, J.; Glunz, S. W.; Preu, R.
PECVD-ONO: A new deposited firing stable rear surface passivation layer system for crystalline silicon solar cells
Advances in OptoElectronics ***48****, 5467 (2008).*

17. Höglund, C.; Birch, J.; Beckers, M.; Alling, B.; Czigány, Z.; Mücklich, A.; Hultman, L.
Sc_3AlN - A new perovskite
European Journal of Inorganic Chemistry ***8****, 1193 (2008).*

18. Kulisch, W.; Sasaki, T.; Rossi, F.; Popov, C.; Sippel, C.; Grambole, D.
Hydrogen incorporation in ultrananocrystalline diamond / amorphous carbon films
Physica Status Solidi (RRL) ***2****, 77 (2008).*

19. Lorenz, M.; Wagner, G.; Rahm, A.; Schmidt, H.; Hochmuth, H.; Schmid, H.; Mader, W.; Brandt, M.; Wenckstern, H. von; Grundmann, M.
Homoepitaxial ZnO thin films by PLD: Structural properties
Physica Status Solidi (C) ***5****, 3280 (2008).*

20. Martins, R. M. S.; Beckers, M.; Mücklich, A.; Schell, N.; Silva, R. J. C.; Mahesh, K. K.; Braz Fernandes, F. M.
The interfacial diffusion zone in magnetron sputtered Ni-Ti thin films deposited on different Si substrates studied by HR-TEM
Materials Science Forum ***587-588****, 820 (2008).*

21. Martins, R. M. S.; Mücklich, A.; Reuther, H.; Beckers, M.; Schell, N.; Silva, R. J. C.; Pereira, L.; Braz Fernandes, F. M.
Study of graded Ni-Ti shape memory alloy film growth on Si(100) substrate
Applied Physics A ***91****, 291 (2008).*

22. Martins, R. M. S.; Mücklich, A.; Schell, N.; Silva, R. J. C.; Mahesh, K. K.; Braz Fernandes, F. M.
Characterization of sputtered shape memory alloy Ni-Ti films by cross-sectional TEM and SEM
Microscopy and Microanalysis ***14****, 85 (2008).*

23. Martins, R. M. S.; Schell, N.; Beckers, M.; Silva, R. J. C.; Mahesh, K. K.; Braz Fernandes, F. M.
Role of the substrate on the growth of Ni-Ti sputtered thin films
Materials Science & Engineering A ***4812-482****, 626 (2008).*

24. Martins, R. M. S.; Schell, N.; Reuther, H.; Pereira, L.; Silva, R. J. C.; Mahesh, K. K.; Braz Fernandes, F. M.
Characterization of Ni-Ti (shape memory alloy) thin film by in-situ XRD and complementary ex-situ techniques
Materials Science Forum ***587-588****, 672 (2008).*

25. Martins, R. M. S.; Beckers, M.; Mücklich, A.; Schell, N.; Silva, R. J. C.; Mahesh, K. K.; Braz Fernandes, F. M.
The interfacial diffusion zone in magnetron sputtered Ni-Ti thin films deposited on different Si substrates studied by HR-TEM
Materials Science Forum ***587-588****, 820 (2008).*

26. Morales, E. H.; He, Y.; Vinnichenko, M.; Delley, B.; Diebold, U.
Surface structure of Sn-doped In_2O_3 (111) thin films by STM
New Journal of Physics ***10****, 125030 (2008).*

27. Neidhardt, J.; Mrátz, S.; Schneider, Jochen M.; Strub, E.; Bohne, W.; Liedke, B.; Möller, W.; Mitterer, C.
Experiment and simulation of the compositional evolution of Ti-B thin films deposited by sputtering of a compound target
Journal of Applied Physics ***104****, 063304 (2008).*

28. Pereira, L.; Aguas, H.; Beckers, M.; Martins, R. M. S.; Fortunato, E.
Metal contamination detection in nickel induced crystallized silicon by spectroscopic ellipsometry
Journal of Non-Crystalline Solids ***354****, 2319 (2008).*

29. Pilvi, T.; Puukilainen, E.; Kreißig, U.; Leskelä, M.; Ritala, M.
Atomic layer deposition of MgF_2 thin films using TaF_5 as a novel fluorine source
Chemistry of Materials ***20****, 5023 (2008).*

30. Raaif, M.; El-Hossary, F. M.; Negm, N. Z.; Khalil, S. M.; Kolitsch, A.; Möller, W.; Höche, D.; Kaspar, J.; Schaaf, P.; Mändl, S.
CO_2 laser nitriding of titanium
*Journal of Physics D **41**, 085208 (2008).*

31. Rotshtein, V. P.; Markov, A. B.; Shevchenko, N.; Reuther, H.; Oskomov, K. V.; Shulov, V. A.
Surface doping of VT_6 alloy with zirconium by pulsed electron-beam mixing of predeposited multilayer Zr/Ti film
*Technical Physics Letters **34**, 891 (2008).*

32. Vaupel, M.; Vinnichenko, M.
Influence of local plasma flow on optical properties and thickness of ITO-films observed with spectroscopic imaging ellipsometry
*Physica Status Solidi (C) **5**, 1137 (2008).*

Nanoscale Magnetism

33. Barzola-Quiquia, J.; Höhne, R.; Rothermel, M.; Setzer, A.; Esquinazi, P.; Heera, V.
A comparison of the magnetic properties of proton- and iron-implanted graphite
*European Physical Journal B **61**, 127 (2008).*

34. Cao, C. D.; Klingeler, R.; Leps, N.; Vinzelberg, H.; Kataev, V.; Muranyi, F.; Tristan, N.; Teresiak, A.; Zhou, S.; Löser, W.; Behr, G.; Büchner, B.
Interplay between Kondo-like behavior and short-range antiferromagnetism in $EuCu_2Si_2$ single crystals
*Physical Review B **78**, 064409 (2008).*

35. Fassbender, J.; Liedke, M. O.; Strache, T.; Möller, W.; Menendez, E.; Sort, J.; Rao, K. V.; Deevi, S. C.; Nogues, J.
Ion mass dependence of irradiation-induced local creation of ferromagnetism in Fe60Al40 alloys
*Physical Review B **77**, 174430 (2008).*

36. Fassbender, J.; McCord, J.
Magnetic patterning by means of ion irradiation and implantation
*Journal of Magnetism and Magnetic Materials **320**, 579 (2008).*

37. Gupta, R.; Ansari, R.; Khandelwal, A.; Fassbender, J.; Gupta, A.
Influence of Cr-ions on the magnetic behaviour of FeCo film
*Nuclear Instruments and Methods in Physics Research B **266**, 1407 (2008).*

38. Höhne, R.; Esquinazi, P.; Heera, V.; Weishart, H.; Setzer, A.; Spemann, D.
The influence of iron, fluorine and boron implantation on the magnetic properties of graphite
*Journal of Magnetism and Magnetic Materials **320**, 966 (2008).*

39. Khanra, S.; Küpper, K.; Weyhermuller, T.; Prinz, M.; Raekers, M.; Voget, S.; Postnikov, A. V.; de Groot, F.; George, S. J.; Coldea, M.; Neumann, M.; Chaudhuri, P.
Star-shaped molecule of (Mn_4O_6)-O-II core with an S-t=10 high-spin state.
A theoretical and experimental study with XPS, XMCD, and other magnetic methods
*Inorganic Chemistry **47**, 4605 (2008).*

40. Küpper, K.; Raekers, M.; Taubitz, C.; Hesse, H.; Neumann, M.; Young, A. T.; Piamonteze, C.; Bondino, F.; Prince, K. C.
Fe valence state of Sr_2FeMoO_6 probed by x-ray absorption spectroscopy: The sample age matters
*Journal of Applied Physics **104**, 036103 (2008).*

41. McCord, J.; Schultz, L.; Fassbender, J.
Hybrid soft-magnetic lateral exchange spring films prepared by ion irradiation
*Advanced Materials **20**, 2090 (2008).*

42. Menendez, E.; Martinavicius, A.; Liedke, M. O.; Abrasonis, G.; Fassbender, J.; Sommerlatte, J.; Nielsch, K.; Surinach, S.; Baro, M. D.; Nogues, J.; Sort, J.
Patterning of magnetic structures on austenitic stainless steel by local ion beam nitriding
*Acta Materialia **56**, 4570 (2008).*

43. Menendez, E.; Sort, J.; Liedke, M. O.; Fassbender, J.; Surinach, S.; Baro, M. D.; Nogues, J.
Two-fold origin of the deformation-induced ferromagnetism in bulk Fe60Al40 (at-%) alloys
*New Journal of Physics **10**, 103030 (2008).*

44. Potzger, K.; Küpper, K.; Xu, Q.; Zhou, S.; Schmidt, H.; Helm, M.; Fassbender, J.
High cluster formation tendency in Co implanted ZnO
*Journal of Applied Physics **104**, 23510 (2008).*

45. Potzger, K.; Zhou, S.; Grenzer, J.; Helm, M.; Fassbender, J.
An easy mechanical way to create ferromagnetic defective ZnO
Applied Physics Letters ***92****, 182504 (2008).*

46. Potzger, K.; Zhou, S.; Xu, Q.; Shalimov, A.; Grötzschel, R.; Schmidt, H.; Mücklich, A.; Helm, M.; Fassbender, J.
Ferromagnetic structurally disordered ZnO implanted with Co ions
Applied Physics Letters ***93****, 232504 (2008).*

47. Suergers, C.; Joshi, N.; Potzger, K.; Strache, T.; Möller, W.; Fischer, G.; von Loehneysen, H.
Magnetic order by C-ion implantation into Mn_5Si_3 and Mn_5Ge_3 and its laterial modification
Applied Physics Letters ***93****, 062503 (2008).*

48. Talut, G.; Potzger, K.; Mücklich, A.; Zhou, S.
Formation of metallic clusters in oxide insulators by means of ion beam mixing
Journal of Applied Physics ***103****, 07D505 (2008).*

49. Xu, Q.; Hartmann, L.; Zhou, S.; Mücklich, A.; Helm, M.; Biehne, G.; Hochmuth, H.; Lorenz, M.; Grundmann, M.; Schmidt, H.
Spin manipulation in Co-doped ZnO
Physical Review Letters ***101****, 076601 (2008).*

50. Xu, Q.; Schmidt, H.; Hochmuth, H.; Lorenz, M.; Setzer, A.; Meinecke, C.; Grundmann, M.
Room temperature ferromagnetism in Nd- and Mn-codoped ZnO films
Journal of Physics D ***41****, 105012 (2008).*

51. Xu, Q.; Schmidt, H.; Zhou, S.; Potzger, K.; Helm, M.; Hochmuth, H.; Lorenz, M.; Meinecke, C.; Grundmann, M.
Magnetic and transport properties of $Cu_{1.05}Cr_{0.89}$ $Mg_{0.05}O_2$ and $Cu_{0.96}Cr_{0.95}$ $Mg_{0.05}Mn_{0.04}O_2$ films
Thin Solid Films ***516****, 8543 (2008).*

52. Xu, Q.; Schmidt, H.; Zhou, S.; Potzger, K.; Helm, M.; Hochmuth, H.; Lorenz, M.; Setzer, A.; Esquinazi, P.; Meinecke, C.; Grundmann, M.
Room temperature ferromagnetism in ZnO films due to defects
Applied Physics Letters ***92****, 082508 (2008).*

53. Zhou, S.; Potzger, K.; Mücklich, A.; Eichhorn, F.; Helm, M.; Skorupa, W.; Fassbender, J.
Structural and magnetic properties of Tb implanted ZnO single crystals
Nuclear Instruments and Methods in Physics Research B ***266****, 589 (2008).*

54. Zhou, S.; Potzger, K.; Talut, G.; Reuther, H.; Küpper, K.; Grenzer, J.; Xu, Q.; Helm, M.; Fassbender, J.; Arenholz, E.
Ferromagnetism of Fe implanted ZnO – a phenomenon related to defects?
Journal of Physics D ***41****, 105011 (2008).*

55. Zhou, S.; Potzger, K.; Talut, G.; Reuther, H.; Borany, J. von; Grötzschel, R.; Skorupa, W.; Helm, M.; Fassbender, J.; Volbers, N.; Lorenz, M.; Herrmannsdörfer, T.
Fe implanted ZnO: Magnetic precipitates versus dilution
Journal of Applied Physics ***103****, 023902 (2008).*

56. Zhou, S.; Potzger, K.; Talut, G.; Shalimov, A.; Grenzer, J.; Skorupa, W.; Helm, M.; Fassbender, J.; Cizmar, E.; Zvyagin, S. A.; Wosnitza, J.
Crystallographically oriented Fe nanocrystals formed in Fe-implanted TiO_2
Journal of Applied Physics ***103****, 083907 (2008).*

57. Zhou, S.; Potzger, K.; Talut, G.; Borany, J. von; Skorupa, W.; Helm, M.; Fassbender, J.
Using X-ray diffraction to identify precipitates in transition metal doped semiconductors
Journal of Applied Physics ***103****, 07D530 (2008).*

58. Zhou, S.; Potzger, K.; Borany, J. von; Grötzschel, R.; Skorupa, W.; Helm, M.; Fassbender, J.
Crystallographically oriented Co and Ni nanocrystals inside ZnO formed by ion implantation and post-annealing
Physical Review B **77***, 035209 (2008).*

59. Zhou, S.; Potzger, K.; Küpper, K.; Grenzer, J.; Helm, M.; Arenholz, E.; Denlinger, J. D.; Fassbender, J.
Ni implanted ZnO single crystals: Correlation between nanoparticle formation and defect structure
Journal of Applied Physics ***103****, 043901 (2008).*

60. Zhou, S.; Xu, Q.; Potzger, K.; Talut, G.; Fassbender, J.; Vinnichenko, M.; Grenzer, J.; Helm, M.; Hochmuth, H.; Lorenz, M.; Grundmann, M.; Schmidt, H.

Room temperature ferromagnetism in carbon-implanted ZnO
Applied Physics Letters ***93****, 232507 (2008).*

Nanostructures

61. Biermanns, A.; Pietsch, U.; Grenzer, J.; Hanisch, A.; Facsko, S.; Carbone, G.; Metzger, T. H.
X-ray scattering and diffraction from ion beam induced ripples in crystalline silicon
Journal of Applied Physics ***104****, 044312 (2008).*

62. Beyer, V.; Eichhorn, F.; Borany, J. von; Mücklich, A.; Müller, T.
Ion beam synthesis and charge storage behavior of Au nanocrystals in thin SiO_2 layers
Journal of Applied Physics ***104****, 024512 (2008).*

63. Beyer, V.; Borany, J. von
Elemental redistribution and Ge loss during ion-beam synthesis of Ge nanocrystals in SiO_2 films
Physical Review B ***77****, 014107 (2008).*

64. Brueser, B.; Pietsch, U.; Grigorian, S.; Panzner, T.; Grenzer, J.; Zeimer, U.
High resolution measurement of the thermal expansion coefficient of semiconductor multilayer lateral nanostructures
Physica Status Solidi (A) ***205****, 316 (2008).*

65. Ivanova, K.; Sarov, Y.; Ivanov, T.; Frank, A.; Zöllner, J.; Bitterlich, C.; Wenzel, U.; Volland, B. E.; Klett, S.; Rangelow, I. W.; Zawierucha, P.; Zielony, M.; Gotszalk, T.; Dontzov, D.; Schott, W.; Nikolov, N.; Zier, M.; Schmidt, B.; Engl, W.; Sulzbach, T.; Kostic, I.
Scanning proximal probes for parallel imaging and lithography
Journal of Vacuum Science & Technology B ***26****, 2367 (2008).*

66. Jebril, S.; Elbahri, M.; Titazu, G.; Subannajui, K.; Essa, S.; Niebelschütz, F.; Röhlig, C.-C.; Cimalla, V.; Ambacher, O.; Schmidt, B.; Kabiraj, D.; Avasti, D.; Adelung, R.
Integration of thin-film-fracture-based nanowires into microchip fabrication
Small ***4****, 2214 (2008).*

67. Keller, A.; Facsko, S.; Möller, W.
Minimization of topological defects in ion-induced ripple patterns on silicon
New Journal of Physics ***10****, 063004 (2008).*

68. Keller, A.; Roßbach, S.; Facsko, S.; Möller, W.
Simultaneous formation of two ripple modes on ion sputtered silicon
Nanotechnology ***19****, 135303 (2008).*

69. Oates, T. W. H.; Keller, A.; Noda, S.; Facsko, S.
Self-organized metallic nanoparticle and nanowire arrays from ion-sputtered silicon templates
Applied Physics Letters ***93****, 063106 (2008).*

70. Salditt, T.; Krüger, S. P.; Fuhse, C.; Bähtz, C.
High-transmission planar X-ray waveguides
Physical Review Letters ***100****, 184801 (2008).*

Microelectronic Materials

71. Anwand, W.; Skorupa, W.; Schumann, Th.; Posselt, M.; Schmidt, B.; Grötzschel, R.; Brauer, G.
Implantation-caused open volume defects in Ge after flash lamp annealing (FLA) probed by slow positron implantation spectroscopy (SPIS)
Applied Surface Science ***255****, 81 (2008).*

72. Anwand, W.; Xiong, S. Z.; Wu, C. Y.; Gebel, Th.; Schumann, Th.; Brauer, G.; Skorupa, W.
Structural changes in flash lamp annealed amorphous Si layers probed by slow positron implantation spectroscopy
Acta Physica Polonica A ***113****, 1273 (2008).*

73. Brandt, M.; Wenckstern, H. von; Schmidt, H.; Rahm, A.; Biehne, G.; Benndorf, G.; Hochmuth, H.; Lorenz, M.; Meinecke, C.; Butz, T.; Grundmann, M.
High electron mobility of phosphorous-doped homoepitaxial ZnO thin films grown by pulsed-laser deposition
Journal of Applied Physics ***104****, 013708 (2008).*

74. Chernyshev, V.; Meijer, J.; Grambole, D.; Herrmann, F.; Dagkaldiran, U.; Wieck, A.
n-type diamond produced by MeV lithium implantation in channeling direction
Diamond and Related Materials ***17****, 1933 (2008).*

75. Cizek, J.; Zaludova, N.; Vlach, M.; Danis, S.; Kuriplach, J.; Prochazka, I.; Brauer, G.; Anwand, W.; Grambole, D.; Skorupa, W.; Gemma, R.; Kirchheim, R.; Pundt, A.
Defect studies of ZnO single crystals electrochemically doped with hydrogen
Journal of Applied Physics ***103****, 053508 (2008).*

76. Cizek, J.; Prochazka, I.; Vlach, M.; Zaludova, N.; Danis, S.; Brauer, G.; Anwand, W.; Mücklich, A.; Gemma, R.; Kirchheim, R.; Pundt, A.
Defect studies of hydrogen-loaded nanocrystalline Gd films
Applied Surface Science ***255****, 251 (2008).*

77. Danesh, P.; Pantchev, B.; Schmidt, B.
Infrared absorption strengths of ion-implanted hydrogenated amorphous silicon
Thin Solid Films ***516****, 3383 (2008).*

78. Fitting, H.-J.; Salh, R.; Schmidt, B.
Thermal decomposition and new luminescence bands in wet, dry, and additional oxygen implanted silica layers
Journal of Non-Crystalline Solids ***354****, 1697 (2008).*

79. Gao, F.; Zhang, Y.; Posselt, M.; Weber, W. J.
Computational study of anisotropic epitaxial recrystallization in 4H-SiC
Journal of Physics: Condensed Matter ***20****, 125203 (2008).*

80. Gu, Q.; Ling, C.; Brauer, G.; Anwand, W.; Skorupa, W.; Hsu, Y.; Djurisic, A.; Zhu, C.; Fung, S.; Lu, L.
Deep level defects in a nitrogen-implanted ZnO homogeneous p-n junction
Applied Physics Letters ***92****, 222109 (2008).*

81. Heera, V.; Höhne, R.; Ignatchik, O.; Reuther, H.; Esquinazi, P.
Absence of superconductivity in boron-implanted diamond
Diamond and Related Materials ***17****, 383 (2008).*

82. Kabiraj, D.; Grötzschel, R.; Ghosh, S.
Modification of charge compensation in semi-insulating semiconductors by high energy light ion irradiation
Journal of Applied Physics ***103****, 053703 (2008).*

83. Kögler, R.; Ou, X.; Skorupa, W.; Möller, W.
The origin of the energy-dose window in separation-by-implanted-oxygen (SIMOX) materials processing
Applied Physics Letters ***92****, 181906 (2008).*

84. Kögler, R.; Ou, X.; Skorupa, W.; Möller, W.
The role of implantation-induced point defects for the redistribution of oxygen in silicon at high-temperature processing
Journal of Applied Physics ***104****, 103502 (2008).*

85. Krickl, R.; Nasdala, L.; Götze, J.; Grambole, D.; Wirth, R.
Alpha-irradiation effects in SiO_2
European Journal of Mineralogy ***20****, 517 (2008).*

86. Lanzerath, F.; Buca, D.; Trinkaus, H.; Goryll, M.; Mantl, S.; Knoch, J.; Breuer, U.; Skorupa, W.; Ghyselen, B.
Boron activation and diffusion in silicon and strained silicon-on-insulator by rapid thermal and flash lamp annealing
Journal of Applied Physics ***104****, 044908 (2008).*

87. Ling, C. C.; Cheung, C. K.; Gu, Q. L.; Dai, X. M.; Xu, S. J.; Zhu, C. Y.; Luo, J. M.; Tam, K. H.; Djurisic, A. B.; Beling, C. D.; Fung, S.; Lu, L. W.; Brauer, G.; Anwand, W.; Skorupa, W.; Ong, H. C.
Defect study in ZnO related structures - a multi-spectroscopic approach
Applied Surface Science ***255****, 58 (2008).*

88. Lu, L. W.; So, C. K.; Zhu, C. Y.; Gu, Q. L.; Li, C. J.; Fung, S.; Brauer, G.; Anwand, W.; Skorupa, W.; Ling, C. C.
Influence of electron irradiation on hydrothermally grown zinc oxide single crystals
Semiconductor Science & Technology ***23****, 095028 (2008).*

89. Ou, X.; Kögler, R.; Mücklich, A.; Skorupa, W.; Möller, W.; Wang, X.; Gerlach, J. W.; Rauschenbach, B.
Efficient oxygen gettering in Si by co-implantation of hydrogen and helium
Applied Physics Letters ***93****, 161907 (2008).*

90. Posselt, M.; Gao, F.; Bracht, H.
Correlation between self-diffusion in Si and the migration mechanisms of vacancies and self-interstitials: An atomistic study
Physical Review B ***78****, 035208 (2008).*

91. Posselt, M.; Schmidt, B.; Anwand, W.; Grötzschel, R.; Heera, V.; Mücklich, A.; Wündisch, C.; Skorupa, W.; Hortenbach, H.; Gennaro, S.; Bersani, M.; Giubertoni, D.; Möller, A.; Bracht, H.
P implantation into preamorphized germanium and subsequent annealing: Solid phase epitaxial regrowth, P diffusion, and activation
Journal of Vacuum Science & Technology B ***26****, 430 (2008).*

92. Skorupa, W.
Short time thermal processing: From electronics via photonics to pipe organs of the 17th century
Materials Science Forum ***573-574****, 417 (2008).*

93. Tyschenko, I. E.; Cherkov, A. G.; Voelskow, M.; Popov, V. P.
SiGe heterostructures-on-insulator produced by Ge^+-ion implantation and subsequent hydrogen transfer
Solid State Phenomena ***131-133****, 143 (2008).*

94. Tyschenko, I. E.; Voelskow, M.; Cherkov, A. G.; Popov, V. P.
The properties of the nanometer thick Si/Ge films-on-insulator produced by Ge^+–ion implantation and subsequent hydrogen transfer
Physica Status Solidi (C) ***5****, 3724 (2008).*

95. Voelskow, M.; Yankov, R.; Kups, T.; Pezoldt, J.; Skorupa, W.
Buried melting in germanium implanted silicon by millisecond flash lamp annealing
Applied Physics Letters ***93****, 151903 (2008).*

96. Volbers, N.; Lautenschläger, S.; Leichtweiss, T.; Laufer, A.; Graubner, S.; Meyer, B. K.; Potzger, K.; Zhou, S.
Arsenic doped zinc oxide
Journal of Applied Physics ***103****, 123106 (2008)*

97. Zhu, C. Y.; Ling, C. C.; Brauer, G.; Anwand, W.; Skorupa, W.
Vacancy-type defects in 6H–silicon carbide induced by He-implantation: A positron annihilation spectroscopy approach
Journal of Physics D ***41****, 195304 (2008).*

Optoelectronic Materials

98. Dreyhaupt, A.; Peter, F.; Winnerl, S.; Nitsche, S.; Wagner, M.; Schneider, H.; Helm, M.; Köhler, K.
Leistungsstarke Emitter und einfach handhabbare Detektoren für die Terahertz-Time-Domain-Spektroskopie
Technisches Messen ***75****, 3 (2008).*

99. Fritsch, D.; Schmidt, H.; Schmidt-Grund, R.; Grundmann, M.
Intensity of optical absorption close to the band edge in strained ZnO films
Journal of the Korean Physical Society ***53****, 123 (2008).*

100. Kachurin, G. A.; Cherkova, S. G.; Marin, D. V.; Yankov, R. A.; Deutschmann, M.
Formation of light-emitting Si nanostructures in SiO_2 by pulsed anneals
Nanotechnology ***19****, 355305 (2008).*

101. Kanjilal, A.; Rebohle, L.; Voelskow, M.; Skorupa, W.; Helm, M.
Influence of annealing on the Er luminescence in Si-rich SiO_2 layers co-implanted with Er ions
Journal of Applied Physics ***104****, 103522 (2008).*

102. Kehr, S. C.; Cebula, M.; Mieth, O.; Härtling, T.; Seidel, J.; Grafström, S.; Eng, L. M.; Winnerl, S.; Stehr, D.; Helm, M.
Anisotropy contrast in phonon-enhanced apertureless near-field microscopy using a free-electron laser
Physical Review Letters ***100****, 256403 (2008).*

103. Müller, S.; Lorenz, M.; Czekalla, C.; Benndorf, G.; Hochmuth, H.; Grundmann, M.; Schmidt, H.; Ronning, C.
Intense white photoluminescence emission of V-implanted ZnO oxide thin films
Journal of Applied Physics ***104****, 123504 (2008).*

104. Peter, F.; Winnerl, S.; Schneider, H.; Helm, M.; Köhler, K.
Terahertz emission from a large-area GaInAsN emitter
Applied Physics Letters ***93****, 101102 (2008).*

105. Prucnal, S.; Rebohle, L.; Skorupa, W.
Investigation of the temperature degradation and re-activation of the luminescent centres in rare earth implanted SiO_2 layers
Solid State Phenomena ***131-133****, 595 (2008).*

106. Prucnal, S.; Rebohle, L.; Nazarov, A. N.; Skorupa, W.
Reactivation of damaged rare earth luminescence centers in ion-implanted metal-oxide-silicon light

emitting devices
*Applied Physics B **91**, 123 (2008).*

107. Prucnal, S.; Sun, J. M.; Skorupa, L.; Rebohle, W.
Energy transfer from Gd to Er atoms in SiO_2(GdEr)-MOSLEDs produced by ion implantation
*Materials Science & Engineering B **146**, 241 (2008).*

108. Rauter, P.; Fromherz, T.; Winnerl, S.; Zier, M.; Kolitsch, A.; Helm, M.; Bauer, G.
Terahertz Si:B blocked-impurity-band detectors defined by nonepitaxial methods
*Applied Physics Letters **93**, 261104 (2008).*

109. Rebohle, L.; Lehmann, J.; Prucnal, S.; Kanjilal, A.; Nazarov, A.; Tyagulskii, I.; Skorupa, W.; Helm, M.
Blue and red electroluminescence of Europium-implanted MOS structures as a probe for the dynamics of microstructure
*Applied Physics Letters **93**, 071908 (2008).*

110. Ribbeck, H.-G. von; Brehm, M.; van der Weide, D. W.; Winnerl, S.; Drachenko, O.; Helm, M.; Keilmann, F.
Spectroscopic THz near-field microscope
*Optics Express **16**, 3430 (2008).*

111. Schmidt-Grund, R.; Rheinländer, B.; Kaidashev, E. M.; Lorenz, M.; Fritsch, D.; Schubert, M.; Schmidt, H.; Herzinger, C. M.
Vacuum ultraviolet dielectric function and band structure of ZnO
*Journal of the Korean Physical Society **53**, 88 (2008).*

112. Schneider, H.; Liu, H. C.; Winnerl, S.; Drachenko, O.; Helm, M.; Faist, J.
Room-temperature mid-infrared two-photon photodetector
*Applied Physics Letters **93**, 101114 (2008).*

113. Schneider, H.; Maier, T.; Liu, H. C.; Walther, M.
Two-photon photocurrent autocorrelation using intersubband transitions at nearly-resonant excitation
*Optics Express **16**, 1523 (2008).*

114. Stehr, D.; Wagner, M.; Schneider, H.; Helm, M.; Andrews, A. M.; Roch, T.; Strasser, G.
Two-color pump-probe studies of intraminiband relaxation in doped GaAs/AlGaAs superlattices
*Applied Physics Letters **92**, 051104 (2008).*

115. Sun, J. M.; Rebohle, L.; Prucnal, S.; Helm, M.; Skorupa, W.
Giant stability enhancement of rare-earth implanted SiO_2 light-emitting devices by an additional SiON protection layer
*Applied Physics Letters **92**, 071103 (2008).*

116. Tsvetkova, T.; Balabanov, S.; Avramov, L.; Borisova, E.; Bischoff, L.
Si^+ implantation induced photoluminescence enhancement in PMMA
*Przegląd Elektrotechniczny **84**, 72 (2008).*

117. Wenzel, M. T.; Härtling, T.; Olk, P.; Kehr, S. C.; Grafström, S.; Winnerl, S.; Helm, M.; Eng, L. M.
Gold nanoparticle tips for optical field confinement in infrared scattering near-field optical microscopy
*Optics Express **16**, 12302 (2008).*

118. Wienold, M.; Semtsiv, M. P.; Dressler, S.; Masselink, W. T.; Potzger, K.; Winnerl, S.; Helm, M.
Fe-implantation for rear-facet coatings of InP-based quantum cascade lasers
*Electronics Letters **44**, 293 (2008).*

119. Winnerl, S.; Nitsche, S.; Peter, F.; Drachenko, O.; Schneider, H.; Helm, M.; Köhler, K.
Easy-to-use scalable antennas for coherent detection of THz radiation
*Springer Proceedings in Physics **119**, 167 (2008).*

120. Winnerl, S.; Peter, F.; Dreyhaupt, A.; Zimmermann, B.; Wagner, M.; Schneider, H.; Helm, M.; Köhler, K.
Generation and detection of THz radiation with scalable antennas based on GaAs substrates with different carrier lifetimes
*IEEE Journal of Selected Topics in Quantum Electronics **14**, 449 (2008).*

121. Tribuzy, C. V.-B.; Ohser, S.; Sellesk, M.; Winnerl, S.; Schneider, H.; Helm, M.; Neuhaus, J.; Dekorsy, T.; Biermann, K.; Künzel, H.
Inefficiency of intervalley transfer in narrow InGaAs/AlAsSb quantum wells
*Physica Status Solidi (C) **5**, 229 (2008).*

122. Zhong, Y.; Djurišič, A. B.; Hsu, Y. F.; Wong, K. S.; Brauer, G.; Ling, C. C.; Chan, W. K.
Exceptionally long exciton photoluminescence lifetime in ZnO tetrapods
*Journal of Physical Chemistry C **112**, 16286 (2008).*

Others

123. Arroyo-De Dompablo, M. E.; Amador, U.; Gallardo–Amores, J. M.; Bähtz, C.; Biskup, N.; Morán, E.
High pressure materials for energy storage. The case of V_2O_5
Journal of Physics: Conference Series ***121****, 032001 (2008).*

124. Balabanov, S.; Tsvetkova, T.; Borisova, E.; Avramov, L.; Bischoff, L.
Dose dependence of visible range diffuse reflectivity for Si^+ and C^+ ion implanted polymers
Journal of Physics: Conference Series ***113****, 012038 (2008).*

125. Balabanov, S.; Tsvetkova, T.; Borisova, E.; Avramov, L.; Bischoff, L.
Spectral distribution of UV range diffuse reflectivity for Si^+ ion implanted polymers
Journal of Physics: Conference Series ***113****, 012039 (2008).*

126. Bischoff, L.; Akhmadaliev, Ch.
An alloy liquid metal ion source for lithium
Journal of Physics D ***41****, 052001 (2008).*

127. Bürger, W.; Lange, H.; Petr, V.
A new method of improving the acceleration voltage stability of Van de Graaff accelerators
Nuclear Instruments and Methods in Physics Research A ***586****, 160 (2008).*

128. Cizek, J.; Prochazka, I.; Brauer, G.; Anwand, W.; Gemma, R.; Nikitin, E.; Kirchheim, R.; Pundt, A.
Hydrogen interaction with vacancies in electron irradiated niobium
Acta Physica Polonica A ***113****, 1293 (2008).*

129. Georgievskaya, M.; Albert, B.; Bubnova, R.; Cordier, G.; Bähtz, C.; Filatov, S.
Thermal "order-disorder" behaviour in $(Na_{1-x}K_x)_4B_8O_{14}$ solid solutions investigated by X-ray powder diffraction
Crystal Research and Technology ***43****, 1150 (2008).*

130. Haubner, K.; Jaehne, E.; Adler, H.-J. P.; Köhler, D.; Loppacher, C.; Eng, L. M.; Grenzer, J.; Herasimovich, A.; Scheinert, S.
Assembly, structure, and performance of an ultra-thin film organic field-effect transistor (OFET) based on substituted oligothiophenes
Physica Status Solidi (A) ***205****, 430 (2008).*

131. Jungmann, M.; Krause-Rehberg, R.; Müller, A.; Krille, A.; Brauer, G.
Construction and timing system of the EPOS beam system
Applied Surface Science ***255****, 42 (2008).*

132. Kämpf, H.; Heuer, B.; Mrlina, J.; Reuther, H.
Combined xenolith and receiver function study, western bohemian massif, central europe
Geochimica et Cosmochimica Acta ***72****, A447 (2008).*

133. Khanduyeva, N.; Senkovskyy, V.; Beryozkina, T.; Bocharova, V.; Simon, F.; Nitschke, M.; Stamm, M.; Grötzschel, R.; Kiriy, A.
Grafting of poly(3-hexylthiophene) from poly(4-bromostyrene) films by kumada catalyst-transfer polycondensation: Revealing of the composite films structure
Macromolecules ***41****, 7383 (2008).*

134. Kibsgaard, J.; Tuxen, A.; Levisen, M.; Lægsgaard, E.; Gemming, S.; Seifert, G.; Lauritsen, J.; Besenbacher, F.
Atomic-scale structure of Mo_6S_6 nanowires
Nano Letters ***8****, 3928 (2008).*

135. Kosev, K.; Nankov, N.; Friedrich, M.; Grosse, E.; Hartmann, A.; Heidel, K.; Junghans, A. R.; Schilling, K. D.; Schwengner, R.; Sobiella, M.; Wagner, A.
A high-resolution time-of-flight spectrometer with tracking capabilities for fission fragments and beams of exotic nuclei
Nuclear Instruments and Methods in Physics Research A ***594****, 178 (2008).*

136. Krause-Rehberg, R.; Brauer, G.; Jungmann, M.; Krille, A.; Rogov, A.; Noack, K.
Progress of the intense positron beam project EPOS
Applied Surface Science ***255****, 22 (2008).*

137. Krille, A.; Krause-Rehberg, R.; Jungmann, M.; Becvar, F.; Brauer, G.
Digital positron lifetime spectroscopy at EPOS
Applied Surface Science ***255****, 93 (2008).*

138. Lehmann, M.; Jahr, M.; Donnio, B.; Graf, R.; Gemming, S.; Popov, I.
Star-shaped oligobenzoates: Non-conventional mesogens forming columnar helical mesophases
Chemistry - A European Journal ***14****, 3562 (2008).*

139. Lipavský, P.; Morawetz, K.; Kolácek, J.; Brandt, E. H.
Non-linear theory of deformable superconductors
Physical Review B ***78****, 174516 (2008).*

140. Lipavský, P.; Morawetz, K.; Kolácek, J.; Brandt, E. H.; Schreiber, M.
Contribution of the surface dipole to deformation of superconductors
Physical Review B ***77****, 014506 (2008).*

141. Lipavský, P.; Morawetz, K.; Kolavcek, J.; Brandt, E. H.
Surface deformation caused by the Abrikosov vortex lattice
Physical Review B ***77****, 184509 (2008).*

142. Morawetz, K.; Gemming, S.; Luschtinetz, R.; Eng, L. M.; Seifert, G.; Kenfack, A.
Current without bias and diode effect in shuttling transport of nanoshafts
New Journal of Physics ***10****, 1 (2008).*

143. Morawetz, K.; Lipavsky, P.; Kolacek, J.; Brandt, E. H.
Surface energy and magnetocapacitance of superconductors under electric field bias
Physical Review B ***78****, 054525 (2008).*

144. Morawetz, K.; Olbrich, C.; Gemming, S.
Reduction of surface coverage of finite systems due to geometrical steps
European Physical Journal B ***62****, 311 (2008).*

145. Novak, P.; Chaplygin, I.; Seifert, G.; Gemming, S.; Laskowski, R.
Ab-initio calculation of exchange interactions in $YMnO_3$
Computational Materials Science ***44****, 79 (2008).*

146. Popov, I.; Gemming, S.; Okano, S.; Ranjan, N.; Seifert, G.
Electromechanical switch based on Mo_6S_6 nanowires
Nano Letters ***8****, 4093 (2008).*

147. Preoteasa, E. A.; Preoteasa, E.; Kuczumow, A.; Gurban, D.; Harangus, L.; Grambole, D.; Herrmann, F.
Broad-beam PIXE and μ-PIXE analysis of normal and in vitro demineralized dental enamel
X-Ray Spectrometry ***37****, 517 (2008).*

148. Zharnylskaya, A. L.; Volkhin, V. V.; Shcherban, M. G.; Reuther, H.
Synthesis of a precursor for an alumina ceramic reinforced by zirconium dioxide from inorganic compounds in the presence of urea
Russian Journal of Applied Chemistry ***81****, 1147 (2008.)*
Originally published in russian: Zurnal Prikladnoj Chimii ***81****, 1069 (2008).*

Invited Conference Talks

1. Brauer, G.; Kuriplach, J.; Djurisic, C. C.; Ling, A. B.
Activities towards p-type doping of ZnO
8th International Conference on Position Sensitive Detectors (PSD 2008), 1.-5.09.2008, Prague, Czech Republic

2. Borany, J. von; Beyer, V.; Heinig, K.-H.; Mücklich, A.; Schmidt, B.; Skorupa, W.
Synthesis, modification and applications of Ge nanoclusters embedded in SiO_2 films
IUMRS International Conference in Asia 2008 (IUMRS-ICA2008), Session M "Innovative Material Technologies Utilizing Ion Beams", 8.-13.12.2008, Nagoya, Japan

3. Fassbender, J.
Ions hit magnetism - New challenges for the design of artificial nanostructures
Workshop "Recent Trends in Nanomagnetism", 5.02.2008, Leuven, Belgium

4. Fassbender, J.
Magnetic thin film materials tailored by ion irradiation
72. Jahrestagung der DPG und DPG Frühjahrstagung des Arbeitskreises Festkörperphysik, 25.-29.02.2008, Berlin, Germany

5. Krause, M.; Abrasonis, G.; Berndt, M.; Mücklich, A.; Munnik, F.; Kolitsch, A.; Möller, W.
Morphology, structure and growth pathways of carbon:transition metal nanocomposite thin films

prepared by ion beam co-sputtering
4th Szeged International Workshop on Advances in Nanoscience (SIWAN 2008), 9.-10.10.2008, Szeged, Hungary

6. Küpper, K.; Wintz, S.; Buess, M.; Raabe, J.; Quitmann, C.; Fassbender, J.
Dynamic interaction between vortices, antivortices and holes in domain walls investigated by means of time resolved photoemission electron microscopy (PEEM)
IEEE International Magnetics Conference (IIntermag 2008), 4.-8.05.2008, Madrid, Spain
Workshop on High Temporal and Spatial Resolution Studies of Magnetic Nanostructures, 27.06.-2.07.2008, Augustow, Poland

7. Menendez, E.; Sort, J.; Liedke, M. O.; Fassbender, J.; Gemming, T.; Weber, A.; Heydermann, Laura J.; Surinach, S.; Concustell, A.; Rao, K. V.; Deevi, S. C.; Baro, M. D.; Nogues, J.
Micro-/ nano-scale magnetic patterning of paramagnetic FeAl intermetallic alloys
1st Winter School "Women in Nano", 7.-9.02.2007, Kranjska Gora, Slovenia

8. Menendez, E.; Sort, J.; Liedke, M. O.; Strache, T.; Fassbender, J.; Möller, W.; Gemming, T.; Weber, A.; Heyderman, Laura J.; Surinach, S.; Deevi, S. C.; Rao, K. V.; Sommerlatte, J.; Nielsch, K.; Baro, M. D.; Nogues, J.
Direct generation of nanoscale ferromagnetic dots by selective ion irradiation of paramagnetic FeAl alloys
16th International Conference on Ion Beam Modification of Materials, 31.08.-5.09.2008, Dresden, Germany

9. Menendez, E.; Sort, J.; Liedke, M. O.; Strache, T.; Fassbender, J.; Möller, W.; Gemming, T.; Weber, A.; Heydermann, Laura J.; Surinach, S.; Deevi, S. C.; Rao, K. V.; Sommerlatte, J.; Nielsch, K.; Baro, M. D.; Nogues, J.
Direct nanoscale magnetic patterning in FeAl alloys by means of ion irradiation
Trends in Nanotechnology, TNT 2008, 1.-5.09.2008, Oviedo, Spain

10. Möller, W.
Fundamentals and modelling of reactive magnetron sputtering
Tutorial "Fundamentals and Trends of Plasma Surface Processing", 14.09.2008, Garmisch-Partenkirchen, Germany

11. Möller, W.
Reactive magnetron sputtering of nitrides and oxides: Understanding the process and optimizing the film quality
Plasmas, Surfaces and Thin Films, 11.06.2008, London, United Kingdom

12. Morawetz, K.; Lipavsky, P.; Kolacek, J.; Brandt, E. H.
Surface deformation and magnetocapacitance of superconductors
1st Bilateral Estonian-German Workshop, 30.04.-2.05.2008, Tartu, Estland

13. Pešić, Z. D.; Hellhammer, R.; Sulik, B.; Stolterfoht, N.
Fragmentation of water molecule by slow multiply charged ions
Radiation Damage in Biomolecular Systems (RADAM 2008), 13.-15.06.2008, Debrecen, Hungary

14. Potzger, K.; Zhou, S.; Talut, G.; Küpper, K.; Reuther, H.; Mücklich, A.; Grenzer, J.; Helm, M.; Fassbender, J.; Schmidt, H.; Xu, Q.; Lorenz, M.
The truth about ferromagnetic ZnO
72. Jahrestagung der DPG und DPG Frühjahrstagung des Arbeitskreises Festkörperphysik, 25.-29.02.2008, Berlin, Germany

15. Rebohle, L.; Cherkouk, C.; Prucnal, S.; Helm, M.; Skorupa, W.
Rare earth implanted Si-based light emitters and their use for smart biosensor applications
7th International Conference on Ion Implantation and other Applications of Ions and Electrons (ION 2008), 16.-19.06.2008, Kazimierz Dolny, Poland

16. Reuther, H.
Mössbauer spectroscopy as a tool to explore diluted magnetic semiconductors
International Symposium on the Industrial Applications of the Mössbauer Effect (ISIAME'08), 17.-22.08.2008, Budapest, Hungary

17. Schmidt, B.
Ionenstrahlen – ein Werkzeug zur Herstellung von Nanostrukturen
Internationale Fachmesse für Feinwerktechnik, Ultrapräzision, Micro- und Nanotechnologien –MiNat
MiNat Hot Spot WGL - Nanotechnologie in der Leibnizgesellschaft (WGL), 7.-8.10.2008, Stuttgart, Germany

18. Schneider, H.
Tutorial on "Intersubband devices: Quantum well infrared photodetectors"
Optoschool 2008, 27.07.-2.08.2008, Mumbai, India

19. Schneider, H.
Tutorial on "Intersubband devices: Quantum cascade laser"
Optoschool 2008, 27.07.-2.08.2008, Mumbai, India

20. Schneider, H.
Two-photon photocurrent studies of electron intersubband dynamics in multiple quantum wells
International Workshop on Nonequilibrium Nanostructures (NONNA'08), 1.-6.12.2008, Dresden, Germany

21. Seidel, W.
THz free-electron laser FELBE at the radiation source ELBE
FLASH Users-meeting and Kick-off Workshop: THz Beamline, 8.-10.09.2008, Hamburg, Germany

22. Skorupa, W.
Short time thermal processing: From electronics via photonics to pipe organs of the 17th century
VIIth International Conference on Ion Implantation and Other Applications of Ions and Electrons, 16.-19.06.2008, Kazimierz Dolny, Poland

23. Skorupa, W.; Rebohle, L.; Prucnal, S.; Cherkouk, Ch.; Helm, M.
Rare earth ion beam processing for silicon photonics
MRS Fall Meeting 2008, Symposium D: Rare-Earth Doping of Advanced Materials for Photonic Applications, 1.-5.12.2008, Boston MA, USA

24. Skorupa, W.; Rossner, M.; Werner, H.; Eule, A. C.; Schucknecht, T.; Rafaja, D.; Hausmann, U.; Wegscheider, K.
Casting experiments and materials studies for restoring lead pipes in historical organs
25th Congress of the International Society of Organbuilders (ISO), 21.-26.09.2008, Stralsund,Germany and Gdansk, Poland

25. Sort, J.; Menendez, E.; Liedke, M. O.; Strache, T.; Fassbender, J.; Gemming, T.; Weber, A.; Heydermann, L. J.; Surinach, S.; Rao, K. V.; Deevi, S. C.; Baro, M. D.; Nogues, J.
Magnetic lithography on paramagnetic FeAl alloys by selective ion irradiation
9th International Conference on Nanostructured Materials, 1.-6.06.2008, Rio de Janeiro, Brazil

26. Vinnichenko, M.; Rogozin, A.; Cornelius, S.; Shevchenko, N.; Munnik, F.; Gago, R.; Mücklich, A.; Kolitsch, A.; Möller, W.
Electrical properties and structure of transparent conductive oxide films deposited by pulsed reactive magnetron sputtering
11th International Conference on Plasma Surface Engineering, 15.-19.09.2008, Garmisch-Partenkirchen, Germany

27. Yankov, R.; Kolitsch, A.; Munnik, F.; Möller, W.; Donchev, A.; Schütze, M.
Plasma immersion ion implantation of fluorine: An efficient technique for enhancing the oxidation resistance of TiAl alloys
11th International Conference on Plasma Surface Engineering, 15.-19.09.2008, Garmisch-Partenkirchen, Germany

28. Zhou, S.; Potzger, K.; Xu, Q.; Lorenz, M.; Skorupa, W.; Helm, M.; Fassbender, J.; Grundmann, M.; Schmidt, H.
Transition metal implanted ZnO: A diluted magnetic semiconductor?
VIIth International Conference on Ion Implantation and other Applications of Ions and Electrons, 16.-19.06.08, Kazimierz Dolny, Poland

29. Zhou, S.; Schmidt, H.
Semiconductor-based tunnel structures: Preparation and application
International Workshop on Advances in Spintronic Materials: Theory and Experiment, 26.-28.11.2008, Duisburg, Germany

Conference Contributions

1. Berndt, M.; Abrasonis, G.; Krause, M.; Mücklich, A.; Kolitsch, A.; Möller, W.
The interplay of PVD growth parameter and nanostructuring of C:Co and C:V nanocomposites
72. Jahrestagung der DPG und DPG Frühjahrstagung des Arbeitskreises Festkörperphysik, 25.-29.2.2008, Berlin, Germany

2. Berndt, M.; Abrasonis, G.; Krause, M.; Mücklich, A.; Munnik, F.; Kolitsch, A.; Möller, W.
Morphology and structure of C:Co, C:V and C:Cu nanocomposite films
11th International Conference on Plasma Surface Engineering, 15.-19.09.2008, Garmisch-Partenkirchen, Germany

3. Berndt, M.; Krause, M.; Abrasonis, G.; Mücklich, A.; Munnik, F.; Kolitsch, A.; Möller, W.
Influence of the transition metal affinity on the encapsulating carbon medium during the growth of carbon:transition metal nanocomposite films
22nd International Winterschool on Electronic Properties of Novel Materials, 1.-8.03.2008, Kirchberg, Austria

4. Biermanns, A.; Pietsch, U.; Grenzer, J.; Hanisch, A.; Facsko, S.; Carbone, G.; Metzger, H.
X-ray scattering and diffraction from Xe-induced ripples in crystalline (001) silicon
16th International Conference on Ion Beam Modification of Materials, 31.08.-5.09.2008, Dresden, Germany

5. Biermanns, A.; Pietsch, U.; Grenzer, J.; Hanisch, A.; Facsko, S.; Carbone, G.; Metzger, T. H.
X-ray scattering and diffraction from ion beam induced ripples in crystalline silicon
9th Biennial Conference on High Resolution X-Ray Diffraction and Imaging (XTOP 2008), 15.-19.09.2008, Linz, Austria

6. Biermanns, A.; Pietsch, U.; Grigorian, S.; Grenzer, J.; Facsko, S.; Hanisch, A.; Carbone, D.; Metzger, H.
X-ray scattering and diffraction from Xe-induced ripples in crystalline silicon
72. Jahrestagung der DPG und DPG Frühjahrstagung des Arbeitskreises Festkörperphysik, 25.-29.02.08, Berlin, Germany

7. Bischoff, L.; Schmidt, B.; Lange, H.; Donzev, D.
Nano-structures for sensors on SOI by writing FIB implantation and subsequent anisotropic wet chemical etching
16th International Conference on Ion Beam Modification of Materials, 30.08.-5.09.2008, Dresden, Germany

8. Bischoff, L.; Schmidt, B.; Lange, H.
NEMS structures on SOI by writing FIB implantation and subsequent anisotropic wet chemical etching
Workshop "Ionenstrahlphysik und Nanotechnologie", 11.-12.04.2008, Darmstadt, Germany

9. Bolse, W.; Paulus, H.; Bolse, T.; Bischoff, L.
Nano-structures made by swift heavy ions
72. Jahrestagung der DPG und DPG Frühjahrstagung des Arbeitskreises Festkörperphysik, 25.-29.02.2008, Berlin, Germany

10. Brueser, B.; Pietsch, U.; Grigorian, S.; Panzner, T.; Grenzer, J.; Zeimer, U.
High resolution measurement of the thermal expansion coefficient of semiconductor multilayer lateral nanostructures
72. Jahrestagung der DPG und DPG Frühjahrstagung des Arbeitskreises Festkörperphysik, 25.-29.02.2008, Berlin, Germany

11. Bürger, D.; Schmidt, H.; Xu, Q.; Kolitsch, A.; Winnerl, S.; Schneider, H.; Zhou, S.; Potzger, K.; Helm, M.; Biehne, G.; Gottschalch, V.
Manganese implanted GaAs films
72. Jahrestagung der DPG und DPG Frühjahrstagung des Arbeitskreises Festkörperphysik, 25.-29.02.2008, Berlin, Germany

12. Bürger, D.; Zhou, S.; Grenzer, J.; Reuther, H.; Anwand, W.; Gottschalch, V.; Helm, M.; Schmidt, H.
The influence of annealing on manganese implanted GaAs films
16th International Conference on Ion Beam Modification of Materials, 31.08.-5.09.2008, Dresden, Germany

13. Cantelli, V.; Grenzer, J.; Borany, J. von; Fassbender, J.
The effect of the sputtering gas (Ar, Xe) on FePt clusters formation: Structural and magnetic properties
53rd Conference on Magnetism and Magnetic Materials, 10.-14.11.2008, Austin, Texas, USA

14. Cantelli, V.; Grenzer, J.; Borany, J. von; Fassbender, J.
Tailoring the FePt orientation on amorphous substrates by magnetron sputtering: Structural and magnetic investigations
53rd Conference on Magnetism and Magnetic Materials, 10.-14.11.2008, Austin, Texas, USA

15. Catoir, J.; Grisshammer, M.; Wolke, W.; Preu, R.; Trassl, R.; Grambole, D.
Analysis of hydrogen passivation by sputtered silicon nitride
23th European Photovoltaic Solar Energy Conference and Exhibition, 1.-5.09.2008, Valencia, Spain

16. Cherkouk, C.; Rebohle, L.; Skorupa, W.; Helm, M.
Estrogen detection in drinking water by Silicon based light emitters
E-MRS 2008 Spring Meeting, 26.-30.05.2008, Strasbourg, France

17. Dev, B. N.; Fassbender, J.; Grenzer, J.; Schell, N.; Bischoff, L.; Schmidt, B.; Grötzschel, R.; Allenstein, F.; Beddies, G.; Mccord, J.
Ion beam induced magnetic transformation in layered structures: Nonmagnetic to ferromagnetic and vice versa
16th International Conference on Ion Beam Modification of Materials, 31.08.-5.09.2008, Dresden, Germany

18. Donchev, A.; Kolitsch, A.; Möller, W.; Schütze, M.; Yankov, R. A.
The fluorine effect for high temperature oxidation protection of TiAl-alloys for automotive and aero-engine applications
The Minerals, Metals & Materials Society Annual Meeting, 9.-13.03.2008, New Orleans, USA

19. Drachenko, O.; Kozlov, D.; Gavrilenko, V.; Maremyanin, K.; Ikonnikov, A.; Zvonkov, B.; Goiran, M.; Leotin, L.; Fasching, G.; Winnerl, S.; Schneider, H.; Wosnitza, J.; Helm, M.
Cyclotron resonance absorption of 2D holes in strained InGaAs/GaAs quantum wells under high magnetic fields
Workshop of GDR-E "Semiconductor sources and detectors of THz frequencies", 26.-27.09.2008, Paris, France

20. Fassbender, J.; Liedke, M. O.; Keller, A.; Facsko, S.; Marko, D.; Hanisch, A.; Grenzer, J.; Cizmar, E.; Zvyagin, S.
Self-organized surface ripples as a source of magnetic anisotropies
72. Jahrestagung der DPG und DPG Frühjahrstagung des Arbeitskreises Festkörperphysik, 25.-29.02.2008, Berlin, Germany

21. Fitting, H.-J.; Salh, R.; Kourkoutis, L.; Schmidt, B.
Cluster growth and luminescence in ion-implanted silica
14th European Microscopy Congress, 1.-5.09.2008, Aachen, Germany

22. Frank, A.; Zöllner, J.-P.; Sarov, Y.; Ivanov, Tz.; Klett, S.; Gotszalk, T.; Zielony, M.; Zawierucha, P.; Schmidt, B.; Zier, M.; Nikolov, N.; Engl, W.; Sulzbach, T.; Langlotz, E.; Dontsov, D.; Schott, W.; Rangelow, I. W.
Investgation of crosstalk in cantilever arrays
Eurosensors XXII, 7.-10.09.2008, Dresden, Germany

23. Fritsch, D.; Schmidt, H.
Empirical pseudopotential calculation of strain induced birefringence in ZnO
72. Jahrestagung der DPG und DPG Frühjahrstagung des Arbeitskreises Festkörperphysik, 25.-29.02.2008, Berlin, Germany

24. Gabriel, A.; Posselt, M.
Molecular dynamics simulation of solid phase epitaxial regrowth of amorphous Ge layers
16th International Conference on Ion Beam Modification of Materials, 31.08.-5.09.2008, Dresden, Germany

25. Gabriel, A.; Posselt, M.
Atomistic simulation of amorphous germanium
72. Jahrestagung der DPG und DPG Frühjahrstagung des Arbeitskreises Festkörperphysik, 25.-29.02.2008, Berlin, Germany

26. Gabriel, A.; Posselt, M.
Atomistic simulation of amorphous germanium
E-MRS 2008 Spring Meeting, Symposium J: Beyond Silicon Technology: Materials and Devices for Post-Si CMOS, 26.-30.05.2008, Strasbourg, France

27. Gabriel, A.; Posselt, M.
Atomistic simulation of amorphous germanium
9th International Conference on Computer Simulation of Radiation Effects in Solids (COSIRES 2008), 12.-17.10.2008, Beijing, China

28. Gabriel, A.; Posselt, M.
Molecular dynamics simulation of solid phase epitaxial regrowth of amorphous Ge layers
E-MRS 2008 Spring Meeting, Symposium J: Beyond Silicon Technology: Materials and Devices for Post-Si CMOS, 26.-30.05.2008, Strasbourg, France

29. Gemming, S.; Enyashin, A. N.; Seifert, G.; Eng, L. M.
Modelling a nanoscale ferroic OFET
72. Jahrestagung der DPG und DPG Frühjahrstagung des Arbeitskreises Festkörperphysik, 25.-29.02.2008, Berlin, Germany

30. Gemming, S.; Kundin, J.; Radke De Cuba, M.; Yu, C.-J.; Emmerich, H.
A hybrid modelling approach for the structural evolution of surfaces
72. Jahrestagung der DPG und DPG Frühjahrstagung des Arbeitskreises Festkörperphysik, 25.-29.02.2008, Berlin, Germany

31. Gemming, S.; Wündisch, C.; Posselt, M.
Point defects in germanium - theory and experiment
72. Jahrestagung der DPG und DPG Frühjahrstagung des Arbeitskreises Festkörperphysik, 25.-29.02.2008, Berlin, Germany

32. Gotszalk, T.; Zawierucha, P.; Woszczyna, M.; Zielony, M.; Ivanov, T.; Ivanova, K.; Volland, B. E.; Sarov, Y.; Persaud, A.; Dontzov, D.; Schmidt, B.; Nikolov, N.; Kostic, I.; Engl, W.; Sulzbach, T.; Mielczarski, J.; Kolb, S.; Pedreau, R.; Huq, S. E.; Edinger, K.; Fortagne, O.; Blom, H. O.; Rangelow, I. W.
Application of self-actuated 32 cantilever array in atomic force surface measurements
34th Micro and Nano Engineering Conference(MNE08), 15.-18.09.2008, Athens, Greece

33. Graham, Jeremy F.; Kell, Copeland D.; Gray, Jennifer L.; Wolf, Stuart A.; Floro, Jerry A.; Bischoff, L.; Hull, R.
Controlled assembly and nanoscale doping of epitaxial Si(Ge) quantum dot nanostructures
2008 MRS Fall Meating, 1.-5.12.2008, Boston, USA

34. Grenzer, J.; Bähtz, C.; Beckers, M.; Jeutter, N. M.; Borany, J. von
In-situ investigations at BM20-ROBL
Congress on Materials Science and Engineering 2008 (MSE08), 1.-4.09.2008, Nürnberg, Germany

35. Grenzer, J.; Bischoff, L.; Biermanns, A.
X−ray investigations on $CoSi_2$ nano wires manufactured by focused ion beam synthesis
72. Jahrestagung der DPG und DPG Frühjahrstagung des Arbeitskreises Festkörperphysik, 25.-29.02.2008, Berlin, Germany

36. Grenzer, J.; Bischoff, L.; Biermanns, A.
X−ray investigations on $CoSi_2$ nano wires manufactured by focused ion beam synthesis
9th Biennial Conference on High Resolution X-Ray Diffraction and Imaging (XTOP 2008), 15.-19.09.2008, Linz, Austria

37. Grimm, C. V.-B.; Pfau, C.; Ohser, S.; Winnerl, S.; Schneider, H.; Helm, M.; Biermann, K.; Künzel, H.
Intersubband relaxation and dephasing in narrow InGaAs/AlAsSb quantum well structures
35th International Symposium on Compound Semiconductors, 21.-24.09.2008, Europa-Park, Rust, Germany

38. Hanisch, A.; Grenzer, J.; Facsko, S.; Biermanns, A.; Pietsch, U.; Metzger, T. H.; Carbone, G.
High energy Xe^+ ion beam induced rippled patterns on silicon
16th International Conference on Ion Beam Modification of Materials, 31.08.-5.09.08, Dresden, Germany

39. Hanisch, A.; Grenzer, J.; Facsko, S.; Winkler, I.; Biermanns, A.; Grigorian, S.; Pietsch, U.
High energy Xe^+ ion beam induced ripple structures on silicon
72. Jahrestagung der DPG und DPG Frühjahrstagung des Arbeitskreises Festkörperphysik, 25.-29.02.08, Berlin, Germany

40. Heera, V.; Herrmannsdörfer, T.; Ignatchik, O.; Mücklich, A.; Posselt, M.; Reuther, H.; Schmidt, B.; Skorupa, W.; Voelskow, M.; Wündisch, C.; Wosnitza, J.; Helm, M.
Superconducting Ge:Ga layers produced by ion implantation and flash lamp annealing
16th International Conference on Ion Beam Modification of Materials, 31.08.-5.09.2008, Dresden, Germany

41. Heinig, K.-H.; Numazawa, S.
Surface patterning by ion erosion – atomistic computer simulations
16th International Conference on Ion Beam Modification of Materials, 31.08.-5.09.2008, Dresden, Germany

42. Heinig, K.-H.; Röntzsch, L.
Facetting morphology of crystallites under ion irradiation – a 3D kinetic lattice monte carlo study
16th International Conference on Ion Beam Modification of Materials, 31.08.-5.09.2008, Dresden, Germany

43. Heintze, C.; Recknagel, C.; Bergner, F.; Hernández-Mayoral, M.; Kolitsch, A.
Ion-irradiation-induced damage of steels characterized by means of nanoindentation
16th International Conference on Ion Beam Modification of Materials, 31.08.-5.09.2008, Dresden, Germany

44. Henkel, C.; Biehne, G.; Grundmann, M.; Wagner, G.; Stoffel, M.; Schmidt, O. G.; Schmidt, H.
Charge accumulation in a type-II Ge/Si heterostructure

72. Jahrestagung der DPG und DPG Frühjahrstagung des Arbeitskreises Festkörperphysik, 25.-29.02.2008, Berlin, Germany

45. Iacomi, F.; Scarlat, C.; Calin, G.; Cazacu, M. M.; Goian, V.
ZnO:Co thin films grown by spin-coating method
Advanced Processing for Novel Functional Materials (APNFM 2008), 23.-25.01.2008, Dresden, Germany

46. Järvi, T. T.; Pohl, D.; Albe, K.; Rellinghaus, B.; Schultz, L.; Fassbender, J.; Kuronen, A.; Nordlund, K.
Untwinning of alloyed nanoparticles via intermediate amorphization
16th International Conference on Ion Beam Modification of Materials, 31.08.-5.09.2008, Dresden, Germany

47. Jaworowicz, J.; Kisielewski, M.; Maziewski, A.; Sveklo, I.; Jamet, J.-P.; Ferre, J.; Mougin, A.; Vernier, N.; Fassbender, J.
Ga^+ ion irradiation-induced out-of-plane magnetization in Pt/Co(3nm)/Pt films
International Magnetics Conference, 4.-8.05.2008, Madrid, Spain

48. Jaworowicz, J.; Kisielewski, M.; Maziewski, A.; Sveklo, I.; Jamet, J.-P.; Ferre, J.; Mougin, A.; Vernier, N.; FassbenderJ.; Henschke, A.; Bourhis, E.; Gierak, J.
Ga^+ ion irradiation-induced changes of magnetic ordering in Pt/Co(3nm)/Pt films
16th International Conference on Ion Beam Modification of Materials, 31.08.-5.09.2008, Dresden, Germany

49. Jaworowicz, J.; Kisielewski, M.; Maziewski, A.; Sveklo, I.; Jamet, J.-P.; Ferre, J.; Mougin, A.; Vernier, N.; Fassbender, J.; Henschke, A.; Bourhis, E.; Gierak, J.
Ga^+ ion irradiation-induced changes of magnetic ordering in Pt/Co(3nm)/Pt films
Louis Neel Colloquim, 30.09.-3.10.2008, La Grande Motte, France

50. Kachurin, G. A.; Cherkova, S. G.; Marin, D. V.; Yankov, R. A.
Light-emitting Si nanostructures formed in Si implanted SiO_2 layers by pulsed anneals
16th International Conference on Ion Beam Modification of Materials, 31.08.-5.09.2008, Dresden, Germany

51. Kachurin, G. A.; Cherkova, S. G.; Yankov, R. A.; Marin, D. V.
Light-emitting Si quantum dots formed by pulsed annealing
Workshop on Recent Advances of Low Dimensional Structures and Devices (WRA-LDSD), 7.-9.04.2008, Nottingham, United Kingdom

52. Kachurin, G. A.; Cherkova, S. G.; Yankov, R. A.; Marin, D. V.
Luminescing quantum-size Si nanostructures formed in Si rich SiO_2 by intense light pulses
15th International Conference on Luminescence and Optical Spectroscopy of Condensed Matter (ICL'08), 7.-11.07.2008, Lyon, France

53. Kachurin, G. A.; Cherkova, S. G.; Yankov, R. A.; Marin, D. V.
Light-emitting Si nanostructures formed in Si-rich SiO_2 by pulsed annealing
16th Annual International Conference on Composites/Nano Engineering (ICCE-16), 20.-26.06.2008, Kunming (City of Eternal Spring), China

54. Kachurin, G. A.; Cherkova, S. G.; Yankov, R. A.; Marin, D. V.
Pulsed annealing creation of light-emitting Si nanostructures in SiO_2 layers implanted with Si ions
9th International Conference on Applications of Nuclear Techniques, 8.-14.06.2008, Crete, Greece

55. Kachurin, G. A.; Yankov, R. A.; Cherkova, S. G.; Marin, D. V.
Fabrication of light-emitting Si quantum dots by pulsed annealing of Si-rich SiO_2 layers
15th International Conference on Semiconductor Dots, 11.-16.05.2008, Gyeongju, Korea

56. Kämpf, H.; Heuer, B.; Mrlina, J.; Reuther, H.
Combined xenolith and receiver function study, western bohemian massif, central europe
Goldschmidt Conference 2008, 13.-18.07.2008, Vancouver, Canada

57. Kanjilal, A.; Rebohle, L.; Voelskow, M.; Skorupa, W.; Helm, M.
Inverse energy transfer process during electroluminescence in Er-doped SiO_2 layers containing Ge nanocrystals
16th International Conference on Ion Beam Modification of Materials, 31.08.-5.09.2008, Dresden, Germany

58. Kanjilal, A.; Rebohle, L.; Voelskow, M.; Skorupa, W.; Helm, M.
Electrically driven reverse energy transfer process in Er-doped SiO_2 layers containing Ge nanocrystals
7th International Conference: Ion Implantation and Other Applications of Ions and Electrons, 16.-19.06.2008, Kazimierz Dolny, Poland

59. Kanjilal, A.; Rebohle, L.; Voelskow, M.; Skorupa, W.; Helm, M.
Energy transfer from the Er^{3+} to Ge nanocrystals during electroluminescence in MOSLEDs.
2008 MRS Fall Meeting, 1.-5.12.2008, Boston, MA, USA

60. Kanjilal, A.; Rebohle, L.; Voelskow, M.; Skorupa, W.; Helm, M.
Strong Er luminescence in rapid thermal annealed Er-doped SiO_2 layers containing Si nanoclusters
E-MRS 2008 Spring Meeting, 26.-30.05.2008, Strasbourg, France

61. Kanjilal, A.; Rebohle, L.; Voelskow, M.; Skorupa, W.; Helm, M.
Strong Er luminescence at 1.53 µm in rapid thermal annealed Si-rich SiO_2 layers co-implanted with Er
72. Jahrestagung der DPG und DPG Frühjahrstagung des Arbeitskreises Festkörperphysik, 25.-29.02.2008, Berlin, Germany

62. Keller, A.; Facsko, S.; Möller, W.
Evolution of ion-induced ripple patterns on SiO_2 surfaces
17th International Workshop on Inelastic Ion-Surface Collisions, 21.-26.09.2008, Porquerolles, France

63. Keller, A.; Facsko, S.; Möller, W.; Peverini, L.; Kozhevnikov, I. V.
Anisotropic scaling of ion-induced ripple morphologies on Si
NanoSteps - Self-organized nanostructures on crystal surfaces, 30.06.-12.07.2008, Cargèse, France

64. Keller, A.; Facsko, S.; Peverini, L.; Kozhevnikov, I. V.; Möller, W.
Evolution of ripple morphologies on silicon during sub-keV ion sputtering
16th International Conference on Ion Beam Modification of Materials, 31.08.-5.09.2008, Dresden, Germany

65. Khan, S.; Heinig, K.-H.; Avasthi, D.
Nanocomposite Au-SiO_2 thin film deposition by co-sputtering: Comparison of experiments with atomistic simulations
16th International Conference on Ion Beam Modification of Materials, 31.08.-5.09.2008, Dresden, Germany

66. Kögler, R.; Ou, X.
The impact of implantation defects in SIMOX processing
Arbeitstreffen "Punktdefekte", 3.-4.04.2008, Dresden, Germany

67. Krickl, R.; Grambole, D.; Götze, J.; Wirth, R.; Nasdala, L.
Effects of alpha-irradiation on SiO_2 phases
European Geosciences Union General Assembly, 13.-18.04.2008, Vienna, Austria

68. Krickl, R.; Nasdala, L.; Wildner, M.; Grambole, D.
New Insights into the formation of radiohaloes: Effects of artificial alpha–irradiation on cordierite
86th Annual Meeting of the German Mineralogical Society, 14.-17.09.2008, Berlin, Germany

69. Küpper, K.; Buess, M.; Raabe, J.; Quitmann, C.; Fassbender, J.
Dynamic vortex − antivortex interaction in a single cross-tie wall
72. Jahrestagung der DPG und DPG Frühjahrstagung des Arbeitskreises Festkörperphysik, 25.-29.02.2008, Berlin, Germany

70. Kunze, T.; Gemming, S.; Olbrich, C.; Chaplygin, I.; Schmidt, P.; Schreiber, M.
An anisotropic Heisenberg model on the trigonal lattice for multiferroic oxides
72. Jahrestagung der DPG und DPG Frühjahrstagung des Arbeitskreises Festkörperphysik, 25.-29.02.2008, Berlin, Germany

71. Liedke, M. O.; Cantelli, V.; Grenzer, J.; Markó, D.; Mücklich, A.; Fassbender, J.
The strong correlation between structural properties of the buffer layer and the exchange bias phenomena
72. Jahrestagung der DPG und DPG Frühjahrstagung des Arbeitskreises Festkörperphysik, 25.-29.02.2008, Berlin, Germany

72. Liedke, B.; Facsko, S.; Fassbender, J.; Heinig, K.-H.; Möller, W.; Jaworowicz, J.; Ferre, J.; Maziewski, A.; Vernier, N.
Simulation of defects and composition after Ga^+ irradiation of ultrathin Pt/Co/Pt film
16th International Conference on Ion Beam Modification of Materials, 31.08.-5.09.2008, Dresden, Germany

73. Liedke, B.; Facsko, S.; Fassbender, J.; Jaworowicz, J.; Ferre, J.; Maziewski, A.; Vernier, N.; Möller, W.
Simulation of defects and composition after irradiation of ultrathin Pt/Co/Pt film with Ga^+
Physics of Magnetism 2008, 24.-27.06.2008, Poznan, Poland

74. Liedke, B.; Facsko, S.; Heinig, K.-H.; Möller, W.
Surface modification using binary collision approximation and 3D lattice kinetic Monte Carlo simulation
16th International Conference on Ion Beam Modification of Materials, 31.08.-5.09.2008, Dresden, Germany

75. Liedke, M. O.; Liedke, B.; Marko, D.; Keller, A.; Mücklich, A.; Facsko, S.; Fassbender, J.; Cizmar, E.; Zvyagin, S.; Wosnitza, J.
Magnetic anisotropies in ferromagnetic and exchange-coupled systems on rippled surfaces

72. Jahrestagung der DPG und DPG Frühjahrstagung des Arbeitskreises Festkörperphysik, 25.-29.02.2008, Berlin, Germany

76. Liedke, M. O.; Strache, T.; Fassbender, J.; Möller, W.; Menéndez, E.; Sort, J.; Gemming, T.; Weber, A.; Heyderman, L. J.; Rao, K. V.; Deevi, S. C.; Nogués, J.
Ion irradiation induced sub-100 nm ferromagnetic patterns
Physics of Magnetism 2008, 24.-27.06.2008, Poznan, Poland

77. Maennel, M.; Lipavský, P.; Morawetz, K.; Schreiber, M.
Bose condensation for attractive interaction?
International Workshop on Nonequilibrium Nanostructures, 1.-6.12.2008, Dresden, Germany

78. Maennel, M.; Morawetz, K.; Schreiber, M.
Phase diagram for interacting bose systems
72. Jahrestagung der DPG und DPG Frühjahrstagung des Arbeitskreises Festkörperphysik, 25.-29.02.2008, Berlin, Germany

79. Maennel, M.; Morawetz, K.; Schreiber, M.
Phase diagram for interacting bose systems
72. Jahrestagung der DPG und DPG Frühjahrstagung des Arbeitskreises Festkörperphysik, 25.-29.02.2008, Berlin, Germany

80. Markó, D.; Potzger, K.; Küpper, K.; Xu, Q.; Zhou, S.; Schmidt, H.; Fassbender, J.; Lorenz, M.; Arenholz, E.; Denlinger, J. D.
Determination of charge state in Co- and Mn-doped ZnO films
72. Jahrestagung der DPG und DPG Frühjahrstagung des Arbeitskreises Festkörperphysik, 25.-29.02.2008, Berlin, Germany

81. Martin, N.; Hamann, C.; Mccord, J.; Fassbender, J.; Quandt, E.; Gerber, A.; Bigall, N.; Eychmüller, A.; Schultz, L.
Characterization of hybrid amorphous-partially crystalline thin films
72. Jahrestagung der DPG und DPG Frühjahrstagung des Arbeitskreises Festkörperphysik, 25.-29.02.2008, Berlin, Germany

82. Martinavičius, A.; Abrasonis, G.; Möller, W.; Chumlyakov, Y.
Nitrogen diffusion in single crystalline austenitic stainless steel: Ion energy and flux effects
22nd International Conference on Surface Modification Technologies (SMT22), 24.09.2008, Trollhättan, Sweden

83. Martinavičius, A.; Abrasonis, G.; Möller, W.; Templier, C.; Rivière, J. P.; Declémy, A.; Chumlyakov, Y.
Nitrogen diffusion in single crystalline austenitic stainless steel during ion beam nitriding and subsequent thermal annealing
11th International Conference on Plasma Surface Engineering, 16.09.2008, Garmisch-Partenkirchen, Germany

84. Martins, R. M. S.; Schell, N.; Silva, R.; Pereira, L.; Mahesh, K.K.; Braz Fernandes, F.M.
Texture development and phase transformation behaviour of sputtered shape memory alloy Ni-Ti films
ESRF User Meeting 2008, 5.-7.02.2008, Grenoble, France

85. Martins, R. M. S.; Schell, N.; Borany, J. von; Mücklich, A.; Siva, R. J. C.; Mehesh, K. K.; Branz-Fernandes, F. M.
Ion bombardment of shape memory alloy (SMA) Ni-Ti films
Microscience 2008, 23.-26.06.2008, London, United Kingdom

86. Martins , R.M.S.; Schell , N.; Silva, R.; Pereira, L.; Mahesh, K.K.; Braz Fernandes, F.M.
Texture development and phase transformation behaviour of sputtered Ni-Ti films
2008 International Conference for Shape Memory and Superelastic Technologies, 21.-25.09.2008, Stresa, Italy

87. Martins, R.M.S; Schell, N.; Borany, J. von; Bähtz, C.
In-situ study of film growth by synchrotron radiation scattering
2008 International Conference for Shape Memory and Superelastic Technologies, 21.-25.09.2008, Stresa, Italy

88. Mccord, J.; Kaltofen, R.; Quandt, E.; Fassbender, J.
Irradiation induced magnetic patterning of soft-magnetic thin films
16th International Conference on Ion Beam Modification of Materials, 31.08.-5.09.2008, Dresden, Germany

89. Mello, C. B.; Ueda, M.; Beloto, A. F.; Mücklich, A.; Reuther, H.
Nanocrystals formation in a–Si/SiO_2 layer by ion mixing and plasma immersion ion implantation in different energy ranges
16th International Conference on Ion Beam Modification of Materials, 31.08.-5.09.2008, Dresden, Germany

90. Mello, C. B.; Ueda, M.; Geraldo, A. S.; Nascimento, D. P.; Lepienski, C. M.; Reuther, H.
Tribological effects of plasma immersion ion implantation heating treatments on SS304 stainless steel

VII Encontro da SBPMat, Symposium C – Mechanical properties of surfaces, thin films and coatings, 28.09.-2.10.2008, Guarujá, Brazil

91. Menendez, E.; Martinavicius, A.; Liedke, M. O.; Abrasonis, G.; Fassbender, J.; Sommerlatte, J.; Nielsch, K.; Surinach, S.; Baro, M. D.; Nogues, J.; Sort, J.
Generation of micro / nano-scaled magnetic structures on AISI 304L austenitic stainless steel by ion beam nitriding
16th International Conference on Ion Beam Modification of Materials, 31.08.-5.09.2008, Dresden, Germany

92. Menendez, E.; Martinavicius, A.; Liedke, M. O.; Abrasonis, G.; Fassbender, J.; Sort, J.; Surinach, S.; Baro, M. D.; Nogues, J.
Patterning of magnetic structures on austenitic stainless steel by ion beam nitriding
International Magnetics Conference, 4.-8.05.2008, Madrid, Spain

93. Menendez, E.; Sort, J.; Liedke, M. O.; Fassbender, J.; Gemming, T.; Weber, A.; Heydermann, L. J.; Surinach, S.; Rao, K. V.; Deevi, S. C.; Baro, M. D.; Nogues, J.
Creation of sub-100 nm ferromagnetic dots by selective irradiation of a paramagnetic intermetallic alloy
International Magnetics Conference, 4.-8.05.2008, Madrid, Spain

94. Morawetz, K.
Enhancement of pairing near reasonant atoms
International Workshop on Chaos and Collectivity in Many-Body Systems, 5.-8.03.2008, Dresden, Germany

95. Morawetz, K.
Fluctuations due to nonlocal collisions
International Workshop on Chaos and Collectivity in Many-Body System, 5.-8.03.2008, Dresden, Germany

96. Morawetz, K.
Enhancement of T_c due to charge transfer
International Workshop on Physics and Chemistry of FeAs-based Superconductors, 27.-29.10.2008, Dresden, Germany

97. Morawetz, K.; Lipavsky, P.; Kolacek, J.; Brandt, E. H.; Schreiber, M.
Contribution of the surface dipole to deformation of superconductors
72. Jahrestagung der DPG und DPG Frühjahrstagung des Arbeitskreises Festkörperphysik, 25.-29.02.2008, Berlin, Germany

98. Morawetz, K.; Lipavsky, P.; Kolacek, J.; Brandt, E. H.; Schreiber, M.
The concept of correlated density and its application
72. Jahrestagung der DPG und DPG Frühjahrstagung des Arbeitskreises Festkörperphysik, 25.-29.02.2008, Berlin, Germany

99. Morawetz, K.; Lipavsky, P.; Kolacek, J.; Brandt, E. H.; Schreiber, M.
Surface superconductivity and capacitance of superconductors under electric and magnetic fields
72. Jahrestagung der DPG und DPG Frühjahrstagung des Arbeitskreises Festkörperphysik, 25.-29.02.2008, Berlin, Germany

100. Morawetz, K.; March, N. H.; Squire, R. H.
The chemical potential for the inhomogeneous electron liquid in terms of its kinetic and potential parts with special consideration of the surface po tential step and BCS-BEC crossover
72. Jahrestagung der DPG und DPG Frühjahrstagung des Arbeitskreises Festkörperphysik, 25.-29.02.2008, Berlin, Germany

101. Morawetz, K.; Schreiber, M.
Dominant motion vs. localization in quasiperiodic chains
72. Jahrestagung der DPG und DPG Frühjahrstagung des Arbeitskreises Festkörperphysik, 25.-29.02.2008, Berlin, Germany

102. Nasdala, L.; Gigler, A. M.; Wildner, M.; Grambole, D.; Zaitsev, A. M.; Harris, J. W.; Hofmeister, W.; Milledge, H. J.; Satitkune, S.
Alpha-radiation damage in diamond
Goldschmidt Conference 2008, 13.-18.07.2008, Vancouver, Canada

103. Nasdala, L.; Grambole, D.; Harris, J. W.; Wildner, M.; Hofmeister, W.
Radiation damage in helium-implanted diamond
8th International Conference on Raman Spectroscopy Applied to the Earth Sciences (GeoRaman08), 2.-6.06.2008, Ghent, Belgium

104. Nazarov, A. N.; Tyagulskii, I. P.; Tyagulskii, S. I.; Rebohle, L.; Skorupa, W.; Biskupek, J.; Kaiser, U.
Correlation between electroluminescence and charge trapping in multi-color Eu-implanted Si-based light-emitting diodes
EMRS 2008 Spring Meeting, 26.-30.05.2008, Strasbourg, France

105. Nazarov, A.; Tyagulskii, I.; Tyagulskiy, S.; Rebohle, L.; Prucnal, S.; Lehmann, J.; Biskupek, J.; Kaiser, U.; Skorupa, W.
Electroluminescence, charge trapping and clustering in rare-earth implanted SiO_2-Si light-emitting diodes
2008 MRS Fall Meeting, 1.-5.12.2008, Boston, USA

106. Neve, S.; Masset, P. J.; Yankov, R. A.; Kolitsch, A.; Zschau, H.-E.; Schütze, M.
High temperature oxidation resistance of fluorine-treated TiAl alloys: Chemical vs. ion beam fluorination techniques
16th International Conference on Ion Beam Modification of Materials, 31.08.-5.09.2008, Dresden, Germany

107. Nomura, K.; Rykov, A.; Iio, S.; Hirose, Y.; Hasegawa, I.; Reuther, H.
^{57}Fe and ^{119}Sn CEMS study of SnO_2 films implanted with ^{57}Fe
International Symposium on the Industrial Applications of the Mössbauer Effect (ISIAME'08), 17.-22.08.2008, Budapest, Hungary

108. Ódor, G.; Liedke, B.; Heinig, K.-H.
Mapping of two-plus-one-dimensional KPZ growth onto driven lattice gas model of dimers
International Workshop on Nonequilibrium Nanostructures, 1.-6.12.2008, Dresden, Germany

109. Ou, X.; Kögler, R.; Mücklich, A.; Skorupa, W.; Möller, W.; Wang, X.
Cavity layer introduction in SIMOX technology
72. Jahrestagung der DPG und DPG Frühjahrstagung des Arbeitskreises Festkörperphysik, 25.-29.02.2008, Berlin, Germany

110. Ou, X.; Kögler, R.; Skorupa, W.; Möller, W.; Wang, X.; Rauschenbach, B.
The origin of the energy-dose window in SIMOX processing and defect engeneering
European Materials Research Society Conference, 25.-30.05.2008, Strasbourg, France

111. Ou, X.; Kögler, R.; Mücklich, A.; Skorupa, W.; Möller, W.; Wang, X.
Oxygen gettering in the initial stage of SIMOX process
16th International Conference on Ion Beam Modification of Materials, 31.08.-5.09.2008, Dresden, Germany

112. Pankoke, V.; Gemming, S.
Simulation of a nano-scale magnetic switch
Junior Euromat 2008, 14.-18.07.2008, Lausanne, Switzerland

113. Pešić, Z. D.; Hellhammer, R.; Sulik, B.; Stolterfoht, N.
Strong forward-backward asymmetry of water ionic fragments by slow highly charged ions impact
14th International Conference on the Physics of Highly Charged Ions, 1.-5.09.2008, Tokyo, Japan

114. Peter, F.; Winnerl, S.; Nitsche, S.; Dreyhaupt, A.; Schneider, H.; Helm, M.; Köhler, K.
THz detection with scalable photoconductive antennas
72. Jahrestagung der DPG und DPG Frühjahrstagung des Arbeitskreises Festkörperphysik, 24.-29.02.2008, Berlin, Germany

115. Peter, F.; Winnerl, S.; Schneider, H.; Helm, M.; Köhler, K.
Terahertz wave emission from an InGaAsN large area emitter
GDR-E-2008 THz Workshop, 25.-26.09.2008, Paris, France

116. Peyre, H.; Pezoldt, J.; Voelskow, M.; Skorupa, W.; Camassel, J.
SIMS investigation of Ge_x(4H-SiC)$_{1-x}$ solid solutions synthesized by Ge-ion implantation up to x = 0.2
7th European Conference on Silicon Carbide and Related Materials, 7.-11.09.2008, Barcelona, Spain

117. Pflumm, R.; Schütze, M.; Yankov, R.; Kolitsch, A.
Self- growing shark skin pattern on the surface of gamma-TiAl alloys
Congress on Materials Science and Engineering, 1.-4.09.2008, Nürnberg, Germany

118. Pohl, D.; Järvi, T. T.; Mohn, E.; Fassbender, J.; Albe, K.; Schultz, L.; Rellinghaus, B.
The influence of ion irradiation on the structure of binary nanoparticles
16th International Conference on Ion Beam Modification of Materials, 31.08.-5.09.2008, Dresden, Germany

119. Pollmann, K.; Raff, J.; Fahmy, K.; Borany, J. von; Grenzer, J.; Herrmansdörfer, T.
Bacterial surface layers (S-layers) as building blocks for nanocomposites
Nanofair 2008, 11.-12.03.2008, Dresden, Germany

120. Pollmann, K.; Raff, J.; Marquard, A.; Scholz, A.
Bacterial surface layers (S-layers) as building blocks for photocatalytic nanocomposites
NanoBioEurope 2008, 9.-13.06.2008, Barcelona, Spain

121. Posselt, M.
Atomistic simulation of solid phase epitaxial regrowth in Si: A critical review
E-MRS 2008 Spring Meeting, 26.-30.05.2008, Strasbourg, France

122. Posselt, M.; Gabriel, A.-A.
A critical review on atomistic simulations of solid-phase epitaxial regrowth of amorphous Si and Ge layers
9th International Conference on Computer Simulation of Radiation Effects in Solids (COSIRES2008), 12.-17.10.2008, Beijing, China

123. Potzger, K.; Zhou, S.
Sources for ferromagnetism in ion implanted ZnO
16th International Conference on Ion Beam Modification of Materials, 31.08.-5.9.2008, Dresden, Germany

124. Prinz, M.; Raekers, M.; Küpper, K.; Chaudhuri, P.; George, S. J.; Neumann, M.
Magnetism of the high spin molecules $[Mn_4L_6](BF_4)_2 \cdot 2CH_3\text{-}CN \cdot H_2O$ and $[CrIIIMnII_3\ (PyA)_6Cl_3]$
72. Jahrestagung der DPG und DPG Frühjahrstagung des Arbeitskreises Festkörperphysik, 25.-29.02.2008, Berlin, Germany

125. Raabe, J.; Buess, M.; Küpper, K.; Fassbender, J.; Quitmann, C.
The dance of the domains: Excitations in magnetic microstructures studied by X-ray microscopy
MRS Spring Meeting 2008, Symposium: Advances and Applications of Surface Electron Microscopy, 24.-28.03.2008, San Francisco, USA

126. Raekers, M.; Taubitz, C.; Küpper, K.; Blundell, S. J.; Prabhakaran, D.; Neumann, M.
Investigation of the electronic structure of $LuFe_2O_4$ by means of XPS, XAS, XES and calculations
72. Jahrestagung der DPG und DPG Frühjahrstagung des Arbeitskreises Festkörperphysik, 25.-29.02.2008, Berlin, Germany

127. Rebohle, L.; Cherkouk, C.; Prucnal, S.; Skorupa, W.; Helm, M.
Si-based light emitters and their use for smart biosensor applications
E-MRS 2008 Spring Meeting, 26.-30.05.2008, Strasbourg, France

128. Rebohle, L.; Cherkouk, C.; Skorupa, W.; Prucnal, S.; Helm, M.
Si-based light emitters as a key element for smart biosensors
Eurosensors XXII, 7.-10.09.2008, Dresden, Germany

129. Rebohle, L.; Lehmann, J.; Kanjilal, A.; Prucnal, S.; Nazarov, A.; Tyagulskii, I.; Skorupa, W.; Helm, M.
The correlation between electroluminescence properties and the microstructure of Eu-implanted MOS light emitting devices
16th International Conference on Ion Beam Modification of Materials, 31.08.-5.09.2008, Dresden, Germany

130. Rebohle, L.; Lehmann, J.; Prucnal, S.; Nazarov, A.; Tyagulskii, I.; Skorupa, W.; Helm, M.; Biskupek, J.; Kaiser, U.
The complex dynamics between the Eu^{2+} and Eu^{3+} electroluminescence of Eu-implanted MOS light emitting devices
E-MRS 2008 Spring Meeting, 26.-30.05.2008, Strasbourg, France

131. Rebohle, L.; Sun, J.; Prucnal, S.; Nazarov, A.; Tyagulskii, I.; Helm, M.; Skorupa, W.
Huge performance increase of Tb-implanted MOS light emitting devices with SiO_xN_y layers moderating hot carrier effects
2008 MRS Fall Meeting, 1.-5.12.2008, Boston, USA

132. Redondo-Cubero, A.; Vinnichenko, M.; Krause, M.; Gago, R.
Structural investigations of ZnO thin films grown by reactive pulsed magnetron sputtering at different substrate temperatures
Charged and neutral particles channeling phenomena (Channeling 2008), 25.10.-1.11.2008, Erice, Italy

133. Rogozin, A.; Vinnichenko, M.; Shevchenko, N.; Kreißig, U.; Kolitsch, A.; Möller, W.
In situ study of the effect of Sn doping on the electrical properties of indium oxide
14th International Conference on Thin Films & Reactive Sputter Deposition 2008, 17.-20.11.2008, Ghent, Belgium

134. Rother, A.; Gemming, S.; Geiger, D.; Spaldin, N.
(Multi-)ferroic domain walls - a combined ab-initio and microscopical investigation
14th European Microscopy Conference (EMC 2008), 31.08.-5.09.2008, Aachen, Germany

135. Rotshtein, V. P.; Markov, A. B.; Shevchenko, N.; Reuther, H.; Oskomov, K. V.; Shulov, V. A.
Surface alloying of Ti–6Al–4V with zirconium by pulsed electron-beam melting of Zr/Ti multilayers
9th International Conference on Modification of Materials with Particle Beams and Plasma Flows, 21.-26.09.2008, Tomsk, Russia

136. Scarlat, C.; Schmidt, H.; Xu, Q.; Vinnichenko, M.; Kolitsch, A.; Helm, M.; Iacomi, F.
Polycrystalline Mn-alloyed indium tin oxide films
72. Jahrestagung der DPG und DPG Frühjahrstagung des Arbeitskreises Festkörperphysik, 25.-29.02.2008, Berlin, Germany

137. Schmidt, B.; Heinig, K.-H.; Beyer, V.; Stegemann, K.-H.
Electroluminescence in silicon nanocrystals fabricated by ion beam mixing and annealing of gate oxide/silicon interfaces
E-MRS Spring Meeting, 26.-30.05.2008, Strasbourg, France

138. Schmidt, B.; Heinig, K.-H.; Mücklich, A.; Akhmadaliev, C.
Shaping of nanospheres into disks and rods with swift heavy ions
Workshop "Ionenstrahlphysik und Nanotechnologie", 11.-12.04.2008, Darmstadt-Wixhausen, Germany

139. Schmidt, B.; Heinig, K.-H.; Mücklich, A.; Akhmadaliev, C.
Swift-heavy-ion-induced shaping of spherical Ge nanoparticles into disks and rods
16th International Conference on Ion Beam Modification of Materials, 31.08.-5.09.2008, Dresden, Germany

140. Schneider, H.; Winnerl, S.; Liu, H. C.; Drachenko, O.; Helm, M.; Walther, M.; Faist, J.
Quadratic detection and autocorrelation measurements with two-photon quantum well infrared photodetectors
9th International Conference on Mid-Infrared Optoelectronics: Materials and Devices (MIOMD-IX), 7.-11.09.2008, Freiburg, Germany

141. Seeger, S.; Grötzschel, R.; Ellmer, K.
Reactive magnetron sputtering of $CuInS_2$ adsorbers for thin film photovoltaic: Relation between deposition parameters and film morphology
23rd European Photovoltaic Solar Energy Conference, 1.-4.09.2008, Feria Valencia, Spain

142. Seidel, W.; Cizmar, E.; Drachenko, O.; Helm, M.; Justus, M.; Lehnert, U.; Michel, P.; Ozerov, M.; Schneider, H.; Schurig, R.; Stehr, D.; Wagner, M.; Winnerl, S.; Wohlfarth, D.; Zvyagin, S.; Kehr, S. C.; Eng, L. M.
Three years of cw-operation at FELBE - Experiences and applications
30th International Free Electron Laser Conference FEL 2008, 24.-29.08.2008, Gyeongju, Korea

143. Shalimov, A.; Potzger, K.; Talut, G.; Geiger, D.; Reuther, H.; Zhou, S.; Bähtz, C.; Misiuk, A.; Fassbender, J.
Fe nanoparticles embedded in MgO crystals
16th International Conference on Ion Beam Modification of Materials, 31.08.-5.09.2008, Dresden, Germany

144. Shevchenko, N.; Kolitsch, A.
Porous metal surfaces produced by ion implantation
9th International Conference on Modification of Materials with Particle Beams and Plasma Flows, 21.-26.09.2008, Tomsk, Russia

145. Shevchenko, N.; Kolitsch, A.
Nanoporous stainless steel surfaces produced by plasma immersion ion implantation
16th International Conference on Ion Beam Modification of Materials, 31.08.-5.09.2008, Dresden, Germany

146. Shevchenko, N.; Rogozin, A.; Vinnichenko, M.; Kolitsch, A.; Möller, W.
Real-time monitoring of ITO film structure during annealing: Effect of film thickness
9th International Conference on Modification of Materials with Particle Beams and Plasma Flows, 21.-26.09.2008, Tomsk, Russia

147. Shevchenko, N.; Rogozin, A.; Vinnichenko, M.; Kolitsch, A.; Möller, W.
The effect of ITO film thickness on the microstructure evolution and crystallization kinetics during annealing
14th International Conference on Thin Films & Reactive Sputter Deposition 2008, 17.-20.11.2008, Ghent, Belgium

148. Skorupa, W.; Rebohle, L.; Prucnal, S.; Kanjilal, A.; Sun, J. M.; Cherkouk, C.; Helm, M.; Nazarov, A.; Behar, M.
Nanocluster in implantierten Lichtemitter-Bauelementen durch ms-Temperung
Workshop Ionenstrahlphysik und Nanotechnologie, 11.-12.04.2008, Darmstadt, Germany

149. Stehr, D.; Wagner, M.; Schneider, H.; Helm, M.; Andrews, A. M.; Roch, T.; Strasser, G.
Intraminiband relaxation in doped GaAs/AlGaAs superlattices studied by two-color infrared pump-probe experiments
29th International Conference on the Physics of Semiconductors, 27.07.-1.08.2008, Rio de Janeiro, Brazil

150. Strache, T.; Fassbender, J.; Grenzer, J.; Möller, W.; Kaltofen, R.; Mönch, I.; Mccord, J.
Magnetic microstructures created by local interface mixing
16th International Conference on Ion Beam Modification of Materials, 31.08.-5.09.2008, Dresden, Germany

151. Strache, T.; Grenzer, J.; Fassbender, J.; Möller, W.; Kaltofen, R.; Mönch, I.
Magnetic microstructures produced by local ion irradiation induced interfacial mixing
72. Jahrestagung der DPG und DPG Frühjahrstagung des Arbeitskreises Festkörperphysik, 25.-29.02.2008, Berlin, Germany

152. Strache, T.; Liedke, M. O.; Fassbender, J.; Möller, W.; Menendez, E.; Sort, J.; Gemming, T.; Weber, A.; Heyderman, Laura J.; Rao, K. V.; Deevi, S. C.; Nogues, J.
Ion irradiation induced local creation of ferromagnetism in Fe60Al40 alloys
72. Jahrestagung der DPG und DPG Frühjahrstagung des Arbeitskreises Festkörperphysik, 25.-29.02.2008, Berlin, Germany

153. Strache, T.; Liedke, M. O.; Fassbender, J.; Möller, W.; Menéndez, E.; Sort, J.; Suriñach, S.; Baró, M. D.; Gemming, T.; Weber, A.; Heyderman, Laura J.; Rao, K. V.; Deevi, S. C.; Nogues, J.
Ion irradiation induced local creation of ferromagnetism in Fe60Al40 alloys
Ionenstrahlphysik und Nanotechnologie, GSI-Workshop, 11.-12.04.2008, Darmstadt, Germany

154. Strache, T.; Tibus, S.; Springer, F.; Rohrmann, H.; Albrecht, M.; Fassbender, J.
Tuning coercivity in CoCrPt-SiO_2 hard disk material
16th International Conference on Ion Beam Modification of Materials, 31.08.-5.09.2008, Dresden, Germany

155. Sürgers, C.; Joshi, N.; Montbrun, R.; von Löhneysen, H.; Potzger, K.; Möller, W.
Modification of magnetic order in Mn_5Si_3 and Mn_5Ge_3 by C ion implantation
72. Jahrestagung der DPG und DPG Frühjahrstagung des Arbeitskreises Festkörperphysik, 25.-29.02.2008, Berlin, Germany

156. Talut, G.; Reuther, H.; Grenzer, J.; Zhou, S.
Origin of ferromagnetism in iron implanted rutile single crystals
International Symposium on the Industrial Applications of the Mössbauer Effect, 17.-22.08.2008, Budapest, Hungary

157. Thieme, M. B.; Gemming, S.
New density functional theory investigations of vanadium silicides
72. Jahrestagung der DPG und DPG Frühjahrstagung des Arbeitskreises Festkörperphysik, 25.-29.02.2008, Berlin, Germany

158. Thieme, M. B.; Gemming, S.; Potzger, K.; Anwand, W.; Grötzschel, R.; Grenzer, J.
The system vanadium:silicon - An ion-beam generated diluted magnetic semiconductor? – A case study
16th International Conference on Ion Beam Modification of Materials, 31.08.-5.09.2008, Dresden, Germany

159. Tyschenko, I. E.; Voelskow, M.; Cherkov, A. G.; Popov, V. P.
Endotaxial growth of InSb nanocrystals at the bonding interface of the In^+ and Sb^+ ion implanted SOI structure
16th International Conference on Ion Beam Modification of Materials, 31.08.-5.09.2008, Dresden, Germany

160. Tyschenko, I. E.; Voelskow, M.; Cherkov, A. G.; Popov, V. P.
Nanometer-thick SGOI structures produced by Ge^+ ion implantation of SiO_2 film and subsequent hydrogen transfer of Si layer
16th International Conference on Ion Beam Modification of Materials, 31.08.-5.09.2008, Dresden, Germany

161. Ueda, M.; Diaz, C.; Lepienski, C. M.; Reuther, H.
Nitrogen PIII in SS304 stainless steel using different temperature time-histories
16th International Conference on Ion Beam Modification of Materials, 31.08.-5.09.2008, Dresden, Germany

162. Villas-Boas Grimm, C.; Pfau, C.; Ohser, S.; Winnerl, S.; Schneider, H.; Helm, M.; Biermann, K.; Künzel, H.
Intersubband relaxation and dephasing in narrow InGaAs/AlAsSb quantum well structures
29th International Conference on the Physics of Semiconductors, 27.07.-1.08.2008, Rio de Janeiro, Brazil

163. Vinnichenko, M.; Gago, R.; Rogozin, A.; Shevchenko, N.; Cornelius, S.; Jimenez, I.; Kolitsch, A.; Möller, W.
Effect of substrate temperature on Al-doping of ZnO films
E-MRS 2008 Spring Meeting, 26.-30.05.08, Strasbourg, France

164. Vinnichenko, M.; Rogozin, A.; Cornelius, S.; Shevchenko, N.; Gago, R.; Jimenez, I.; Kolitsch, A.; Möller, W.
Effect of elevated temperature on electrical properties and structure of ZnO:Al films with different dopant concentrations
2nd International Symposium on Transparent Conductive Oxides, 22.-26.10.2008, Hersonissos, Crete, Greece

165. Vinnichenko, M.; Rogozin, A.; Kolitsch, A.; Grambole, D.; Möller, W.; Stenzel, O.; Wilbrandt, S.; Chuvilin, A.; Kaiser, U.
Optimierung optischer und mechnischer Eigenschaften magnetrongesputterter Niobpentoxidschichten
OptoNet Workshop: Funktionale Oberflächen für optische Anwendungen, 12.11.2008, Jena, Germany

166. Vinnichenko, M.; Rogozin, A.; Shevchenko, N.; Kolitsch, A.; Möller, W.
Effect of isothermal annealing on electrical and optical properties of Al-doped ZnO films
72. Jahrestagung der DPG und DPG Frühjahrstagung des Arbeitskreises Festkörperphysik, 25.-29.02.2008, Berlin, Germany

167. Voelskow, M.; Pécz, B.; Stoemenos, J.; Skorupa, W.
Epitaxial 3C-SiC nanocrystal formation at the SiO_2/Si interface after carbon implantation and annealing in CO atmosphere
16th International Conference on ion Beam Modification of Materials, 31.08.-5.09.2008, Dresden, Germany

168. Voelskow, M.; Pezoldt, J.; Kups, T.; Skorupa, W.
Controlled localised melting in silicon by high dose germanium implantation and flash lamp annealing
16th International Conference on Ion Beam Modification of Materials, 31.08.-5.09.2008, Dresden, Germany

169. Wagner, M.; Schneider, H.; Helm, M.; Schartner, S.; Andrews, A. M.; Roch, T.; Strasser, G.
THz sideband generation in multi quantum wells
GDRE-THz Workshop 2008 Paris, 25.-26.09.08, Paris, France

170. Wagner, M.; Schneider, H.; Helm, M.; Schartner, S.; Andrews, A. M.; Roch, T.; Strasser, G.
THz sideband generation in multi quantum wells
EOS Annual Meeting 2008, 29.09.-2.10.2008, Paris, France

171. Wagner, M.; Schneider, H.; Helm, M.; Schartner, S.; Andrews, A. M.; Roch, T.; Strasser, G.
THz sideband generation in multi quantum wells
Nonna 2008 - Workshop on Nonequilibrium Nanostructures, 1.-6.12.2008, Dresden, Germany

172. Wagner, M.; Stehr, D.; Schneider, H.; Winnerl, S.; Helm, M.; Andrews, M.; Roch, T.; Strasser, G.
Two-color pump-probe spectroscopy of electron dynamics in superlattices
72. Jahrestagung der DPG und DPG Frühjahrstagung des Arbeitskreises Festkörperphysik, 25.-29.02.2008, Berlin, Germany

173. Wang, C. Y.; Kuznetsova, L.; Diehl, L.; Kärtner, F.; Belkin, M.; Schneider, H.; Liu, H. C.; Capasso, F.
Stable mode-locked pulses from mid-infrared quantum cascade lasers
Conference on Lasers and Electro-Optics, Quantum Electronics and Laser Science Conference, 4.-9.05.2008, San Jose, USA

174. Weißbach, T.; Führlich, T.; Wunderlich, F.; Leisegang, T.; Dshemuchadse, J.; Rother, A.; Souptel, D.; Behr, G.; Chaplygin, I.; Seifert, G.; Gemming, S.; Meyer, D. C.
Site-specific substitution of Fe in $YMn_{2-x}Fe_xO_5$: X-ray investigations and DFT
16th International Conference on Solid Compounds of Transition Elements (SCTE2008), 26.-31.07.2008, Dresden, Germany

175. Weißbach, T.; Souptel, D.; Behr, G.; Führlich, T.; Wunderlich, F.; Meyer, D. C.; Gemming, S.
Evolution of the crystal structure of $YMn_{2-x}Fe_xO_5$ due to iron doping and DFT calculations for the x = 1 compound
72. Jahrestagung der DPG und DPG Frühjahrstagung des Arbeitskreises Festkörperphysik, 25.-29.02.2008, Berlin, Germany

176. Weißbach, T.; Wunderlich, F.; Führlich, T.; Dshemuchadse, J.; Souptel, D.; Behr, G.; Gemming, S.; Meyer, D. C.
Evolution of the crystal structure of $YMn_{2-x}Fe_xO_5$ due to substitution of iron for manganese
16th Jahrestagung der Deutschen Gesellschaft für Kristallographie, 3.-6.03.2008, Erlangen, Germany

177. Westhäuser, W.; Mangler, T.; Fischer, T.; Gemming, S.; Seifert, G.; Ganteför, G.
W_nS_m-clusters: Possible building blocks for new nanomaterials?
72. Jahrestagung der DPG und DPG Frühjahrstagung des Arbeitskreises Festkörperphysik, 25.-29.02.2008, Berlin, Germany

178. Winnerl, S.; Zimmermann, B.; Peter, F.; Schneider, H.; Helm, M.
Terahertz vector beams
33rd International Conference on Infrared, Millimeter, and Terahertz Waves, 14.-19.09.2008, Pasadena, USA

179. Wintz, S.; Küpper, K.; Buess, M.; Raabe, J.; Quitman, C.; Fassbender, J.
The influence of non centric holes on the magnetization dynamics of landau structures
72. Jahrestagung der DPG und DPG Frühjahrstagung des Arbeitskreises Festkörperphysik, 25.-29.02.2008, Berlin, Germany

180. Wündisch, C.; Posselt, M.; Anwand, W.; Schmidt, B.; Grötzschel, R.; Mücklich, A.; Skorupa, W.; Simoen, E.; Clarysse, T.; Satta, A.; Hortenbach, H.; Möller, A.; Pelzing, P.

n^+ doping of Ge by P or As implantation and flash-lamp annealing
E-MRS 2008 Spring Meeting, 26.-30.05.2008, Strasbourg, France

181. Wündisch, C.; Posselt, M.; Anwand, W.; Schmidt, B.; Grötzschel, R.; Mücklich, A.; Skorupa, W.; Simoen, E.; Clarysse, T.; Satta, A.; Hortenbach, H.; Möller, A.; Pelzing, P.
n^+ doping of Ge by P or As implantation and flash-lamp annealing
16th International Conference on Ion Beam Modification of Materials, 31.08.-5.09.2008, Dresden, Germany

182. Wündisch, C.; Posselt, M.; Anwand, W.; Schmidt, B.; Mücklich, A.; Skorupa, W.; Clarysse, T.; Simoen, E.
RTA and FLA of ultra-shallow implanted layers in Ge
16th IEEE International Conference on Advanced Thermal Processing of Semiconductors (IEEE RTP 2008), 30.09.-3.10.2008, Las Vegas, NV, USA

183. Xu, Q.; Hartmann, L.; Schmidt, H.; Hochmuth, H.; Lorenz, M.; Spemann, D.; Grundmann, M.
Magnetoresistance in n-type conducting Co-doped ZnO
72. Jahrestagung der DPG und DPG Frühjahrstagung des Arbeitskreises Festkörperphysik, 25.-29.02.2008, Berlin, Germany

184. Xu, Q.; Schmidt, H.; Zhou, S.; Potzger, K.; Helm, M.; Hochmuth, H.; Lorenz, M.; Meinecke, C.; Grundmann, M.
Magnetic properties of amorphous, p-type conducting $CuCr_{0.95}Mg_{0.05}O_2$ and $CuCr_{0.93}Mg_{0.05}Mn_{0.02}O_2$
72. Jahrestagung der DPG und DPG Frühjahrstagung des Arbeitskreises Festkörperphysik, 25.-29.02.2008, Berlin, Germany

185. Yankov, R. A.; Kolitsch, A.; Munnik, F.; Donchev, A.; Schütze, M.
Plasma immersion ion implantation of fluorine for oxidation-resistant TiAl alloys
16th International Conference on Ion Beam Modification of Materials, 31.08.-5.09.2008, Dresden, Germany

186. Yankov, R. A.; Kolitsch, A.; Munnik, F.; Donchev, A.; Schütze, M.
Ion implantation of fluorine: Towards high-temperature oxidation-resistant TiAl alloys
2008 MRS Fall Meeting, 1.-5.12.2008, Boston, USA

187. Zhou, S.; Bürger, D.; Beyer, V.; Schmidt, B.; Helm, M.; Schmidt, H.
Defect formation in Mn-implanted silicon probed by frequency and temperature dependent capacitance measurements on MOS capacitors
16th International Conference on Ion Beam Modification of Materials, 31.08.-5.09.08, Dresden, Germany

188. Zhou, S.; Potzger, K.; Küpper, K.; Xu, Q.; Schmidt, H.; Helm, M.; Fassbender, J.
Synthesis of inverted spinel ferrite nanocrystals inside ZnO by ion implantation and post-annealing
16th International Conference on Ion Beam Modification of Materials, 31.08.-5.09.2008, Dresden, Germany

189. Zhou, J.; Facsko, S.; Keller, A.; Möller, W.
Nanopatterning of semiconductor surfaces by sputtering from an inductively coupled plasma
Workshop Complex Nanostructures, 6.-7.10.2008, Dresden, Germany

190. Zhou, S.; Potzger, K.; Talut, G.; Borany, J. von; Skorupa, W.; Helm, M.; Fassbender, J.
Using X-ray diffraction to identify precipitates in transition metal doped semiconductors
72. Jahrestagung der DPG und DPG Frühjahrstagung des Arbeitskreises Festkörperphysik, 25.-29.02.2008, Berlin, Germany

191. Zier, M.; Schmidt, B.
Fabrication of ultra-shallow p-n junctions in Si using fast and ultra-fast annealing
16th International Conference on Ion Beam Modification of Materials 2008, 31.08.-5.09.2008, Dresden, Germany

192. Zschornak, M.; Leisegang, T.; Gutmann, E.; Stöcker, H.; Meyer, D. C.
Anisotropic anomalous scattering in rutile TiO_2
16. Jahrestagung der Deutschen Gesellschaft für Kristallographie, 3.-6.03.2008, Erlangen, Germany

193. Zschornak, M.; Leisegang, T.; Stöcker, H.; Weißbach, T.; Gemming, S.; Meyer, D. C.
Site-selective determination of coordination symmetries by anisotropic anomalous X-ray scattering
XXI Congress and General Assembly of the International Union of Crystallography, 23.-31.08.2008, Osaka, Japan

Lectures / Talks

1. Abrasonis, G.
Surface diffusion assisted phase separation during the growth of carbon:transition metal thin films
Seminar, Australian Synchrotron, 28.11.2008, Melbourne, Victoria, Australia

2. Bischoff, L.
Focused ion beam activities at FZD
Seminar, Ruhr-Universität Bochum, 14.11.2008, Bochum, Germany

3. Bischoff, L.
Application of focused ion beams
Materials Science Seminar at FZD, 28.10.2008, Dresden, Germany

4. Bischoff, L.
Nanoschreiben mit fokussierten Ionen
Lange Nacht der Wissenschaften Dresden, 4.07.2008, Dresden, Germany

5. Bischoff, L.; Akhmadaliev, Ch.; Pilz, W.; Schmidt, B.
Application of mass-separated focused ion beams
Seminar at Carl Zeiss NTS, 7.05.2008, Oberkochen, Germany

6. Borany, J. von
Aktivitäten des FZD für die (Dünnschicht) Photovoltaik
EFDS Fachausschuss "Großflächenbeschichtung für solar- und lichttechnische Anwendungen", 10.07.2008, Dresden, Germany

7. Brauer, G.
Activities towards p-type doping of ZnO
Seminar, Physics Department, University of Hong Kong, 26.11.2008, Hong Kong, China

8. Fassbender, J.
Ions hit magnetism - new challenges for the design of artificial nanostructures
Colloquium, Department of Physics, University of Glasgow, 6.05.2008, Glasgow, United Kingdom

9. Fassbender, J.
Prospects and applications of nanofunctional magnetic elements
Seminar, KIST Europe, 29.05.2008, Saarbrücken, Germany

10. Fassbender, J.
Nanomagnets - created and tailored by ions
Kolloquium „Physik von Nanostrukturen“, 19.12.2008, Dresden, Germany

11. Fassbender, J.; Liedke, M. O.; Strache, T.; Marko, D.; Lenz, K.; Keller, A.; Facsko, S.; Tibus, S.; Springer, F.; Albrecht, M.; Rohrmann, H.
Periodically modulated surfaces and interfaces: Introducing artificial length scales to tailor magnetic properties
Seminar, Institut für Physik, TU Ilmenau, 30.10.2008, Ilmenau, Germany

12. *Seminar, National Institute of Standards and Technology, 3.11.2008, Boulder, USA*

13. Gemming, S.
Modelling in materials science
Materials Science Seminar at FZD, 31.01.2008, Dresden, Germany

14. Heinig, K.-H.
Old physics for modern manotechnologies - Studies of nano-scale ordering by simulations and experiments
Fizikai és Anyagtudományi Kutatóintézet Tanácstermében, 21.05.2008, Budapest, Hungary

15. Helm, M.
Pump-probe studies of electron dynamics in quantum wells and superlattices
Seminar, Institute of Industrial Science, Tokyo University, 27.02.2008, Tokyo, Japan

16. *Seminar, Research Institute of Electrical Communication (RIEC), Tohoku University, 14.03.2008, Sendai, Japan*

17. Helm, M.
The development of intersubband semiconductor light sources: From MOSFETs to quantum cascade lasers
Seminar, Institute for Laser Engineering, Osaka University, 17.03.2008, Osaka, Japan

18. Helm, M.
Time resolved and nonlinear spectroscopy of semiconductor quantum structures using an infrared free-electron laser
Seminar, Universität Marburg, 7.11.2008, Marburg, Germany

19. Helm, M.
THz physics at the Research Center Dresden-Rossendorf: From scalable antennas to free-electron laser based near-field microscopy
Seminar, Institute for Laser Engineering, Osaka University, 5.03.2008, Osaka, Japan

20. Keller, A.; Facsko, S.; Möller, W.
Self-organized nanopatterns by ion erosion
Seminar, Interdisciplinary Nanoscience Center (iNANO), University of Aarhus, 18.11.2008, Aarhus, Denmark

21. Keller, A.; Facsko, S.; Möller, W.
Ion-induced nanopatterns on silicon: Experiment, theory, and application
Seminar, Universidad Carlos III de Madrid, 15.02.2008, Madrid, Spain

22. *Seminar, Centro de Micro-Análisis de Materiales, Universidad Autónoma de Madrid, 27.02.2008, Madrid, Spain*

23. Liedke, B.; Heinig., K.-H.; Facsko, S.; Möller, W.
Ion bombardment of solids - unified simulation of damage formation and thermally activated relaxation
Seminar at MFA, KFKI Budapest, 11.11.2008, Budapest, Hungary

24. Möller, W.
Nanostructures by ion-driven self-organisation
Kolloquium, Max-Planck-Institutes für Plasmaphysik, 18.04.2008, Garching/ München, Germany

25. Möller, W.
Nanostructures by ion-driven self-organisation: Can ions induce order?
VERA-Seminar, 5.06.2008, Vienna, Austria

26. Morawetz, K.
Nonlocal kinetic theory
Colloquium, University College Dublin, 14.08.2008, Dublin, Ireland

27. Morawetz, K.
Quantum kinetic theory beyond quasiparticle picture - Bernoulli potential in superconductors
International Center for Condensed Matter Physics, 29.09.2008, Brasilia, Brazil

28. *Interviewtalk for Professorship, 16.11.2008, Loughborogh, United Kingdom*

29. Morawetz, K.
Transport in OFETs by surface Green functions
Seminar, Technische Universität Chemnitz, 17.12.2008, Chemnitz, Germany

30. Posselt, M.; Wündisch, C.; Schmidt, B.; Anwand, W.; Grötzschel, R.; Mücklich, A.; Skorupa, W.; Hortenbach, H.; Gennaro, S.; Bersani, M.; Guibertoni, D.; Möller, A.; Pelzing, P.; Clarysse, T.; Simoen, E.; Satta, A.; Bracht, H.
n^+ doping of Ge by P implantation and subsequent RTA or FLA
Seminar, IMEC Leuven, 7.02.2008, Leuven, Belgium

31. Schmidt, B.
PRONANO – technology for the production of massively parallel intelligent cantilever-probe platforms for nanoscale analysis and synthesis
European Project Seminar, TU Dresden, Institut für Angewandte Photophysik, 3.07.2008, Dresden, Germany

32. Schmidt, H.
Semiconductor-based spintronics
FZD Lecture, 5.05.2008, Dresden, Germany

33. Schneider, H.
Quantum well infrared photodetector array development and applications
Seminar, Shanghai Institute of Technical Physics, Chinese Academy of Science, 24.03.2008, Shanghai, China

34. *Seminar, Suzhou Institute of Nano-tech and Nano-bionics, Chinese Academy of Science, 27.03.2008, Suzhou, China*

35. *Seminar, Institute of Semiconductors, Chinese Academy of Science, 2.04.2008, Beijing, China*

36. Schneider, H.
Time-resolved semiconductor spectroscopy in the mid-infrared and Terahertz regimes
Seminar, Bhabha Atomic Research Centre, Mumbai, India, 7.08.2008, Mumbai, India

37. Schneider, H.
Ultrafast infrared and THz spectroscopy of semiconductor quantum structures
Seminar, IIN-IFW Dresden, 12.12.2008, Dresden, Germany

38. Skorupa, W.
Short time thermal processing: From electronics via photonics to pipe organs of the 17th century
Materials Science Seminar at FZD, 12.03.2008, Dresden, Germany

39. *Mattson International Technology Seminar, 7.05.2008, Ulm, Germany*

40. *23. Nutzertreffen Kurzzeittemperung, 8.05.2008, Erlangen, Germany*

41. Skorupa, W.
Short time thermal processing of materials -Beyond electronics and photonics to pipe organ materials
Seminar, Walter-Schottky-Institute, TU München, 12.02.2008, Garching, Germany

42. Skorupa, W.
Diffusion suppression etc. during electrical activation in implanted Ge and Si-SOI
24. Nutzertreffen Kurzzeittemperung, 23.10.2008, Dortmund, Germany

43. Skorupa, W.
A short review on flash lamp annealing
Industrie-Projekttreffen mit BASF und Zentrum für Sonnenenergie-& Wasserstoff-Forschung Baden-Württemberg (ZSW), 18.11.2008, Stuttgart, Germany

44. Skorupa, W.
Sächsische Forschung im Herzen Europas: Zu Ursprüngen und Befindlichkeiten
Treffen des Bundesausschusses der FDP zu Fragen der Technologie, 5.07.2008, Dresden, Germany

45. Strache, T.; Liedke, M. O.; Fassbender, J.; Möller, W.; Menéndez, E.; Sort, J.; Suriñach, S.; Baró, M. D.; Gemming, T.; Weber, A.; Heyderman, Laura J.; Rao, K. V.; Deevi, S. C.; Nogues, J.
Ion irradiation induced local creation of ferromagnetism in Fe60Al40 alloys
GSI-Workshop" Ionenstrahlphysik und Nanotechnologie",11.-12.04.2008, Darmstadt, Germany

46. Zier, M.
Ultra-shallow p-n junctions fabrication by ion beam processing
Materials Science Seminar at FZD, 29.04.2008, Dresden, Germany

PhD Theses

1. Dreyhaupt, A.
Terahertz-Strahlung auf der Basis beschleunigter Ladungsträger in GaAs
TU Dresden, 29.04.2008, Wissenschaftlich-Technische Berichte FZD-498, 2008

2. Martins, R. M. S.
In-situ X-ray diffraction studies during growth of Ni-Ti shape memory alloy films and their complementary ex-situ characterization
Universidade Nova de Lisboa, Portugal, 17.10.2008

3. Zhou, S.
Transition metal implanted ZnO: A correlation between structure and magnetism
TU Dresden, 22.04.2008

Master & Diploma Theses

1. Bollmann, A.
Gepulste Terahertzspektroskopie in Transmission und Reflexion
Fachhochschule Jena, 18.07.2008

2. Bürger, D.
Untersuchung der elektrischen, magnetischen und strukturellenEigenschaften von Mn-implantiertem Galliumarsenid nach unterschiedlichen Ausheilmethoden
TU Dresden, 31.10.2008

3. Cornelius, S.
Einfluss der Substrattemperatur und des Sauerstoffpartialdruckes auf die elektrischen Eigenschaften von PVD-ZnO:Al-Schichten.
TU Dresden, 30.11.2008

4. Fritsche, M.
Untersuchungen zum Wachstum dünner Metallschichten auf gestuften Halbleiter-Oberflächen mit Hilfe der Rastertunnel-Mikroskopie
TU Dresden, 26.09.2008

5. Gabriel, A.
Atomistic simulation of solid-phase epitaxial regrowth of amorphous germanium
TU Dresden, 20.05.2008

6. Kallauch, O.
Development of a compact fiber based THz - spectrometer for applications in pulsed magnetic fields
TU Dresden, 30.11.2008

7. Körner, M.
Magnetische Nanoschichten auf durch Ionenerosion modulierten Substraten
HTW Dresden, 30.11.2008

8. Mok, K. M.
Optical investigation of NiO thin films on sapphire and ZnO substrates
Universität Leipzig, 30.10.2008

9. Nitsche, S.
Bildgebendes Verfahren zur Terahertzspektroskopie
HTW Dresden, 25.09.2008

10. Pfau, C.
Dephasierung und Intersubbandrelaxation in InGaAs/AlAsSb-Halbleiter-Quantenstrukturen
TU Dresden, 15.12.2008

11. Schreiber, S.
Cs-Inventar in Si unter Sputter-Bedingungen
TU Dresden, 31.10.2008

12. Zimmermann, B.
Photoleitende Terahertzemitter und -detektoren für kompakteTerahertzübertragungssysteme
TU Dresden, 31.10.2008

Organization of Conferences

1. Möller, W., Rauschenbach, B.
16th International Conference on Ion Beam Modification of Materials (IBMM-2008)
31.08.-5.09.2008, Dresden, Germany

Laboratory Visits

1. Abrasonis, G.
Lawrence Berkeley National Lab, Berkeley, USA; 27.03.-1.04.2008
ESRF Grenoble, France; 21.-27.04.2008

2. Berndt, M.
ESRF Grenoble, France; 21.-27.04.2008

3. Bischoff, L.
Ruhr-Universität Bochum, Germany; 12.-15.11.2008

4. Borany, J. von
ESRF Grenoble, France; 4.-17.02., 28.04.-3.05., 26.11.-3.12.2008
Lisbon University, Portugal; 16.-21.10.2008

5. Brauer, G.
City University of Hongkong, China; 20.-23.04.2008
Charles University Prague, Czech Republic; 4.-13.06.2008

6. Bürger, D.
ESRF Grenoble, France; 2.-6.05.2008

7. Cantelli, V.
ESRF Grenoble, France; 28.04.-3.05.2008
HMI Berlin, Germany; 7.-10.08.2008

8. Drachenko, O.
Kurchatov Institut Moskau/Institute for Microstructures Nishni Novgorod, Russia; 19.-26.04.2008
LNCMP Toulouse, France; 6.-18.05., 12.-21.07., 12.-17.09., 2.-22.11.2008

9. Fassbender, J.
Lawrence Berkeley National Lab, Berkeley, USA; 1.-12.11.2008
Barcelona University, Spain; 25.-27.11.2008

10. Grenzer, J.
ESRF Grenoble, France; 2.-8.05., 1.-15.07., 30.09.-7.10., 3.-5.12.2008

11. Hanisch, A.
ESRF Grenoble, France; 13.-19.02., 30.09.-7.10.2008

12. Heinig, K.-H.
KFKI Budapest, Hungary; 19.-22.05., 17.-20.08.2008

13. Helm, M.
Osaka University, Japan; 16.02.-19.03.2008

14. Kallauch, O.
Universität Konstanz, Germany; 8.-13.09.2008

15. Kanjilal, A.
ESRF Grenoble, France; 27.-31.08.2008

16. Keller, A.
ESRF Grenoble, France; 25.-27.05.2008
Aarhus University, Denmark; 17.-19.11.2008

17. Kolitsch, A.
Bratislava University, Slovakia; 18.-20.05., 9.-11.11.2008

18. Kovacs, G.
ESRF Grenoble, France; 21.-27.04.2008

19. Küpper, K.
Lawrence Berkeley National Lab, Berkeley, USA; 26.3.-9.04.2008
Swiss Light Source, PSI Villigen, Switzerland; 16.-19.04.2008

20. Liedke, B.
KFKI Budapest, Hungary; 29.07.-20.08., 2.-19.11.2008

21. Marko, D.
Lawrence Berkeley National Lab, Berkeley, USA; 26.03.-2.04., 18.-22.07.2008

22. Merchel, S.
Newcastle University, United Kingdom; 15.-22.11.2008

23. Martinavicius, A.
ESRF Grenoble, France; 21.-27.04.2008

24. Morawetz, K.
ICCMP Brasilia, Brazil; 7.-27.09., 30.10.-19.11.2008

25. Numazawa, S.
KFKI Budapest, Hungary; 2.-19.11.2008

26. Pilz, W.
Ruhr-Universität Bochum, Germany; 12.-15.11.2008

27. Rogozin, A.
ESRF Grenoble, France; 27.10.-4.11.2008

28. Reichel, A.
Swiss Light Source, PSI Villigen, Switzerland; 26.11.-3.12.2008

29. Schneider, H.
Tata-Institute, Mumbai, India; 25.07.-10.08.2008
Universität Freiburg, Germany; 12.-17.05., 20.-22.07.2008

Shanghai Institute of Technical Physics, Suzhou Institute of Nano-tech, Institute of Semiconductors, Beijing, China; 29.03.-6.04.2008

30. Shalimov, A.
ESRF Grenoble, France; 20.-24.06., 27.-31.08.2008

31. Shevchenko, N.
Tomsk University, Russia; 15.-18.07., 11.-26.09.2008
ESRF Grenoble, France; 27.10.-4.11.2008

32. Strache, T.
Swiss Light Source, PSI Villigen, Switzerland; 7.-15.07., 26.11.-3.12.2008

33. Strauch, U.
Fa. Eifeler, Düsseldorf, Germany; 10.-14.11.2008

34. Talut, G.
ESRF Grenoble, France; 2.-6.05., 20.-24.06., 8.-15.07.2008

35. Vinnichenko, M.
BESSY Berlin, Germany; 28.10.-2.11.2008

36. Weise, A.
Fa. Vectors Accelerated, San Jose, USA; 20.-27.06.2008

37. Winkler, G.
Fa. Vectors Accelerated, San Jose, USA; 20.-27.06.2008

38. Wintz, S.
Swiss Light Source, PSI Villigen, Switzerland; 23.-29.04., 13.-19.06., 7.-15.07., 26.11.-3.12.2008
Lawrence Berkeley National Laboratory, Berkeley, USA; 25.07.-2.08., 2.-15.11.2008

39. Zhou, S.
ESRF Grenoble, France; 27.-31.08.2008

40. Zschintzsch, M.
ESRF Grenoble, France; 4.-17.02., 15.-22.07., 26.11.-3.12.2008

41. Zschornak, M.
DESY Hamburg, Germany; 5.-11.10., 9.-17.11.2008

Guests

1. Aharonovich, I.
University of Melbourne, Australia; 15.-18.01.2008

2. Behar, M.
Universidade Federal do Rio Grande do Sul, Brazil; 5.-23.05.2008

3. Bocan, J.
Nuclear Physics Institute Prague, Czech Republic; 28.04.-5.05.2008

4. Chalykh, Y.
University of Lipetsk, Russia; 31.01.-18.02.2008

5. Dev, B.
Indian Association for the Cultivation of Science, Jadavpur, Kolkata, India; 8.-12.09.2008

6. Diebold, U.
Tulane University New Orleans, USA; 2.-20.06.2008

7. Dzenisevich, S.
Grodno State University, Belarus; 9.06.-31.08.2008

8. Geza, O.
KEKI Budapest, Hungary; 2.-11.06., 5.-19.10., 30.11.-11.12.2008

9. Ghosh, S.
Indian Institute of Technology New Delhi, India; 14.-18.07.2008

10. Khan, S. A.
Inter-University Accelerator Center New Delhi, India; 14.02.-30.04.2008

11. Kono, J.
Rice University Houston, Texas, USA; 28.09.-13.10.2008

12. Kropman, D.
University of Technology Tallin, Estonia; 7.04.-9.05.2008

13. Som, T.
Institute of Physics Sachivalaya Marg Orisa, India; 13.06.-19.09.2008

14. Kuriplach, J.
Charles University Prague, Czech Republic; 13.-27.11.2008

15. Liu, H. C.
Institute for Microstructural Science Montreal, Canada; 9.-18.07.2008

16. Mahieu, S.
University of Ghent, Belgium; 4.02.-16.03.2008

17. Markov, A.
Russian Academy of Science Tomsk, Russia; 8.10.-8.12.2008

18. Mazarov, P.
Ruhr-Universität Bochum, Germany; 19.05.-16.07., 9.-12.09.2008

19. Melikhova, O.
Charles University Prague, Czech Republic; 21.05.-6.06., 3.-17.07.2008

20. Menendez Dalmau, E.
Universidade Autonoma de Barcelona, Spain; 31.01.-19.02., 10.03.-10.05.2008

21. Merritt, T.
Virginia Tech, USA; 7.-12.12.2008

22. Minniti, M.
University Calabria, Italy; 1.01.-23.12.2008

23. Mukherjee, S.
Institute for Plasma Research Gandhinagar, India; 30.08.-15.09.2008

24. Nazarov, A.
Ukrainian Academy of Science, Ukraine; 23.08.-11.09.2008

25. Oates, T.
University of Sydney, Australia; 28.07.-8.08.2008

26. Pandey, M.
Bhabha Atomic Research Center Mumbai, India; 5.05.-28.07.2008

27. Prucnal, S.
University Maria Sklodowska-Curie Lublin, Poland; 7.04.-9.05., 1.-31.10.2008

28. Rice, B.
Rice University Houston, Texas, USA; 28.09.-13.10.2008

29. Savchenko, E.
National Academy of Science Kharkov, Ukraine; 5.-20.09.2008

30. Shoshan, N.
Technion - Israel Institute of Technology, Haifa, Israel; 3.11.2008 – 4.02.2009

31. Ster, A.
Research Institute for Technical Physics and Materials Science Budapest, Hungary; 14.-18.04.2008

32. Stolterfoht, N.
University of Florida, USA; 18.09.-2.10.2008

33. Süle, P.
MFA Budapest, Hungary; 1.-4.06., 5.-19.10.2008

34. Tripathi, J. K.
Institute of Physics Sachivalaya Marg Orisa, India; 13.06.-19.09.2008

35. Tyagulskyy, I.
Academy of Science, Ukraine; 15.05.-16.07.2008

36. Tyagulskiy, S.
Ukrainian Academy of Science, Ukraine; 19.05.-16.07., 29.09.-10.12.2008

37. Virsek, M.
Jozef Stefan Institute Ljubljana, Slovenia; 1.-30.04.2008

AIM Visitors

1. Abdel-Al, S.
IEMT Warsaw, Poland; 30.03.-5.04.2008

2. Adam, J. P.
Uni Paris-Sud, France; 24.-25.01.2008

3. Arabal, R. G.
Spanish Research Council Madrid, Spain; 25.-30.05.2008

4. Barlak, M.
Soltan Institute for Nuclear Studies, Otwock, Poland; 8.-11.12.2008

5. Caciolli, A.
INFN Padua, Italy; 27.07.-9.08.2008

6. Carbajal Galan, L.
CIEMT Madrid, Spain; 9.-13.06.2008

7. Dubois, P.
ETH Lausanne, Switzerland; 16.-18.04.2008

8. Fülöp, Z.
ATOMKI Debrecen, Hungary; 7.-11.07.2008

9. Gago, R.
University Madrid, Spain; 2.-5.11.2008

10. Gonzales Arrabal, R.
CSIC Madrid, Spain; 23.11.-4.12.2008

11. Gyürky, G.
ATOMKI Debrecen, Hungary; 20.-27.07.2008

12. Hernandez Mayoral, M.
CIEMAT Madrid, Spain; 9.-13.06.2008

13. Jeynes, C.
Uni Surrey, United Kingdom; 11.-12.02.2008

14. Jozwik, I.
IEMT Warsaw, Poland; 23.-28.11.2008

15. Korman, A.
IEMT Warsaw, Poland; 30.03.-5.04.2008

16. Krickl, R.
University Vienna, Austria; 30.11.-3.12.2008

17. Lorenz, K.
Instituto Tecnologico e Nuclear Sacavem, Portugal; 8.-13.09.2008

18. Mackova, A.
UJF Rez, Czech Republic; 10.-12.06.2008

19. Meissl, W.
TU Vienna, Austria; 4.-23.02., 18.04.-1.05., 8.-12.07.2008

20. Memegazzo, R.
INFN Padua, Italy; 18.-23.08.2008

21. Menyhard, M.
KFKI Budapest, Hungary; 14.-18.12.2008

22. Nasdala, L.
University Vienna, Austria; 18.-20.08.2008

23. Naydenova, T.
Institute of Electronics Sofia, Bulgaria; 10.-23.08.2008

24. Nikolov, V.
National Institute of Archeology Sofia, Bulgaria; 14.-20.04.2008

25. Pagowska, K.
IEMT Warsaw, Poland; 10.-16.02.2008

26. Palmero, A.
University Sevilla, Spain; 28.01.-8.02.2008

27. Pecz, B.
KFKI Budapest, Hungary; 24.-27.02.2008

28. Ratajczak, R.
IEMT Warsaw, Poland; 10.-16.02., 4.-5.05.2008

29. Romaniec, M.
IEMT Warsaw, Poland; 13.-19.07.2008

30. Romero, P.
University Sevilla, Spain; 28.01.-8.02.2008

31. Roschel, N.
University Vienna, Austria; 18.-22.08.2008

32. Sartowska, N.
Soltan Institute for Nuclear Studies, Otwock, Poland; 8.-11.12.2008

33. Stoemenos, I.
University Thessaloniki, Greece; 24.-27.02.2008

34. Stonert, A.
IEMT Warsaw, Poland; 30.03.-5.04., 13.-19.07., 23.-28.11.2008

35. Stoyanova, P.
Sofia University, Bulgaria; 14.-20.04.2008

36. Szücs, T.
ATOMKI Debrecen, Hungary; 3.-16.08.2008

37. Tsvetkova, T.
Bulgarian Academy of Sciences Sofia, Bulgaria; 19.-28.04.2008

38. Turos, A.
IEMT Warsaw, Poland; 10.-16.02., 4.-10.05.2008

39. Webb, M.
University Surrey, United Kingdom; 11.-16.02.2008

40. Winkelehner, D.
TU Vienna, Austria; 4.-21.02., 18.04.-1.05.2008

IA-SFS Visitors

1. Aleksa, V.
Vilnius University, Lithuania; 16.-24.04.2008

2. Austin, D.
University of Sheffield, United Kingdom; 10.-14.06.2008

3. Bukys, J.
Vilnius University, Lithuania; 5.-9.05., 13.-17.07., 17.-22.08.2008

4. Porter, N.
University of Sheffield, United Kingdom; 15.-19.09.2008

5. Sablinskas, V.
Vilnius University, Lithuania; 16.-24.04., 5.-9.05., 13.-17.07., 17.-22.08.2008

6. Strazdaite, S.
Vilnius University, Lithuania; 13.-17.04., 17.-22.08.2008

7. Wilson, L.
University of Sheffield, United Kingdom; 17.-20.06., 15.-19.09.2008

8. Zibik, E.
University of Sheffield, United Kingdom; 17.-20.06.2008

ROBL-MRH Visitors

1. Barbatti, C.
Max-Plack-Institut für Eisenforschung, Düsseldorf, Germany; 18.-26.03.2008

2. Braz-Fernandez, F. M.
CENIMAT, Materials Science Department, Caparaica, Portugal; 6.-12.02.2008

3. Beckers, M.
Thin Films Group, Linköping University, Sweden; 11.-18.03., 18.-26.11.2008

4. Cardinali, D.
Max-Plack-Institut für Eisenforschung, Düsseldorf, Germany; 18.-26.03.2008

5. Erikson, F.
Thin Films Group, Linköping University, Sweden; 11.-18.03.2008

6. Eisenschmidt, C.
Fachgruppe Festkörperanalytik, Universät Halle-Wittenberg, Germany; 4.-9.09.2008

7. Esconjauregui, C. S.
Department of Engineering, University Cambridge, United Kingdom; 20.-28.10.2008

8. Hanke, M.
Fachgruppe Festkörperanalytik, Universät Halle-Wittenberg, Germany; 4.-9.09.2008

9. Henke, B.
Fachgruppe Festkörperanalytik, Universät Halle-Wittenberg, Germany; 4.-9.09.2008

10. Höglund, C.
Linköping University, Sweden; 18.-26.11.2008

11. Krüger, S.
Institut für Röntgenphysik, Universität Göttingen, Germany; 25.-29.04., 5.-9.09.2008

12. Mahesh, K. K.
CENIMAT, Materials Science Department, Caparaica, Portugal; 6.-12.02.2008

13. Neubauer, H.
Institut für Röntgenphysik, Universität Göttingen, Germany; 25.-29.04., 5.-9.09.2008

14. Novikov, D. V.
HASYLAB at DESY Hamburg, Germany; 8.-15.07.2008

15. Paiva Brito, P.
Max-Plack-Institut für Eisenforschung, Düsseldorf, Germany; 18.-26.03.2008

16. Pinto, H.
Max-Plack-Institut für Eisenforschung, Düsseldorf, Germany; 18.-26.03.2008

17. Prinz, H.
AMD Saxony Dresden, Germany, 10.-17.06.2008

18. Rinderknecht, J.
AMD Saxony Dresden, Germany, 10.-17.06.2008

19. Salditt, T.;
Institut für Röntgenphysik, Universität Göttingen, Germany; 25.-29.04., 5.-9.09.2008

20. Silva Cordeiro, R. J.
CENIMAT, Materials Science Department, Caparaica, Portugal; 6.-12.02.2008

21. Tolkiehn, M.
Institut für Röntgenphysik, Universität Göttingen, Germany; 25.-29.04.2008

22. Walz, B.
HASYLAB at DESY Hamburg, Germany; 8.-15.07.2008

23. Wirth, C.T.
Department of Engineering, University Cambridge, United Kingdom; 17.-21.06., 20.-28.10.2008

24. Zienert, I.
AMD Saxony Dresden, Germany, 10.-17.06.2008

Colloquium

1. Albe, K. – Technische Universität Darmstadt, Germany
   Atomic scale modelling of binary nanoalloys: Structure thermodynamics and ion-beam modification
   24.01.2008

2. Bockstedte, M. – Universität Erlangen-Nürnberg, Germany
   Dopants, defect kinetics and defect identifcation in SiC: The merits of linking theory and experiment
   23.10.2008

3. Bracht, H. – Universität Münster, Germany
   Small but big: Point defects in semiconductors
   11.12.2008

4. Faupel, F. – Universität Kiel, Germany
   Polymer-metal nanocomposites for functional applications
   13.11.2008

5. Gnauck, P. – Carl Zeiss NTS GmbH, Germany
   He ion microscopy - Technology and applications
   30.10.2008

6. Gregorkiewicz, T. – Van der Waals-Zeeman Institute, Netherlands
   Optical spectroscopy of Er-doped Si nanostructures
   6.06.2008

7. Hillebrands, B. – Technische Kaiserslautern, Germany
   Optics with new light: Optics with spin waves
   2.10.2008

8. Horstmann, M. – AMD Saxony LLC & Co. KG Dresden, Germany
   SOI transistor technologies for high performance microprocessors
   3.07.2008

9. Jungwirth, T. - Academy of Sciences of the Czech Republic / University of Nottingham, United Kingdom
   Semiconductor spintronics in ferromagnetic and non-magnetic p-n junctions
   27.11.2008

10. Ronning, C. – Universität Jena, Germany
    Ion beam doping of semiconductor nanowires
    10.07.2008

11. Schenkel, T. – Lawrence Berkeley National Laboratory, Berkeley, USA
    Exploration of quantum computer architectures with spins in silicon and diamond
    4.12.2008

12. Schmidt, O. – Leibniz-Institute für Festkörper- und Werkstoffforschung Dresden, Germany
    Shaped nanomembranes for inderdisciplinary research
    26.06.2008

13. Sigmund, P. – University Odense, Denmark
    Abbremsung schneller Ionen und die damit verbundene Elektronenemission
    10.01.2008

14. Singer, K. - Universität Ulm, Germany
    Experimental demonstration of a deterministic single ion source with an expected implantation resolution of a few nm
    9.10.2008

15. Spiecker, E. – Universität Kiel, Germany
    Quantitative Trnasmissionselektronenmikroskopie an Dünnschichtsystemen, Grenzflächen und Nanostrukturen
    7.02.2008

16. Van de Sanden, M. C. M. – Eindhoven University, Netherlands
    Plasmas, thin films and the solar terawatt challenge
    21.02.2008

17. Wendt, K. – Universität Mainz, Germany
Resonance ionization for selective production, spectroscopy and analytics of exotic species
8.05.2008

Seminars

1. Aharonovich, I. - University of Melbourne, Australia
Controlled formation of single photon centres in diamond for quantum applications
17.01.2008

2. Benyoucef, M. – Institute for Integrative Nanosciences, IFW Dresden, Germany
Single dot spectroscopy
11.07.2008

3. Berkov, D. - Innovent Jena, Germany
Spin-current-induced non-linear magnetization dynamics in nanodevices: Numerical simulations survey
12.12.2008

4. Bernert, K. – Technische Universität Bergakademie Freiberg, Germany
Untersuchung der Ladungsspeicherung in Charge-Trapping-Flash-Speicherzellen
6.06.2008

5. Buljan, M. - Rudjer Boskovic Institute Zagreb, Croatia
Growth and characterization of carbon nanoclusters in amorphous matrix
21.11.2008

6. Bunce, C. - University of York, United Kingdom
TR-MOKE studies of the magnetisation dynamics in magnetite thin-films and in HAMR media
26.08.2008

7. Chason, E. – Brown University, USA
Residual stress during thin film growth: Effect of non-equilibrium conditions
8.10.2008

8. Das Kanungo, P. - MPI für Mikrostrukturphysik Halle, Germany
Ex-situ n- and p- type doping of silicon nanowires by ion implantation
15.12.2008

9. Erbe, A. – Universität Konstanz, Germany
Current transport through molecular structures on the nanometer scale
8.10.2008

10. Gerstl, S. - Imago Scientific Instruments Corp., Madison, USA
Advanced experimental materials research: Atomic scale microscopy in 3-dimensions
9.06.2008

11. Ghosh, S. – Institute of Technology Delhi, India
Nanoscale modification of oxide and nitride films by energetic ions
18.07.2008

12. Heiermann, W. – Forschungszentrum Juelich, Germany
Study of Sb ion implantation in strained and unstrained Si: Rapid thermal & flash lamp annealing
12.11.2008

13. Janisch, R. - University Erlangen-Nürnberg, Germany
DFT Investigation of magnetism in cobalt-doped anatase
3.03.2008

14. Kono, J.- Rice University, Houston, Texas, USA
High-magnetic field phenomena in carbon nanotubes
2.10.2008

15. Kuriplach, J.- University of Prague, Czech Republic
Vacancy – hydrogen complexes in ZnO
11.07.2008

16. Lenk, A. – Triebenberg Lab, Institute of Structure Physics, TU Dresden, Germany
Influence of FIB-preparation on the potential structure of complementarily doped semiconductors

investigated by electron-holographic methods
30.04.2008

17. Lenz, K. – Freie Universität Berlin, Germany
Ferromagnetic resonance – a smart tool to study static and dynamic magnetic properties
28.01.2008

18. Lenz, K. – Freie Universität Berlin, Germany
Ferromagnetic resonance to study dynamic phenomena
23.04.2008

19. Léotin, J. - Laboratoire National de Champs Magnétiques Pulsés, Toulouse, France
Magneto-spectroscopy of AlP quantum wells
27.05.2008

20. Mattheis, R. - IPHT Jena, Germany
Domain walls in GMR nanowires and their application in new magnetoelectronic devices
1.12.2008

21. Mazarov, P. - Ruhr-Universität Bochum, Germany
Entwicklung einer Wismut-Flüssigmetallionenquelle (Bi LMIS) und ihre Anwendung in der Oberflächenmodifizierung und –analyse
11.09.2008

22. Moser, J. - Universität Konstanz, Germany
Magnetoresistive effects in Co/Pd multilayers on self-assembled nanospheres
21.01.2008

23. Nazarov, A. N. - National Academy of Sciences of the Ukraine Kyiv, Ukraine
Charge trapping, electroluminescence and clustering in RE implanted Si-based MOSLEDs
10.07.2008

24. Nazarov, A. N. - National Academy of Sciences of the Ukraine Kyiv, Ukraine
Hydrogen plasma treatment of ion implanted SiO_2-Si structures
8.09.2008

25. Ney, A. – Universität Duisburg-Essen, Germany
ZnO- and GaN- based DMS – Is there still hope for intrinsic ferromagnetism?
7.04.2008

26. Prucnal, S. - Marie-Sklodowska-Curie University, Lublin, Poland
Stable MOS Light emitting devices with rare earth´s and germanium: Mechanism of electroluminescence
28.04.2008

27. Radu, I. – Universität Regensburg, Germany
Ultrafast dynamics of the laser-induced magnetic phase transitions on FeRh alloy
24.04.2008

28. Shorubalko, I. - ETH Zürich, Switzerland
Gate-defined and etched quantum dots in InAs nanowires
8.10.2008

29. Sordan, R. - Interuniversity Center Como, Italy
Nanoelectronic and nanofluidic devices in two-dimensional systems
13.10.2008

30. Spoddig, D. – Universität Leipzig, Germany
Anisotropy of magnetic parameters, damping and g-factor in magnetic heterostructures detected by conventional and locally resolved FMR
24.04.2008

31. Utke, I. - EMPA Material Science and Technology, Switzerland
Nanofabrication with focused electron and ion beams
10.10.2008

32. Wolny, F. – Leibniz Institut für Frestkörper- und Werkstoffforschung Dresden, Germany
Iron filled carbon nanotubes as probes for magnetic force microscopy
9.04.2008

33. Zhang, X. - MPI für Festkörperforschung Stuttgart, Germany
Growth mechanism and structural properties of di-indenoperylene on metal and dielectric surfaces
26.08.2008

Projects

1. 03/2004 – 02/2009 European Union EU
IA-SFS - Integrating activity on synchrotron and free electron laser science
Prof. M. Helm Tel.: 0351 260-2260 m.helm@fzd.de

2. 11/2004 – 12/2009 Silicon Sensor Berlin GmbH Industry
Hochenergie-Ionenimplantation für optische Sensoren
Dr. J. von Borany Tel.: 0351 260 3378 j.v.borany@fzd.de

3. 01/2005 – 12/2008 European Union EU
EuroMagNET – A coordinated approach to access, experimental development and scientific exploitation of European large infrastructures for high magnetic fields
Prof. M. Helm Tel.: 0351 260 2260 m.helm@fzd.de

4. 04/2005 – 03/2010 European Union EU
PRONANO – Technology for the production of massively parallel intelligent cantilever-probe platforms for nanoscale analysis and synthesis
Dr. B. Schmidt Tel.: 0351 260 2726 bernd.schmidt@fzd.de

5. 06/2005 – 06/2008 Deutsche Forschungsgemeinschaft DFG
Mössbauerspektroskopie an ionenimplantierten magnetischen Halbleitern
Dr. H. Reuther Tel.: 0351 260 2898 h.reuther@fzd.de

6. 09/2005 – 02/2010 European Union EU
FOREMOST – Fullerene-based opportunities for robust engineering: Making optimised surfaces for tribology
Prof. A. Kolitsch Tel.: 0351 260 3348 a.kolitsch@fzd.de

7. 01/2006 - 12/2009 European Union EU
ITS-LEIF - Ion technology and spectroscopy at low energy ion beam facilities
Dr. S. Facsko Tel.: 0351 260 2987 s.facsko@fzd.de

8. 02/2006 - 01/2010 European Union EU
AIM - Center for application of ion beams to materials research
Prof. A. Kolitsch Tel.: 0351 260 3348 a.kolitsch@fzd.de

9. 07/2006 - 10/2009 Deutsche Forschungsgemeinschaft DFG
Magnetschicht (FOR520)
Dr. S. Gemming Tel.: 0351 260 2470 s.gemming@fzd.de

10. 12/2006 - 11/2008 Qimonda Dresden Industry
Ionenstreu-Analysen an Halbleiter-Materialien
Dr. R. Grötzschel Tel.: 0351 260 3294 r.groetzschel@fzd.de

11. 12/2006 - 11/2008 Arbeitsgemeinschaft industrieller Forschungsvereinigungen AiF
Nanomorph - Amorphe Nanostrukturen
Prof. A. Kolitsch Tel.: 0351 260 3348 a.kolitsch@fzd.de

12. 11/2006 – 06/2008 SARAD GmbH Industry
Entwicklung und Herstellung von ionenimplantierten Si-Strahlungsdetektoren
Dr. B. Schmidt Tel.: 0351 260 2726 bernd.schmidt@fzd.de

13. 12/2006 – 12/2009 VKTA e.V. Dresden Bilateral
Durchführung von REM- bzw. EDX- sowie Mössbauer-spektroskopischen Untersuchungen an Metallproben
Dr. H. Reuther Tel.: 0351 260 2898 h.reuther@fzd.de

14. 02/2007 - 03/2008 Alexander-von-Humboldt-Stiftung AvH
Gastaufenthalt Dr. C. Grimm
Prof. M. Helm Tel.: 0351 260 2260 m.helm@fzd.de

15. 004/2007 - 03/2009 Arbeitsgemeinschaft industrieller Forschungsvereinigungen AiF
Unterdrückung der Sauerstoffversprödung von Titanlegierungen
Prof. A. Kolitsch Tel.: 0351 260 3348 a.kolitsch@fzd.de

16. 04/2007 - 03/2010 Deutsche Forschungsgemeinschaft DFG
Ion-beam induced rippling at the amorphous-crystalline interface in silicon
Dr. J. Grenzer Tel.: 0351 260 3389 j.grenzer@fzd.de

17. 05/2007 - 06/2009 Deutsche Forschungsgemeinschaft DFG
Strukturübergänge eingebetteter magnetischer Nanopartikel
Dr. K. Potzger Tel.: 0351 260 3148 k.potzger@fzd.de

18. 07/2007 - 12/2008 Deutsche Forschungsgemeinschaft DFG
Hybride Magnetische Materialien
Dr. J. Fassbender Tel.: 0351 260 3096 j.fassbender@fzd.de

19. 08/2007 - 07/2009 Arbeitsgemeinschaft industrieller Forschungsvereinigungen AiF
Grenzen des Halogeneffektes für TiAl-Hochtemperaturleichtbaulegierungen unter industriellen Bedingungen
Prof. A. Kolitsch Tel.: 0351 260 3348 a.kolitsch@fzd.de

20. 08/2007 - 11/2010 Deutsche Forschungsgemeinschaft DFG
Nanostrukturierung von Oberflächen mit direkter Extraktion der Ionen aus Plasmaquellen
Dr. S. Facsko Tel.: 0351 260 2987 s.facsko@fzd.de

21. 08/2007 - 10/2010 Deutsche Forschungsgemeinschaft DFG
Selbstorganisierte Nanostrukturen durch niederenergetische Ionenstrahlerosion
Dr. K.-H. Heinig Tel.: 0351 260 3288 k.h.heinig@fzd.de

22. 08/2007 - 08/2008 Bundesministerium für Bildung und Forschung BMBF
Magnetoelektronik ferromagnetischer Traps
Dr. H. Schmidt Tel.: 0351 260 2724 heidemarie.schmidt@fzd.de

23. 08/2007 - 02/2009 Deutsche Forschungsgemeinschaft DFG
Ferromagnetism in transition metal doped ZnO
Dr. H. Schmidt Tel.: 0351 260 2724 heidemarie.schmidt@fzd.de

24. 09/2007 - 08/2009 European Union EU
TEMPUS courses of materials science
Prof. W. Möller Tel.: 0351 260 2245 w.moeller@fzd.de

25. 09/2007 - 02/2008 AMD Saxony Industry
Experimente an ROBL-Beamline
Dr. J. von Borany Tel.: 0351 260 3378 j.v.borany@fzd.de

26. 09/2007 - 10/2010 Deutsche Forschungsgemeinschaft DFG
Infrared scattering near-field optical microscopy near dielectric (polaritonic) resonances using a free-electron laser
Prof. M. Helm Tel.: 0351 260 2260 m.helm@fzd.de

27. 10/2007 - 08/2009 Alexander-von-Humboldt-Stiftung AvH
Gastaufenthalt Dr. A. Kanjilal
Prof. M. Helm Tel.: 0351 260 2260 m.helm@fzd.de

28. 10/2007 - 09/2009 Dechema Dechema
Haifischhaut
Prof. A. Kolitsch Tel.: 0351 260 3348 a.kolitsch@fzd.de

29. 11/2007 - 10/2009 Eifeler GmbH Industry
Technologietransfer c-BN II
Prof. A. Kolitsch Tel.: 0351 260 3348 a.kolitsch@fzd.de

30. 12/2007 - 11/2009 Deutsche Forschungsgemeinschaft DFG
Mössbauerspektroskopie an magnetischen Halbleitern II
Dr. H. Reuther Tel.: 0351 260 2898 h.reuther@fzd.de

31. 12/2007 - 05/2010 Qimonda Dresden GmbH Industry
NanoAnalytik
Dr. J. von Borany Tel.: 0351 260 3378 j.v.borany@fzd.de

32. 01/2008 - 12/2008 SGS Institut Fresenius GmbH Industry
Struktur- und Elementanalytik Fresenius
Dr. J. von Borany Tel.: 0351 260 3378 j.v.borany@fzd.de

33. 01/2008 - 01/2009 IXYS Semiconductor GmbH Industry
Laserannealing
Dr. J. von Borany Tel.: 0351 260 3378 j.v.borany@fzd.de

34. 01/2008 - 12/2009 Deutscher Akademischer Austauschdienst DAAD
Projektbezogener Personenaustausch mit Hongkong
Dr. W. Skorupa Tel.: 0351 260 3612 w.skorupa@fzd.de

35. 01/2008 - 12/2009 Deutscher Akademischer Austauschdienst DAAD
Projektbezogener Personenaustausch mit Ungarn
Dr. K.-H. Heinig Tel.: 0351 260 3288 k.h.heinig@fzd.de

36. 01/2008 - 12/2009 Deutsche Forschungsgemeinschaft DFG
Oxidkristalle
Dr. S. Gemming Tel.: 0351 260 2470 s.gemming@fzd.de

37. 01/2008 - 12/2009 Deutsche Forschungsgemeinschaft DFG
Ferroelektrika
Dr. S. Gemming Tel.: 0351 260 2470 s.gemming@fzd.de

38. 02/2008 - 02/2010 Deutsche Forschungsgemeinschaft DFG
Hybridmodell II
Dr. S. Gemming Tel.: 0351 260 2470 s.gemming@fzd.de

39. 03/2008 - 10/2008 Sächsisches Staatsministerium für Wissenschaft und Kunst SMWK
6-MV-Tandetron
Prof. W. Möller Tel.: 0351 260 2245 w.moeller@fzd.de

40. 05/2008 - 12/2008 AMD Industry
Synchrotronuntersuchungen an der Beamline ROBL
Dr. J. von Borany Tel.: 0351 260 3378 j.v.borany@fzd.de

41. 05/2008 - 12/2008 Sunfilm AG Großröhrsdorf Industry
Raman-Messungen
Dr. J. v. Borany Tel.: 0351 260 3378 j.v.borany@fzd.de

42. 05/2008 - 04/2010 FHR Anlagenbau Ottendorf-Okrilla/IHP Frankfurt/O. Industry
Blitztemperung 200
Dr. W. Skorupa Tel.: 0351 260 3612 w.skorupa@fzd.de

43. 07/2008 - 12/2010 Bundesministerium für Bildung und Forschung WTZ
WTZ Russland: Duplexbehandlung rostfreier Stähle
Prof. A. Kolitsch Tel.: 0351 260 3348 a.kolitsch@fzd.de

44. 07/2008 - 06/2011 Deutsche Forschungsgemeinschaft DFG
Morphologie-induzierte magnetische Anisotropie- und Dämpfungsphänomene
Dr. J. Fassbender Tel.: 0351 260 3096 j.fassbender@fzd.de

45. 07/2008 - 07/2011 Bundesministerium für Bildung und Forschung BMBF
Multifunktionale Speicherkonzepte
Dr. J. Fassbender Tel.: 0351 260 3096 j.fassbender@fzd.de

46. 09/2008 - 12/2010 TU Dresden Bilateral
Modellieren der Bedeckung keramischer Oberflächen mit Wachstumsproteinen (BIOMIN)
Dr. S. Gemming Tel.: 0351 260 2470 s.gemming@fzd.de

47. 11/2008 - 02/2009 BASF Ludwigshafen Industry
Ionenimplantation BASF
Prof. A. Kolitsch Tel.: 0351 260 3348 a.kolitsch@fzd.de

48. 12/2008 - 12/2008 Sächsisches Staatsministerium für Wissenschaft und Kunst SMWK
Kopplung eines 6MV-Beschleunigers für Hochenergieionenstrahlen mit Experimentierkammern der Ionenstrahlanalytik des Ionenstrahlzentrums im Forschungszentrum Dresden-Rossendorf
Prof. A. Kolitsch Tel.: 0351 260 3348 a.kolitsch@fzd.de

49. 12/2008 – 02/2009 Zeiss NTS Oberkochen Industry
Entwicklung und Test von Legierungs-Flüssigmetall-Ionenquellen
Dr. W. Pilz Tel.: 0351 260 3101 w.pilz@fzd.de

Experimental Equipment

1. Accelerators, Ion Implanters and Ion-Assisted-Deposition

⇒	Van de Graaff Accelerator	(VdG)	1,8 MV	*TuR Dresden, DE*
⇒	Tandem Accelerator	(Td)	5 MV	*NIIEFA, RU*
⇒	Tandetron Accelerator	(Tdtr)	3 MV	*HVEE, NL*
⇒	Low-Energy Ion Implanter		0.5 - 50 kV	*Danfysik, DK*
⇒	High-Current Ion Implanter		20 - 200 kV	*Danfysik, DK*
⇒	High-Energy Ion Implanter		40 - 500 kV	*HVEE, NL*
⇒	Plasma Immersion Ion Implantation		5 - 60 keV	*GBR, DE/Home-built*
⇒	Focused Ion Beam (15 nm)		30 keV, 10 A/cm²	*Orsay Physics, FR*
⇒	Highly-Charged Ion Facility		25 eV – 25 keV × Q Q = 1…40 (Xe)	*Home-built*
⇒	Dual-Beam Magnetron Sputter Deposition			*Roth & Rau, DE*
⇒	Ion-Beam-Assisted Deposition			*Danfysik, DK*
⇒	Ion-Beam Sputtering		200 - 2000 V	*Home-built*
⇒	UHV Ion Irradiation (Ar, He, etc.)		0 - 5 keV Scan 10×10 mm²	*VG, USA*

2. Ion Beam Analysis (IBA)

A wide variety of advanced IBA techniques are available at the MeV accelerators (see figure).

⇒	RBS	Rutherford Backscattering	(1), (2), (3), (8)	*VdG, Td, Tdtr*
⇒	RBS/C	RBS + Channelling	(1), (2), (3), (8)	*VdG, Td, Tdtr*
		High-Resolution RBS/C	(7), (10)	*Tdtr*
⇒	ERDA	Elastic Recoil Detection Analysis	(2), (4), (5)	*VdG, Td*
		High-resolution ERDA	(7)	*Td*
⇒	PIXE	Proton-Induced x-ray Emission	(3)	*Td*
⇒	PIGE	Proton-Induced γ Emission	(3)	*Td*
⇒	NRA	Nuclear Reaction Analysis	(4)	*Td*
⇒	NRRA	Nuclear Resonance Reaction Analysis	(6)	*Td*
⇒	NμP	Nuclear Microprobe	(9)	*Tdtr*

Some stations are equipped with additional process facilities which enable *in-situ* IBA investigations during ion irradiation, sputtering, deposition, annealing etc.

3. Other Particle Based Analytical Techniques

⇒	SEM	Scanning Electron Microscope	1 - 30 keV + EDX	*Hitachi, JP*
⇒	TEM	Transmission Electron Microscope (Titan 80-300 with Image Corrector)	80 - 300 keV + EDX, +GIF	*FEI, NL*
⇒	FIB/SEM	Focused Ion / Electron Cross Beam (NVision 40 with Elphy Plus Litho)	0.5 – 30 keV + IL, + EDX	*Zeiss-NTS, DE* *Raith, Bruker, DE*
⇒	AES	Auger Electron Spectroscopy	+ XPS	*Fisions, UK*
⇒	CEMS	Mössbauer Spectroscopy	^{57}Fe source	*Home-built*
⇒	PAS	Positron Annihilation Spectroscopy	^{22}Na source 30 V - 36 kV	*Home-built*

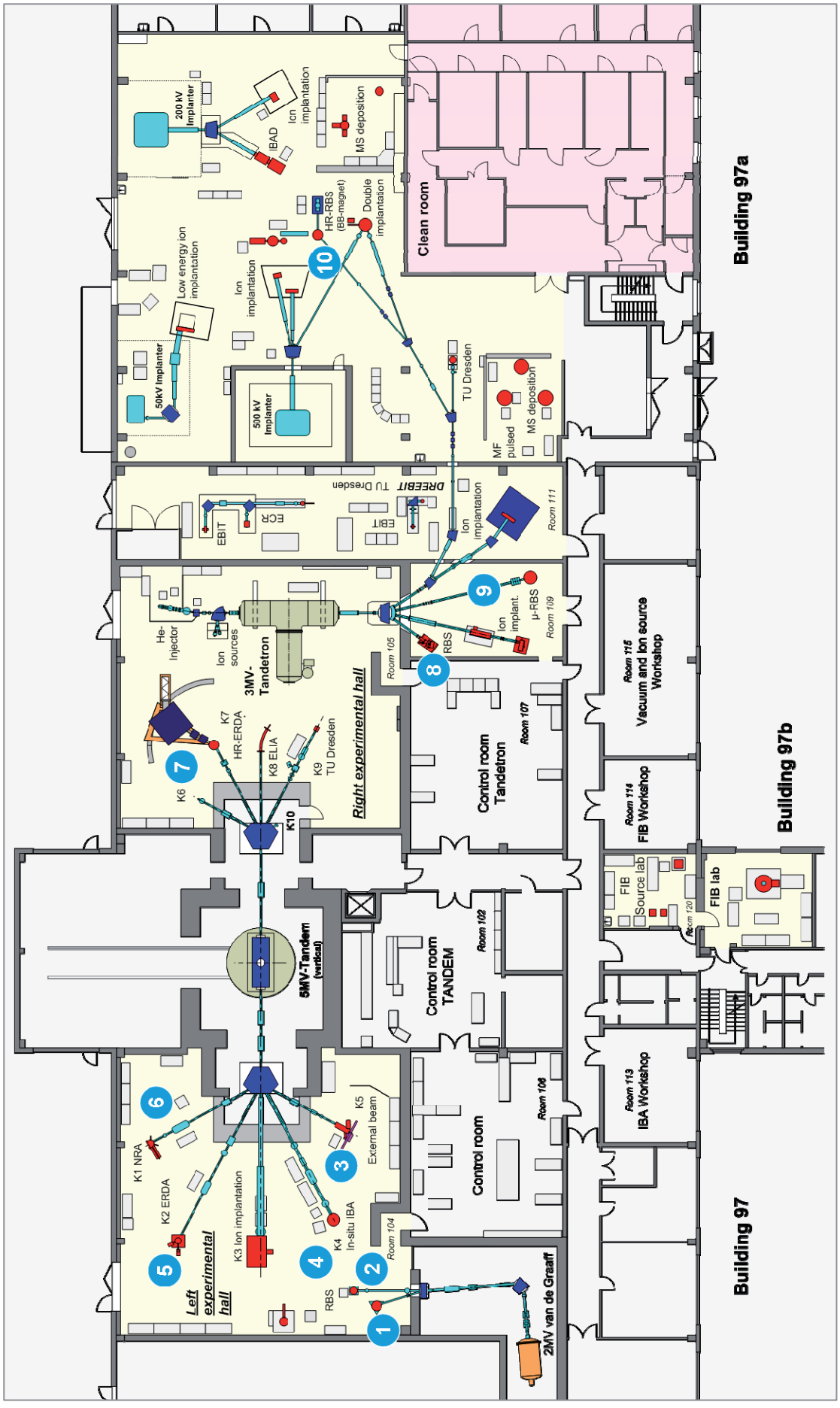

Ion Beam Centre: Schematic Overview of Installations.

4. Photon Based Analytical Techniques

⇒	XRD/XRR	X-Ray Diffraction and Reflection	Cu-K_α	*Bruker axs, DE*
	HR-XRD	High-Resolution XRD	Cu-K_α	*GE Inspection, DE*
⇒	XRD/XRR	with Synchrotron Radiation	5 – 35 keV	*ROBL at ESRF, FR*
⇒	SE	Spectroscopic Ellipsometry	250 - 1700 nm	*Woolam, US*
⇒	FTIR	Fourier-Transform Infrared Spectr.	600 - 7000 cm^{-1}	*Nicolet, US*
⇒	FTIR	Fourier-Transform Infrared Spectr.	50 - 15000 cm^{-1}	*Bruker, DE*
⇒		Ti:Sapphire Femtosecond Laser		*Spectra Physics, US*
⇒		Femtosecond Optical Parametric Osci.		*APE, DE*
⇒		Ti:Sapphire Femtosecond Amplifier		*Femtolasers, AT*
⇒		Femtosecond Optical Parametric Amplifier		*Light Conversion, LI*
⇒	THz-TDS	Terahertz Time-Domain Spectroscopy	0.1 - 4 THz	*Home-built*
⇒	Raman	Raman Spectroscopy	45 cm^{-1} shift	*Jobin-Yvon-Horiba, FR*
⇒	PL	Photoluminescence	300 - 1500 nm	*Jobin-Yvon-Horiba, FR*
⇒	TRPL	Time-Resolved PL	τ = 3 ps - 2 ns	*Hamamatsu Phot., JP*
			τ > 5 ns	*Stanford Research, US*
⇒	EL	Electroluminescence (10-300 K)	300 - 1500 nm	*Jobin-Yvon-Horiba, FR*
		Optical Split-Coil Supercond. Magnet	7 T	*Oxford Instrum., UK*
⇒	PR	Photomodulated Reflectivity	300 - 1500 nm	*Jobin-Yvon-Horiba, FR*
⇒	PLE	Photoluminescence Excitation	300 - 1500 nm	*Jobin-Yvon-Horiba, FR*

5. Magnetic Thin Film Deposition and Analysis

⇒	MBE	Molecular Beam Epitaxy with in-situ FIB		*CreaTec, DE*
⇒	MBE	Molecular Beam Epitaxy		*Home-built*
⇒	PLD	Pulsed Laser Deposition		*SURFACE, DE*
⇒	MFM	Magnetic Force Microscope	~ 50 nm resol.	*VEECO / DI, US*
⇒	SQUID	Supercond. Quantum Interf. Device	± 7 T	*Quantum Design, US*
⇒	MOKE	Magneto-Optic Kerr Effect (in-plane)	± 0.35 T	*Home-built*
⇒	MOKE	Magneto-Optic Kerr Effect (perpend.)	± 2 T	*Home-built*
⇒	SKM	Scanning Kerr Microscope		*Home-built*
⇒	TR-MOKE	Time-Resolved MOKE (Pump-Probe)		*Home-built*
⇒	VNA-FMR	Vector Network Analyzer Ferromagnetic Resonance		*Agilent / Home-built*
⇒	ME	Magnetoellipsometer		*LOT, DE; AMAC, US*

6. Other Analytical and Measuring Techniques

⇒	STM	Scanning Tunneling Microscope (with AFM-Option)		*DME, DK*
⇒	STM	*In-situ* Scanning Tunneling Microscope (T variable)		*Omicron, DE*
⇒	AFM	Atomic Force Microscope (Tapping Mode)		*SIS, DE*
⇒	AFM	Atomic Force Microscope (with c-AFM, SCM-Module)		*Veeco Instruments, UK*
⇒	KFM	Kelvin Probe Force Microscopy		*Anfatec, DE*
⇒		Dektak Surface Profilometer		*Veeco, US*
⇒		Micro Indenter / Scratch Tester		*Shimatsu, JP*
⇒		Wear Tester (pin-on disc)		*Home-built*
⇒	SRP	Spreading Resistance Profiling		*Sentech, DE*
⇒	HE	Hall Effect Equipment	(2 - 400 K, ≤ 9 T)	*LakeShore, US*
⇒	DLTS	Deep Level Transient Spectroscopy	(+ IU / CV) (10 - 300 K, 1 MHz)	*PhysTech, DE*
⇒		Photocapacitance (+I-U/G-V)	(250 - 2500 nm)	*Home-built*
⇒		I-V and C-V Analyzer		*Keithley, US*
⇒		I-V and C-V Semi-Automatic Prober	(-60°C - +300°C)	*Süss, DE; Keithley, US*

7. Processing and Preparation Techniques

⇒	Etching / Cleaning	incl. Anisotropic Selective KOH Etching	
⇒	Photolithography	Mask-Aligner, 2 µm-level	*Süss, DE*
⇒	Thermal Treatment	Room Temperature - 2000°C	
	• Furnace		*InnoTherm, DE*
	• Rapid Thermal Annealing		*ADDAX, FR*
	• Flash-Lamp Units (0.5 – 20 ms)		*Home-built; FHR, DE*
	• RF Heating (Vacuum)		*JIP.ELEC, FR*
⇒	Physical Deposition	Sputtering DC / RF, Evaporation	*Nordiko, UK*
		Electron Beam Evaporation System	*Leybold Optics, DE*
⇒		Thermal Evaporation	*Bal-Tec, LI*
⇒	Dry Etching	Plasma and RIE Mode	*Sentech, DE*
⇒	Bonding Techniques	Ultrasonic Wire Bonding	*Kulicke&Soffa, US*
⇒	Cutting, Grinding, Polishing		*Bühler, DE*
⇒	TEM Sample Preparation	Plan View and Cross Section incl. Ion Milling Equipment	*Gatan, US*

Services

Main Areas of Competence:

- Ion implantation in a broad range of ion energy (~ 200 eV to ~ 50 MeV) and substrate temperature
- Advanced ion beam technologies (high energy ion implantation, plasma immersion ion implantation, focused ion beam) for (micro)electronic applications
- Deposition of functional coatings using ion-assisted physical vapor deposition
- Development and fabrication of sensors and detectors for charged particle spectroscopy
- High energy ion implantation service for power devices and laser structures
- Doping of semiconductors, in particular wide bandgap semiconductors
- Surface analysis of solid materials with high energy ion beams
- Computer simulation of ion beam interaction with materials
- Optical characterization of materials (luminescence, FTIR, Raman)

Offers:

- Consultation and problem evaluation for ion beam applications
- Process development for ion beam processing of metals, ceramics, semiconductors, thin films
- Preparation and treatment of material samples, tools or complex parts of devices
- Ion implantation and ion beam analysis services
- Preparation / fabrication of semiconductors or silicon radiation sensors under clean room conditions
- Structural diagnostics of materials surfaces including e-beam- (SEM, TEM, AES) and X-ray techniques (XRD, XRR with both Cu-K and Synchrotron (5-35 keV) radiation).

Contact:

Please direct your inquiry about the application of ion beams for modification and analysis of materials to one of the following experts:

Field of application	Name	Phone / Fax	E-mail
Ion implantation (metals, ceramics, polymers, biomaterials)	Prof. Andreas Kolitsch	3348 / 2703	a.kolitsch@fzd.de
Ion implantation (semiconduc-tors, in particular high energy)	Dr. Johannes von Borany	3378 / 3438	j.v.borany@fzd.de
Thin film deposition	Prof. Andreas Kolitsch	3348 / 2703	a.kolitsch@fzd.de
High energy ion beam analysis	Dr. Rainer Grötzschel	3294 / 2870	r.groetzschel@fzd.de
Semiconductor preparation, Detector / Sensor fabrication	Dr. Bernd Schmidt	2726 / 3285	bernd.schmidt@fzd.de
Focused ion beams	Dr. Lothar Bischoff	2963 / 3285	l.bischoff@fzd.de
Structural diagnostics	Dr. Johannes von Borany	3378 / 3438	j.v.borany@fzd.de
Materials research with Synchro-tron radiation at ROBL (ESRF)	Dr. Carsten Bähtz	2367 / 2505	baehtz@esrf.fr
Optical materials characterization	Dr. Harald Schneider	2880 / 3285	h.schneider@fzd.de

For all phone/ fax-numbers choose the country / local code: +49 351 260 - (for FZD)
+33 47 688 - (for ROBL)

The institute also recommends the homepages of its spin-off companies

- "GeSiM mbH" www.gesim.de
- "APT Dresden" www.apt-dresden.de
- "IONServices" www.ions.de

Forschungszentrum Dresden - Rossendorf e.V.

Institute of Ion Beam Physics and Materials Research (IIM)

Postfach 51 01 19
D-01314 Dresden

Tel.: 0351 260 2245
Fax: 0351 260 3285
http://www.fzd.de/FWI

DIRECTORS

Prof. Dr. Wolfhard Möller 2245

Prof. Dr. Manfred Helm 2260

DIVISIONS

ION TECHNOLOGY (FWII)
Prof. Dr. Andreas Kolitsch / 3326

- MeV accelerators
- Ion Implanter / PIII operation
- Ion Beam and Plasma Assisted Deposition
- Biotechnological Materials
- Industrial Services and Projects

SEMICONDUCTOR MATERIALS (FWIM)
Dr. Wolfgang Skorupa / 3612

- Semiconductors
- Optoelectronic Applications
- Rapid Thermal Annealing Processes
- Defect Engineering
- Positron Annihilation Spectroscopy

NANOFUNCTIONAL FILMS (FWIN)
Dr. Jürgen Fassbender / 3096

- Modification of Magnetic Materials
- High Anisotropy Nanoparticles
- Magnetic Semiconductors / Spintronics
- Magnetization Dynamics
- Fullerene-like Materials

SEMICONDUCTOR SPECTROSCOPY (FWIH)
Dr. Harald Schneider / 2880

- Semiconductor Quantum Structures
- Terahertz Spectroscopy
- Femtosecond Spectroscopy
- Free Electron Laser at ELBE
- Optical Characterization (PL, FTIR, Raman)

ION BEAM ANALYSIS (FWIA)
Dr. Rainer Grötzschel / 3294

- Ion-Solid-Interaction
- High-Energy Ion Beam Analysis
- Channeling Studies of Crystal Defects
- Non-destructive Analysis of Art Objects
- Composition / Modification of Materials

STRUCTURAL DIAGNOSTICS (FWIS)
Dr. Johannes von Borany / 3378

- Electron Microscopy (TEM, SEM)
- Electron Spectroscopy (AES, XPS)
- Mössbauer Spectroscopy
- X-ray Analysis
- Materials Research with Synchr. Radiation

THEORY (FWIT)
Dr. Matthias Posselt / 3279

- Ion-Beam Synthesis of Nanostructures
- Formation and Evolution of Defects
- Atomistic Simulation of Ion implantation and Ion-Assisted Deposition
- Interatomic Potentials for Solids
- Reaction-Diffusion-Models

PROCESS TECHNOLOGY (FWIP)
Dr. Bernd Schmidt / 2726

- Semiconductor Technology
- Focused Ion Beam Technology
- Thin Film Deposition
- Computer Aided Structure Design
- Electrical Characterization
- Clean Room Operation

List of Personnel 2008

Directors: Prof. W. Möller, Prof. M. Helm

Office: S. Kirch, L. Post

Scientific Staff:

Permanent:

Dr. G. Abrasonis
Dr. C. Akhmadaliev
Dr. C. Bähtz
Dr. L. Bischoff
Dr. J. von Borany
Dr. S. Facsko
Dr. J. Fassbender
Dr. S. Gemming
Dr. J. Grenzer
Dr. R. Grötzschel
Dr. V. Heera
Dr. K.-H. Heinig
Dr. R. Kögler
Prof. A. Kolitsch
Dr. S. Merchel
Dr. A. Mücklich
Dr. F. Munnik
Dr. C. Neelmeijer
Dr. M. Posselt
Dr. K. Potzger
Dr. L. Rebohle
Dr. H. Reuther
Dr. A. Rogozin
Dr. B. Schmidt
Dr. H. Schneider
Dr. W. Skorupa
Dr. D. Stehr
Dr. M. Voelskow
Dr. S. Winnerl

Post Docs:

Dr. N. Jeutter
Dr. G. Kovacs
Dr. K. Küpper
Dr. K. Lenz
Dr. Z. Pesic
Dr. S. Zhou

Projects:

W. Anwand
Dr. G. Brauer
Dr. C. Bunce
Dr. W. Bürger
Dr. O. Drachenko
Dr. M. Friedrich
Dr. D. Grambole
Dr. C. V.-B. Grimm
Dr. A. Kanjilal
Dr. M. Krause
Dr. M. O. Liedke
Dr. K. Morawetz
V. Pankoke
Dr. W. Pilz
D. Reichel
Dr. H. Schmidt
Dr. A. Shalimov
Dr. N. Shevchenko
Dr. M. Vinnichenko
Dr. Q. Xu
Dr. R. Yankov
Dr. M. Zier

PhD Students:

C. Baumgart
M. Berndt
K. Bernert
V. Beyer
D. Bürger
V. Cantelli
R. Cheng
C. Cherkouk
A. Dreyhaupt
M. Fritsche
A. Hanisch
R. Heller
R. Jacob
A. Keller
M. Kosmata
T. Kunze
B. Liedke
R. Mukesh
D. Markó
A. Martinavicius
S. Numazawa
X. Ou
H. Peng
F. Peter
J. Potfajova
H. G. von Ribbeck
O. Roshchupkina
C. Scarlat
M. Schmidt
A. Silze
T. Strache
G. Talut
M. Thieme
M. Vieluf
M. Wagner
S. Wintz
C. Wündisch
J. Zhou
M. Zschintzsch
M. Zschornak
S. Zybell

Diploma Students:

A. Bollmann
S. Cornelius
F. Fischer
A.-A. Gabriel
R. Hubrich
O. Kallauch
J. König
M. Körner
J. Lehmann
K. M. Mok
S. Nitsche
C. Pfau
S. Schreiber
M. Seeger
B. Zimmermann

Technical Staff:

Permanent:

Rb. Aniol
Ry. Aniol
G. Anwand
E. Christalle
H. Felsmann
B. Gebauer
H.-J. Grahl
D. Hanf
J. Haufe
A. Henschke
G. Hofmann
S. Klare
J. Kreher
A. Kunz
H. Lange
U. Lucchesi
F. Ludewig
R. Mester
M. Mißbach
C. Neisser
S. Probst
E. Quaritsch
A. Reichel
M. Roch
B. Scheumann
G. Schnabel
A. Schneider
J. Schneider
A. Scholz
T. Schumann
U. Strauch
K. Thiemig
A. Vetter
J. Wagner
R. Weidauer
A. Weise
J. Winkelmann
G. Winkler
I. Winkler
L. Zimmermann
J. Zscharschuch

Projects:

S. Eisenwinder
M. Steinert
I. Skorupa